Effects of plastic strain history on the properties of stainless steel boiler tube welds

Thesis

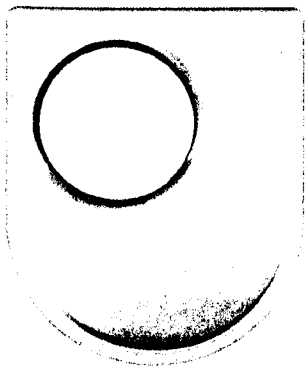

The Open University

Faculty of Mathematics, Computing & Technology

Department of Design, Development, Environment and Materials

EFFECTS OF PLASTIC STRAIN HISTORY ON THE PROPERTIES OF STAINLESS STEEL BOILER TUBE WELDS

by

Murat Özgün ACAR

December 2011

A THESIS SUMMITTED TO THE DEPARTMENT OF DESIGN, DEVELOPMENT, ENVIRONMENT AND MATERIALS OF THE OPEN UNIVERSITY FOR THE DEGREE OF DOCTOR OF PHILOSOPHY

DATE OF SUBMISSION : 9 DEC 2011

DATE OF AWARD : 2 APR 2012

Abstract

The subject of this dissertation is the study of the effects of fabrication history (prestraining, welding and heat treatment) on the mechanical properties of austenitic stainless steel thin wall boiler tubes. These tubes are usually cold bent to shape, and sometimes swaged, prior to interconnection by welding. The bends require solution heat treatment before welding. In addition, subsequent to welding, the residual stresses should be relieved. It is sometimes not practically feasible to follow these constructional practices strictly especially when a whole boiler is constructed as a single unit and becomes too large and complex and contains different tubing materials. As a result of this fabrication history, the mechanical properties of boiler tube materials can be significantly altered. Sample tubes simulating the fabrication steps were supplied by British Energy for this project. The primary aim of the study was to determine spatially resolved room-temperature tensile properties using digital image correlation (DIC) by testing cross-weld specimens machined from the thin wall welded tubes (with plain or prestrained base metal) before and after the heat treatment. The experimental procedure which is used to retrieve the tensile properties from these integrated tests was validated through finite element simulation.

Digital image correlation, which is a full-field strain measurement technique, was implemented in order to obtain the local stress-strain curves from regions less than a square millimetre in area and to extract the corresponding local tensile properties such as offset proof strength. The variation of the 0.2% offset proof strength was successfully obtained along these specimens. Evidence of strain hardening due to constraint and weld thermomechanical cycles was found in the plain base metal near the weld pool and evidence of softening was seen in prestrained base metal. On the other hand, after the heat treatment, the effect of prestraining and welding is cleaned out and the strength along the specimen was almost homogenized. However, as-welded cross-weld specimens with prestrained base metal have demonstrated unusual local stress-strain behavior in the weld-affected region. For a better understanding of this behavior, tension test of a cross-weld specimen with a high strength mismatch between the weld metal and base metal was simulated using the finite element method. It was found that the strength mismatch in the specimen, in combination with the experimental procedure, may cause some anomalies in the local stress-strain curves. It was also confirmed that these anomalies are not very detrimental for the determination of the proof strength on the specimens with strength mismatch.

Material characterization of the welds and detailed hardness surveys on cross-weld specimens were performed. Plastic strain is known to be detrimental for high temperature performance of austenitic stainless steel tubes, therefore, the degree of the plastic deformation should be known before these tubes enter service. DIC, hardness, electron back-scattered diffraction and neutron diffraction (peak width and anisotropy strain) were used to determine the amount of plastic strain in the as-welded tubes. It was observed that there is a good agreement between the predictions of plastic strain in 20% prestrained and welded tube.

Acknowledgement

I would like to acknowledge the Open University for giving me this opportunity to do my PhD study and its financial support. I am grateful to British Energy Generation Limited for funding support as well as the material for this dissertation.

I would like to thank my supervisors Dr. Salih Gungor and Prof. Mike Fitzpatrick for their continuous support, guidance and encouragement. I am also thankful to Prof. John Bouchard for his valuable contribution and guidance during this study. Special thanks to Dr. Joao Fonseca for his contribution to the neutron diffraction experiments and the related conference publication.

I am indebted to Mike Spindler and Dave Dean, who are working in structural integrity group at British Energy, for their enormous technical advice and help in getting this project together.

I would like to acknowledge Peter Ledgard for his high-skilled workshop assistance, Stan Hiller for his instruction and help on metallography, and Gordon Imlach for his support and advice on electron microscopy and electron back-scattered diffraction.

I would also like to express my gratitude to the beam line scientists Dr. M. Hoffman at FRMII, Dr. A. Paradowska at ISIS and A. Evans at PSI.

I am very grateful to M. Burak Toparli and Asim Zeybek, who are more than being my sincere friends, for having a great and unforgettable time all together. Thanks to all of my sincere friends in Turkey, UK and USA for their emotional support and help. Also special thanks to Yeli Traore and Sanjoo Padea for their great friendship during my study.

Thanks to all my colleagues Dr. Mehmet Kartal, Sue Storer, Yuki Sakanashi, Bama Perumal, David Githinji, Dr. Ashwin Rao, Dr. Olivier Zanellato, Dr. Himanshu Lalvani and other fresh students, members and staffs in materials engineering group for their friendship and support which made my three years stay worthwhile and memorable.

Finally, my deepest and sincere regards to my family for all their encouragement and good wishes.

Murat Ozgun ACAR
December 2011

Preface

This thesis is submitted for the degree of Doctor of Philosophy of The Open University, United Kingdom. The work described in this thesis was carried out in the Department of Materials Engineering, Faculty of Mathematics, Computing and Technology, between January 2008 and December 2011, under the supervision of Dr. Salih Gungor and Prof. Michael Edward Fitzpatrick.

It is entirely the work of the author except where clearly referenced. None of this work has been submitted for a degree or other qualification at this or any other university. Some of the results of this work have been published in conference proceedings as listed below:

1 Acar MO, Gungor S, Ganguly S, Bouchard PJ, Fitzpatrick ME. Variation of mechanical properties in a multi-pass weld measured using digital image correlation. Society of Experimental Mechanics (SEM) Annual Conference Proceeding 2009:288.

2 Acar MO, Gungor S, Bouchard PJ, Fitzpatrick ME. Effect of prior cold-work on the mechanical properties of weldments. Society of Experimental Mechanics (SEM) Annual Conference Proceeding 2010:283.

3 Acar MO, Bouchard PJ, Fonseca JQ, Fitzpatrick ME, Gungor S. Intergranular strains in pre-strained and welded pipes. Material Science Forum 2010;651:13.

4 Acar MO, Gungor S, Fitzpatrick ME, Bouchard PJ. Numerical Study of Strength Mismatch in Cross-Weld Tensile Testing. Proceeding of the 63th Annual Assembly & International Conference of the International Institute of Welding (AWST) 2011:233.

Murat Ozgun ACAR
December 2011

TABLE OF CONTENTS

List of Tables

List of Figures

Figure 7.25 The comparison of plastic deformation predictions in tube A_{20} using EBSD, local stress-strain curves obtained by DIC, hardness, neutron diffraction 111 peak width measurements (ND-peak widths) and anisotropy strain (ND-anisotropy strain) and. Horizontal bars show the covered area where the measurement is done.

Chapter 1

Introduction

The majority of the electric energy in industrial countries is supplied by fossil fuel (i.e. coal and gas) and nuclear power plants. Due to the increasing demand for energy, new power plants are built and existing power plants are modernized to improve the efficiency and to extend their service life. In the UK, 17% of electricity is supplied by nuclear power plants according to electricity supplied by fuel type statistics (2009) provided by the UK's Department of Energy and Climate Change [1]. In the UK most of the first generation nuclear power plants (Magnox reactors) have been closed due to the completion of their life-time (the remaining two will be closed in 2012) and the currently operational advanced gas-cooled (AGR) reactors are scheduled to be closed by 2023 [2]. In the UK, there is an on-going research to improve the efficiency and to extend the service life of those nuclear power plants by deepening understanding of unexpected degradation in the structural components in service, for example in pipes and welds.

There is a schematic view of an AGR type reactor in Figure 1.1. In this type of reactor, the heat is generated in the reactor core and transferred to boilers via a gas circulated in the reactor chamber. Water in the boiler tubes is heated by gas outside the reactor core and is converted by evaporation into steam. Finally, the steam drives the turbines and electricity is generated. However, unexpected failure of the boiler tubes operating at elevated temperatures and pressures can cause shut-downs of the

reactors for the repair or the replacement. Degradation of the welds in the boiler units is one of the most critical issues limiting the efficiency of the power plant [3]. Therefore, a good understanding of the structural integrity of the boiler welds is required to improve the efficiency of the power plant and to extend the service life.

A boiler unit in Hinkley B station (which began generating electricity in 1976) is demonstrated in Figure 1.2(a). In this unit the tube material is AISI Type 316H austenitic stainless steel. C-Mn steel and 9Cr1Mo steel are also used in the manufacture of boiler units. It can be seen in Figure 1.2(a) that many parts of the unit contain bended tubes and tube junctions such as bifurcations which are usually produced by welding onto a bended tube as shown in Figure 1.2(b). The welding process causes the material properties in the weld area to change and can introduce defects from which failure may initiate. For this reason, weldments are usually the weakest and most structurally vulnerable areas of the boiler units. Moreover very little is known about the effects of welding onto plastically deformed tube. The ASME Boiler and Pressure Vessel Design code [4] specifies that the limit of forming strain for Type 316H material is 20% when the operating temperature is between 580°C and 675°C. In cases where this strain threshold is exceeded, the material should be annealed before welding at a minimum temperature of 1040°C to restore its mechanical properties, tensile strength, creep strength and creep ductility to the start of life values. Current construction practices in the UK for 316H boiler tubes forbid welding onto material that has experienced more than 15% plastic strain, without first solution heat treating the material [5]. Post weld heat treatment (PWHT) is also recommended to relieve the weld residual stresses which is one of the factors that can

contribute to the premature failure during operation [6]. Although the standards and construction codes of practice provide fabrication guidance, it is not always possible to follow the rules, for example in the case of a whole boiler constructed as a single unit too large and too complex with different tubing materials to be heat treated [7]. As a result of welding onto a plastically deformed tube, the heat dissipation during arc welding will greatly alter the properties of the plastically deformed tube near the weld pool. In the case of welding onto a plain tube, the welding thermo-mechanical cycles can also induce local plastic straining due to constraint effects and the imposition of welding residual stresses [8].

The properties of the virgin tube material are greatly altered after a fabrication process involving plastic deformation, welding and heat treatment. The boiler tubes enter into service with these altered material properties. Structural integrity assessment of components and structures operating at elevated temperatures requires knowledge of the variation of mechanical properties, especially in the weldment zone where the failures mostly initiate.

Sample welded tubes with plain and prestrained (10, 15, 20 and 25%) base metal were supplied by British Energy to simulate the fabrication history of boiler units. Test specimens were cut for different experimental purposes and half the batch of test specimens were heat-treated.

The primary aim of the study was to determine spatially resolved room-temperature tensile properties using digital image correlation (DIC) by testing cross-weld specimens machined from the thin wall welded tubes (with plain or prestrained base metal) before and after the heat treatment. The experimental procedure which is

used to retrieve the tensile properties from these integrated tests was validated through finite element simulation. The room temperature tensile properties are of key importance because it is possible to predict the tensile properties at elevated temperatures using those at the room temperature [9]. Many engineering assessments, including pressure vessel design (such as ASME Boiler and Pressure Vessel Code), fracture assessments (such as R6: Assessment of the Integrity of Structures containing Defects [10]) and elevated temperature life assessments (such as R5: Assessment Procedure for High Temperature Response of Structures [11]) use tensile properties as a key input. Moreover detailed knowledge of the variation in stress-strain properties across boiler tube weldments is expected to contribute to the understanding and the assessment of the premature failures that have been observed in AGRs. In addition to the determination of the local mechanical properties, material characterization of the welds was done using optical microscopy, scanning electron microscopy and by hardness survey. The variation in plastic strain across the weldments was quantified using hardness, DIC, electron back-scattered diffraction (EBSD) and neutron diffraction (ND). Plastic strain is of particular significance because it has a great influence on creep properties [8].

1.1 Outline of the thesis

This thesis presents research carried out mainly to investigate the mechanical properties of austenitic stainless steel welds (with a prestrained base metal) before and after heat treatment. The structure of the thesis is as follows.

Chapter 2 presents a literature review covering basic concepts of deformation behavior and welding of austenitic stainless steels. The properties of austenitic stainless steels are given first. The deformation behavior of stainless steel is explained using the basic concepts of macroscopic stress-strain relationship, work hardening (cold-work) effect and the plastic deformation of face-centred-cubic polycrystalline materials. Relevant research on the effect of prior cold work on the subsequent mechanical properties and the anisotropic behavior of austenitic stainless steels is reviewed. The welding metallurgy, post-weld heat treatment (PWHT), weld defects and the mechanical properties of stainless steel welds are then explained in the final section of this chapter.

The experimental techniques used in this research are described in Chapter 3. The fundamental working principle of optical and scanning electron microscopes, hardness testing, tensile testing, digital image correlation (DIC) and neutron diffraction are explained. In addition, the optimization of DIC parameters is discussed in detail.

The manufacturing details of the welded tube samples supplied by British Energy and the details of the test specimens extracted from these tubes are given in Chapter 4.

Chapter 5 presents the microstructural analysis of the plain tube material, prestrained tube material and the welds before and after heat treatment. The variation of hardness values across the weld for all the conditions are also given in this chapter.

The tensile properties of the plain tube material, prestrained material and welds are presented in Chapter 6. Digital image correlation (DIC) was integrated into the tension tests of the plain and prestrained tube material and the welds. The results obtained from DIC are compared with those from extensometer and strain gauges. Local stress-strain curves were obtained using DIC in the tension tests of the welds and used to determine the spatially resolved tensile properties across the weld. The reliability of the DIC experimental procedure to obtain local stress-strain curves and the offset proof strength distribution across the weld is tested through 2D finite element simulation of the tension tests of welds with different strength mismatch levels (bi-material model and multi-material model) and the results are discussed in this chapter.

Chapter 7 presents predictions of effective plastic strain in the prestrained and welded tube based on neutron diffraction, EBSD, hardness and DIC correlations. The correlations rely on crystallographic changes such as the development of intergranular residual strains, increase in dislocation density and dislocation structures with plastic deformation as well as local stress-strain curves obtained by DIC.

Chapter 8 presents the overall conclusions drawn from this work. Suggestions for the future work to advance the current understanding of the effect fabrication history on the performance of the welds are also given in this final chapter.

1.2 References

[1] UK Energy in Brief 2010. Department of Energy and Climate Change, 2010.

[2] Existing Nuclear Power Stations. Department of Energy and Climate Change (www.decc.gov.uk), 2010.

[3] Sherry AH. Fission Materials Overview [Presentation]. Energy Materials: Meeting the Challenge. Loughborough University, UK, 2008.

[4] ASME Section I, ASME Boiler and Pressure Vessel Code, Section I: Rules for Construction of Power Boilers. New York, USA, ASME, 2010.

[5] Spindler M. Effects of plastic strain and heat treatment on microstructure and properties of 316 stainless steel tubing (Personal communication). 2008.

[6] Lampman S. Weld integrity and performance: ASM International, 1997.

[7] Spindler M. Post-weld heat treatment of austenitic stainless steel welds in boiler units (Personal communication). 2011.

[8] Wilshire B, Willis M. Mechanisms of strain accumulation and damage development during creep of prestrained 316 stainless steels. Metallurgical and Materials Transactions A 2004;35:563.

[9] BS EN 10314: Method for the Derivation of Minimum Values of Proof Strength of Steel at Elevated Temperatures. British Standards Institute, 2002.

[10] R6 Revision 4 Assessment of the Integrity of Structures containing Defects. Gloucester, UK: British Energy Generation Limited, 2009.

[11] R5 Issue 3 Assessment Procedure for High Temperature Response of Structures. Gloucester, UK: British Energy Generation Limited, 2003.

[12] Hartnell P. Manufacture of Reproduction Superheater Bifurcations and Tube Butt welds for Creep-Fatigue Testing by British Energy (Report No: 29285-B-TR-00-001). Doosan Babcock Energy, 2008.

1.3 Tables & Figures

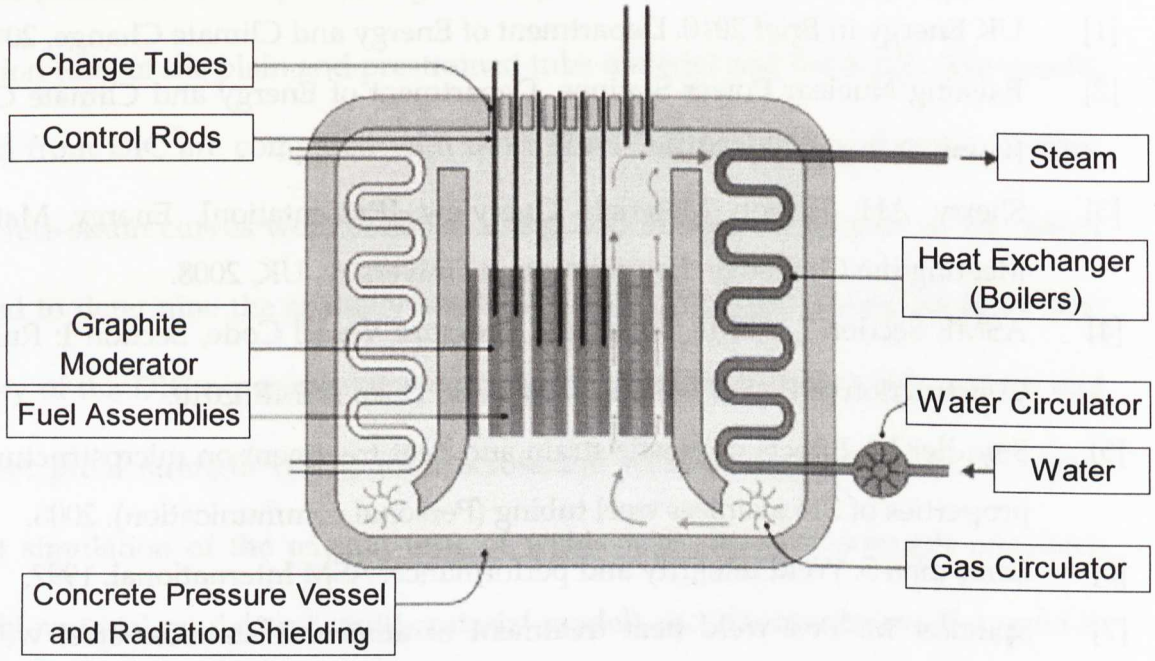

Figure 1.1 The schematic view of British advanced gas-cooled reactor (AGR) design

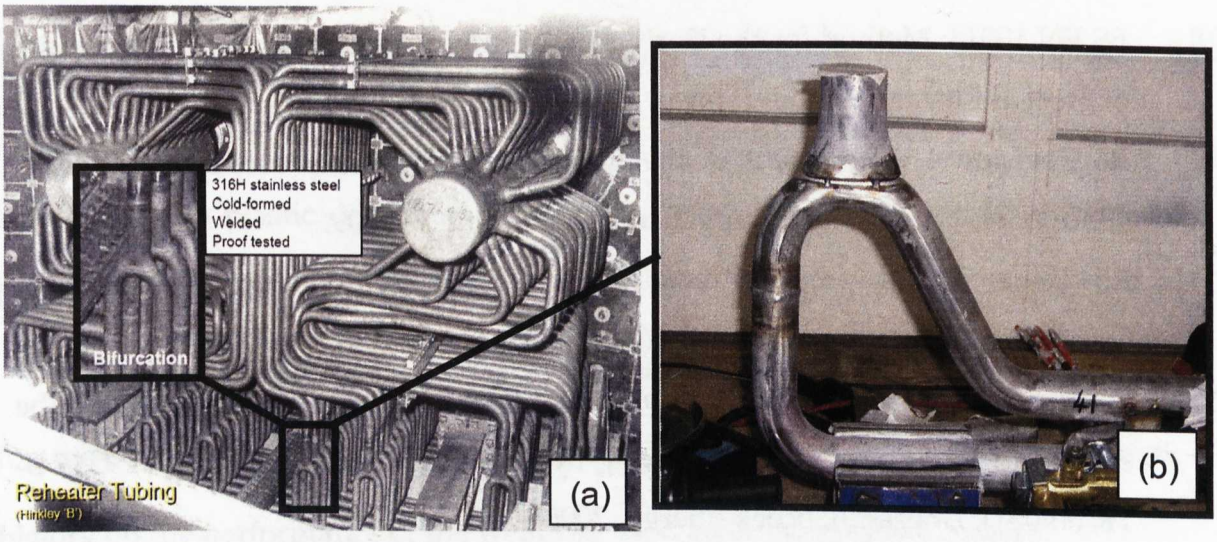

Figure 1.2 Reheater tubing unit in Hinkley B station [3] (a) One of the designs of tube junctions (bifurcation) [12] (b)

Chapter 2

Literature Review

2.1 Stainless Steels

Stainless steels are extremely versatile engineering materials which are extensively used in dairy and food-processing plants, health and sanitation applications, petroleum and petrochemical plants, and the power generation and transportation industries due to their corrosion and/or heat resistance. Stainless steel alloys are based on iron (Fe) and carbon (C) composition with the addition of mainly chromium (Cr) and nickel (Ni) and low amount of other alloying elements such as molybdenum (Mo), tungsten (W), manganese (Mn).

Chromium has relatively high affinity for oxygen and consequently oxidizes very easily. The oxide film which forms rapidly on the surface of the chromium is very stable and strongly adherent to the surface. Although the oxide film is extremely thin, it protects the alloy from further attack of oxygen. The stainless steel alloys exhibit these corrosion resisting properties particularly when the chromium content is more than 12% [1].

Chromium also contributes to some extent to the heat resistance/creep resistance of the alloy by ordinary substitutional solid solution. However, the high temperature strength is primarily achieved by dispersion hardening provided by the carbides and nitrides of the other alloying elements [1].

Stainless steels are classified in 5 groups: martensitic stainless steels, ferritic stainless steels, austenitic stainless steels, duplex (ferritic-austenitic) stainless steels, and precipitation-hardening stainless steels [2]. In this thesis, the American Iron and Steel Institute (AISI) nomenclature will be used for the classification of the stainless steels. According to AISI, three subsequent numbers are used to define the stainless steels. For example, 100 series are used for austenitic chromium-nickel-manganese alloys, 200 series for austenitic chromium-nickel-manganese alloys, 300 series for austenitic chromium-nickel alloys, 400 series for ferritic and martensitic chromium alloys [3]. Austenitic stainless steels will be described in details in the following section since they have been the focus of the investigation in this study.

2.1.1 Austenitic stainless steels

Austenitic stainless steels are the group of stainless steels that preserve the face-centred cubic (FCC) structure at room temperature. The types of the austenitic stainless steels and their composition are given in Table 2.1. The main alloying elements in these steel alloys are chromium, nickel, molybdenum and manganese.

The corrosion resistance is mainly achieved with the addition of chromium as mentioned earlier. Since chromium is a ferrite stabilizer, its amount in the steel is compensated for with other alloying elements (for example, Ni) in order to retain the austenite in steel at room temperature. Nickel, which is an austenite stabilizing element, is responsible for improved toughness and high strength at both high and low temperatures [4].

Ferrite-stabilizing alloying elements such as chromium and molybdenum have body-centred cubic (BCC) crystal structure and easily dissolve in ferrite so they

favour the ferrite transformation from austenite. Similarly, austenite-stabilizing alloying elements such as nickel, carbon and manganese have face-centred cubic (FCC) crystal structure and retard the austenite to ferrite transformation as well as contributing to the precipitation of carbides [1].

The austenite in 300 series austenitic stainless steels is thermodynamically unstable at room temperature for the initial solution treated state. Unstable austenite promotes the precipitation of carbides and intermetallics during elevated temperature service for long periods of time or martensite formation during deformation. Although the M_s (the temperature at which the martensite formation starts) is well below the room temperature for some steels, diffusionless shear transformation of austenite to martensite occurs if the deformation is done below M_d (the temperature below which the martensite formation starts by deformation) [5].

Austenitic stainless steels are non-magnetic in the annealed condition. They possess high strength and also exceptional toughness, ductility and formability. They usually have good cryogenic properties and exhibit excellent strength and oxidation resistance at elevated temperatures. Additionally, austenitic alloys are generally considered to be very weldable provided that proper precautions are taken during welding.

Considering all of these distinct engineering advantages, particularly with respect to formability and weldability, austenitic stainless steels are used in architectural applications such as roofing and cladding, food processing plants, heat exchangers, ovens and chemical tanks.

2.1.1.1 AISI 316 type austenitic stainless steels

The 300 series alloys are by far the most widely used austenitic grade stainless steel and AISI 316 type is one of the most commonly used among 300 series. These alloys contain 0.01-0.08% C, 17% Cr, 12% Ni, 2% Mo and 0-0.13% N. L grades represent low-carbon variants with a nominal C level of 0.03% whereas H grades have carbon levels approaching 0.1%. 316L is used as a weld filler material since its low carbon level reduces the formation of carbides and hence improves the resistance to intergranular attack in corrosive environments [6]. 316H alloys are used at elevated temperature since they have higher elevated temperature strength than standard or L grades. 2% Mo improves the pitting corrosion resistance of the alloy. 0.13% N is also added to improve the strength and pitting corrosion resistance and 316N and 316LN alloys are preferred to be used at cryogenic applications.

2.2 The Basics of Plastic Deformation and Deformation Behaviour of Stainless Steels

In this section the deformation of stainless steel will be discussed in macro- and micro-scale.

The macroscopic stress-strain relation in a polycrystalline under tension will be explained initially to have a better understanding of the tension test results which will be demonstrated in the following chapters.

Some of the tubes which have been used in this project were exposed to cold working by axial stretching for the purpose of simulating the plastic deformation

introduced after the shaping/bending of the original tubes to construct the heat exchanger units. The cold working effect on the material properties can be described with the work hardening effect. Therefore, a general description of work hardening will be given. The effect of cold work on the mechanical properties of stainless steel will also be discussed.

Stainless steel which has a FCC structure is an anisotropic material; therefore it exhibits a directional dependant response at loading. Residual strains develop between different crystallographic *hkl* grain families because of the anisotropy. Some researchers have proposed that these residual strains are indicative of macroscopic plastic strain [7-9]. As a part of this project the relationship between intergranular residual strains and macroscopic plastic strain was also investigated. Therefore, the anisotropy in stainless steel will be described in detail following a general explanation of plastic deformation of FCC polycrystalline materials in micro-scale.

2.2.1 Macroscopic stress-strain relationship

Solid materials deform when subjected to an external load. When the external axial load P is applied on a uniform rectangular bar as shown in Figure 2.1, it is balanced by the internal resisting force $\int \sigma \, dA$, where σ is the stress normal to the cutting plane and A is the cross-sectional area of the bar. The equilibrium equation is given as:

$$P = \int \sigma \, dA \tag{2.1}$$

If the stress σ is distributed uniformly or constant over the area A, Eq. (2.1) becomes

$$P = \int \sigma \, dA = \sigma A \quad \text{or} \quad \sigma = \frac{P}{A} \tag{2.2}$$

The stress σ is represented by a scalar called *engineering stress* or *nominal stress* that represents an average stress over the initial cross-sectional area A, meaning that the stress in the cross-section is uniformly distributed.

Depending on the level of the load the bar undergoes either recoverable or irreversible deformation. Strain is the term that describes the amount of deformation. The *engineering strain* or *nominal strain* e of a bar axially loaded as shown in Figure 2.1 is expressed as the change in length ΔL per unit of the original length L_0 of the bar (Eq. (2.3)).

$$e = \frac{L - L_0}{L_0} = \frac{\Delta L}{L_0} = \frac{1}{L_0} \int_{L_0}^{L} dL \tag{2.3}$$

The mechanical properties of a ductile material can be obtained from a tension test, in which a suitably designed specimen is subjected to increasing axial load until it fractures. Engineering stress (σ) and strain (e) are calculated with Eq. (2.4) and (2.5) by using the load (P) and elongation (L) recorded during the test and then engineering stress-strain curve is plotted as shown in Figure 2.2. The engineering stress σ is obtained by dividing the load by the original cross-sectional area (A_0) of the specimen (Eq. (2.4)). The engineering strain e is the average linear strain which is measured in the gauge length of an extensometer.

$$\sigma = \frac{P}{A_0} \tag{2.4}$$

$$e = \frac{\Delta L}{L_0} \tag{2.5}$$

The recovery of the original dimensions when the load is removed is known as *elastic behaviour*. In the elastic region stress is linearly proportional to strain. The linearity between stress and strain is described with Hooke's Law;

$$\sigma = \mathrm{E}\, e \tag{2.6}$$

where E (*elastic modulus*) is the slope of the linear line. *Elastic modulus,* a material property, is a measure of the stiffness of the material. When the load exceeds the yield strength (σ_y) the material undergoes *plastic deformation*. Beyond that point the deformation is irreversible and permanent. When a yield stress is not easily defined based on the shape of the stress-strain curve an *offset yield stress* or *proof stress* is arbitrarily defined. On the engineering stress-strain curve *proof stress* is the stress corresponding to the point which is the intersection of original curve and a line parallel to the elastic part of the curve offset by a specified strain such as 0.2% or 1.0 % [10]. The volume of the specimen remains constant during plastic deformation, that is, $AL = A_0 L_0$. As the specimen elongates, the cross-sectional area decreases (*poisson effect*) and the material undergoes work hardening. This hardening tends to increase the load-carrying capacity of the specimen as deformation increases. The plastic strain is uniform in the gauge length until the ultimate tensile strength (*UTS*), which corresponds to the maximum load that the sample can carry, is reached. Once stress reaches *UTS* necking or localized deformation starts because the increase in stress

due to decrease in the cross-sectional area of the specimen becomes greater than the increase in the loading-carrying ability of the metal due to work hardening. The specimen fails soon after necking. For engineering design purposes, yield stress σ_y (or proof stress) and ultimate tensile stress (*UTS*) are used as the strength parameters of the material. These tensile properties for austenitic stainless steels at room temperature are a key input into all engineering assessments such as pressure vessel design [11], fracture assessments [12] and elevated temperature life assessments [13]. 0.2% offset proof strength and ultimate tensile strength of some austenitic stainless steels at room temperature are given in Figure 2.3.

2.2.2 Work-hardening effect

After the yield point as the plastic deformation increases, the metal becomes stronger so that the stress required extending the specimen increases with further straining. An atomistic approach of work hardening effect will be explained in section 2.2.3.1. On the engineering stress-strain curve it can be seen that beyond *UTS* stress drops down with increasing strain. This is because the stress and strain are calculated using the original dimensions (A_0, L_0), rather than instantaneous dimensions. Although the use of engineering stress-strain curves is perfectly acceptable while considering elastic deformation of materials, true stress-strain curves need to be used to understand the *strain hardening* or *work hardening* (Figure 2.4(a)) when the deformation is well in the plastic regime. *True stress* (σ_{true}) is ratio of the load on the actual (instantaneous) cross-sectional area (A) (Eq. (2.7)) and *true strain* (ε) is the

integration of the instantaneous change in length divided by the instantaneous gauge length (Eq. (2.8)) [14]. That is,

$$\sigma_{true} = \frac{P}{A} \tag{2.7}$$

$$\varepsilon = \sum \frac{L_1 - L_0}{L_0} + \frac{L_2 - L_1}{L_1} + \frac{L_3 - L_2}{L_2} + \ldots = \int_{L_0}^{L} \frac{dL}{L} = \ln \frac{L}{L_0} \tag{2.8}$$

True strain can be written as a function of *engineering strain* as shown below (Eq. (2.9));

$$e = \frac{\Delta L}{L_0} = \frac{L - L_0}{L_0} = \frac{L}{L_0} - 1$$

$$e + 1 = \frac{L}{L_0}$$

$$\varepsilon = \ln \frac{L}{L_0} = \ln(e + 1) \tag{2.9}$$

The volume of the material remains constant during plastic deformation, so, the following relation can be written for the uniform strain region before the necking starts;

$$\frac{A_0}{A} = \frac{L}{L_0} = e + 1$$

Hence, *true stress* can be calculated from the *engineering stress* as;

$$\sigma_{true} = \frac{P}{A_0} \frac{A_0}{A} = \frac{P}{A_0}(e + 1) = \sigma_{eng}(e + 1) \tag{2.10}$$

The true stress-strain curve in the region of the uniform plastic deformation can be expressed mathematically by strain hardening rule;

$$\sigma = K \varepsilon^n \tag{2.11}$$

where K is the strength coefficient and n is the strain hardening exponent.

The material becomes stronger as the loading proceeds beyond the yield point. When the material is unloaded as shown in Figure 2.4(b), it has already been deformed plastically and hardened. The true stress-strain curve of the subsequent loading starts at ε_0 and it follows the same trend with the previous curve in the plastic region. The amount of strain hardening ε_0 that the material received prior to the subsequent loading can be put in Eq. (2.11) as follows [15];

$$\sigma = K\,(\varepsilon_0 + \varepsilon^n) \tag{2.12}$$

In the next part the effect of prior cold work on the performance or the structural integrity of stainless steels will be discussed.

2.2.2.1 Effect of prior cold work on the mechanical properties of stainless steels

Prior cold work or pre-straining which induces plastic deformation has a considerable influence on subsequent material properties. This can be simply explained with the rearrangement of the microstructure or the development of damage after the plastic deformation.

The strength of the austenitic stainless steels can not be improved with heat treatment but they are easily strengthened by cold working. However, the effect of cold work is no more present at elevated temperatures ($> T_{melting}/2$) due to recrystallization [2]. As a result of recrystallization, deformed grains transform into new strain free grains.

The effect of monotonic or cyclic pre-straining on room temperature tensile behavior of 316 stainless steel was studied by Liaw and Landes [16]. They observed

that monotonic or cyclic pre-straining generally increases yield and ultimate tensile strength and also changes hardening behaviour compared to the virgin material (Figure 2.5). The increase in yield strength can be attributed to the work hardening effect. The work hardening effect will be explained in 2.2.4.1 with an atomistic approach. Annealed type 316 has yield strength between 200MPa and 300 MPa, but after 5-30% cold working (at room temperature) yield strength rises to between 400MPa and 600MPa. However, the ductility reduces from 60-75% in the annealed state to 20-30% after 20% pre-straining [17].

The effect of pre-strain on creep of types 304 and 316 stainless steel reveals that creep resistance is improved whilst creep ductility is significantly decreased [5]. Similar to that, Willis *et al* reported that the tensile ductility at 575°C and creep strain at failure at 575°C for 316 type stainless steel decrease with increasing pre-strain at room temperature as shown in Figure 2.6 [18].

It was also reported that prior plastic deformation up to 10-20% reduces the corrosion resistance of 316 type austenitic stainless steels in $MgCl_2$ [5].

In the following parts, the room temperature tensile properties of 316H stainless steel after several processes such as cold work, welding and heat treatment will be focused on.

2.2.3 Plastic deformation of face-centred cubic (FCC) polycrystalline materials

Plastic deformation in solids involves, at the atomistic scale, the breaking of bonds with original neighbouring atoms and reforming bonds with new neighbours

as large number of atoms move relative to each other with a process called slip. Slip takes place with the help of the dislocations in the material. Dislocations which form as a result of the misalignment of some atomic bonding in a crystal can be determined as edge dislocations (Figure 2.7(a)), screw dislocations (Figure 2.7(b)) and mixed dislocations. Under load the room temperature deformation predominantly takes place with the help of these defects. Twinning is the other mechanism during deformation however it is not a dominant mechanism in metals which have many slip systems.

The term slip is used to define how the dislocations move in the crystals and slip occurs in the most densely packed planes and directions. The slip mechanisms are principally related to the crystal structure. Therefore, for face-centred cubic (FCC) metals there are 12 slip systems on which the dislocations easily move with the effect of the load. $\{111\}$ family of planes are favourable to slip on top of each other in $\langle 1\bar{1}0 \rangle$ directions. In Figure 2.8, 111 plane is shown with its corresponding slip directions.

If we consider the deformation of a single crystal under a tensile load, the slip takes place on the most densely packed plane when the shear stress on this plane is large enough to break the atomic bonds (Figure 2.9(a)). The minimum shear stress which is necessary to initiate the slip is called *critical resolved shear stress,* τ_R (Eq. (2.13)). τ_R reaches its maximum when $\lambda = \phi = 45°$, so that $\tau_R = \frac{1}{2} P/A$.

$$\tau_R = \frac{F}{A'} = \frac{P\cos\lambda}{A/\cos\phi} = \frac{P}{A}\cos\lambda\cos\phi \qquad (2.13)$$

As the deformation proceeds, the slip plane tends to rotate towards the loading axis as shown in Figure 2.9(b). At the beginning of the plastic deformation, the dislocations are able to move over relatively large distances without encountering barriers. Therefore, most of the dislocations escape from the crystal surface while deformation occurs only on primary slip system. Thereafter, the resolved shear stress becomes equal for another slip system (conjugate slip system) and slip also starts on the conjugate slip system. This duplex slip system is called multiple slip [14]. With the activation of second slip system, the dislocation density increases. Deformation by duplex slip results in a high degree of strain hardening because of interaction between dislocations on two intersecting slip systems (dislocation pile-ups). Dislocation pile-ups create some regions called dislocation tangles which are dislocation free regions surrounded with extensive amount of dislocations. Finally, the stresses are high enough to move dislocations which were suppressed due to the obstacles at lower stresses. At high stresses screw dislocations are activated and cross slip occurs. Cross-slip creates dislocation bands inside the grains.

In a polycrystalline material, the shape of a crystal can change with the operation of five different slip systems. This is related to the fact that an arbitrary deformation is specified by the six components of the strain tensor. But, because of the requirement of constant volume ($\Delta V = 0 = \varepsilon_{11} + \varepsilon_{22} + \varepsilon_{33}$) there are only five independent strain components. Although small plastic elongation may be obtained if there is twinning or favourable preferred orientation, crystals which do not have five independent slip systems are never ductile in polycrystalline form. Hence, FCC metals, which have 12 active slip systems, have higher ductility at room temperature

in polycrystalline form compared to HCP (hexagonal close-packed) metals, or other low symmetry metals, which have less than 5 active slip systems [14].

The deformation of polycrystalline materials is very complex because of various grain orientations and the geometrical constraints. The grains sustain the mechanical integrity along the grain boundaries during deformation; that is, they do not open up or come apart. As a consequence, each grain is constrained by the adjacent grains and, hence greater stresses are required to initiate slip. A single grain can not deform until the adjacent and less favourably oriented grains are capable of slip. Therefore, the deformation of polycrystalline materials requires higher stress levels. Empirical studies have shown that the yield strength of the material depends on the grain size by the following equation, known as the Hall-Petch equation (Eq. (2.14)).

$$\sigma_y = \sigma_0 + \frac{K}{\sqrt{d}} \tag{2.14}$$

where d is the average grain diameter and σ_0 and K are material constants. This means that fine-grained materials are harder and stronger than the coarse-grained material.

2.2.3.1 Work hardening

Work hardening is caused by dislocations interacting with each other and with barriers which impede their motion through the crystal lattice. When the material is deforming plastically under a load, the dislocations start to move. Meanwhile, as the deformation proceeds, the number of dislocations in a crystal increases over the number present in the annealed crystal. After a while, these dislocations start to interact with each other or some of them are hindered by solute atoms, precipitates or

grain boundaries. This hindering effect and the dislocation pile-ups produce back stress which opposes the applied stress. Therefore, higher stress is required to continue the plastic deformation in the material. This effect is called work hardening. When the load is released, the back stresses, which arise due to the dislocation pile-ups and hindering mechanism, remain in the material [14]. If the material is reloaded (Figure 2.4(b)), it will start to yield at a higher stresses, i.e. the yield strength of the material will increase.

2.2.4 Anisotropy in stainless steel

Anisotropy in a material is the directional dependence of the physical properties. A single crystal is, by its nature, highly anisotropic and a polycrystalline material can be anisotropic if there exists a preferential alignment of certain crystal structures (i.e. texture) in its structure, which may be caused by some manufacturing processes such as rolling, extrusion or directional solidification.

The stainless steel has both elastic and plastic anisotropy. Elastic anisotropy means that the elastic stiffness of the material is directional dependant. The macroscopic elastic stiffness of stainless steel is 190-210 GPa. However, Pang *et al* [19] performed an in-situ tensile loading test of 309H stainless steel using neutron diffraction which provides the stress-strain curve of each crystallographic plane and found that the elastic stiffness of crystallographic planes in the FCC unit cell of this stainless steel ranges from 129 GPa for the 200 plane to 239 GPa for the 111 plane. As well as the elastic stiffness, the yield strength varies for different planes. The directional dependent yield strength means the material has plastic anisotropy. Daymond *et al* performed an in-situ tensile test of an austenitic stainless steel by

using neutron diffraction and observed that yield point ranges from 200MPa for (331) plane to 250MPa for (220) plane [7]. The elastic and plastic anisotropy in the stainless steel is summarized in Figure 2.10.

2.2.4.1 Texture

Texture is a term which is used to statistically quantify the distribution of the crystal orientations in a polycrystal with respect to the macroscopic coordinate system. A material can behave very different depending on its texture. Therefore, the macroscopic response of the material is mainly controlled by the texture. A material in which the crystal orientations are all random as in a powder form is said to possess *'random texture'*. The degree of the texture is quantified as *'multiple of random'* by using the random texture as a reference.

Gooch [20] suggests that texture is one of the factors being worthy of consideration to understand the higher creep crack rates in the pre-straining (or rolling) direction.

The development of the texture can be attributed to the deformation mechanisms such as twinning and slip. Recrystallization in a preferred direction or phase transformation can also result in a considerable amount of texture.

2.2.4.2 Residual intergranular strains

It was mentioned earlier that the residual intergranular strains due to the anisotropic deformation behaviour of a polycrystalline material are fingerprints of macroscopic plastic strain. Therefore, in this section the residual intergranular strains

will be described and the relation between the macroscopic plastic strain and residual intergranular strains will be explained.

Plastic strain has detrimental effects on the subsequent mechanical performance of stainless steel. The introduction of plastic strain increases the susceptibility of the tubing to stress corrosion cracking, creep damage and influences the fracture properties [21]. For instance, bent and swaged tubes in power generation plants are very susceptible to intergranular stress corrosion cracking in which the crack progressively nucleates and grows by localized corrosion along the grain boundaries in the presence of stress/strain [5]. Furthermore, the creep ductility of the cold-worked tubes is significantly less whereas the creep strength and creep strain rate is improved compared to the virgin tubes [5]. However, there is no direct method to quantify the plastic deformation introduced to the materials. For that reason, we measured intergranular strains after different manufacturing steps such as cold-working, welding and heat treatment since it was reported that intergranular strains have been used to provide a semi-quantitative fingerprint of the macroscopic plastic deformation [22] .

Development of internal strains during deformation, and residual intergranular strains

In an elastically and plastically anisotropic polycrystal when it is loaded different internal strains develop on different planes. As the deformation proceeds after yielding grains are re-oriented. When the load is released after the polycrystal is plastically deformed, residual intergranular strains develop between grains having different plane orientations.

In recent years, by using neutron diffraction many researchers have studied the development of internal strains in a polycrystal subjected to a uniaxial tensile or compressive load. Daymond and Bouchard [23] have tested a 316H specimens under uniaxial tensile load at room and elevated temperatures. At room temperature the development of internal strains with the applied load for 111, 311 and 200 planes in axial and transverse direction is as shown in Figure 2.11. It can be seen that the stress-strain curves of different planes are not identical and show different elastic and plastic behaviour. The difference between the total strain on each grain family and the extrapolated elastic line is termed as plastic intergranular strains. In Figure 2.12 the variation of the axial plastic intergranular strains with the macroscopic strain is given. It can be seen that the intergranular strains increase as the macroscopic plastic strain increases. Additionally, by comparing the experimental and slip based modelling results they concluded that slip is the dominant deformation mechanism up to 450°C. Similar to that, Clausen *et al* performed the same experiment for another type of stainless steel and obtained very similar results for the specific planes [24]. However, they measured the intergranular strains after the load is removed at several plastic strains as shown in Figure 2.13. In a broader sense, Peng *et al* have extended this study and analysed the variation of residual intergranular strain as a function of the sample direction on the austenitic stainless steel samples which were produced by unloading from a peak strain of 0.2%, 7.5%, 29.8% and 44.7% [25]. They observed that the residual strains along the loading axis were the largest while they were essentially zero along the normal direction as shown in Figure 2.14.

Macroscopic plastic strain and anisotropy strain

Further analysis of in-situ tensile testing with neutron diffraction revealed that there is a correlation between the macroscopic plastic strain and residual intergranular strains. Daymond *et al* introduced the term *anisotropy strain* which is the difference between the intergranular strains on the *hkl* planes having two extremes of elastic stiffness and it is calculated as given in Eq. (2.15) [7].

$$\varepsilon_{h00} - \varepsilon_{hkl} = A_{hkl}\varepsilon_A \tag{2.15}$$

where ε_A is the anisotropy strain, ε_{hkl} is the intergranular strain on *hkl* plane, A_{hkl} is the anisotropy factor describing the degree of variation of the crystal stiffness with orientation. The 200 and 111 planes represent the extremes of elastic stiffness in stainless steel. He tried to evaluate the plastic strain history of a ring which was compressed along the diameter by calibrating the plastic strain behaviour using the data obtained from a neutron diffraction experiment of in-situ tensile testing of a stainless steel which is very similar to ring material. The plastic strain prediction for this compressed ring was also validated with finite-element modelling as shown in Figure 2.15. Korsunsky *et al* have investigated the in-situ deformation of a fine-grained Al alloy reinforced with SiC particles in four-point bending to observe the relation between the anisotropy strain and the macroscopic plastic strain [8]. They reported that a direct correlation was found between the matrix plastic strain and the anisotropy strain as shown in Figure 2.16. These results show that the prediction of plastic strain using anisotropy strain is a promising technique to determine the plastic deformation in a material after exposed to different manufacturing steps such as prestraining and welding.

2.3 Welding of Stainless Steel

Welding is a process of joining two similar or dissimilar materials through the formation of primary chemical bonding under the combined effect of heat and pressure. The continuity of the joint or the atomic bonding across the joint is generally obtained by three mechanisms: solid phase plastic deformation with or without recrystallization, diffusion or melting and solidification [26]. These mechanisms are acquired with different combinations of heat and pressure. Most of the welding processes have been designed on the theory of melting and solidification. This type of welding in which the continuity is attained by melting and solidification of a filler material in-between or the joint surfaces itself is called *fusion welding*.

Welding is the preferred mechanism from joining the metals because weld joints have exceptional structural integrity and they do not loosen or disassemble. Using welding as the primary joining method when manufacturing components with complex shapes may be more cost effective compared to those methods of producing the component as a single unit, such as by casting or machining. However, it requires considerable operation skill. In case of non-skilled operation, the welded part may distort due to the unbalanced heat input. Even though the heat input is carefully adjusted, residual stresses develop during welding. The heat also degrades the base metal properties. Both degradation of the base metal and residual stress may cause pre-mature failure of the component in service.

Depending on the geometrical challenges in industry manufacturers have been generally applying 4 common types of joints: butt, T, corner and lap (Figure 2.17) [27].

The butt type joints are particularly used in welding pipes (Figure 2.18) and plates in ship construction.

2.3.1 Types of fusion welding

The melting of the filler metal or the joint surfaces requires heat. According to the heat source fusion welding can be classified in four groups: gas welding, arc welding, resistance welding and high-energy beam welding [28].

In gas welding, the heat to melt the filler metal is generated with an exothermic reaction of a fuel gas and oxygen. Oxyacetylene welding (OAW) which is the most common gas welding produces heat as a result of the combustion of acetylene (C_2H_2) with oxygen. The flame temperature reaches up to 2500°C. Due to the high heat input the heat-affected zone is large and distortions are likely to occur.

Arc welding is based on the electric arc between the workpiece and the electrode, each at different polarities. The arc consists of thermally emitted electrons and positive ions from the electrode and workpiece. By applying a potential field between the electrode and the workpiece the electrons or positive ions are accelerated. They convert their kinetic energy when they collide with the opposite charged element and this produces heat for fusion [26]. The electrodes are either consumable or non-consumable. Shielding is applied by different means such as inert gases to prevent oxidation of the highly reactive molten weld metal. The advantage of this type of welding is that the heat for fusion can be generated efficiently, concentrated at a very small point and sufficiently controlled. Depending on the type of electrode consumption and the theory of the electric arc generation, researchers have designed several arc welding processes. Most common types of electric arc

welding are shielded metal arc welding (SMAW), gas-tungsten arc welding (GTAW) or tungsten inert gas welding (TIG), plasma arc welding (PAW), gas metal arc welding (GMAW) or metal inert gas welding (MIG), flux-cored arc welding (FCAW), submerged arc welding (SAW), electroslag welding (ESW). In this dissertation since the test samples were produced with tungsten inert gas (TIG) welding, a detailed explanation of TIG processes will be given.

Resistance welding such as resistance spot welding produces heat through the resistance of the workpiece between the two terminals of the electrical circuit.

High-energy beam welding such as electron-beam (EBW) or laser-beam welding (LBW) employs a source of high-intensity electromagnetic radiation for fusion to produce the weld.

2.3.1.1 Gas tungsten arc welding (GTAW)

GTAW process consists of a non-consumable tungsten electrode, a filler metal and a shielding gas. The electric arc is generated between the workpiece and the tungsten electrode to melt the filler metal under the shielding gas as shown in Figure 2.19. The shielding gas protects the reactive molten metal from the air contamination. If an inert gas such as argon or helium is used as a shielding gas, GTAW is called tungsten inert gas (TIG) welding.

Three different polarities for the electrode are used for GTAW process as shown in Figure 2.20. Direct current electrode negative (DCEN) which is the most commonly used polarity provides deep penetration and narrow weld area. 70% of the heat is concentrated on the workpiece and the rest is concentrated in the tungsten

electrode. Direct current electrode positive (DCEP) supplies only 30% of the heat in the workpiece and the remaining heat stays in the electrode, therefore the electrode should be cooled during the operation. This forms a shallow penetration and wide weld area. The heat in alternating current (AC) polarity is evenly distributed between the workpiece and electrode. The penetration and the weld area are intermediate between DCEP and DCEN.

Tungsten electrodes containing 2% cerium or thorium are generally used in GTAW process. Compared to the pure tungsten electrodes, these types of electrodes have better electron emissivity (low temperature is required to emit the electrons so that arc starting is easier and the risk of melting at electrode tip is less), current carrying capacity and resistance to contamination [26].

Argon, helium or their mixture is used as a shielding gas in the GTAW process. Due to the fact that the ionization of argon is easier than helium, it is easier to start the arc and the voltage drop across the arc is lower with argon. Argon is also heavier and this provides effective shielding [28].

2.3.2 Welding of austenitic stainless steel

Compared to the other types of stainless steels, austenitic stainless steels are generally the most weldable of the stainless steel alloys. The welding behaviour of austenite is very different due to its physical properties. Thermal conductivity of austenite is lower than ferrite, therefore compared to the ferritic steels less heat is needed to weld the austenitic steels in order to get a similar depth of penetration [29]. In contrast, the thermal expansion of austenite is greater than ferrite, which can cause

solidification cracking after welding. However, balancing the austenite with some amount of ferrite makes these alloys less susceptible to solidification cracking [30].

2.3.2.1 Welding metallurgy

Before explaining the welding metallurgy of austenitic stainless steels, it is beneficial to understand how the integrity of the welded parts is attained at the atomic scale. The filler metal is melted with the heat source and it fills the weld gap. Some of the grains in the liquid/solid interface also become molten with the effect of the heat; this removes oxides in the interface. The atoms in the molten metal can freely move however the atoms of the base metal are in poly-crystalline form. The formation of the molten pool is explained schematically in Figure 2.21(a). Once the temperature of the molten metal begins to fall, the heat flows through the base metal therefore the free atoms in the molten metal lose their energy. The free atoms close to the base metal attach onto the surface and subsequent atoms carry on attaching on top of each other. This structure which is called dendrite progressively grows towards the centre of the weld pool as illustrated in Figure 2.21(b). At the end of the solidification all dendrites have already been connected to each other.

As a result of heat flow through the base metal during solidification of the weld pool, distinct metallurgical zones are formed in the base metal alloy as shown in Figure 2.22. *Fusion zone* (FZ) is the region where the filler metal becomes molten and fills the weld gap. If the temperature of the base metal next to the fusion zone is between the solidus and liquidus temperature, a *partially-melted zone* (PMZ) is produced. Still farther from the weld centreline, the heat influences the properties of

the base metal by some solid-phase transformations such as allotropic phase changes, recrystallization/grain growth, and aging or precipitation. The region where the heat alters the microstructure is called as *heat-affected zone* (HAZ). Beyond that region the heat is not high enough to affect the properties of the base metal.

On the other hand, in multi-pass welding processes the thermal cycles after each subsequent pass cause expansions and contractions in and around the weld. These volume changes accumulate plastic strain in the base metal [31-33]. This region which is strain-hardened by heating up and cooling down is sometimes referred to as *strain affected zone* (SAZ).

Phase Diagrams

The phase diagrams are used to predict the microstructural phases present in alloys. However, the phase diagrams available in the literature for austenitic stainless steels are very limited due to the complexity of the multi-component thermodynamic calculations and the transformation kinetics [34].

Bechtoldt and Vacher have proposed a quaternary iron-chromium-molybdenum-nickel equilibrium diagram in which the iron content is 70% [35, 36]. Figure 2.23 represents the isothermal profiles at 1093°C and 816°C of iron-chromium-molybdenum-nickel phase diagram. It is seen that at 816°C isothermal profile 17Cr-12Ni-2Mo (AISI 316X) stainless steel is still austenitic. The occurrence of σ (sigma), χ (chi) and η (Laves) phases is generally expected during the heat treatment process and long-time exposure to elevated temperatures since the rate of precipitation for these phases is sluggish [35]. The non-metallic alloying elements such as carbon are

present in relatively small amounts but they may have a significant effect on the microstructure.

Due to the limitation of the equilibrium phase diagrams, some researchers develop practical methods to predict the microstructure. Schaeffler has classified the alloying elements as ferrite and austenite stabilizers, and established a diagram to predict the weld metal microstructure [37]. He developed formulas for chromium and nickel equivalent (Eq. (2.16) and (2.17)) and these formulas include some constants which were empirically defined for each alloying element.

Chromium Equivalent (Ferrite Stabilizing Eq.)	$=(Cr)+2(Si)+1.5(Mo)+5(V)+5.5(Al)+1.75(Nb)+1.5(Ti)+0.75(W)$	(2.16)
Nickel Equivalent (Austenite Stabilizing Eq.)	$=(Ni)+(Co)+0.5(Mn)+0.3(Cu)+30(C)+25(N)$	(2.17)

Fully austenitic weld metals are very susceptible to hot cracking due to high thermal contraction of austenite during solidification and formation of low-melting liquid films along grain boundaries. This can be overcome by ensuring the weld metal contains a little delta-ferrite which minimises the contraction stresses around austenite grains and dissolves the impurities such as sulphur and phosphorus forming the low-melting liquid films [38]. In order to determine the variation in the amount of delta ferrite in austenitic weld metals with compositional changes DeLong has modified Shaeffler's diagram [39] and this form of the diagram (Figure 2.24) was adopted as a standard procedure by the International Welding Institute. It can be

seen that some types of austenitic stainless steels may have considerable amount of ferrite. However it should be noted that this diagram does not take into consideration of the influence caused by cooling rate and aging heat treatments.

Precipitations of carbides and intermetallics

AISI 316 stainless steels may also contain some precipitations and intermetallics. Carbides such as $M_{23}C_6$ and MC constitute the most of the precipitations observed in AISI 316 stainless steel. $M_{23}C_6$ which is the carbide of mostly chromium but also iron and molybdenum is the most predominant carbide form in those particular steels [5]. As discussed above, σ (sigma), χ (chi) and η (Laves) phases are the intermetallics which are observed in iron-chromium-molybdenum-nickel system. The formation of the sigma phase is quicker compared to the other intermetallics [40]. Additionally, it was reported that delta (δ)-ferrite in weld metals promotes the precipitation of carbides and intermetallics due to the high diffusivities of chromium and carbon in ferrite compared with austenite [41].

Time-temperature-precipitation (TTP) diagrams are used to predict the formation of precipitates and intermetallics. Weiss and Stickler have generated a TTP diagram of AISI 316 steel alloys which were solution-heat treated for 1.5 hr and water quenched (Figure 2.25) [40]. It may be seen that the formation of $M_{23}C_6$ is delayed when the alloy is solution-heat treated at 1090°C because the delta ferrite, which promotes the nucleation of precipitations, does not form at 1090°C whereas it does at 1200°C. In the annealed condition of the alloy solution heat treated at 1090°C, if the cooling rate is above 250°C/hr or the isothermal aging treatment at 810°C is not longer than ~1hr, precipitation of $M_{23}C_6$ is not expected to occur (Figure 2.25(a)).

When the alloy is cold worked, the time-temperature-precipitation curves shifts left, that is, the transformations take place in somewhat shorter time (Figure 2.25(b)). The formation of $M_{23}C_6$ is expected to happen after nearly 10 minutes during aging treatment at 810°C.

Welding onto cold worked stainless steel

When the metal is deformed most of the energy during the deformation dissipates as heat whereas small amount of energy is stored in the metal. This stored energy generates a metastable state and may modify the rate of the transformations if the metal is heated to a temperature above solidus temperature. This is why, as previously discussed, cold work influences the precipitation kinetics (Figure 2.25(b)).

At elevated temperatures the amount of crystal defects in the metal start to decrease. The point defects sink at grain boundaries. Subgrains are formed with the rearrangement and annihilation of the dislocations. Additionally as a result of dislocation climb the subgrain coalescence is observed. This stage of transformation in which the defects are modified is called *recovery*. The next stage is the nucleation of new strain free grains and this is called *recrystallization*. The stored energy is a driving force for recrystallization. The nucleated grains start to grow in the next stage which is called *grain growth* [42].

The welding of a cold worked stainless steel produces two types of microstructures as shown in Figure 2.26 [43]. For the cold worked single phase alloy, the heat generated during welding process flows through the base metal, and this results in a temperature variation across the region. As the heat flows in the region very close to the fusion zone recrystallization takes place and new strain free grains

start to grow. Further away from the fusion zone where the temperature is still sufficiently high, recrystallization may still take place, however, grain growth may be very limited due to time and temperature constraints (Figure 2.26(a)). For a cold worked alloy which undergoes allotropic transformations the microstructure after welding is more complex. It may have two recrystallization zones as shown in Figure 2.26(b). The first fine grained zone results from recrystallization of the cold-worked lower temperature phase. The second fine grained zone appears as a result of allotropic transformation to the high temperature phase, not from recrystallization. In fully austenitic stainless steel, the first type of microstructure is expected.

2.3.3 Post-weld heat treatment

Residual stresses are generated after the welding process and these stresses may cause premature failures during the service of the welded components. Therefore, post weld heat treatment (PWHT) is required to relieve these weld residual stresses. This process, however, can modify the microstructure depending on the temperature chosen for the treatment. Stress-relief heat treatments are generally conducted in the temperature range 550-650°C. PWHT in this range does not cause any microstructure modification for the first couple of hours. But as the holding time increases, it is likely to cause carbide precipitation [6]. To relieve the residual stresses more effectively the temperature can be increased between 650 and 900°C. It is reported that PWHT at 750°C for one hour to relieve the residual stresses in a welded 316H component results in 75% reduction in residual stress without any significant modifications to the microstructure or mechanical properties of the HAZ [44, 45]. Post weld heat treatment in the range 950-1100°C completely relieves the residual stresses

and also modifies the as welded microstructure without forming carbides or sigma phase.

On the other hand, the plastic strain caused by either welding [31-33] or cold-working prior to welding [46] is very detrimental for high temperature performance of the material. Auzoux *et al* stated that the plastic strain decreases the creep ductility due to the fact that the intergranular creep cavity nucleation rate could be increased by high intergranular stresses generated after the heterogeneous plastic flow in FCC polycrystal [33]. According to the pressure vessel and piping code this plastic strain should be eliminated with heat treatment [11].

The variation of the intergranular strains developed by either welding or cold-work prior to welding and the effect of PWHT on these intergranular strains will be discussed in Chapter 7.

2.3.4 Weld defects

The austenitic stainless steels are considered to be weldable; however, they are subject to a number of weldability problems such as solidification cracking, grain boundary sensitization and reheat cracking. Distortion, lack of penetration, porosity, slag or oxide inclusions in the weld metal are generally related to the operational skills [27]. These defects can be eliminated if the proper precautions are taken. Cracking in the weld metal or in the HAZ is the most problematic defect especially in tubing systems of power generation plants.

Weld solidification cracking

Fully austenitic stainless steel welds are very susceptible to solidification cracking because of the formation of low-melting liquid films along grain boundaries

during the last stages of solidification. The remedy is to select a filler material which will allow formation of some ferrite because the impurities, such as sulphur and phosphorus that promote the formation of liquid films, have a higher solubility in ferrite [47].

Grain boundary sensitization

Austenitic stainless steels may be susceptible to stress corrosion cracking when exposed to severely corrosive environments. Stress corrosion cracking of austenitic stainless steel weldments can result from the sensitization of grain boundaries after heat treatment (post weld heat treatment) or after servicing for a while at high temperature. Weld metal containing small amount of ferrite is not very susceptible to stress corrosion cracking because ferrite dissolves more chromium compared to austenite. However, a fully austenitic HAZ is very susceptible to intergranular attack especially when it is strain-hardened. Plastic strain increases the rate of sensitization. The remedies are (1) to anneal the material to remove the prior cold work, (2) to use low heat inputs and to increase the weld cooling rates and (3) solution heat treatment at 900-1100°C after welding to dissolve the precipitates which may form during welding [47].

Reheat cracking

The HAZ region of higher carbon heat resisting austenitic stainless steel (especially 316H) weldments is susceptible to reheat cracking during the post weld heat treatment or during high temperature service. It is generally agreed that reheat cracking is caused by the relaxation of welding residual stresses [48]. When the weldment is reheated during the post weld heat treatment or service temperature,

carbides precipitate in the grain interiors and strengthen these regions relative to the grain boundaries. If significant stress relaxation occurs at that temperature range, failure may occur preferentially along the grain boundaries [6].

2.3.5 Mechanical properties of stainless steel weldments

Precipitation of carbides and intermetallics, formation or decomposition of delta-ferrite, recrystallization and grain growth, residual stresses, post-weld heat treatment strongly alter the mechanical performance of the weldments. In this part the mechanical properties of the weldments will be briefly described.

Tensile Properties

Many researchers measured the tensile properties at different temperatures by using separate tensile specimens from different weld zones [49-52]. For example, Figure 2.27 compares the variation of 0.2% offset proof strength and ultimate tensile strength of wrought 316 stainless steel base and weld metals with increasing temperature [52]. It can be seen in Figure 2.27(a) that the offset proof strength of the base metal and the weld metal are different. However, UTS is almost similar for both metals as shown in Figure 2.27(b).

The tensile properties (elastic modulus and strength) of the weld metal are strongly dependant on the direction of the solidification [49]. Furthermore, for multi-pass weld condition the material in each weld bead has also different tensile properties [5].

In case of welding onto a cold worked stainless steel, the base metal softens as a function of distance from the fusion boundary. This softening depends on the peak temperature of the thermal cycles. The strength variation and hardness across the

weld as a result of softening in a work hardened stainless steel after welding is schematically plotted in Figure 2.28. It can be seen that there is a continuous change in material properties in the weld affected region. The global performance of the weldment is governed with these local material properties.

The global strength and ductility of a weldment can be obtained by doing conventional tensile tests of transverse and longitudinal cross-weld specimens which are shown in Figure 2.29. Transverse cross-weld specimens provide an excellent comparison of the strength of the weld and base metal. The strain is localized in the weakest region during loading. However the ductility of the cross-weld specimen is governed by the weakest region. Transverse cross-weld specimens are tested to obtain the global ductility. This type of design forces all zones of the joint to strain simultaneously and equally.

Tensile properties are key input into all engineering assessments such as pressure vessel design [11], fracture assessments [12] and elevated temperature life assessments [13]. In addition to the global tensile properties of the weldments, the local material properties of different weld zones are also very important for these engineering assessments. Local tensile properties of weld zones are generally obtained by performing tensile tests with separate tensile specimens machined out from different weld zones.

Separate tensile specimens can be machined out from different weld zones to obtain the local mechanical properties only if the geometry of the weldment is suitable to extract separate standard specimens. In the case where the weldment is too small to extract standard size specimens, micro-tensile specimens may be used

[53]. Occasionally, the geometry of the specimen may not be even suitable to extract micro-tensile specimens. For such cases the local properties such as offset proof strength can be obtained from local hardness values on different weld zones using empirical formulas [54]. The spatial resolution and accuracy that can be achieved using micro-specimen is limited by the ability to isolate the individual weld regions. Although the resolution obtainable by the ball indentation is much better, the technique requires several assumptions and semi-empirical formulas. On the other hand, some optical techniques such as moiré interferometry, electron speckle pattern interferometry (ESPI) and digital image correlation (DIC) overcome many of the limitations and disadvantages of the testing of micro-specimens and instrumented ball indentation. They can be used to extract the local mechanical properties in weldments by obtaining full-field strain measurement on the surface of a single cross-weld specimen during a tension test.

Moiré interferometry is an optical technique commonly used for measuring displacement and strain with very high accuracy in materials subjected to mechanical loading. Moiré exhibits patterns of light and dark bands. Moiré fringes occur when two similar but not quite identical gratings (arrays of equally spaced lines) are arranged so that one array can be viewed through the other. Moiré interferometry uses two-beam interference and a specimen grating. As a result of the diffraction of two beams from the specimen surface, constructive interference creates light fringe whereas destructive interference produces dark fringe. The fringes which are formed due to the interference effect between some form of specimen grating and a reference grating are recorded by a digital camera. The surface strain when the specimen is

loaded can be measured analysing the moiré fringes at different loads. Moiré interferometry has a high range of strain sensitivity. However, the experimental setup requires high skill and is very sensitive to the environment e.g. the interference can be affected due to vibration [55].

ESPI is an interferometry-based optical technique. When a coherent beam of light (laser) directed the specimen surface, the roughness of the surface creates speckles which are a result of interference between coherent photons having different path-lengths. The brightness of each speckle is determined by the combination of path-length differences of all the coherent photons reflected into the camera. As the surface is displaced with respect to the light source, the resultant path length is changed and so is the brightness of the speckle. In practice correlation fringes are created by subtracting the image from a reference image in the computer and in this way the speckle pattern can be compared with a moiré grating. By counting the fringes it is possible to infer the variation in displacement over the entire region of interest, without requiring contact with the surface or the use of markers. This technique requires many optical components such as a laser source, mirrors to adjust the illumination direction and a digital camera to store the speckle patterns [56].

DIC, which is another optical technique for full field strain measurement based on digital tracking surface features, does not require many optical components and it is easier to integrate into a tension test of a cross-weld specimen. Moreover, DIC can easily be applied to high temperature tests. Although the strain sensitivity of DIC is not as high as compared to moiré interferometry and ESPI, its major advantage over interferometric techniques is its measurement range; that is, it is possible to measure

small elastic strains and large plastic strains with the same set up. The first application of DIC to measure local mechanical properties in weldments was achieved by Reynolds and Duvall on friction stir welded aluminium sheets [57]. They successfully implemented DIC to the tension test of a cross-weld specimen extracted from friction stir welded 5454 aluminium sheets in order to determine the constitutive behaviour of the weld metal, heat affected zone and base metal. They found that DIC is a promising tool to obtain the local stress-strain curves from various microstructural regions. Similar to their study, the major aim of this dissertation is to determine the room-temperature local tensile strength of austenitic stainless steel weldments in boiler units of the nuclear power plants. This was achieved by using digital image correlation (DIC). The details of the technique and the results will be discussed in Chapter 3 and 6.

Creep properties

The difference in rupture stress at elevated temperatures between the base metal and the weld metal is taken into account for the design of the welded components. However, there is a large scatter in weld metal rupture strength. This scatter could be related to δ-ferrite content and morphology, welding heat input, residual stress, welding process, precipitation rate of carbides and intermetallics [58].

Studies of some cross-weld austenitic stainless steel weldments have shown that failure consistently occurs in the weld metal, that is, the weld metal is the strain limiting factor [59]. The relatively low ductility of the weld metal has been attributed to the following factors; transformation of δ-ferrite to other phases, the precipitation of continuous films of $M_{23}C_6$ carbide along δ/γ boundaries, high δ-ferrite levels, high

inclusion content in the weld metal, hardening of the grain interiors by particle dispersions [5].

Corrosion resistance

For austenitic stainless steels the susceptibility to corrosion attack can increase after welding, because welding produces metallurgical modifications, as well as residual stresses generated by the welding process and these can accelerate the corrosion attack in the weld region [6].

$M_{23}C_6$ carbides of mostly Cr and other metals form preferentially along the grain boundaries in the HAZ of austenitic stainless steels. The Cr-depleted zone along the grain boundaries makes the HAZ very susceptible to corrosion. The attack creates a crack on the surface of the material and in the presence of residual tensile stresses on the surface or the tensile stresses during operation can accelerate the crack propagation [5]. This phenomenon is called "Stress Corrosion Cracking (SCC)". It can be either intergranular or transgranular. Intergranular stress corrosion cracking (IGSCC) is observed most commonly. The chlorides, caustic, and pure water and steam can promote SCC.

2.4 Summary

- Austenitic stainless steels have good corrosion and high temperature properties. Therefore, they are used in boiler units of nuclear power plants.

- The macroscopic stress-strain relationship, work hardening effect, the deformation and anisotropy of FCC polycrystalline metals were explained, to provide

a better understanding of the results which will be presented in the following chapters.

- Work hardening or cold working increases the strength of the austenitic stainless steel and decreases the ductility. As a result of cold working plastic strain is locked in the metal. Residual strains develop between the grains after the cold working and they can be used to determine the amount of plastic strain locked in the metal after any manufacturing step.

- The types of fusion welding processes and the fundamentals of welding metallurgy of austenitic stainless steels were explained. Welding can modify the microstructure of the base metal particularly when it is cold worked. Cold working increases the kinetics of precipitation of carbides and intermetallics in austenitic stainless steels. Welding onto a cold worked steel may cause the precipitation of carbides and intermetallics as well as the modification of the grain size. The effect of cold working on austenitic stainless steels should be eliminated with solution heat treatment if the amount of cold work is above 15-20%. Some of the weld defects such as solidification cracking, stress-corrosion cracking and reheat cracking which were observed in the austenitic stainless steel welds were also explained.

- Welding causes a variation of the mechanical properties such as tensile properties, creep properties and corrosion resistance in the weld affected zones. The base metal near the fusion boundary may be strain hardened as a result of the thermo-mechanical cycles and restraints during welding. On the other hand, cold-worked base metal may soften with the effect of the heat flowing towards the base metal. Welding also introduces residual stresses which can be eliminated with a heat

treatment process. However, the heat treatment process also alters the local mechanical properties of the weldments.

- The global tensile properties can be obtained by doing some conventional tests of transverse and longitudinal cross-weld specimens. The local tensile properties can also be obtained by measuring full field strain maps of the weldment during tension tests using optical techniques.

2.5 References

[1] Higgins RA. Engineering Metallurgy - Applied Physical Metallurgy. London E. Arnold, 1993.

[2] ASM Handbook, Vol. 1: Properties and Selection: Irons, Steels and High Performance Alloys: American Society for Metals, 1990.

[3] Totten GE. Steel heat treatment metallurgy and technologies: Taylor & Francis, 2007.

[4] Krauss G. Steels: processing, structure, and performance: ASM International, 2005.

[5] Marshall P. Austenitic Stainless Steels: Microstructure and Mechanical Properties: Elsevier Applied Science Publishers, 1984.

[6] Lippold JC, Kotecki DJ. Welding Metallurgy and Weldability of Stainless Steel: John Wiley & Sons, 2005.

[7] Daymond MR, Bourke MAM, Von Dreele RB, Clausen B, Lorentzen T. Use of Rietveld refinement for elastic macrostrain determination and for evaluation of plastic strain history from diffraction spectra. Journal of Applied Physics 1997;82:1554.

[8] Korsunsky AM, Daymond MR, James KE. The correlation between plastic strain and anisotropy strain in aluminium alloy polycrystals. Materials Science and Engineering A 2002;334:41.

[9] Lewis SJ, Truman CE. Diffraction measurements for evaluating plastic strain in A533B ferritic steel - a feasibility study. Journal of Physics D: Applied Physics 2010;43:265501.

[10] Ross CTF. Mechanics of Solids: Horwood Pub., 1999.

[11] ASME Section I, ASME Boiler and Pressure Vessel Code, Section I: Rules for Construction of Power Boilers. New York, USA: ASME, 2010.

[12] R6 Revision 4 Assessment of the Integrity of Structures containing Defects. Gloucester, UK: British Energy Generation Limited, 2009.

[13] R5 Issue 3 Assessment Procedure for High Temperature Response of Structures. Gloucester, UK: British Energy Generation Limited, 2003.

[14] Dieter GE, Bacon D. Mechanical Metallurgy: McGraw Hill Book Co., 1988.

[15] Datsko J. Material Properties and Manufacturing Processes: John Wiley & Sons, 1966.

[16] Liaw P, Landes J. Influence of prestrain history on fracture toughness properties of steels. Metallurgical and Materials Transactions A 1986;17:473.

[17] ASM Handbook, Vol. 19: Fatigue and Fracture: American Society for Metals, 1990.

[18] Willis M, McDonaugh-Smith A, Hales R. Prestrain effects on creep ductility of a 316 stainless steel light forging. International Journal of Pressure Vessels and Piping 1999;76:355.

[19] Pang JWL, Holden TM, Wright JS, Mason TE. The generation of intergranular strains in 309H stainless steel under uniaxial loading. Acta Materialia 2000;48:1131.

[20] Gooch DJ. The effect of anisotropy on creep and creep crack growth in cold-worked C---Mn steel at 360°C. Materials Science and Engineering 1987;91:45.

[21] Kamaya M, Wilkinson AJ, Titchmarsh JM. Quantification of plastic strain of stainless steel and nickel alloy by electron backscatter diffraction. Acta Materialia 2006;54:539.

[22] Hutchings MT, Withers PJ, Holden TM, Lorentzen T. Introduction to the characterization of residual stress by neutron diffraction: Taylor & Francis, 2005.

[23] Daymond MR, Bouchard PJ. Elastoplastic Deformation of 316 Stainless Steel Under Tensile Loading at Elevated Temperatures. Metallurgical and Materials Transactions A 2006;37A:1863.

[24] Clausen B, Lorentzen T, Bourke MAM, Daymond MR. Lattice strain evolution during uniaxial tensile loading of stainless steel. Materials Science and Engineering 1999;A259:17.

[25] Peng RL, Oden M, Wang YD, Johansson S. Intergranular strains and plastic deformation of an austenitic stainless steel Materials Science and Engineering 2002;A334:215.

[26] Messler RW. Principles of Welding: Processes, Physics, Chemistry, and Metallurgy: Wiley-VCH, 1999.

[27] Gourd LM. Principles of Welding Technology: Butterworth-Heinemann Ltd, 1995.

[28] Kou S. Welding Metallurgy: Wiley-Blackwell, 2003.

[29] ASM Handbook, Vol. 6: Welding, Brazing and Soldering: American Society for Metals, 1990.

[30] Brooks JA, Thompson AW. Microstructural development and solidification cracking susceptibility of austenitic stainless steel welds. International Materials Reviews 1991;36:16.

[31] Turski M, Smith MC, Bouchard PJ, Edwards L, Withers PJ. Spatially resolved materials property data from a uniaxial cross-weld tensile test. Journal of Pressure Vessel Technology 2009;131:061406.

[32] Smith MC, Smith AC. NeT bead-on-plate round robin: Comparison of residual stress predictions and measurements. International Journal of Pressure Vessels and Piping 2009;86:79.

[33] Auzoux Q, Allais L, Caës C, Monnet I, Gourgues AF, Pineau A. Effect of pre-strain on creep of three AISI 316 austenitic stainless steels in relation to reheat cracking of weld-affected zones. Journal of Nuclear Materials;400:127.

[34] Padilha AF, Rios PR. Decomposition of Austenite in Austenitic Stainless Steels. Iron Steel Inst Jpn 2002;42:325.

[35] Folkhard E. Welding metallurgy of stainless steel: Springer-Verlag Wien New York, 1988.

[36] Bechtoldt CJ, Vacher HC. Phase-diagram study of alloys in the iron-chromium-molybdenum-nickel system. J. Res. Natl. Bur. Stand. 1957;58:7.

[37] Schaeffler AL. Constitution diagram for stainless steel weld metal. Met. Prog. 1949;56:680.

[38] Pickering FB. Physical Metallurgy and the Design of Steels: Applied Science Publishers, 1978.

[39] DeLong WT. Ferrite in austenitic stainless steel weld metal. Welding J. 1974;53:273.

[40] Weiss B, Stickler R. Phase instabilities during high temperature exposure of 316 austenitic stainless steel. Metallurgical and Materials Transactions B 1972;3:851.

[41] Lai JK, Haigh JR. Delta-ferrite transformations in a type 316 weld metal. UK: Central Electricity Research Lab., RD/L/N/159/77, 1978.

[42] Verhoeven JD. Fundamentals of physical metallurgy: John Wiley & Sons, 1975.

[43] Connor LP. Welding Handbook, Vol. 1: Welding Technology: American Welding Society, 1987.

[44] Gladwin DN, Spindler MW. Post-weld heat treatment of type 316H weldments at 750C TEL/MEM/0460/94, Nuclear Electric, UK, 1994.

[45] Coleman SL. Considerations on the effect of a 750C post-weld heat treatment on type 316H heat affected zone. ED/AGR/REP/0095/95, Nuclear Electric, UK, 1995.

[46] Moen RA, Smith GV. A Consideration on Limits of Cold Working in Nuclear Construction. Journal of Engineering Materials and Technology 1975;97:162.

[47] Lampman S. Weld integrity and performance: ASM International, 1997.

[48] Skelton RP, Goodall IW, Webster GA, Spindler MW. Factors affecting reheat cracking in the HAZ of austenitic steel weldments. International Journal of Pressure Vessels and Piping;80:441.

[49] Kimmins ST, Horton CAP. Anisotropy of elastic and plastic properties of type 17Cr-8Ni-2Mo and 19Cr-12Ni-3Mo weld metals TRPD/L/2952/N85, Central Electricity Generating Board, UK, 1986.

[50] Barnett KA, Chastell DJ, Smith RF. The tensile and thoughness properties of the HAZ of type 316H austenitic stainless steel weldments: As welded HAZ and unaged parent material. TD/SEB/MEM/2126/92, Nuclear Electric, UK, 1993.

[51] Bouchard PJ. Preliminary report of measured type 316H base metal and type 316L weld metal tensile properties VORSAC(98)(W027), Nuclear Electric, UK, 1998.

[52] Horton CAP, Thomas RG. Tensile properties of as-welded type 17Cr-8Ni-2Mo and 19Cr-12Ni-3Mo weld metals for use with type 316 stainless steel. RD/L/2229R81, Central Electricity Generating Board, UK, 1982.

[53] Çam G, Erim S, Yeni Ç, Kocak M. Determination of mechanical and fracture properties of laser beam welded steel joint. Welding Journal 1999;78 (6):193.

[54] Malow TR, Koch CC, Miraglia PQ, Murty KL. Compressive mechanical behavior of nanocrystalline Fe investigated with an automated ball indentation technique. Materials Science and Engineering A 1998;252:36.

[55] Dally JW, Riley WF. Experimental Stress Analysis. Tennessee, USA: College House Enterprises LLC, 2005.

[56] Kennedy DM, Schauperl Z, Greene S. Application of ESPI-method for strain analysis in thin wall cylinders. Optics and Lasers in Engineering 2004;41:585.

[57] Reynolds AP, Duvall F. Digital image correlation for determination of weld and base metal constitutive behavior. Welding Research Supplement 1999:355.

[58] Smith JJ, Farrar RA. Influence of microstructure and composition on mechanical properties of some AISI 300 series weld metals. International Materials Reviews 1993;38:25.

[59] Wood DS. The stress rupture properties of austenitic steel weld metals EUR 10124 EN, Commission of the European Communities, Nuclear Science and Technology, UK, 1985.

[60] Daymond MR. Internal Stresses in Deformed Crystalline Aggregates. Reviews in Mineralogy and Geochemistry 2006;63:427.

2.6 Tables & Figures

AISI Designation	Composition, %							
	C	Cr	Ni	Mo	N	Nb	Ti	Other
304	0.08 max	19	10	-	-	-	-	-
304H	0.04-0.10	19	10	-	-	-	-	-
304L	0.03 max	19	10	-	-	-	-	-
304N	0.08 max	19	9.25	-	0.13	-	-	-
309	0.30 max	23	13	-	-	-	-	-
309H	0.04-0.10	23	13	-	-	-	-	-
310	0.25 max	25	20	-	-	-	-	-
310H	0.04-0.10	25	20	-	-	-	-	-
316	0.08 max	17	12	2.5	-	-	-	-
316L	0.03 max	17	12	2.5	-	-	-	-
316N	0.08 max	17	12	2.5	0.13	-	-	-
316H	0.04-0.10	17	12	2.5	-	-	-	-
316LN	0.035 max	17	12	2.5	0.13	-	-	-
317	0.08 max	19	13	3.5	-	-	-	-
317L	0.035 max	19	13	3.5	-	-	-	-
321	0.08 max	18	10	-	-	-	5 × C min, 0.70 max	-
321H	0.04-0.10	18	10	-	-	-	4 × C min, 0.60 max	-
347	0.08 max	18	11	-	-	10 × C min (Min. for Nb+Ta)	-	1.0 (Nb + Ta) max
347H	0.04-0.10	18	11	-	-	8 × C min (Min. for Nb+Ta)	-	1.0 (Nb + Ta) max
348	0.08 max	18	11	-	-	10 × C min (Min. for Nb+Ta)	-	0.10 Ta max, 1.0 (Nb + Ta) max
348H	0.04-0.10	18	11	-	-	8 × C min (Min. for Nb+Ta)	-	0.10 Ta max, 1.0 (Nb + Ta) max
19-9 DL	0.3	19	9	1.25	-	0.4	0.3	1.25 W
19-9 DX	0.3	19.2	9	1.5	-	-	0.55	1.2 W
17-14-CuMo	0.12	16	14	2.5	-	0.4	0.3	3.0 Cu
201	0.15 max	17	4.2	-	0.25 max	-	-	-
202	0.09	18	5	-	0.1	-	-	8.0 Mn
205	0.18	17.2	1.4	-	0.36	-	-	-
216	0.05	20	6	2.5	0.35	-	-	8.5 Mn
Nitronic 32	0.1	18	1.6	-	0.34	-	-	12.0 Mn
Nitronic 33	0.08 max	18	3	-	0.3	-	-	13.0 Mn
Nitronic 50	0.06 max	21	12	2	0.3	0.2	-	5.0 Mn
Nitronic 60	0.10 max	17	8.5	2	-	-	-	8.0 Mn, 0.20 V, 4.0 Si
Carpenter 18-18 Plus	0.1	18	<0.50	1	0.5	-	-	16.0 Mn, 0.40 Si, 1.0 Cu

Table 2.1 Types of austenitic stainless steels according to AISI designation [2]

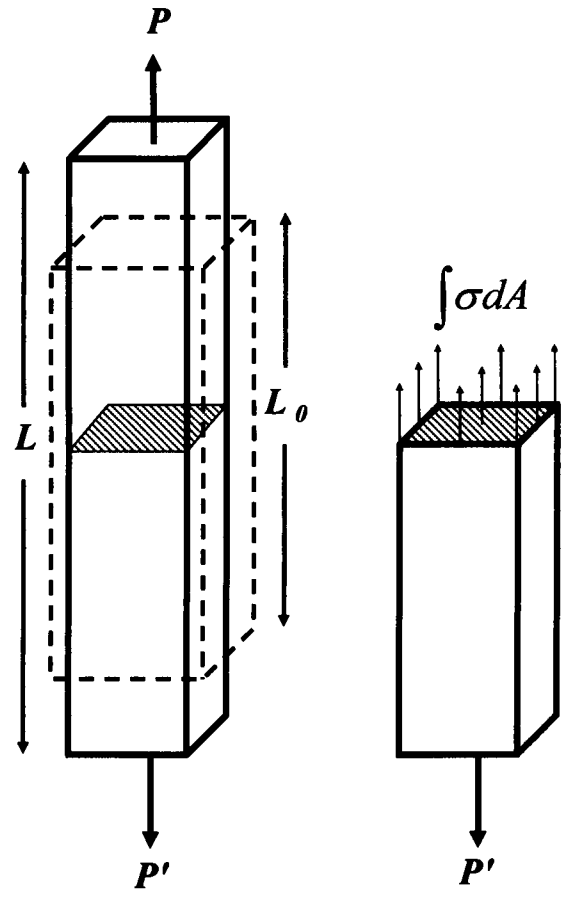

Figure 2.1 Rectangular uniform bar subjected to axial loading

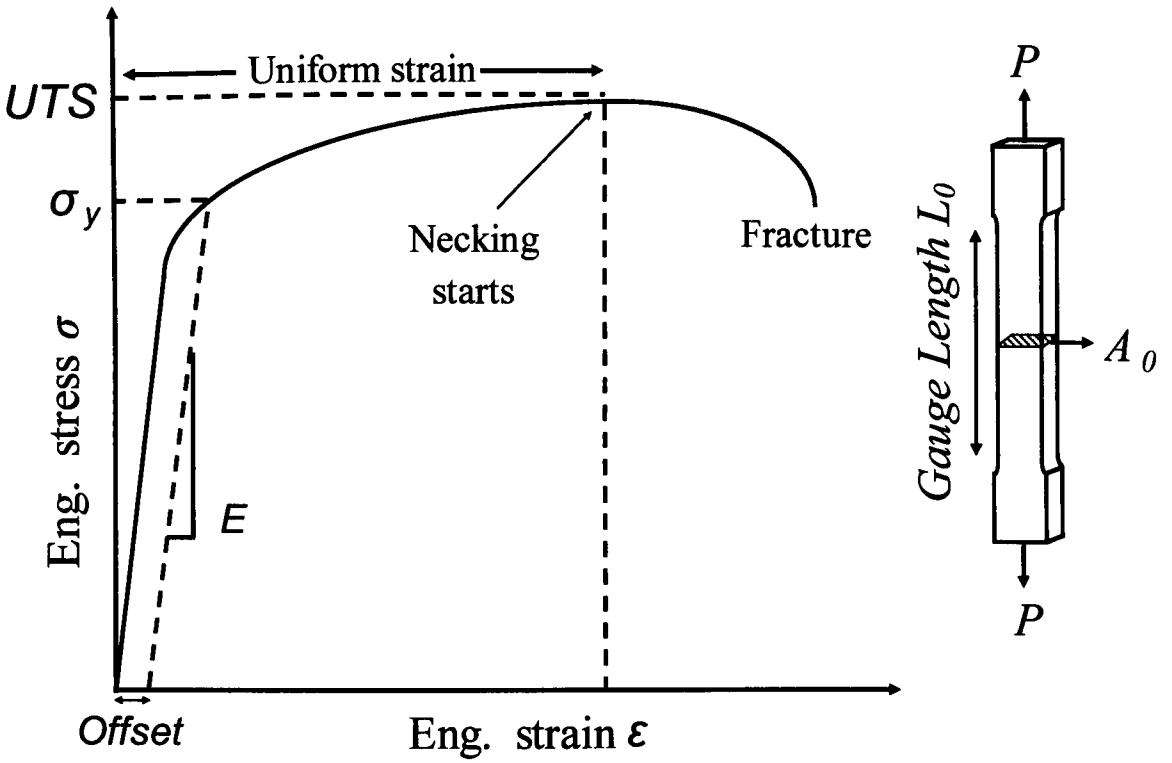

Figure 2.2 Engineering stress-strain curve

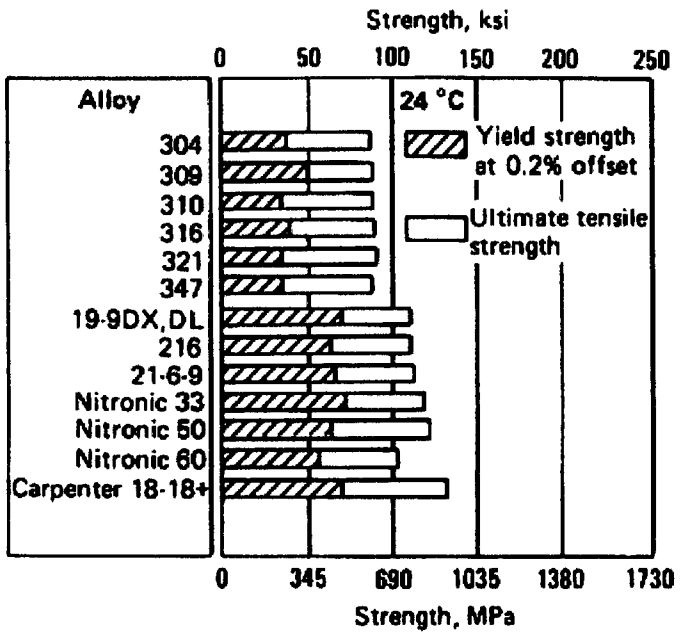

Figure 2.3 0.2% offset proof strength and ultimate tensile strength of austenitic stainless steels at room temperature [2]

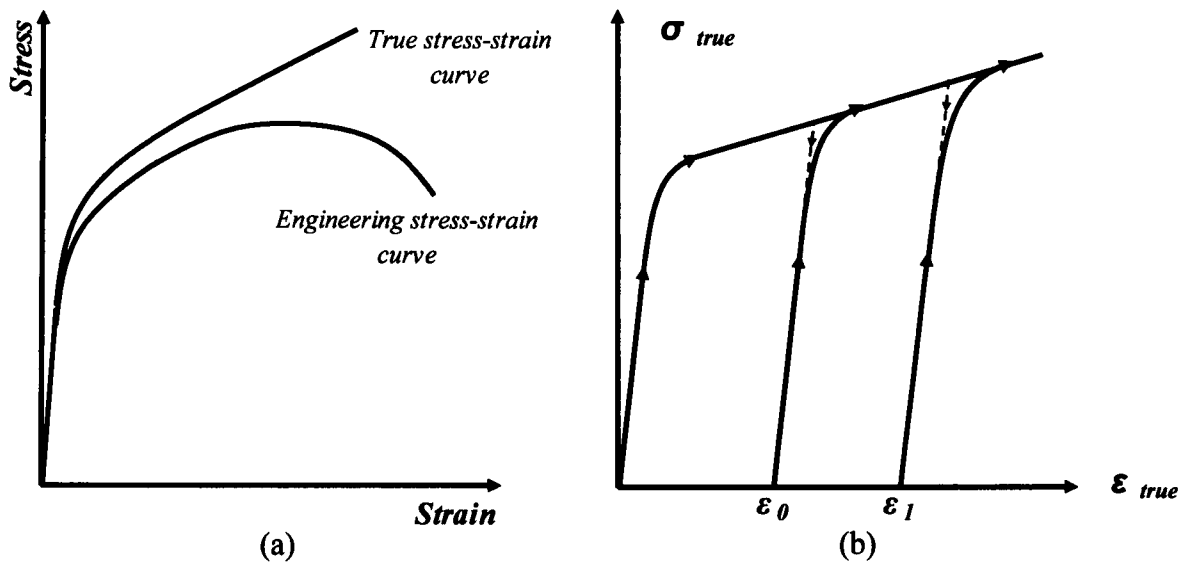

Figure 2.4 (a) Comparison of engineering and true stress-strain curves (b) Loading and unloading paths showing the amount of strain hardening prior to the subsequent loading

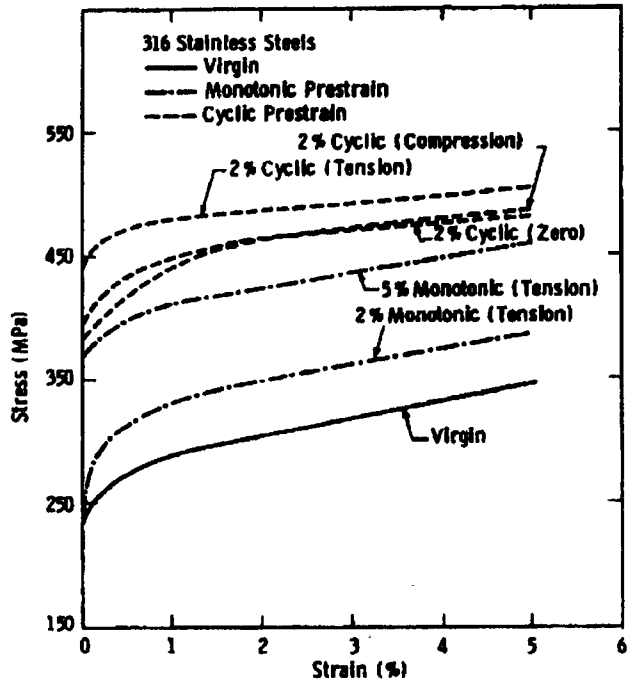

Figure 2.5 The effect of monotonic and cyclic pre-straining on tensile stress-strain curves for type 316 stainless steel at room temperature [16]

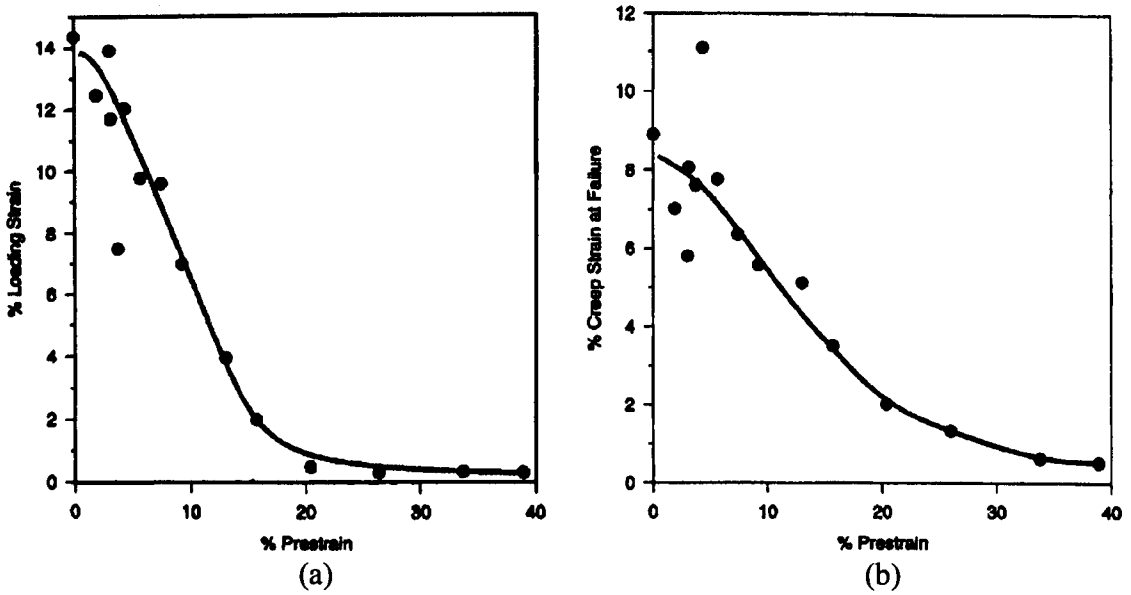

Figure 2.6 The effect of room temperature pre-straining on the high temperature tensile ductility (a) and creep failure strain for a type 316 stainless steel at 575°C [18]

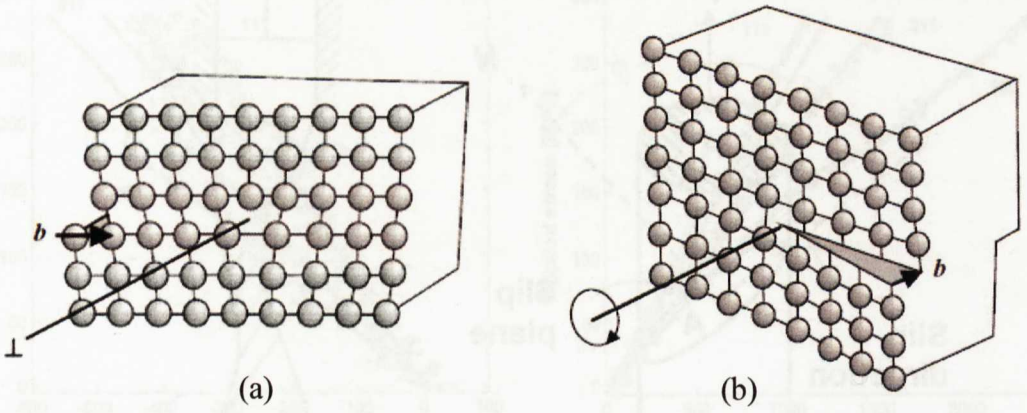

Figure 2.7 Linear defects: edge dislocation (a) and screw dislocation (b)

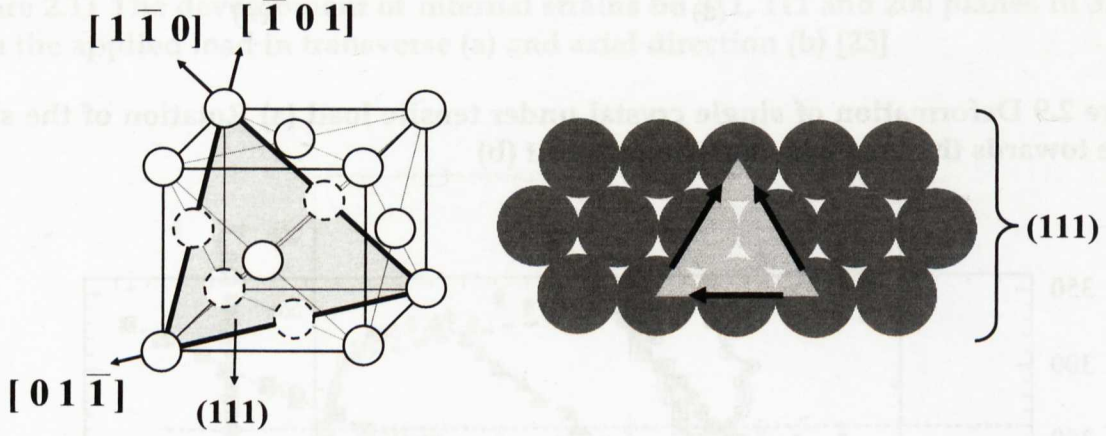

Figure 2.8 FCC crystal structure (a) and slip directions on 111 plane

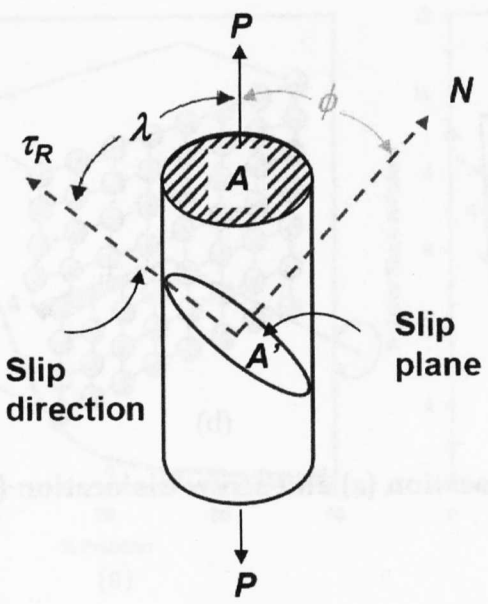

(a)

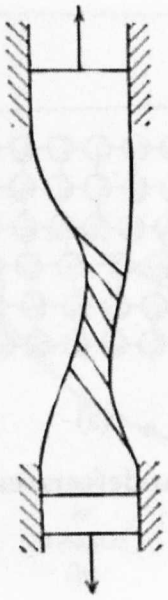

(b)

Figure 2.9 Deformation of single crystal under tensile load (a) Rotation of the slip plane towards the load axis due to constraint (b)

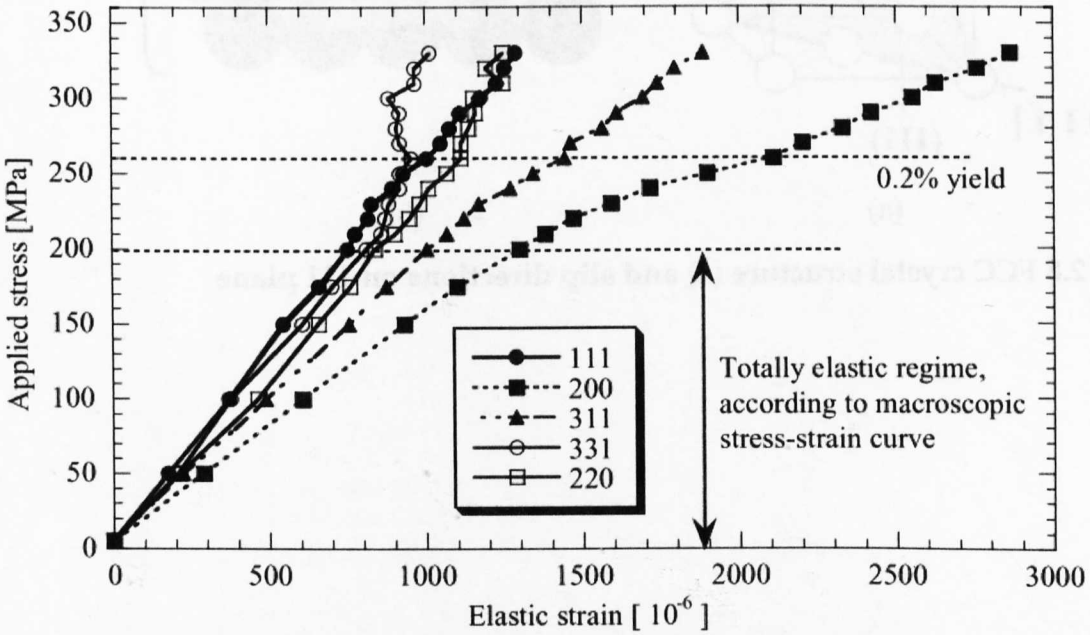

Figure 2.10 The elastic and plastic anisotropy in stainless steel [60]

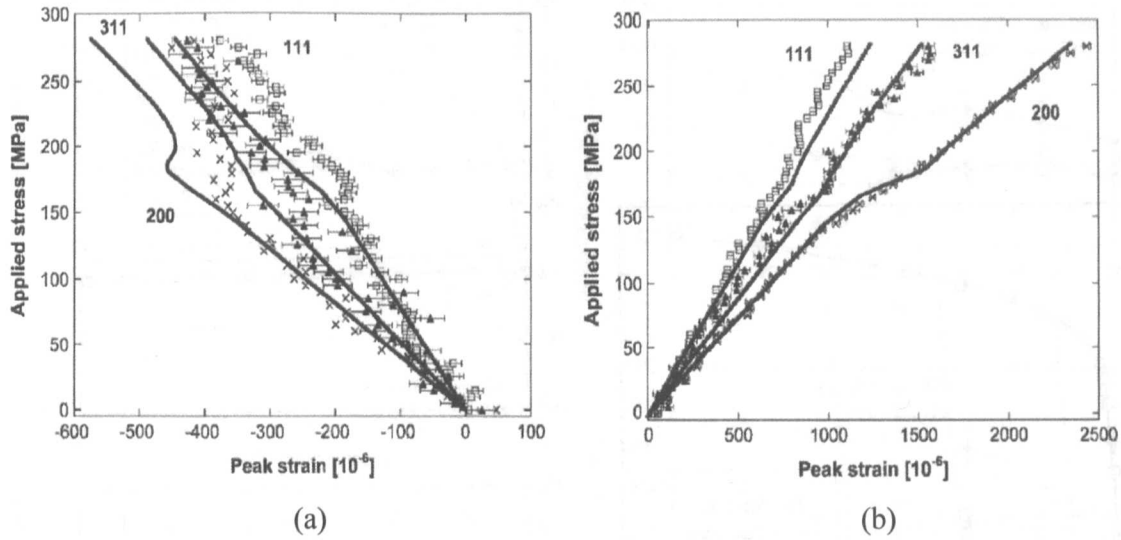

Figure 2.11 The development of internal strains on 311, 111 and 200 planes in 316H with the applied load in transverse (a) and axial direction (b) [23]

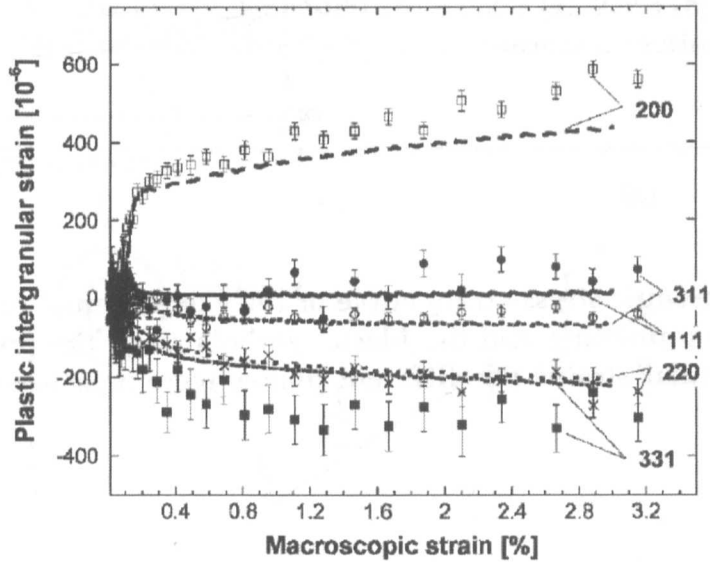

Figure 2.12 Axial plastic intergranular strains [23]

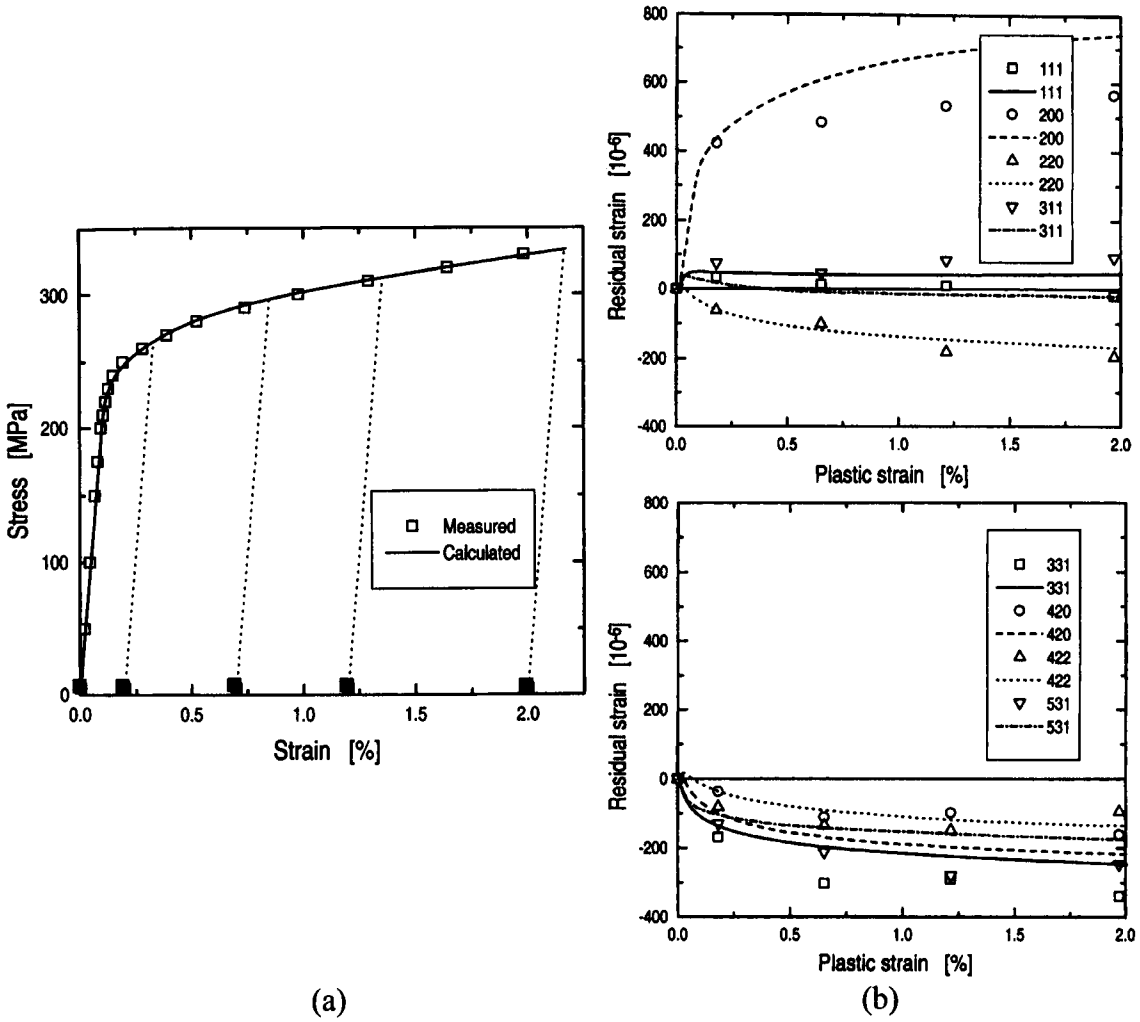

Figure 2.13 Macroscopic stress-strain curve of the experimental test (a) The dashed lines indicate the unloading and the black symbols show the points at which the residual intergranular strains for different planes were measured as shown in (b) [24]

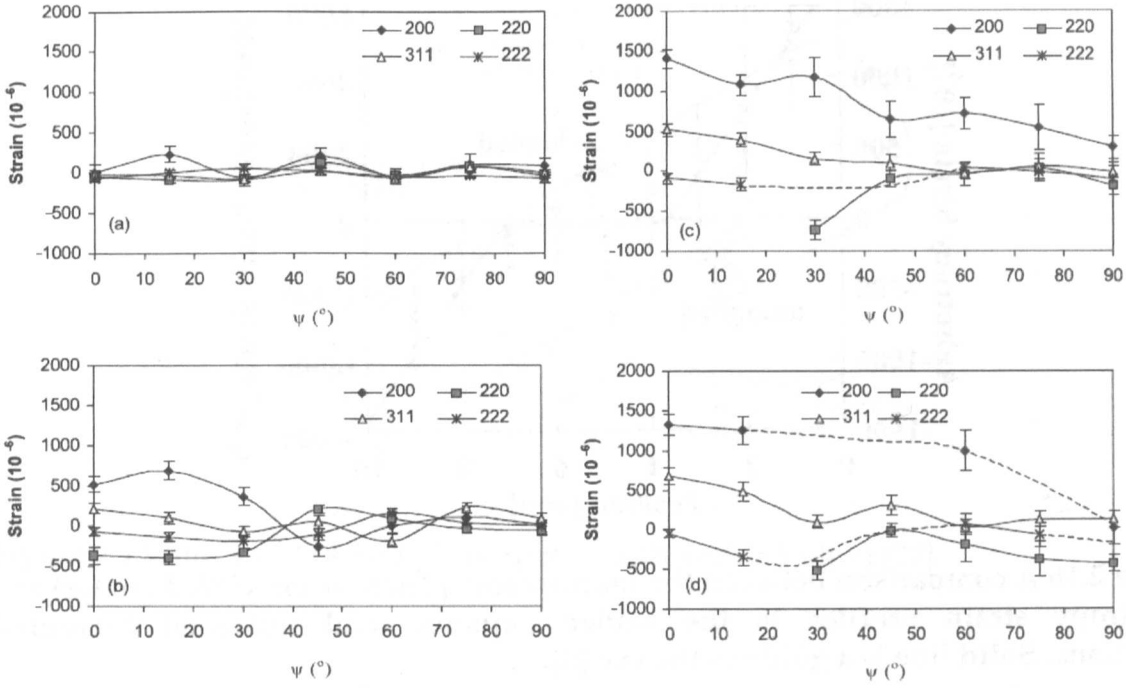

Figure 2.14 The variation of residual intergranular strains as a function of sample direction in samples which were unloaded from 0.2% (a), 7.5% (b), 29.8% (c), 44.7% (d). Ψ=0° is the loading direction and Ψ=90° is the normal direction [25]

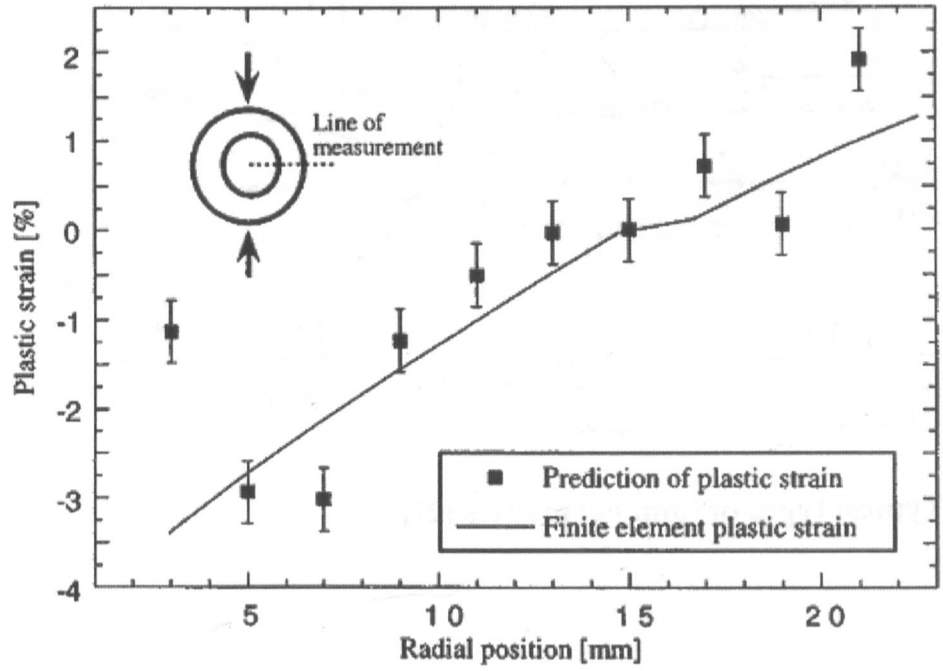

Figure 2.15 The comparison of the predicted plastic strain by using anisotropy strain and finite element model on the line of measurement [7].

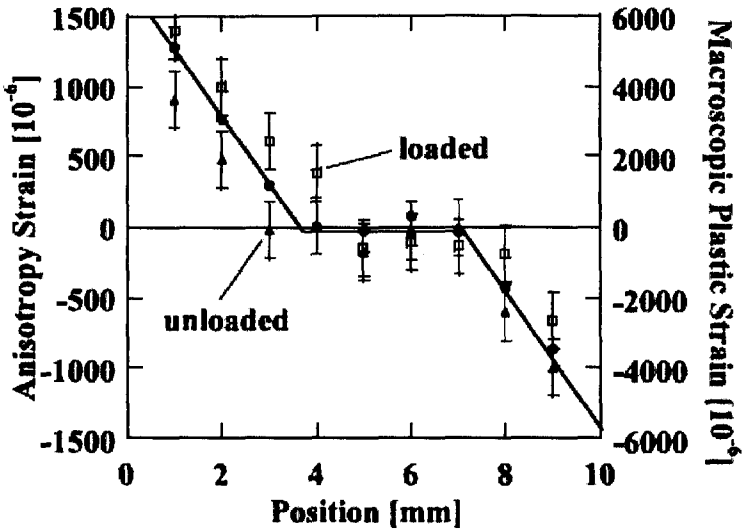

Figure 2.16 A comparison between the macroscopic plastic strain (filled circles) and anisotropy strain profiles in the loaded (squares) and unloaded (triangles) conditions. Solid line is a guide to the eye [8].

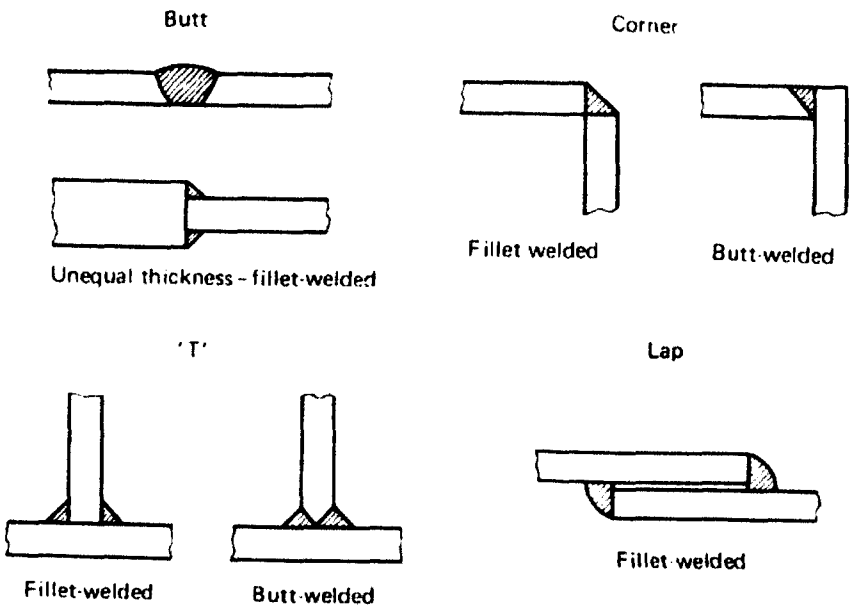

Figure 2.17 Typical types of joint geometries [27]

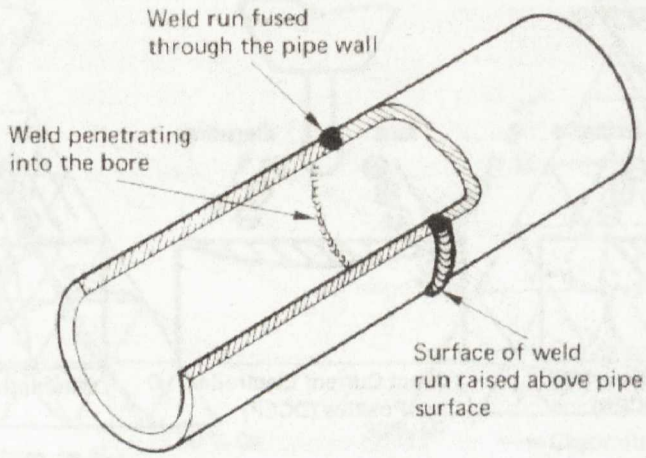

Figure 2.18 Butt weld of two pipes (butt - girth welded pipe) [27]

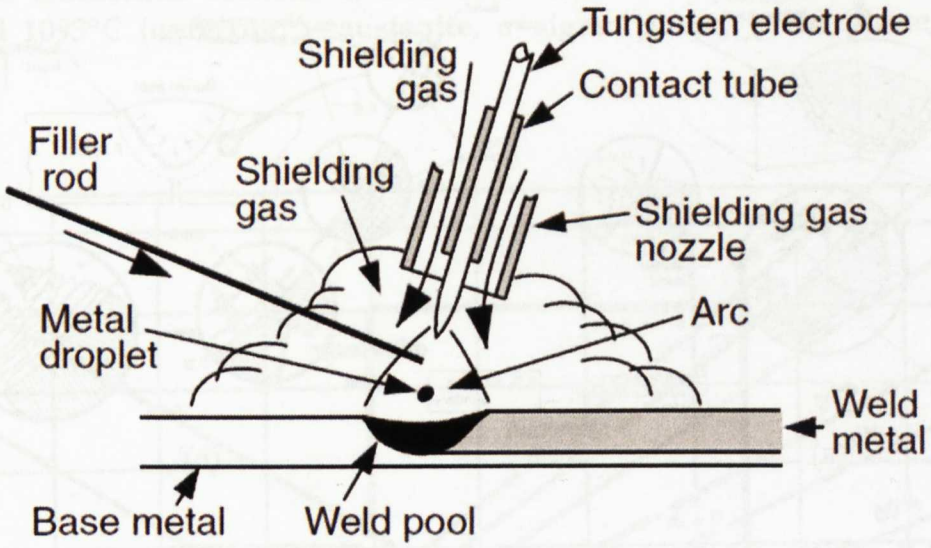

Figure 2.19 Schematic view of the GTAW process

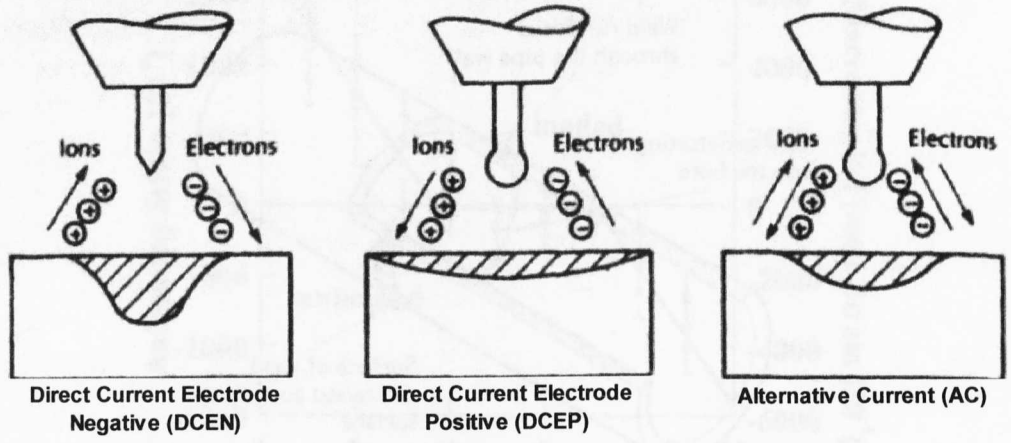

Figure 2.20 Polarities in GTAW process

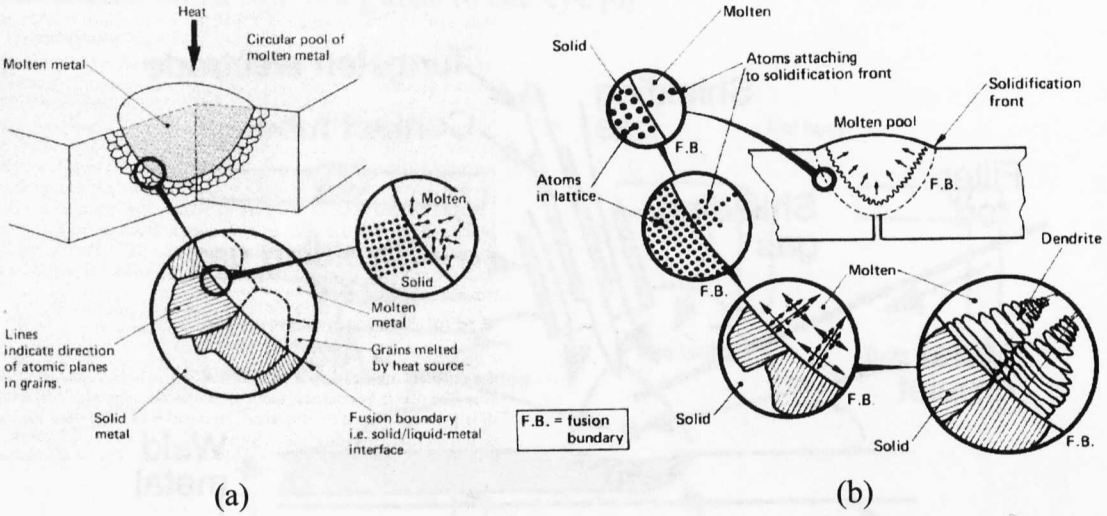

Figure 2.21 Formation of the weld pool (a) and stages of solidification (b) [27]

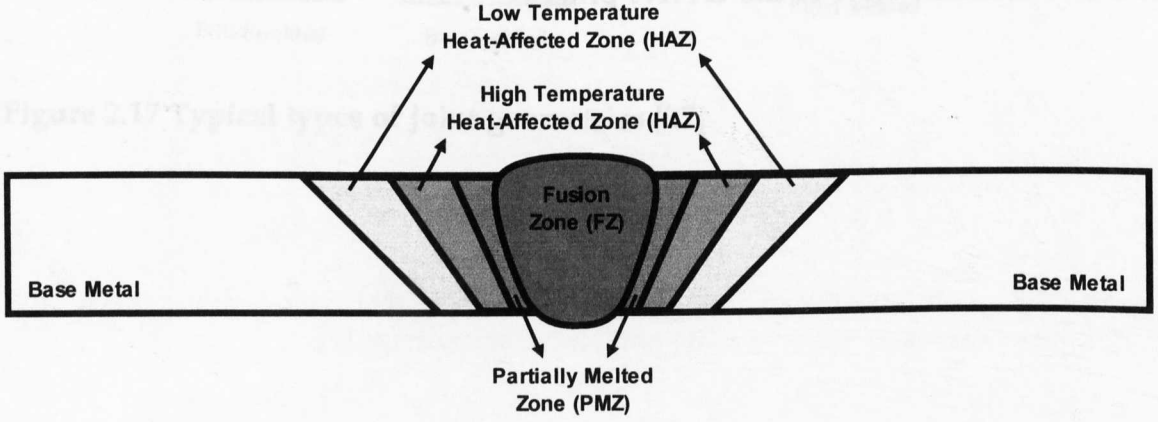

Figure 2.22 Metallurgical zones in a welded alloy plate

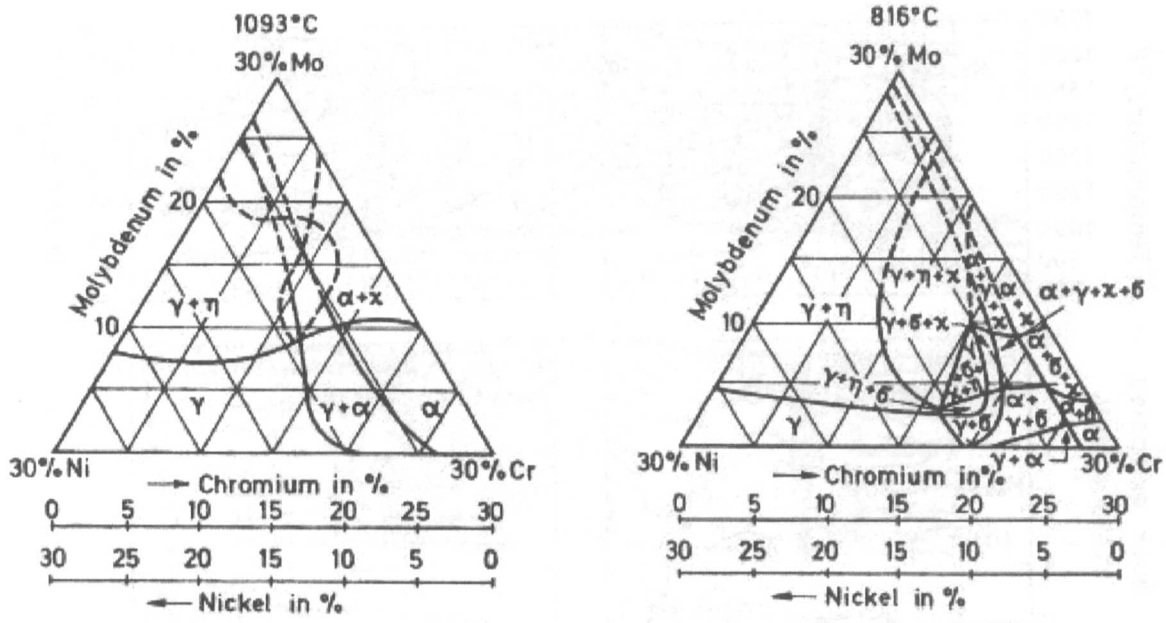

Figure 2.23 Isothermal sections of iron-chromium-nickel-molybdenum system at 816°C and 1093°C (α=ferrite, γ=austenite, σ=sigma phase, χ=chi phase, η=Laves phase) [35]

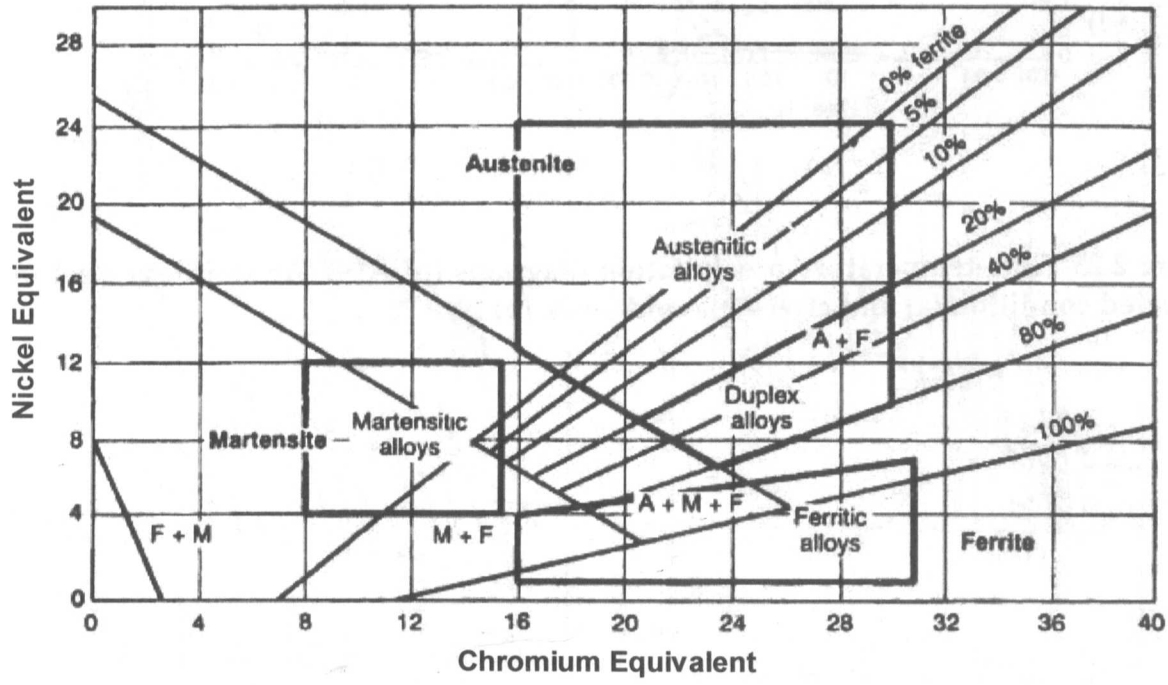

Figure 2.24 Modified Schaeffler's diagram

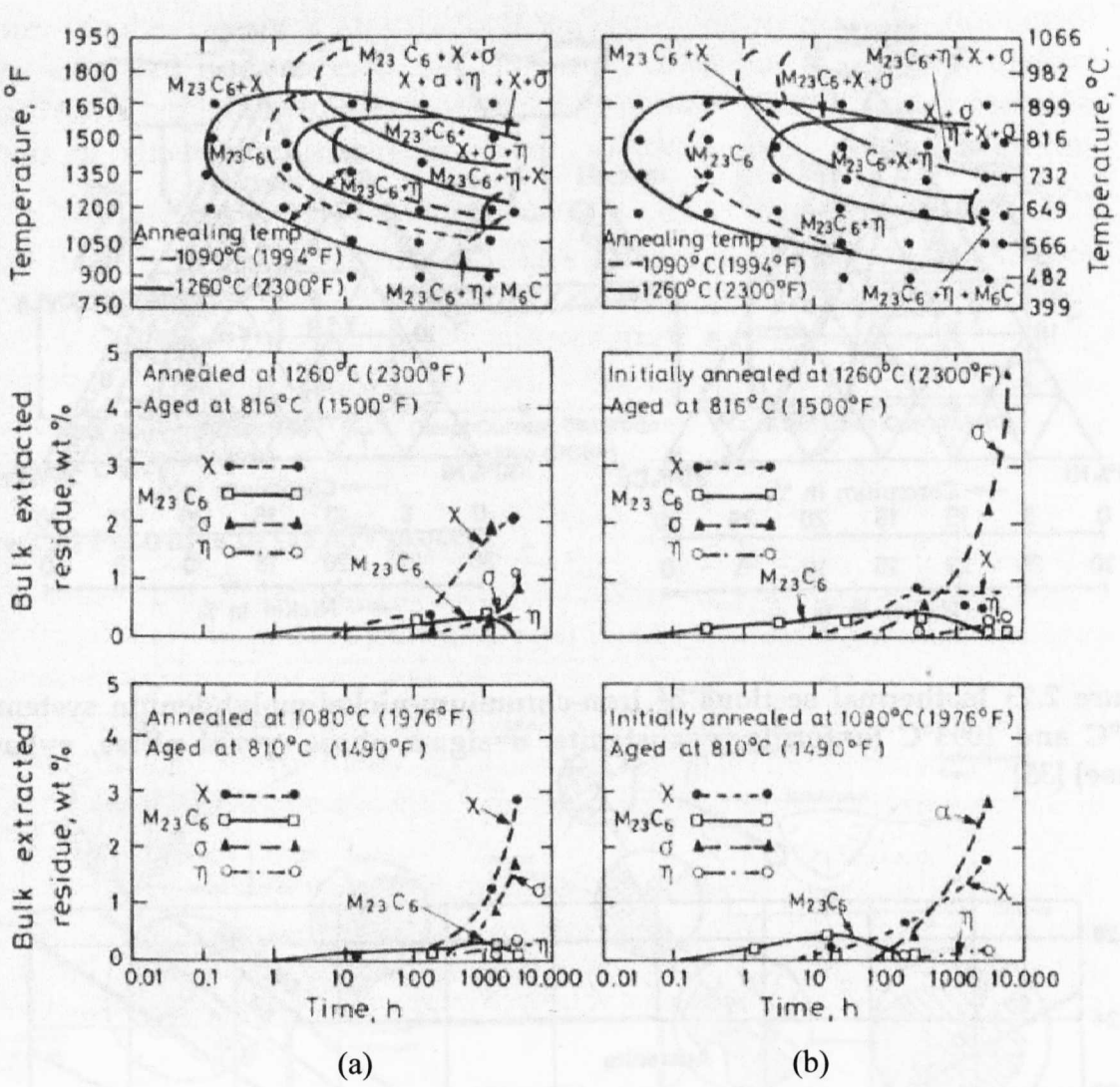

Figure 2.25 Time-temperature-precipitation diagrams for AISI 316 stainless steel in annealed condition (a) and after 20% cold work (b)

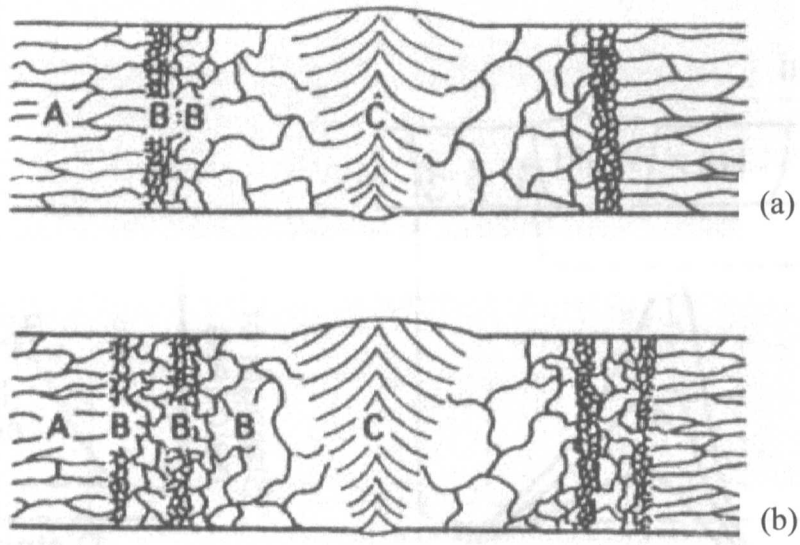

Figure 2.26 Recrystallization and grain growth in HAZ of a cold worked single phase material in which no solid state phase transformation occurs on heating (a) and in HAZ of a cold worked material that undergoes an allotropic transformation on heating (b) [43]

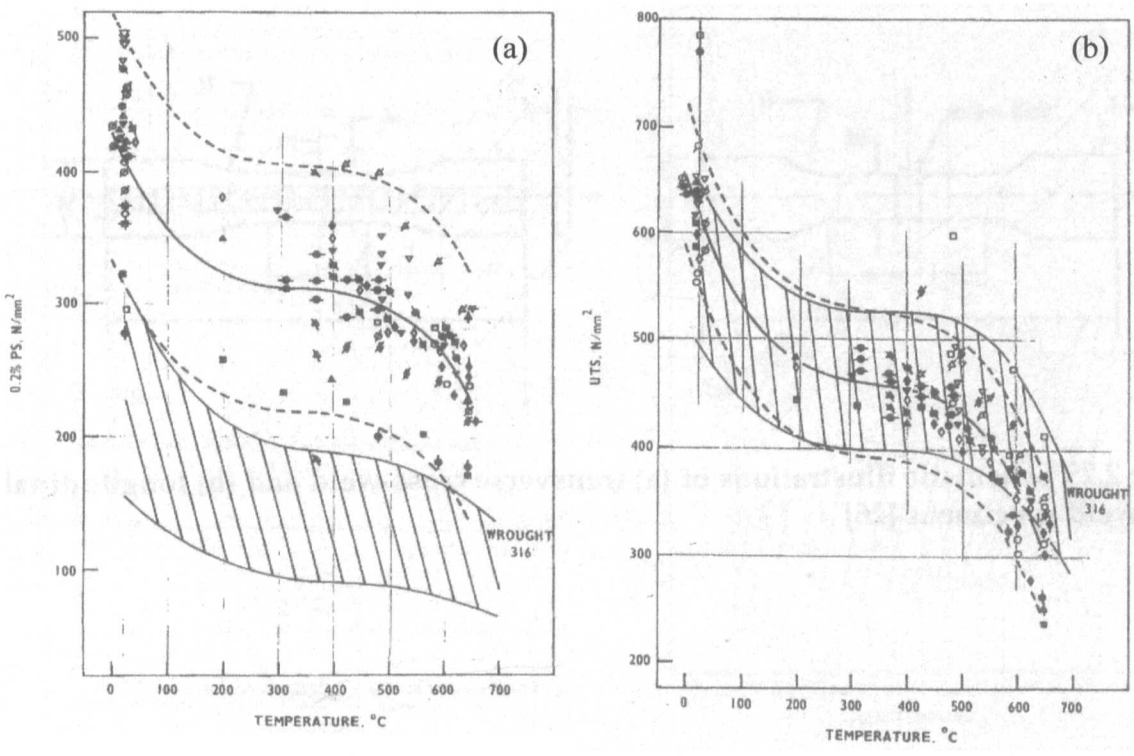

Figure 2.27 0.2% proof strength (a) and ultimate tensile strength (b) data for the some austenitic stainless steel weld metals compared with type 316 wrought material (dashed area: 95% confidence limit, symbols: weld metal) [52]

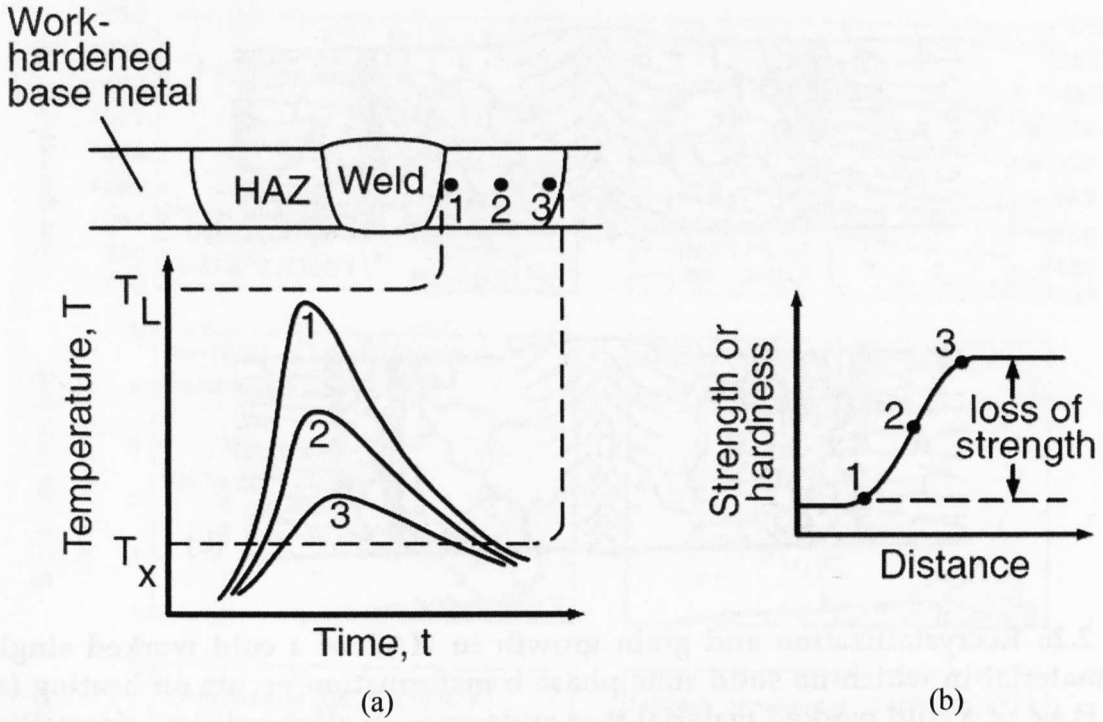

Figure 2.28 Softening in a work hardened material after welding. Thermal Cycles (a) Hardness or strength variation across welding (b) [28]

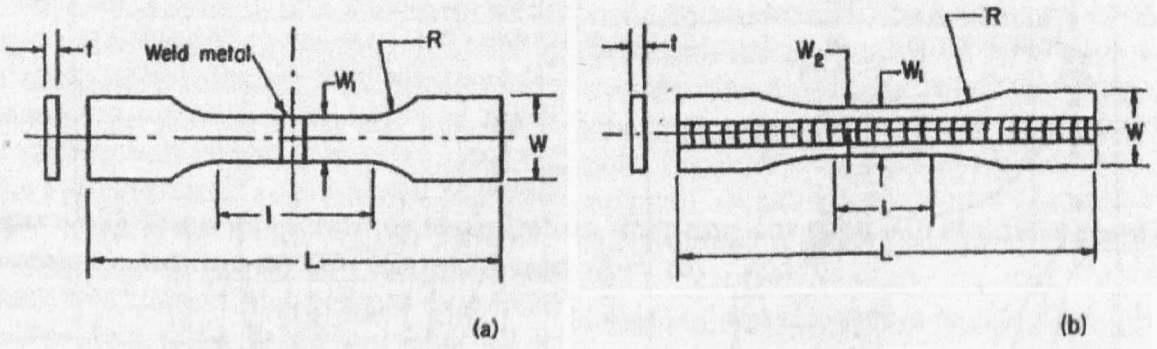

Figure 2.29 Schematic illustrations of (a) transverse cross-weld and (b) longitudinal cross-weld specimens [26]

Chapter 3

Experimental Methods

3.1 Optical (Light) Microscope

The optical microscope or light microscope which consists of magnifying lenses is a very common tool for viewing the microstructure of the metals. Reflected light is used for the study of metals. The polished metal surface is etched with some chemicals. Depending on the chemicals, grain boundaries or some phases in a multi-phase microstructure are attacked and when the light is reflected on the metal surface this creates a contrast between different constituents of the microstructure. The light microscope which was used to obtain the micrographs presented in Chapter 5 is an inverted light microscope in which the orientation of the light path to plane-of-polish of the specimen during observation is as shown in Figure 3.1. Optical microscopes are used for resolutions down to roughly the wavelength of light (about half of a micron) and electron microscopes are used for higher resolution, down to atomic resolution. The magnification range of 50-500× was selected to obtain the micrographs presented in Chapter 5.

3.2 Scanning Electron Microscope

Scanning electron microscopy (SEM) is a method for high-resolution imaging of surfaces by using electrons. It is able to reveal details less than 1 nm. Compared to

the light microscope SEM can reach higher magnifications (100,000×) and has a greater depth of field - up to 100 times that of light microscopy.

The type of SEM available at the Open University and the one used in this work is a field emission gun scanning electron microscope (Zeiss Supra 55VP FEG SEM, Figure 3.2(a)). Its working principle is presented schematically in Figure 3.2(b). In a typical SEM, a beam of incident electrons is generated in the electron gun above the sample chamber. The electrons are produced by a thermal emission source, such as a heated tungsten filament, or, as in the type used in this work, by a field emission cathode. The electrons are focused into a small beam by a series of electromagnetic lenses in the SEM column. Deflection coils near the end of the column direct and position the focused beam onto the sample surface. The incident electrons cause electrons to be emitted from the sample due to scattering within the sample's surface and near-surface material. High-energy electrons that are ejected by a collision of an incident electron with a sample atom's nucleus are referred to as backscattered electrons. The energy of backscattered electrons will be comparable to that of the incident electrons. Lower-energy electrons are also emitted during scattering of the incident beam and are called secondary electrons. The electron beam is scanned in a raster over the surface and SEM images are created by the detection of the emitted electrons in the electron detectors.

3.2.1 Electron back-scattered diffraction (EBSD)

In addition to the use of back-scattered electrons for imaging, they can be also used to study crystallographic features of materials and this technique is called electron back-scattered diffraction (EBSD) technique. EBSD technique was improved

in 1984 by Dingley with the integration of the computer-aided indexing of the kikuchi diffraction patterns captured by a camera in front of the phosphor screen [1].

A polished sample in the SEM chamber is tilted to an angle α which is commonly 70° as shown in Figure 3.3(a). The incident electron beam is directed at a point of interest on the sample surface. As a result of elastic scattering the electrons diverge just below the sample surface and interact with crystallographic planes in all directions. Some electrons which diffract from the crystal planes obey Bragg's law (see section 3.6.1 for explanation) and produce two cones which are produced for each family of planes (Figure 3.3(b)) [2, 3]. These cones can be imaged using a phosphor screen attached to a CCD camera. These cones appear as thin bands on the phosphor screen and these bands are called "Kikuchi bands". Each kikuchi band corresponds to a *hkl* plane family. The resulting pattern on the phosphor screen contains many of these bands. An example of an indexed EBSD pattern is given in Figure 3.3(c). The band width corresponds to d-spacing of the plane and the angle between two bands is related to the angle between corresponding *hkl* planes. The experimental diffraction patterns are indexed by comparing them with known diffraction patterns stored in the software database and then the orientation of the crystal at that indexed measurement point is found.

A Nordlys EBSD detector is attached to the SEM unit at the OU to perform EBSD measurements and the EBSD patterns are analyzed with HKL Channel 5 software. Some important EBSD parameters which are used in our measurements are given in Table 3.1.

3.3 Hardness Testing

Hardness is the resistance of the material to plastic deformation by indentation. Indentation is generally achieved with a non-deformable ball or cone tip. Brinell (measures the diameter of the indentation of a carbide or hardened steel ball), Rockwell (measures the depth of indentation of either a diamond cone or a hardened steel ball) and Vickers (measures the average of the diagonals of the indentation of a diamond pyramidal tip) hardness tests are commonly used in the metals industry to measure hardness. The Vickers hardness tests have been performed on some of the samples in this work with an automated Struers Duramin-A300 Hardness tester (Figure 3.4). Surface hardness maps were obtained by automatically measuring the diagonals of every indent, made with a load of 5kgf, using an image processing procedure.

3.4 Tensile Testing

The tensile test is a mechanical test in which a standardized flat or round sample is subjected to uniaxial loading until failure. The tensile test provides information on elastic modulus, yield strength and ultimate tensile strength of the material, which are used for performance analysis and design purposes.

Tensile tests are commonly performed by a universal testing machine which can also test the materials in compression or under bending. Universal testing machines are either electromechanical (also called screw driven, the cross-head moves up/down by a variable speed electric motor) or hydraulic (the cross-head

moves up/down by a hydraulic piston). The main components of a universal test machine are a load frame (the rigid columns on which the cross-head travels), a load cell (force transducer which is used to convert a force into electrical signal by means of load calibrated strain gauges), a cross-head (which applies the load by moving up and down) and specimen holding grips (threaded, wedge or pin) [4]. In the present work, an Instron 3367 screw-driven universal test machine with a load capacity of 30kN was used to perform the tensile tests of flat specimens with wedge grips (Figure 3.5).

3.4.1 Specimen design

Standardized flat or round tensile test specimens are designed according to ASTM E 8/E 8M - 08: Standard Test Methods for Tension Testing of Metallic Materials [5]. However, the standard dimensions have been modified in this work to be able to extract sufficient number of specimens from the welded tubes. The modified dimensions were checked through finite-element analysis in order to observe if there is any stress concentration. The details of the specimen extraction and the dimensions of the specimens used in our tests are presented in Chapter 4.

3.4.2 Strain measurement techniques

The elongation of the specimen during loading can be determined by the cross-head displacement. However, this is not a very accurate way of measuring elongation in the gauge length of the specimen if the tolerance of the rigidity of the load frame and the connecting parts is high. The use of wedge grips can also influence the total

elongation measured by the cross-head displacement due to the movement of the wedges as the load increases [4].

Clip-on extensometers are commonly used to measure the extension in the gauge section of the specimen. Knife edged arms of the extensometer are attached to the gauge length and the elongation is automatically measured during loading by converting the mechanical displacement between the arms into an electrical signal. A calibrated strain gauge which is usually mounted on a pivoting beam of the extensometer provides the information on the extension. The beam is deflected by the movement of the extensometer knife edge when the specimen is stressed. The attachment of the extensometer should be done carefully so that the knife edges do not slide as the specimen elongates. The extensometer should be calibrated and checked if the readings are correct. The mechanical zero point of the extensometer should be set before the test starts [4]. In the present work, an Instron 2630-100 Series Strain-gauge Clip-on extensometer (Gauge length: 25mm Travel range: +25mm, -2,5mm) was used.

Foil strain gauges are also used to measure the axial strain in the gauge length during tensile testing. A strain gauge is essentially an electrical conductor, consisting of a pattern of resistive wires on a backing material, which is bonded firmly on a test piece using a strong adhesive. They operate on the principle that as the foil is deformed, the resistance of the foil changes. By measuring this change, the strain in the specimen, onto which the strain gauge is attached, can be deduced. Strain gauges are usually connected to special electronic circuits (e.g. a Wheatstone Bridge). As the specimen, hence the strain gauge, deforms the circuit becomes unbalanced due to the

resistance change, which results in a signal output related to the level of the deformation [6]. In the present work, Kyowa KFG-1-120-C1-16L3M3R type strain gauges which are matched to stainless steel were used. In a uniaxial tensile test of a homogenous steel specimen, the poisson strain may introduce some errors in the uniaxial strain readings of the strain gauge because the resistance of the wires can be affected by Poisson strain. This effect is corrected by the manufacturer by taking the Poisson ratio of the steel into consideration. However, any strain gauge which is bonded on (1) a material with different Poisson ratio or (2) steel, but subjected to other than a uniaxial stress state or (3) steel with uniaxial stress field but not aligned perfectly with the loading direction, may exhibit errors due to Poisson strain [6, 7].

3.4.3 Alignment problems

The centreline of the specimen should be precisely aligned with the centrelines of the bottom and top grips and the load carrying parts. Misalignment can cause uneven loading of the specimen which may result in incorrect tensile property measurements. Misalignment may occur due to (1) the poor alignment of the centrelines of the top and bottom grips, (2) poor alignment of the specimen centreline with the centreline of the grips and (3) inaccurate machining of the specimen itself [4, 8, 9]. Universal joints, which are often employed to correct misalignments due to (1) and (2), were attached to the grips of the tensile test machine in this work. The alignment of the grips before and after the specimen is gripped was checked by using a vertical laser beam and the alignment of the specimen in wedge grips was achieved by using grooved plates in which the specimen shoulders were located. The

alignment was tested by checking the uniaxial strain readings from four strain gauges attached to the all edges of a flat specimen under uniaxial elastic stress.

3.5 Digital Image Correlation (DIC)

The digital image correlation (DIC) technique is a non-contact optical method which is able to perform a full-field measurement of displacement. It is based on tracking the small features (when illuminated these features create "speckles" on the digital image) on the sample surface and computing the displacement of these features by correlating images taken from the sample surface before and after the deformation.

This technique has a wide field of application in industry and science from macro-scale to micro-scale. Whilst civil engineers utilize this technique for structural health monitoring of large structures such as bridges [10] and wind turbines [11], biologists use it to investigate the mechanical properties of skin [12]. In material science, DIC is commonly applied to extract the mechanical properties of heterogeneous materials such as welded structures and composite materials in which full-field local displacement measurements are challenging and impossible with conventional equipments like extensometers, strain gauges, LVDTs, etc.. In fracture mechanics, DIC has been used to measure the crack tip opening displacement [13] and the plastic strain at the tip of the crack[14, 15]. It also has applications in the observation of micro-deformation under the Scanning Electron Microscope (SEM) [16].

In 1982, Peters and Ranson [17] proposed a technique which measures the local deformation on the surface of a material under loading by comparing the digitalized ultrasonic images recorded before and after the deformation. In this technique various small regions on the digital image, known as subsets, were compared to measure the local deformation. Using this approach, Sutton *et al* [18] founded the modern day 2D Digital Image Correlation (2D-DIC) system in 1983 by developing numerical algorithms to measure the local deformation using optically recorded images instead of digitalized ultrasonic images. During the next decade, the accuracy and the speed of the DIC method were improved by developing new algorithms for subset-matching [19, 20]. Schreier *et al* [21] has reported an image position accuracy of 0.01 pixels by developing an algorithm based on image reconstruction by using higher order spline interpolation functions to minimize the measurement bias during the matching process. Image reconstruction is applied by the interpolation of the grey value between the pixels to eliminate the sudden grey value jumps between the neighbouring pixels. Current commercial DIC software products use in general Fast-Fourier-Transform (FFT) based algorithm for subset-matching, which was initially developed by Cheng *et al* [22] in 1993 for applications where in-plane strains and rigid body rotations are small. In addition to the measurement of in-plane displacement by 2D-DIC, 3D-DIC was developed to measure the out-of-plane displacement. In 1994, Luo *et al* [23, 24] successfully measured the three-dimensional crack tip deformations by utilizing an automated 3D-DIC system using a two camera stereo vision system.

The experimental setup for a DIC integrated tension test to extract the local mechanical properties from a cross-weld tensile specimen is given in Figure 3.5. This setup is composed of a test sample with speckles on its surface and a tension test machine, an illumination system, a camera and a DIC software. The working principle of such a setup will be explained in the next section (see section 3.5.2).

3.5.1 Background

Before the explanation of the DIC theory, it is useful to mention some background information on (1) the digital image concept and (2) the formation of the speckle patterns.

3.5.1.1 Digital image concept

The digital camera uses a small rectangular silicon sensor which has been segmented into arrays of individual light sensitive cells, known as pixels. More pixels mean higher resolution. In the present work, a digital SLR (single lens reflex) camera (Nikon D300), with a CMOS (complimentary metal-oxide semiconductor) sensor size of 4,288 x 2,848 pixels (12.3 Mega Pixels), and a 200 mm macro lens were used to capture images at each level of loading.

When the photons hit a pixel, they are absorbed by its semi-conductor material. The energy of the photons is transferred to the electron as an electrical charge. The brighter the image is the stronger the electrical charge will be. That is, the magnitude of the electrical charge is related to the light intensity on the pixel. The circuit board then converts the light intensity on each pixel to a binary system, depending on the bit sensitivity of the sensor, and a digital image is formed as a

matrix of light intensity values (Figure 3.6). A scientific camera with a monochromatic sensor records the raw image in greyscale in which the sensitivity of the sensor to resolve the level of light intensity is expressed by its bit value; for instance, if the sensor is 8-bit, the light intensity recorded by the camera ranges from 0 (black) to 2^8=256 (white). Cameras with colour sensors, like the commercial DSLR (Digital single-lens-reflex) cameras, generally record the raw image in RGB (red-green-blue) format. Each pixel on the sensor has one of the red, green or blue colour filter and sensitive to only one colour. However, pixels in a raw image recorded in RGB format individually contain the data for red, green and blue colour. This is achieved by manufacturing the sensor with a special arrangement of the pixels with different colour filters. According to the neighbouring pixels in that special arrangement, the missing colour data is completed for each pixel. As a result, each pixel on the raw image has R, G and B intensities. For the DIC measurements in this work, 3×16-bit RGB raw images captured by a DSLR camera were converted to 8-bit greyscale by using a commercial image analysis software (Corel Photo-Paint X4) before importing into the DIC analysis software (Davis). The conversion of RGB format to greyscale is governed by a formula which is a weighted sum of the R, G, and B components:

$$Grey=0.2989 * R + 0.5870 * G + 0.1140 * B \quad (3.1)$$

3.5.1.2 Illumination of the sample surface and speckle patterns

Illumination of the surface must be stable during the test. Any destabilization due to light source such as alternation of electricity current or position change of incoming light may result in intensity fluctuations on the digital image. For this

reason, in this work a DC current light source was used and the light condition in the laboratory where the images were captured was kept constant by covering the laboratory windows with blinds.

The DIC tracking system is based on random speckle patterns on the digital images. For accurate traceability, the speckle pattern in the images should be unique and include a sufficient number of speckles. Random speckle patterns are usually artificially applied to the sample surface by various methods, including spray painting. In this dissertation, it was found that the surface roughness produced by electro-discharge machining (EDM) produces an adequate speckle pattern under ordinary white illumination (Figure 3.7).

3.5.2 Theory of DIC

The tracking of a subset on a real greyscale image is demonstrated in Figure 3.8. Numerically, the tracking of a subset necessitates complicated DIC algorithms. Here, the fundamental working principle of a DIC algorithm will be explained shortly. Figure 3.9 illustrates schematically a small subset S centred at point M, together with its corresponding deformed shape S_1 centred at M_1. S is an undeformed subset and S_1 is the corresponding deformed subset. If subset S is sufficiently small, the coordinates of any point in S_1 can be approximated by a first order Taylor expansion as follows [25]:

$$x_{n1} = x_m + u_m + \left(1 + \left.\frac{\partial u}{\partial x}\right|_M\right) \cdot \Delta x + \left.\frac{\partial u}{\partial y}\right|_M \cdot \Delta y \tag{3.2}$$

$$y_{n1} = y_m + v_m + \left.\frac{\partial v}{\partial x}\right|_M \cdot \Delta x + \left(1 + \left.\frac{\partial v}{\partial y}\right|_M\right) \cdot \Delta y \tag{3.3}$$

where $\Delta x = x_n - x_m$ and $\Delta y = y_n - y_m$. x_m, y_m are the coordinates of point M. x_n, y_n are the coordinates of point N. x_{nl}, y_{nl} are the coordinates of N_1. u_m, v_m are the displacement of point M in x- and y-directions, respectively.

Assume that $f(x,y)$ and $g(x,y)$ are the grey value distributions of the undeformed and deformed images, respectively. The parameters u_m, v_m, $\left.\frac{\partial u}{\partial x}\right|_M$, $\left.\frac{\partial v}{\partial x}\right|_M$, $\left.\frac{\partial u}{\partial y}\right|_M$, $\left.\frac{\partial v}{\partial y}\right|_M$ are determined by using a least squares correlation coefficient C, which is defined as:

$$C = \frac{\sum_{N \in S}[f(x_n, y_n) - g(x_{n1}, y_{n1})]^2}{\sum_{N \in S}[f(x_n, y_n)]^2} \tag{3.4}$$

where S represents all of the points in the subset surrounding a single point M in the same subset. When the parameters u_m, v_m and their first derivatives are exactly correct the correlation coefficient C should equal to zero. The best estimate of these parameters is established by minimizing the value of C. Minimization of the correlation coefficient is a non-linear optimization process and usually achieved by iterative methods [26] and FFT based algorithms [27].

On a real image, the greyscale intensity values change abruptly from one pixel to the next, which produce significant difficulties when attempting to determine the displacement parameters. In order to prevent that problem and to achieve the determination of the deformation with sub-pixel accuracy, the images are reconstructed by smoothing the intensity data at non-integer positions. Bi-linear interpolation, bi-cubic interpolation and bi-cubic spline interpolation are commonly

used for image reconstruction. High-order interpolation gives more accurate results but needs more computation time [28] .

3.5.3 Image acquisition and analysis

3.5.3.1 Image acquisition

For a single camera DIC integrated tension test, in order to have a good quality set of images one should check the steps listed below before starting the image acquisition:

- the illumination and the camera are tightly fixed
- the experiment area is isolated from vibration and the tensile test machine is fixed in position
- the alignment of the sample in the loading direction and the settlement of the sample in the grips
- the camera and its lens is well positioned up/down and left/right with respect to the sample surface (the lens axis should be perpendicular to the sample surface)
- the camera is well-focused
- the sampling area is correctly sized so that it does not go out of the image during the test
- the lightning is sufficient and consistent to produce the required intensity difference on the sample surface

- the camera settings such as shutter speed and the aperture size are correctly set to capture images representing the intensity difference on the sample surface by taking some dummy photos
- the settings of test machine are correct for tensile testing and data recording
- the camera settings are correct for time-lapse imaging (or image acquisition frequency) and the raw image format

Once the experimental setup is ready for image acquisition, a reference image is taken and then the tension test and the time-lapse image acquisition are started. The images captured by the camera using a time lapse imaging software (Nikon Camera Control Pro 2) were stored in the computer hard drive in uncompressed RGB raw format. The images were then converted to uncompressed greyscale format by using a image analysis software (Corel Photo-Paint X4) and imported into the DIC analysis software, DaVis 7.2 Data Acquisition and Analysis software [27].

3.5.3.2 Image analysis using DIC software

The captured images were processed using the DIC software to compute displacement maps. The accuracy of the computation depends on many user defined parameters and hence need to be selected carefully. The data analysis steps and the user-defined parameters in these steps will be explained in the following part. The most important user-defined parameters were optimized through a test in which a notched tensile monolithic aluminium specimen was loaded to 5.7kN. In this optimization test the displacement and strain in the loading direction near the notch was measured by using various DIC parameters and compared with those obtained

using a finite element model. The notched sample and the measurement positions for the comparison are given in Figure 3.10. The loading of the notched specimen was simulated by a 2D finite element model so that the axial strain distribution between the notch tips could be predicted and compared with DIC results. The model geometry was based on the actual specimen dimensions and a fine mesh was chosen to predict the strain gradient more accurately. The material was assigned to have isotropic elastic-plastic properties and a static analysis was performed for the simulation using plain stress elements.

Step 1: Elimination of rigid body motion

Any camera movement or the settlement of the sample in the grips as the load increases may cause rigid body motion (translation and/or rotation) of the image. In order to measure the accurate local in-plane displacements in the sampling area due to the tensile deformation, the rigid body motion should be removed. The elimination of the rigid body motion is achieved by shift and rotation correction step in the DIC software. Using this step enables the re-positioning of the subsequent images relative to a point selected on the reference image and to end up with a displacement map originated by the tensile deformation. In the tests in this study, the middle of the weld was selected as a reference point for the shift correction step.

Although in-plane translations and rotations can be largely eliminated, out-of-plane displacement can not be eliminated by the DIC software. Out-of-plane displacement arises due to the distance change between the lens and the surface of the specimen. If there is any change in focusing, this means that the specimen moves out-of-plane. To prevent out-of-plane displacement and to minimize the in-plane

translations and rotations, the specimen was slightly pre-loaded in the elastic region before the test was started. The effect of the out-of-plane displacement, due to the necking during deformation of the specimen, on in-plane strain measurements was considered based on the work of Sutton *et al* [29] who investigated this effect for a 2D DIC system. They found the ratio of the out-of-plane displacement of the object to the distance between lens and the object gives pseudo in-plane strain due to out-of-plane displacement. They observed that a linear relationship exists between the out-of-plane displacement and the pseudo in-plane strain due to out-of-plane displacement. In our experiments, the out-of-plane displacement in the necking weld region was estimated as 0.1mm and calculated that 0.1mm out-of-plane displacement produces approximately -200 μstrain in-plane when the original distance between the lens and the object is 500mm. Since this pseudo in-plane strain is very small compared to the large plastic strain during necking, it was neglected.

Step 2: Definition of the work space

This step is used to extract the work space or the sampling area and to remove the background so that the computation time is decreased. Some of the subsets will move out of the sampling area as the deformation proceeds; therefore, the sampling area should be selected carefully.

Step 3: Displacement vector calculation

In data analysis, this is the most important step where the correlation and vector calculation parameters are defined.

The matching process of the subsets in two successive images is called cross-correlation. The cross-correlation can be done either (1) relative to the reference image

(first image) or (2) relative to (n-1)th image. In the former case, the final displacement of a subset in the nth image is computed relative to its original position in the reference image (1*2, 1*3, 1*4 ... 1*n). In the latter, the final displacement of a subset in the nth image is a sum of differential vectors computed by the correlation of every two successive images until nth image (1*2, (1*2+2*3), (1*2+2*3+3*4) ... (1*2+2*3+...+(n-1)*n)). The cross-correlation is enhanced for displacements less than a subset size whereas it is relatively poor for large displacements. Therefore, the second cross-correlation mode was preferred in the present work.

As mentioned above, the displacement vectors are computed for every subset in the image. Therefore, the subset size determines the resolution of the displacement map and can be selected in the DIC software. For example, 4×4, 6×6, 8×8, 12×12, 16×16, 32×32, 64×64, 128×128, 256×256, 512×512, 1024×1024 pixels are the available subset sizes in DaVis 7.2. However, there are crucial considerations when selecting the optimum subset size:

- Each subset should include sufficient number of speckles (~10) [30].
- The displacement of a subset which is computed by using two successive images should be less than a subset size.
- The effect of subset size on the accuracy depends on the form of deformation field to be measured. For relatively homogeneous deformation fields, a large subset size is found to give more accurate displacement measurements, as more data points lead to better correlation But, when the measured deformation field contains high strain gradients, the variation of deformation field within a subset can be considerable if the chosen subset

size is too large, which can lead to errors if the deformation field is not accurately approximated with subset shape functions. Thus, it seems that smaller subset sizes should be chosen for the measurement of heterogeneous deformation fields.

The accuracy of the calculated displacement depends on the subset size as shown in Table 3.2. The effect of subset size on the strain distribution between the notches of the aluminium sample is given in Figure 3.11. It can be seen that the results obtained with a subset size of 32x32 pixels give the best agreement with the FE results near the notches where the strain gradient is high, whereas the results obtained by 64x64 subset size gives somewhat better fit away from the notches. The strain values for the 16x16 subset size, on the other hand, shows quite a large scatter, although the overall agreement with the FE results can be seen. One of the reasons for the large scatter in the results of 16x16 is that the subset size is very close to the average speckle size in the images, which is ~10x10 pixels in this case.

Subset overlapping is another user-defined vector calculation parameter. It is used to increase accuracy without any loss in the resolution of the displacement map. However, it requires more computation time. 0%, 25%, 50% and 75% are the available subset overlaps in DaVis 7.2. For example, if the subset size 64×64 is used with 50% overlap, the resultant subset size will be (64×64) × 50% = (32×32). The displacement vector after subset overlapping is positioned as shown in Figure 3.12. The effect of subset overlapping using 64×64 subset size on the strain distribution between the notches of the aluminium sample is given in Figure 3.13. It was found that subset

overlapping prevents the loss of the resolution of the displacement map but it increases the processing time and does not really improve the accuracy.

The vector calculation in DaVis 7.2 can be done by a single pass or multi-pass iterations. The vector calculation by single pass iteration may not be very accurate although it is very quick and simple. In multi-pass iterations the vector calculation is performed by an arbitrary number of iterations on the same image. In the first pass, the vector field is calculated for every subset and used as a reference vector for the next pass. Using the information of the previous pass the position of the subset in the new pass is shifted. The multi-pass iteration with constant subset size is shown in Figure 3.14. The multi-pass can be done either on a constant subset size or decreasing subset size. The vector calculation is more reliable and accurate by using multi-pass iterations because it helps to correlate the right speckles and decrease the signal to noise ratio [27]. The effect of the number of iterations (or number of passes) on the strain distribution between the notches of the aluminium specimen is given in Figure 3.15. It can be seen that increasing the number of iterations up to 6 passes shifts the measured strain distribution towards FE prediction, but there is no effect when the iteration numbers are increased above 6 passes.

The quality of the displacement vector calculation with optimized parameters can be checked by the ratio of 1st and 2nd correlation peaks. In DaVis 7.2, the following correlation function is used in the standard cyclic FFT based image correlation algorithm:

$$C(dx,dy)=\sum_{x=0,y=0}^{x<n,y<n} I_1(x,y)\cdot I_2(x+dx,y+dy) \quad ,-\frac{n}{2}<dx,dy<\frac{n}{2} \tag{3.5}$$

where I_1 and I_2 are the image intensities of the subset in the 1st and 2nd images, n is the subset size and $\pm n/2$ is the maximum displacement calculated. C gives the correlation strength or peak for all integer displacements (dx, dy). An ideal correlation peak which is related to C is shown for the cross-correlation of a subset on two successive images in Figure 3.16(a). However, the correlation function creates some other correlation peaks as shown in Figure 3.16(b). For such a case the ratio of 1st and 2nd correlation peak which is defined as the peak ratio factor Q $(=\frac{\text{P1}-\min}{\text{P2}-\min}>1)$ in DaVis 7.2 is used to validate the displacement vector. If there is only one correlation peak, it is set to 100. If there are other peaks, Q-factor greater than 1.3 means that the vector is quite likely a valid vector [27].

Step 4: Strain calculation

Once the in-plane displacement map is computed by using the optimized parameters, the strain calculation is performed by using the displacement-strain relation. If we assume u and v are the displacement vectors in x- and y- direction, respectively, the 2D strain tensor is obtained by the following equations:

$$\varepsilon_{xx}=\frac{\partial u}{\partial x},\ \varepsilon_{yy}=\frac{\partial v}{\partial y},\ \varepsilon_{xy}=\frac{1}{2}\left(\frac{\partial u}{\partial y}+\frac{\partial v}{\partial x}\right) \tag{3.6}$$

In DaVis 7.2, the strain computation can be done automatically. However, although the optimized parameters were used to calculate the displacement vector, the strain computation by DaVis 7.2 gives scattered data which needs to be smoothed. Therefore, strain computation was performed by using a script programmed in MatLab in order to have a better control when smoothing the strain data. The flow

chart to calculate the strain in the y-direction is given in Figure 3.17. k is the parameter to define the gauge length for strain computation for the "subset n" in order to smooth the strain data (see the middle plot in Figure 3.17). For example when k=3, the user defined gauge is 7 subset lengths. Strain in y-direction for a subset is defined as the ratio of the displacement difference between the subsets at the two ends of the user-defined gauge length (k=1, 2, 3, 4) to the gauge length which is the y-distance between the centre of the same subsets. This is repeated for all subsets and ultimately the strain map is obtained. The use of a very small gauge length gives large scatter in the strain values, whereas a very large gauge length may result in smearing out of variation in strain profile. For the notched aluminium sample, the effect of the user-defined gauge length in the calculation of strain on line A (Figure 3.10) is given in Figure 3.18. Obviously selection of k in the calculation depends on the case but, in the case of the notched specimen the use of k=3 seemed to give closest values to the finite element results.

3.6 Neutron Diffraction

Neutron diffraction is a very useful tool to measure the internal strain and the bulk texture because it enables data from the depth of the material to be obtained. However, it is a very expensive technique compared to lab x-ray diffraction since it is performed in large neutron facilities. The basics of the neutron diffraction and its use for the measurement of internal strain and bulk texture will be explained in the following part.

3.6.1 Bragg's law

When a beam of electromagnetic radiation such as visible light, X- or γ-rays hits the atoms of the sample material, it is scattered in all directions. Particle beams such as electrons and neutrons can also be considered as waves of radiation. Their wavelength λ is given by the de Broglie wave particle duality equation:

$$\lambda = \frac{h}{mv} \tag{3.7}$$

where h is Planck's constant, m is the mass and v is the velocity of the particle. When the incident radiation beam hits an atom, two types of collisions are possible [31]. If there has been a momentum transfer, inelastic scattering occurs and the wavelength is increased because of the loss of energy. If the collision is elastic (no momentum transfer), the scattered ray has the same wavelength and the same energy as the incident beam. If the elastic scattering of an incident beam of radiation from a crystalline material in which the atoms are arranged in an orderly manner satisfies Eq. (3.8), Bragg's diffraction occurs:

$$\lambda = 2d\sin\theta \tag{3.8}$$

where d is the interplanar spacing of the diffracting planes and θ is the incident angle of the beam.

If the incident beam hits the crystal at an arbitrary angle (θ), the scattered beam from crystallographic planes will interfere with one another. Constructive interference is obtained if the path difference between the incident and scattered beam, which is $2d\sin\theta$, is equal to a multiple of the wavelength λ (Figure 3.19). For

such a scatter satisfying Bragg's law the wavelength of the incident beam of radiation should be smaller than $2d$.

3.6.2 Neutron diffraction

The properties of different types of radiation are given in Table 3.3 which includes light for comparison. Note that neutrons and high energy synchrotron X-rays have high penetration depth in the crystalline material and their wavelengths are very small (close to or less than the inter-planar spacing of many crystalline materials). For these reasons, they are the most popular diffraction techniques for the measurement of internal strain [32] . On the other hand, neutron diffraction is also popular for measuring the bulk texture. In this dissertation, only neutron diffraction will be explained in detail because the internal strain and bulk texture measurements were done by using neutron diffraction.

Neutrons are produced by the fission process in a reactor (monochromatic) neutron source or by a spallation process in a pulsed (time-of-flight) neutron source [33]. In both cases, the primary neutrons are not suitable for measurement purposes due to their very short wavelength and very high energy (MeV). Therefore, the primary neutrons are slowed down in the moderator to give a suitable wavelength (comparable to the inter-planar spacing for most crystalline engineering materials). These thermalised neutrons are then used for measurement purposes [34].

3.6.2.1 Monochromatic neutron source

In monochromatic neutron sources such as FRM-II neutrons are produced by nuclear fission of the U-235 isotope. As explained earlier, the primary neutrons are

cooled down in the moderator. The neutron beam collected from the moderator is polychromatic; however, it becomes monochromatic after it is reflected from the crystal monochromator which is generally made of a single crystal with a known crystallographic direction (e.g. Si(400), Ge(511), PG(002)). The thermalised neutrons are directed onto the monochromator at a specific angle satisfying Bragg's law so that the desired wavelength is obtained. The size of the incident beam towards the sample is determined using beam control slits which are made of neutron opaque materials. The other dimension of the gauge volume where the diffraction data is collected from is defined by the slits in front of the detector. The schematic illustration of diffraction from the sample in a monochromatic neutron source is given in Figure 3.20(a). The detector can be rotated to satisfy the Bragg diffraction to obtain the diffraction from any crystallographic planes in the gauge volume. The diffraction spectrum observed at the detector is stored as intensity vs. 2θ as shown in Figure 3.20(b) [35].

3.6.2.2 Time-of-flight neutron source

In a spallation neutron source such as ISIS, UK, neutrons are produced by a spallation process in which the accelerated high energy protons in a magnetic ring bombard onto a target material such as tungsten (ISIS, UK) or mercury (SNS @ ORNL, USA). The primary neutrons have very high energies and need to be cooled down for the scientific uses. At ISIS, the primary neutrons are cooled down in liquid methane or hydrogen moderators [36]. Unlike the reactor neutron source, the pulse of neutrons after the moderator has a range of wavelengths (also called white beam) rather than a single wavelength (i.e. monochromatic). Therefore, when a pulse of

neutron is directed onto a sample, those with different wavelengths will travel different times to reach the sample at a fixed distance from the moderator. At ISIS, similar to the reactor neutron source, the size of the incident beam is determined by using beam control slits. However, the other dimension of the gauge volume is defined by using different radial collimators (0.5, 1, 2, 3 or 4mm) in front of the detector which are positioned at a fixed angle of 90° with respect to the incident beam as shown in Figure 3.21(a). The collimators consist of a large numbers of elements spanning an angular range of 14°. For a time-of-flight instrument, the use of radial collimators provides a well-defined scattering vector and increased peak intensity [36].

As mentioned earlier, at a fixed flight path (the total distance from the moderator to the sample and from the sample to the detector) the time-of-flight will be different for every wavelength; therefore, every wavelength satisfying Bragg's law will reach the detector at different times. The raw diffraction spectrum obtained in a spallation source is time-of-flight vs. intensity as shown in Figure 3.21(b). Each peak in the spectrum corresponds to an (*hkl*) family of lattice planes [37].

3.6.3 Measurement of internal strain

The strain is described as the ratio of the difference between the final length (l_f) and original length (l_0) to the original length;

$$\varepsilon = \frac{l_f - l_0}{l_0}$$

If the original and final d-spacings are known, the internal strain can be calculated by using strain definition:

$$\varepsilon = \frac{d - d_0}{d_0}$$

In a monochromatic source, the diffraction spectrum observed at the detector is stored as intensity vs. 2θ as shown in Figure 3.20(b) and the wavelength is constant. The strain will introduce a peak shift. Therefore, the internal strain can be calculated by using the incident angle for strain-free state (θ_0) and the incident angle for the strained state (θ) as follows;

$$\varepsilon = \frac{d - d_0}{d_0} = \frac{d}{d_0} - 1 = \frac{\lambda / \sin\theta}{\lambda / \sin\theta_0} - 1 = \frac{\sin\theta_0}{\sin\theta} - 1 \tag{3.9}$$

Note that angles are in radian. The 311 lattice plane is usually selected to measure the internal strain in austenitic stainless steel.

In a time-of-flight instrument the raw diffraction spectrum obtained in a spallation source is time-of-flight vs. intensity as shown in Figure 3.21(b) and it includes many peaks. As mentioned earlier the wavelength of neutrons can be described with Eq. (3.7). Therefore; Bragg's law can be written as follows;

$$\lambda = \frac{h}{mv} = 2d\sin\theta$$

Since the neutron travel path length is known, the velocity can be written as $v = \frac{\mathrm{L}}{t}$ where L is the neutron path length which is the distance from the moderator to the sample plus from sample to the detector and t is the flight time of the neutron. Therefore, the d-spacing can be written as follows;

$$d = \frac{ht}{2m\mathrm{L}\sin\theta}$$

If strain is introduced, the flight time of the neutrons will be influenced as the d-spacing is changed due to strain state i.e. the peak will shift. The internal strain can be calculated as follows;

$$\varepsilon = \frac{d - d_0}{d_0} = \frac{d}{d_0} - 1 = \frac{\frac{ht}{2m\mathrm{L}\sin\theta}}{\frac{ht_0}{2m\mathrm{L}\sin\theta}} - 1 = \frac{t - t_0}{t_0} = \frac{\Delta t}{t_0} \tag{3.10}$$

In this dissertation, the internal strain reported in Chapter 7 was measured at Engin-X at ISIS, UK which is a spallation neutron source.

3.6.4 Measurement of bulk texture

The bulk texture measurement will be explained for a monochromatic source rather than a spallation source since the measurements in this work were performed in Stress-Spec at FRMII which is a monochromatic source. In order to determine the texture of a polycrystal sample, the sample is systematically rotated in a texture goniometer about well-defined angles (χ and ϕ) as shown in Figure 3.22(a). During the rotation of the sample, all of a particular set of lattice planes (e.g. 111 plane) are successively brought into the Bragg condition and the intensities are recorded as a function of these rotation angles. The rotation angles on the goniometer are directly related to the pole figure angles α (radial) and β (azimuthal) (Figure 3.22(b)). α=0 is the north pole of the pole figure and β characterises the rotation around the polar axis. χ ($0< \chi <90$) and ϕ ($0< \phi <360$) correspond to α and β, respectively. High intensity on the pole figure means that particular lattice plane is favourably oriented normal to the sample direction which is given by the pole figure angles at the high intensity points.

3.7 References

[1] Maitland T, Sitzman S. Electron back-scatter diffraction (EBSD) technique and materials characterization examples. In: Zhou W, Wang ZL, editors. Scanning microscopy for nanotechnology techniques and applications. Springer, 2007.

[2] Randle V, Engler O. Introduction to Texture Analysis: Macrotexture, Microtexture & Orientation mapping. Amsterdam: Gordon and Breach Science Publishers 2000.

[3] Baba-Kishi KZ. Review: Electron backscatter Kikuchi diffraction in the scanning electron microscope for crystallographic analysis. Journal of Materials Science 2002;37:1715

[4] Davis JR. Tensile Testing: ASM International, 2004.

[5] ASTM E 8/ E 8M-08: Standard Test Methods for Tension Testing of Metallic Materials. 2008.

[6] Window AL, Holister GS. Strain Gauge Technology: Applied Science Publishers, 1982.

[7] Tech Note TN-509: Errors due to transverse sensitivity in strain gages. Strain Gages and Instruments: Vishay Precision Group Micro-measurements 2011.

[8] Christ BW, Swanson SR. Alignment problems in the tensile test. Journal of Testing and Evaluation (JTE) 1976;4:405.

[9] Gray TGF, McCombe A. Influence of specimen dimension and grip in tensile testing steel to EN 10 002. Ironmaking and Steelmaking 1992;19:402.

[10] Yoneyama S, Kitagawa A, Iwata S, Tani K, Kikuta H. Bridge Deflection Measurement Using Digital Image Correlation. Experimental Techniques 2007;31:34.

[11] Chia Chen C, Jung-Ryul L, Hyung-Joon B. Structural health monitoring for a wind turbine system: a review of damage detection methods. Measurement Science and Technology 2008;19:122001.

[12] Evans SL, Holt CA. Measuring the mechanical properties of human skin in vivo using digital image correlation and finite element modelling. Journal of Strain Analysis for Engineering Design 2009;44:337.

[13] Sutton MA, Yan J, Deng X, Cheng C-S, Zavattieri P. Three-dimensional digital image correlation to quantify deformation and crack-opening displacement in ductile aluminum under mixed-mode I/III loading: SPIE, 2007.

[14] Lee C, Peters WH, Sutton MA, Chao YJ. A study of plastic zone formation by digital image processing. International Journal of Plasticity 1987;3:129.

[15] Korsunsky AM, Song X, Belnoue J, Jun T, Hofmann F, De Matos PFP, Nowell D, Dini D, Aparicio-Blanco O, Walsh MJ. Crack tip deformation fields and fatigue crack growth rates in Ti-6Al-4V. International Journal of Fatigue;31:1771.

[16] Kang J, Ososkov Y, Embury JD, Wilkinson DS. Digital image correlation studies for microscopic strain distribution and damage in dual phase steels. Scripta Materialia 2007;56:999.

[17] Peters WH, Ranson WF. Digital imaging techniques in experimental mechanics Opt. Eng. 1982;21:427.

[18] Sutton MA, Wolters WJ, Peters WH, Ranson WF, McNeill SR. Determination of displacements using an improved digital image correlation method. Image and Vision Computing 1983;1:133.

[19] Sutton MA, Cheng MQ, Peters WH, Chao YJ, McNeill SR. Application of an optimized digital image correlation method to planar deformation analysis. Image and Vision Computing 1986;4:143.

[20] Tian H, Huhns MN. Algorithms for subpixel registration. Computer Vision, Graphics, and Image Processing 1986;35:220.

[21] Schreir HW, Braasch J, Sutton MA. Systematic errros in digital image correlation caused by intenstiy interpolation Optical Engineering 2000;39:2915.

[22] Cheng DJ, Chang FP, Tan YS, Don HS. Digital speckle-displacement measurement using a complex spectrum method. Applied Optics 1993;32:1839.

[23] Luo PF, Chao YJ, Sutton MA, Peters WH. Accurate measurement of three-dimensional deformations in deformable and rigid bodies using computer vision Experimental Mechanics 1993;33:123.

[24] Luo PF, Chao YJ, Sutton MA. Application of stereo vision to three-dimensional deformation analyses in fracture experiments Optical Engineering 1994;33:981.

[25] Chu TC, Ranson WF, Sutton MA, Peters WH. Applications of Digital-Image-Correlation Techniques to Experimental Mechanics. Experimental Mechanics 1985;25:232.

[26] Tay CJ, Quan C, Huang YH, Fu Y. Digital image correlation for whole field out-of-plane displacement measurement using a single camera. Optics Communications 2005;251.

[27] LaVision. DaVis 7.2 Data Acquisition and Visualization Software.

[28] Sutton MA, Orteu J-J, Schreier HW. Image Correlation for Shape, Motion and Deformation Measurements: Basic Concepts, Theory and Applications. New York, USA: Springer, 2009.

[29] Sutton MA, Yan JH, Tiwari V, Schreier HW, Orteu JJ. The effect of out-of-plane motion on 2D and 3D digital image correlation measurements. Optics and Lasers in Engineering 2008;46:746.

[30] Scarano F. Review Article: Iterative image deformation methods in PIV. Measurement Science and Technology 2002;13:R1.

[31] Zanellato O. PhD Thesis: Deformation mechanisms in Zircaloy-4 and Zr-2.5%Nb. Department of Materials Engineering: The Open University, 2009.

[32] Ganguly S. PhD Thesis: Non-destructive measurement of residual stresses in welded aluminium 2024 airframe alloy. Department of Materials Engineering: The Open University, 2004.

[33] Hutchings MT, Withers PJ, Holden TM, Lorentzen T. Introduction to the characterization of residual stress by neutron diffraction: Taylor & Francis, 2005.

[34] Novion CH. The use of neutrons for materials characterisation. In: Fitzpatrick ME, Lodini A, editors. Analysis of residual stresses by diffraction using neutron and synchrotron radiation. London: Taylor & Francis 2003. p.3.

[35] Hofmann M, Schneider R, Seidl GA, Rebelo-Kornmeier J, Wimpory RC, Garbe U, Brokmeier HG. The new materials science diffractometer STRESS-SPEC at FRM-II. Physica B: Condensed Matter 2006;385-386, Part 2:1035.

[36] Oliver EC. PhD Thesis: The generation of internal stresses in single and two phase materials. Manchester Materials Science Centre: University of Manchester, 2003.

[37] Santisteban JR, Daymond MR, James JA, Edwards L. ENGIN-X: A third-generation neutron strain scanner. Journal of Applied Crystallography 2006;39:812.

[38] Daymond MR. Internal Stresses in Deformed Crystalline Aggregates. Reviews in Mineralogy and Geochemistry 2006;63:427.

[39] Principle of digital image correlation. www.correlatedsolutions.com, 2011.

3.8 Tables & Figures

Tilt angle (α):	70°
Step size:	1μm
Working distance:	15±0.1mm
Accelerating voltage:	20kV
Beam current:	2.28nA (high current mode)
CCD camera resolution:	512x434 pixels

Table 3.1 EBSD parameters used in the measurements in the present work.

Subset Size	Accuracy of the calculated vectors
128×128	down to 0.01 - 0.03 pixel
64×64	down to 0.02 - 0.05 pixel
32×32	down to 0.05 - 0.02 pixel
16×16	larger than 0.1 - 0.3 pixel

Table 3.2 Accuracy of the calculated vectors [27]

	Light	Thermal neutrons	Synchrotron X-ray	Lab X-ray (Cu Kα)	Electrons
Wavelength (nm)	400-700	0.05-0.3	0.008-0.04	0.154	0.001-0.01
Energy (eV)	1	10^{-2}	31-150 ($\times10^3$)	8.05×10^3	10^5
Penetration Depth (mm)	-	5-100	0.8-39	0.004-0.076	10^{-3}

Table 3.3 Diffraction properties of radiation [2, 38] (The penetration depth is the extremes among Al, Ti, Fe, Ni, Cu)

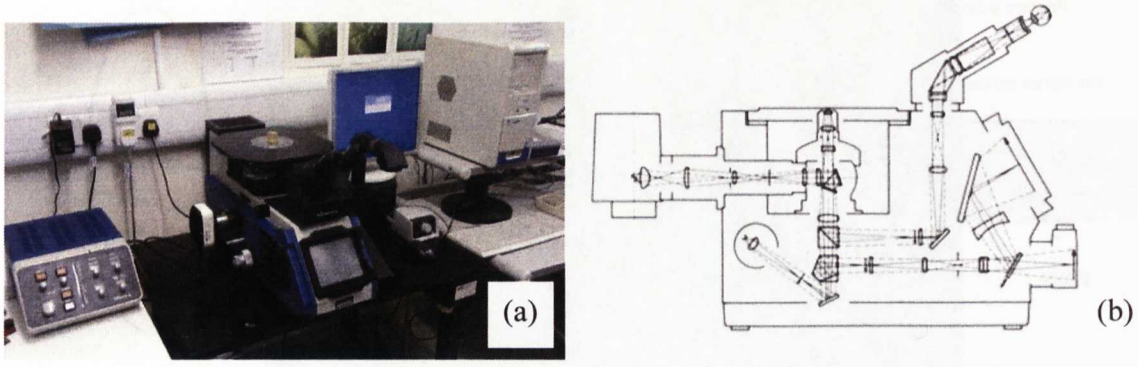

Figure 3.1 (a) Reichert-Jung MeF3 metallurgical microscope and (b) Lenses in an inverted incident light microscope.

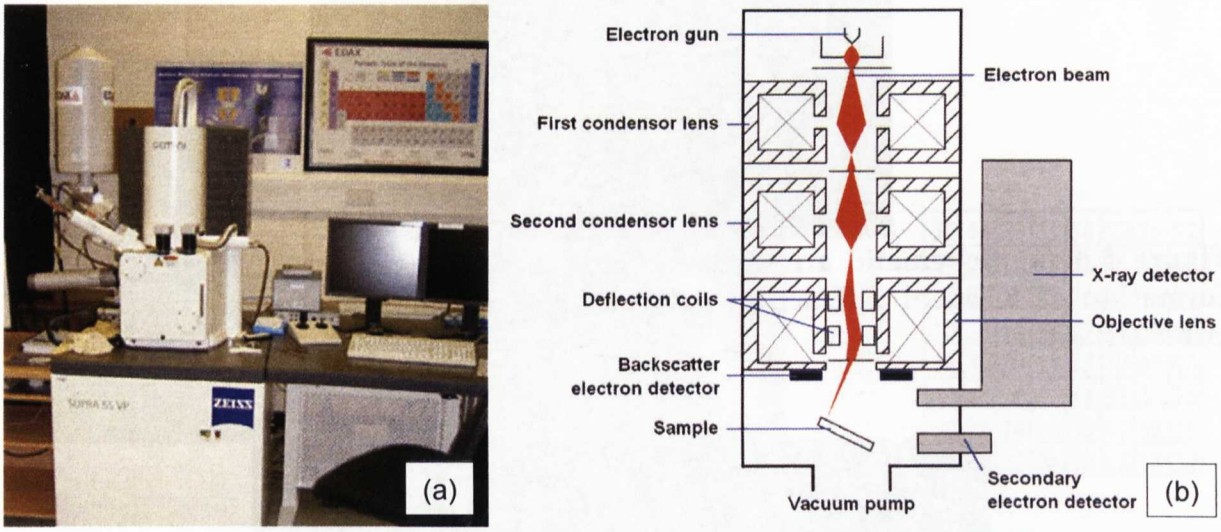

Figure 3.2 (a) Scanning Electron Microscope Zeiss Supra ™ 55VP and (b) its schematic view

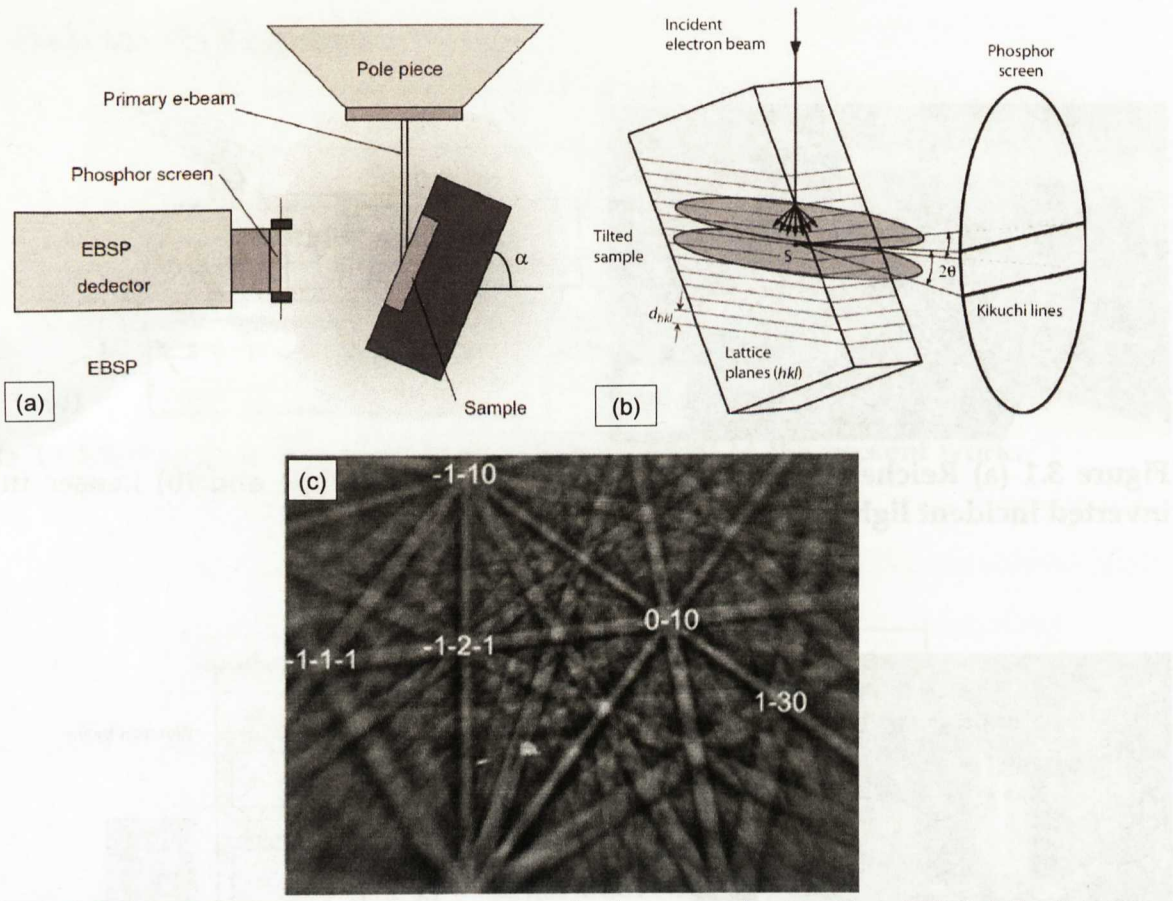

Figure 3.3 (a) Schematic arrangement of the sample in the SEM [1]; (b) The formation of Kikuchi diffraction patterns [2]; (c) Indexed Kikuchi pattern for a cubic structure.

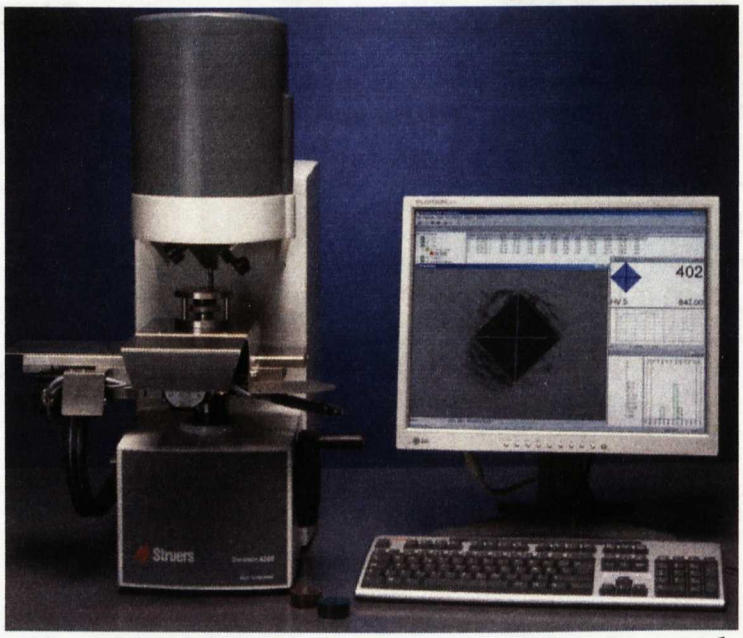

Figure 3.4 Struers Duramin-A300 Hardness tester with automated translation stage and measurement of indentations by image processing

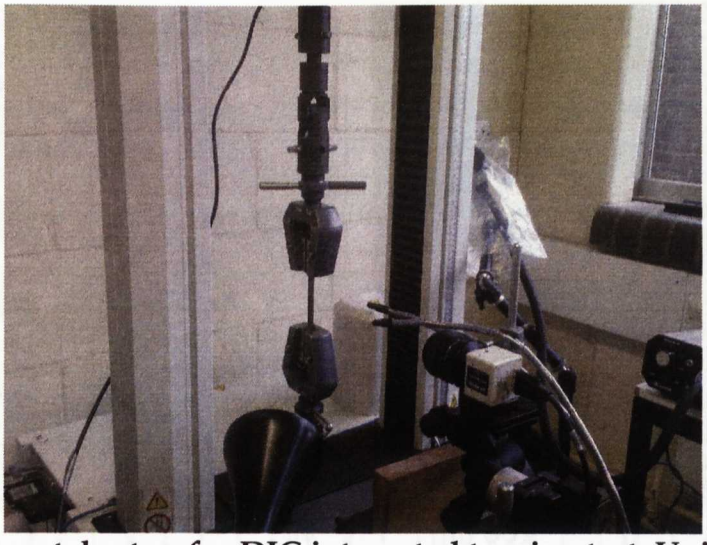

Figure 3.5 Experimental setup for DIC integrated tension test: Universal tensile test machine, wedge grips, flat specimen and illumination system

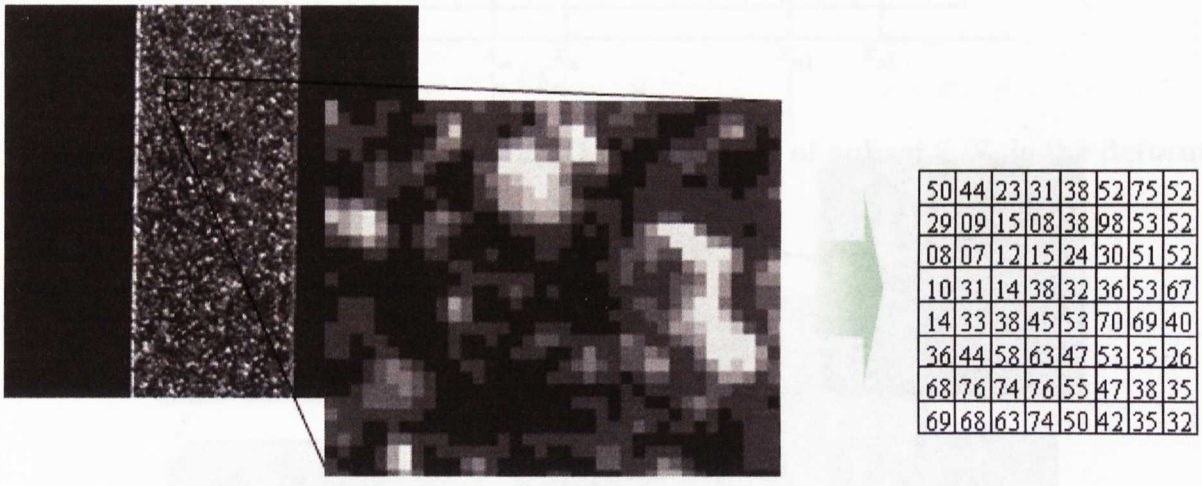

Figure 3.6 Digital image storage in greyscale

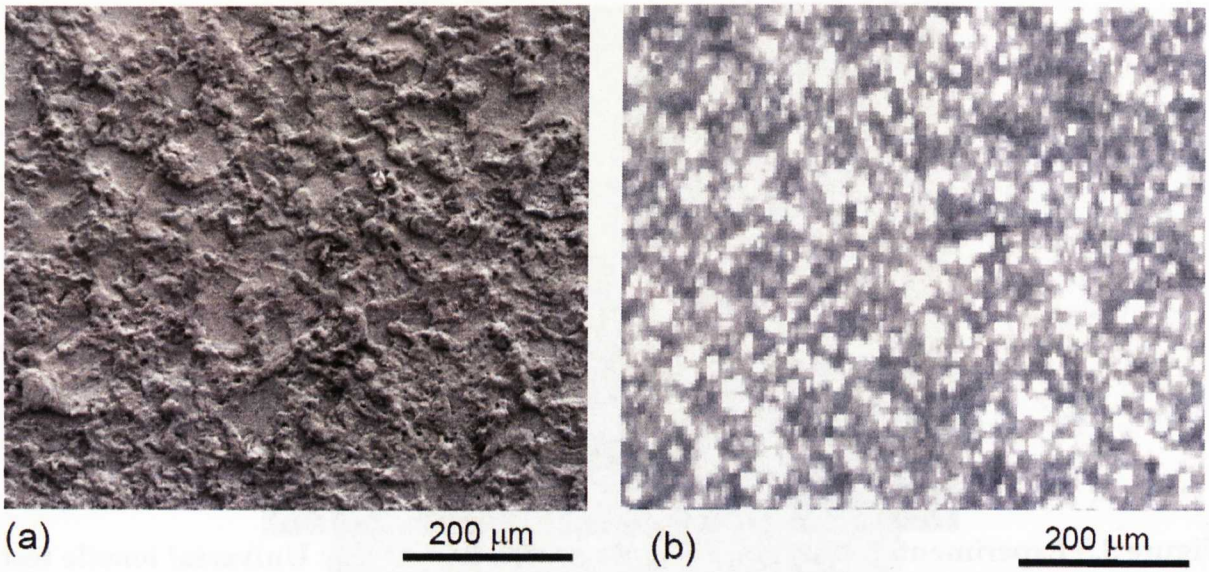

Figure 3.7 (a) The SEM image of an EDM cut aluminium surface, and (b) the speckle pattern as captured by the camera under white light illumination.

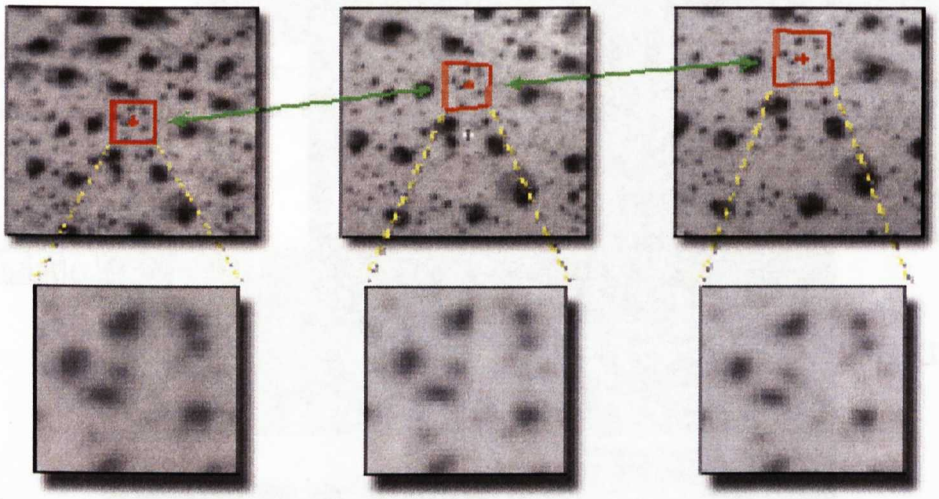

Figure 3.8 Tracking of a pixel pattern with a defined subset size [39]

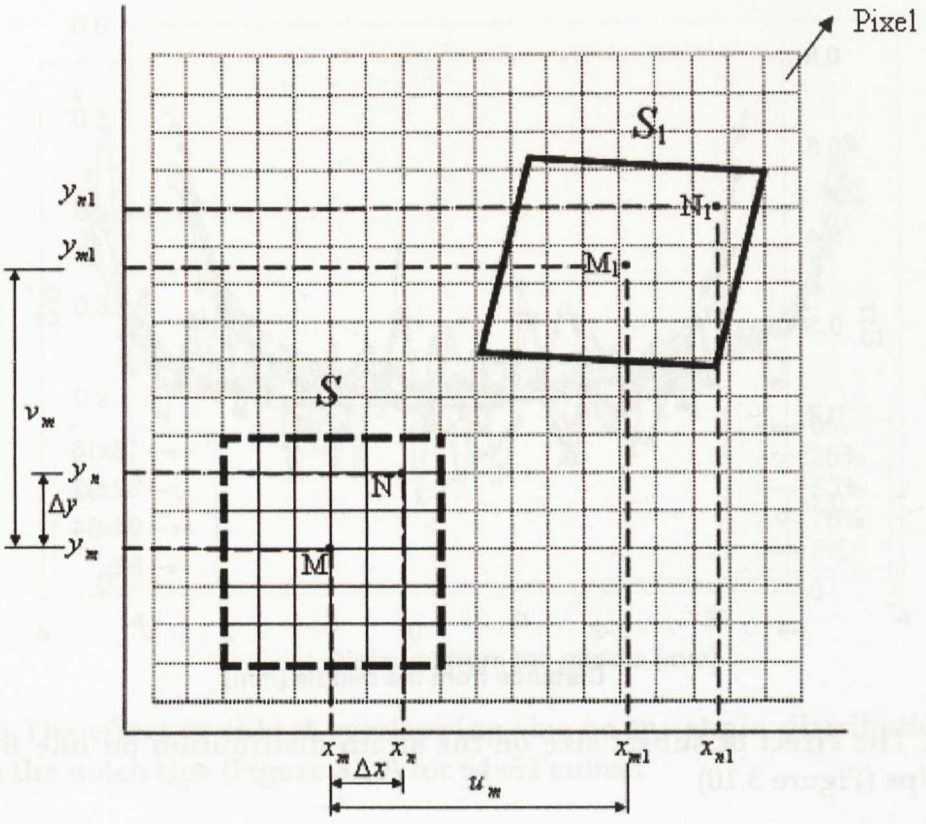

Figure 3.9 Schematic illustration of 2D deformation of subset S (S_1 is the deformed state of the subset S) [26]

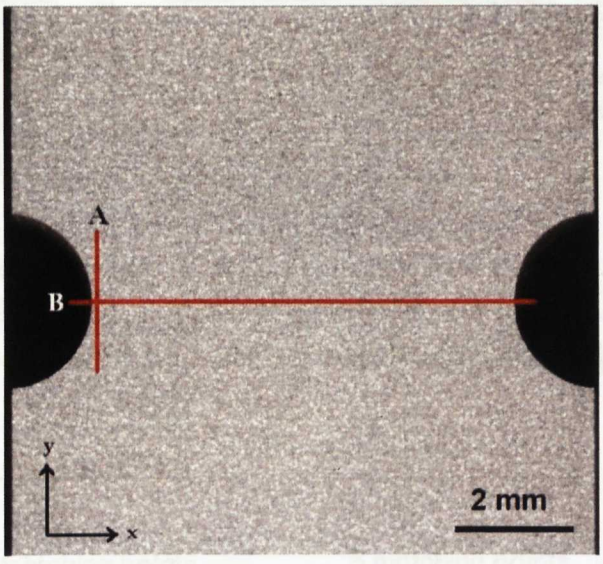

Figure 3.10 The central section of the notched aluminium specimen (Specimen is loaded 5.7kN in y-direction)

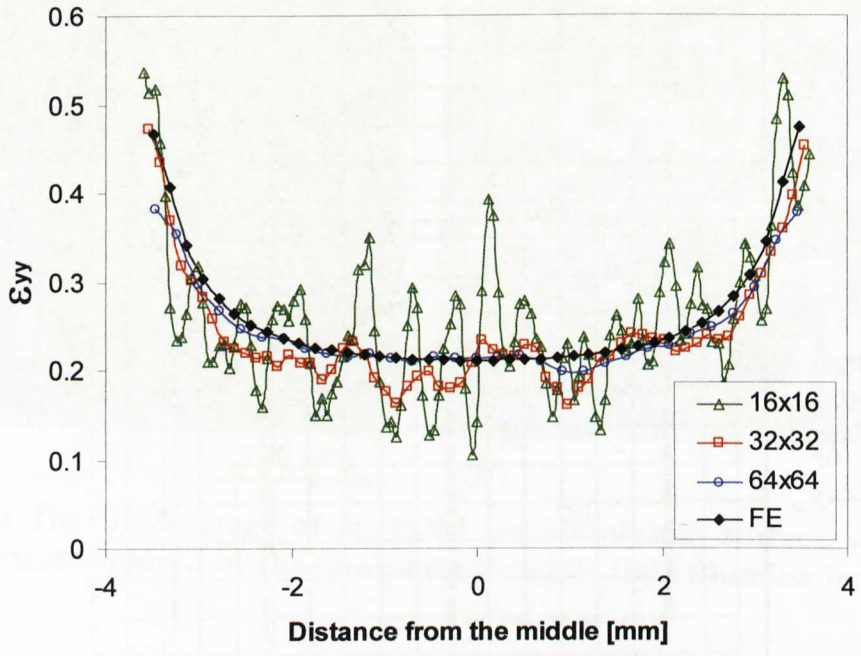

Figure 3.11 The effect of subset size on the strain distribution on line B between the notch tips (Figure 3.10)

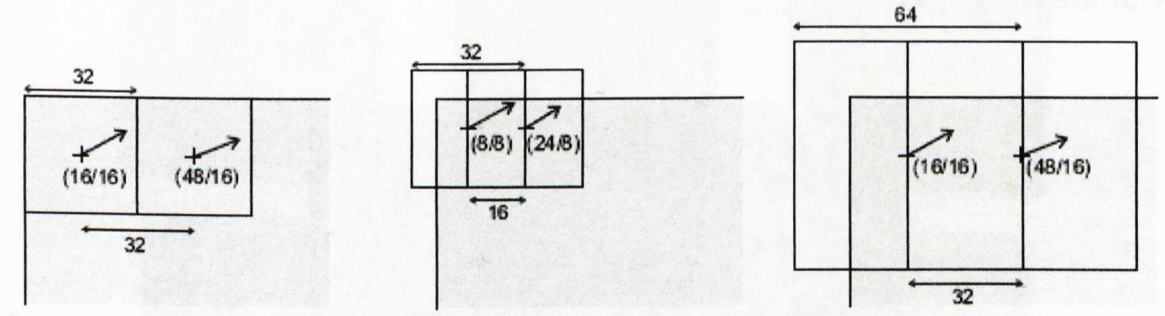

Subset size: 32×32
Overlap: 0%
Final subset size: 32×32

Subset size: 32×32
Overlap: 50%
Final subset size: 16×16

Subset size: 64×64
Overlap: 50%
Final subset size: 32×32

Figure 3.12 Vector position depending on subset size and overlap

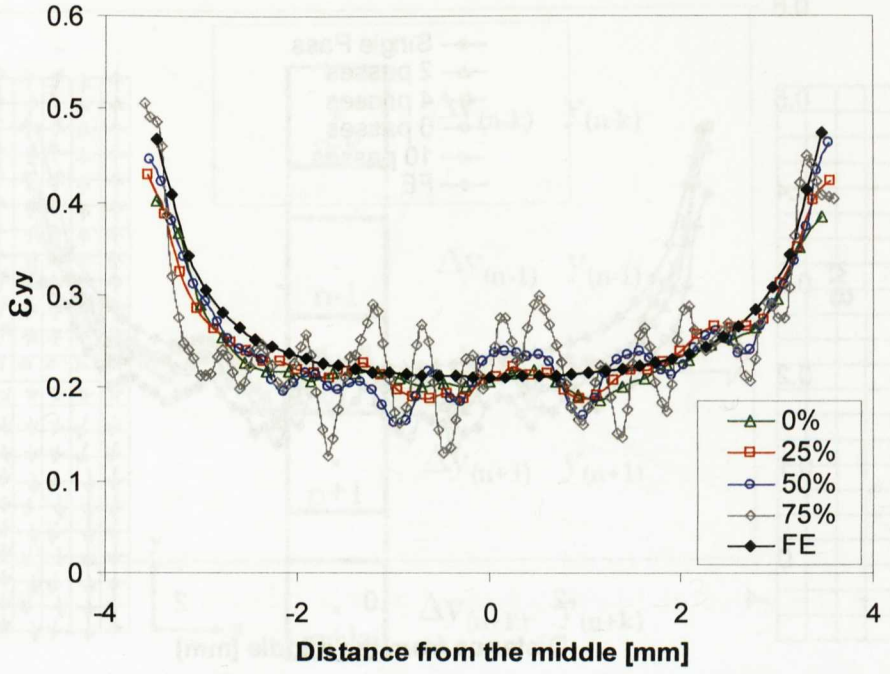

Figure 3.13 The effect of subset overlapping size on the strain distribution on line B between the notch tips (Figure 3.10) for 64×64 subset

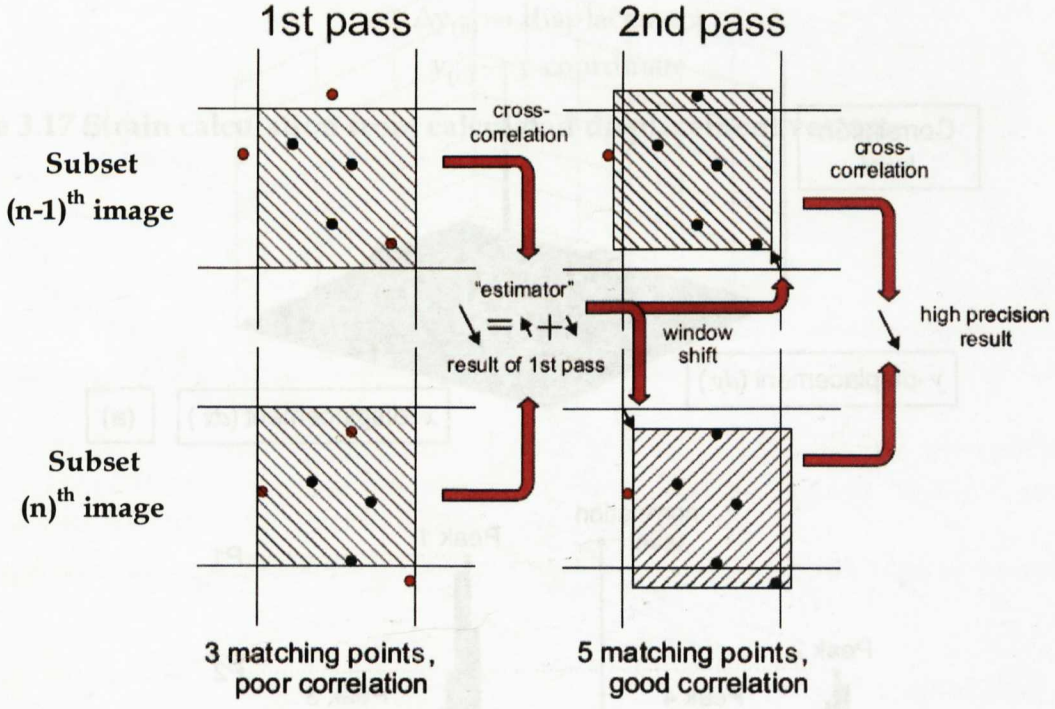

Figure 3.14 Multi-pass iteration with constant subset size [27]

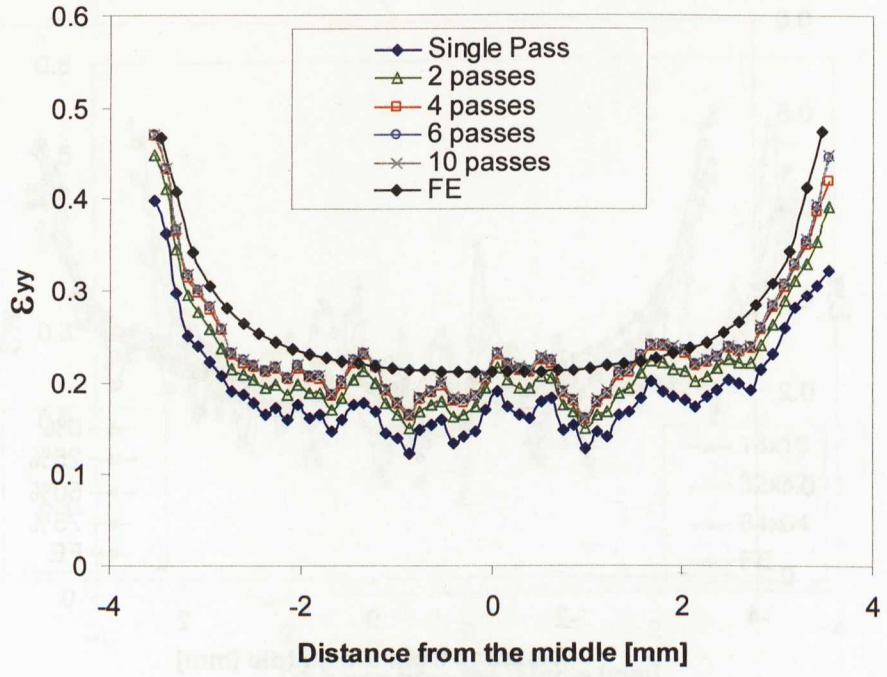

Figure 3.15 The effect of number of iteration (number of passes) size on the strain distribution on line B between the notch tips (Figure 3.10) for 32×32 subset

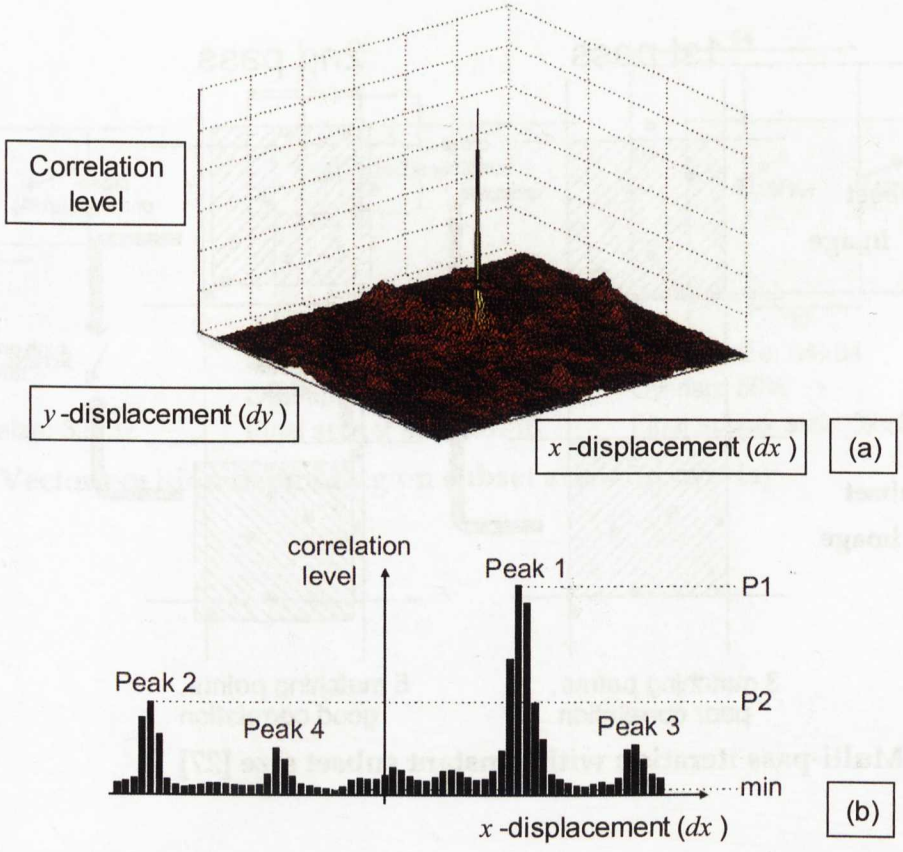

Figure 3.16 (a) 3D visualization of an ideal correlation peak; (b) 2D representation of correlation peaks after cross-correlation of a subset on two successive images

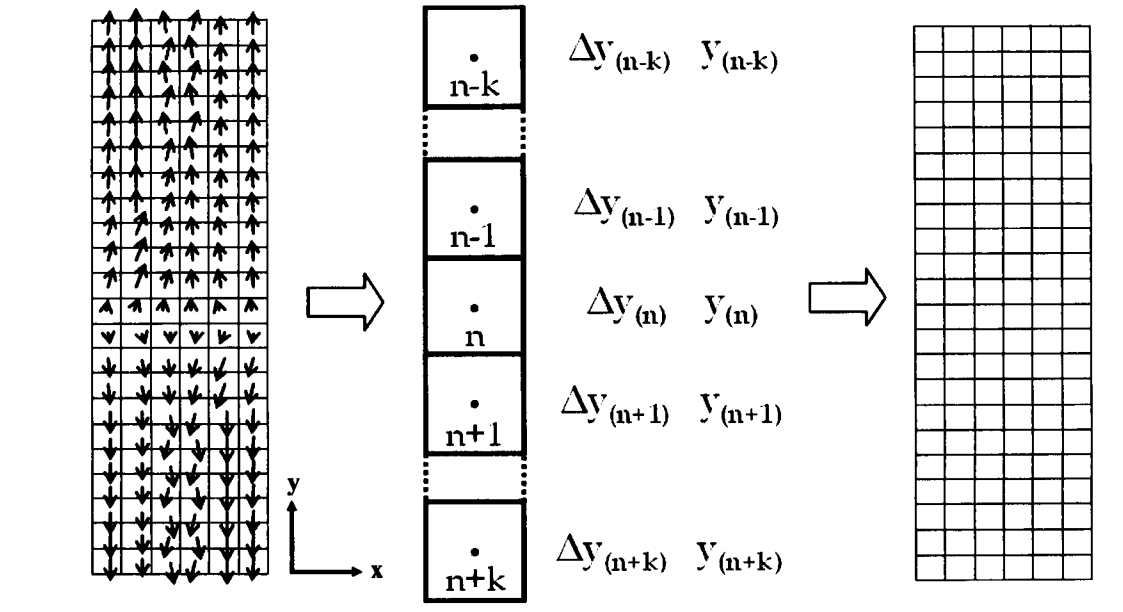

Figure 3.17 Strain calculation from calculated displacement vectors

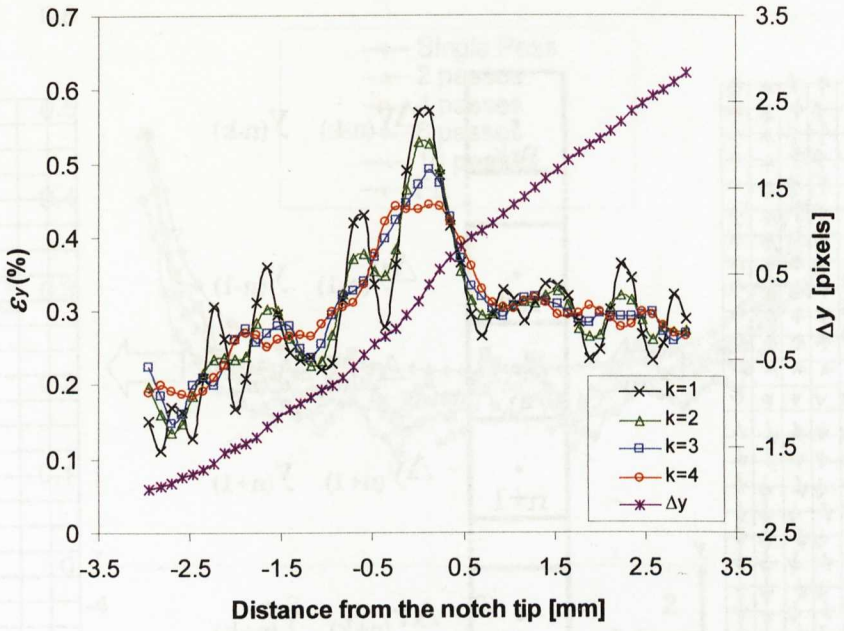

Figure 3.18 The effect of the length of the user-defined gauge length in the calculation of strain from the displacement data obtained at the notched tip on line A (Figure 3.10) for subsets of 32×32

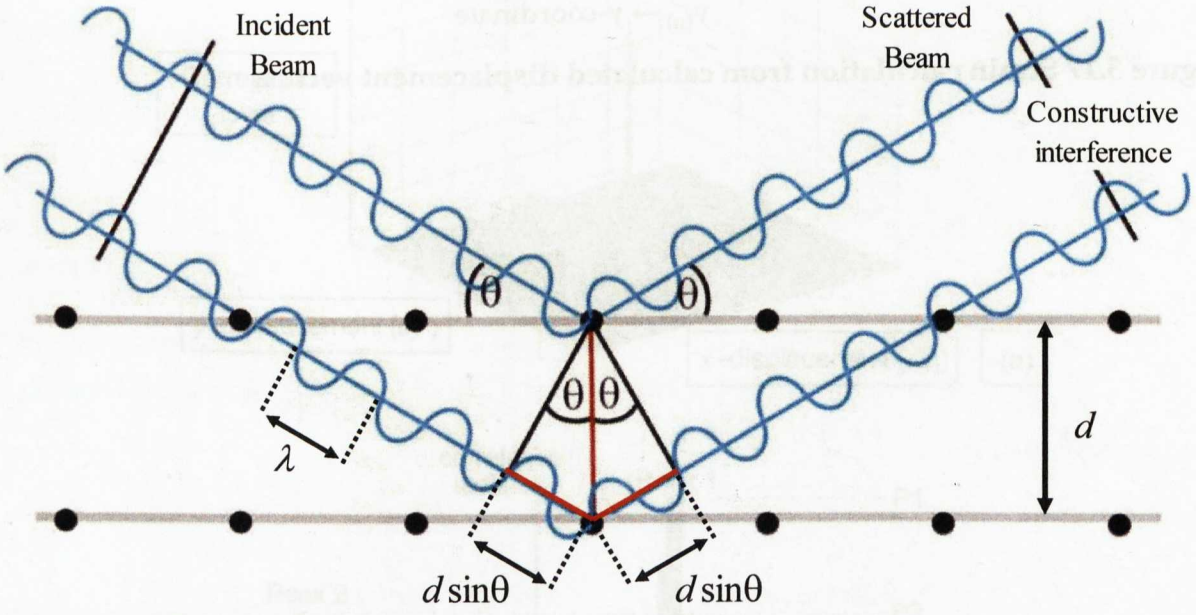

Figure 3.19 Bragg's law

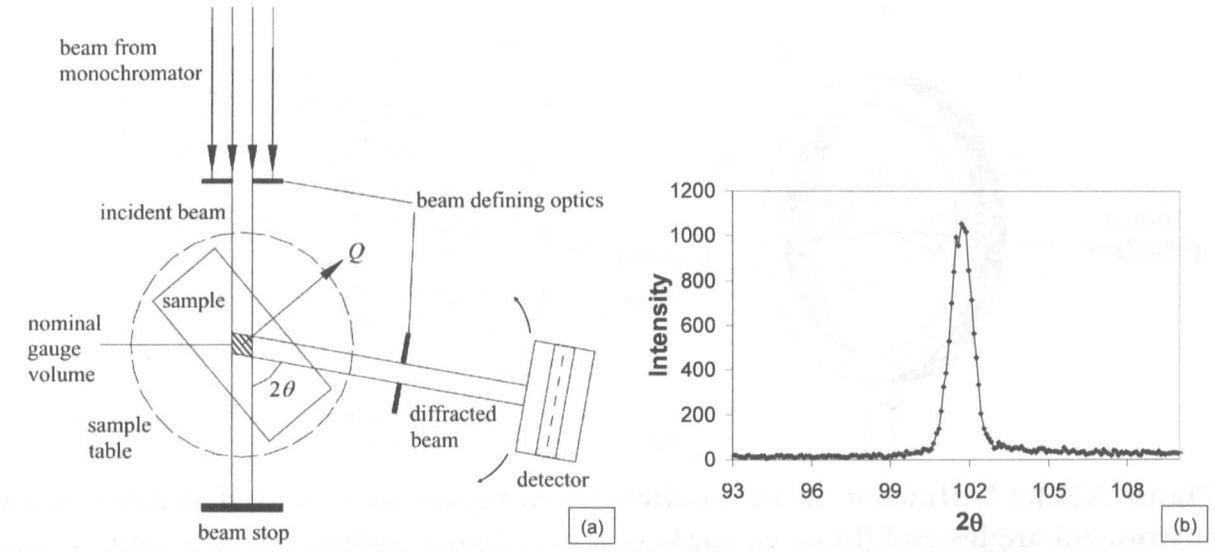

Figure 3.20 (a) Schematic illustration of diffraction in the sample [38] and (b) the diffraction spectrum obtained for 311 plane of 316H stainless steel in Stress-Spec, FRMII monochromatic neutron source

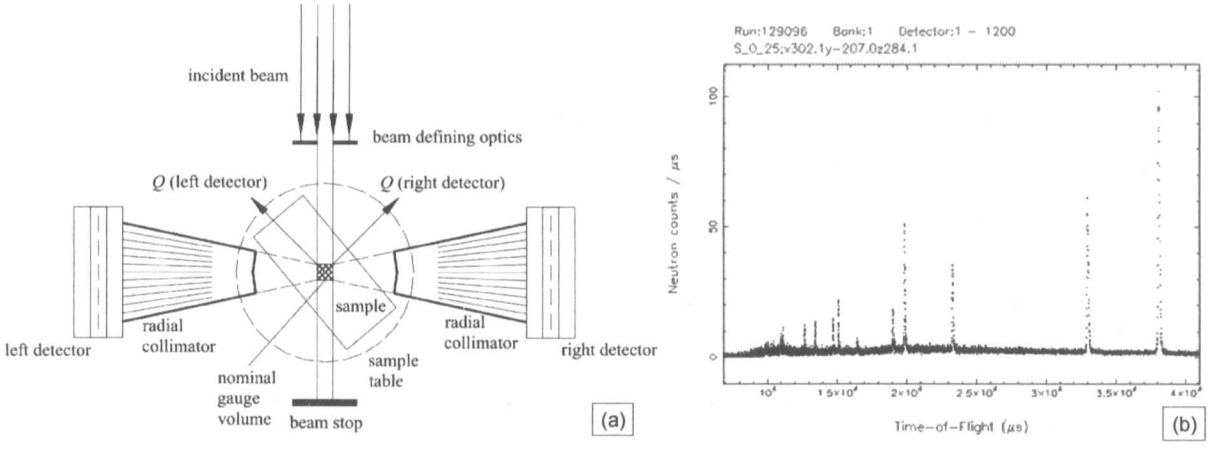

Figure 3.21 (a) Schematic illustration of time-of-flight diffraction in the sample [38] and (b) the diffraction spectrum obtained for *hkl* lattice planes of 316H stainless steel in Engin-X, ISIS spallation neutron source

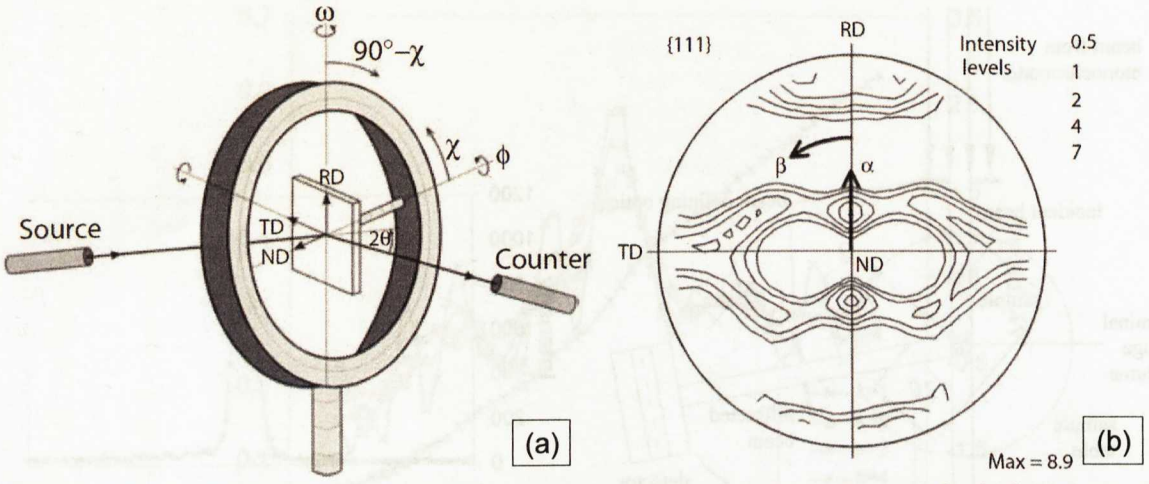

Figure 3.22 (a) Diffraction in a four-circle texture goniometer with definition of the instrument angles and (b) an example of a pole figure with the definition of α and β [2]

Chapter 4

Manufacture of the Tubes & Specimen Designs

4.1 Manufacture of the tubes

A set of butt-welded tubes were supplied by BE/EDF for the experimental programme (Table 4.1). The plain tubes (referred to the tubes before plastic straining and welding) were manufactured by extrusion and then solution annealed at 1100°C for 3 minutes followed by water quenching. The tubing material is AISI Type 316H austenitic stainless steel with the composition given in Table 4.2. The initial tubing geometry was 38 mm in diameter and 4 mm in thickness. The grain size of the material was about 30 μm. The 1% proof strength of the non-strained material was 367 MPa and Young's modulus for this type of material is about 195 GPa. Some of the plain tubes were pre-strained. Four pre-strained tubes and a plain tube were cut in half and matching halves were joined to each other by an arc welding operation. The details of the manufacturing steps are explained in the following sections.

4.1.1 Pre-straining

Four plain tubes were initially pulled uniaxially in tension up to 10, 15, 20 and 25% plastic strain. The pre-straining process was done using a strain rate of ~0.15%/s with a large servo-hydraulic rig. Adaptors were welded to the ends of the pipes so that they could be easily fitted to the universal joints for gripping. The adapters and less deformed parts were cut off after this step. The strain was monitored by a side-

mounted extensometer, and 4 strain gauges fitted at 90° intervals around the circumference of the centre of the pipe and with some markings on the pipe length and the test stopped at the appropriate total strain.

4.1.2 Welding

These strained tubes plus a plain tube were cut into two halves. Matching half-tubes were then welded together (after root tack welding) using a tungsten inert gas (TIG) welding process with Type 316L filler metal. The composition of the filler metal is given in Table 4.2.

Tube butt welds were manufactured in accordance with welding procedure E06/2121/02/002 [1]. The welding specifications are given in Table 4.3. The tubes were root tack welded from two positions, the root gaps measured and the welds were completed with the tube fixed in the vertical position. During the root pass the tacks were incorporated into the weld. All welding parameters were recorded.

4.1.2.1 Manufacture of plain tube butt weld (A_0)

The halves of the plain tube were welded as shown in Figure 4.1. The temperature during welding was measured by 6 thermocouples (Type N) which were positioned as shown in Figure 4.1. Thermocouples 1, 2 and 3 were located at about 5, 10 and 15 mm from the welding edge, respectively. Thermocouples 4, 5 and 6 were put in a similar way 180° away from the position of the thermocouples 1, 2, 3. Both passes were completed in four sections (Figure 4.1). The temperature profile is given in Figure 4.2.

4.1.2.2 Manufacture of pre-strained tube butt welds (A_{10}, A_{15}, A_{20}, A_{25})

The halves of the pre-strained tube were welded as shown in Figure 4.3. Both passes were completed in three sections (Figure 4.3).

4.2 Test samples

4.2.1 Tensile test samples

Flat cross-weld and remote-end tensile test specimens were machined out around the circumference of the tubes by electro-discharge machining (EDM). The cut position and the dimensions of the tensile samples are given in Figure 4.4. It was successfully achieved to extract 6 to 8 cross-weld samples and 8-10 remote-end samples out from each tube. Standardized tensile test specimens are designed according to ASTM E 8/E 8M - 08: Standard Test Methods for Tension Testing of Metallic Materials [2]. However, the standard dimensions are sometimes modified due to the lack of material. For our samples the standard dimensions were modified to be able to extract enough number of specimens from the welded tubes. The modified dimensions were checked for any stress concentration through 2D finite-element analysis.

The tubes, cross-weld and remote-end tensile specimens are labelled as shown in Table 4.1. Half of the same set of samples were heat-treated at a soaking temperature of 1050°C for 15 min under vacuum and quenched to 50°C with nitrogen gas. Note that heat-treated samples were subscripted with "HT".

All tensile test samples were mainly used for tension tests. However, some of the cross-weld specimens (C_0, C_{10}, C_{20}, $C_{0\text{-HT}}$, $C_{10\text{-HT}}$, $C_{20\text{-HT}}$) were used to obtain the hardness profiles across the weld before and after the heat treatment. The hardness profiles are mentioned in Chapter 5. Some of the remote end tensile test samples (B_0, B_{10}, B_{15}, B_{20}, B_{25}) and cross-weld tensile test samples (C_0, C_{20},) were also used for neutron diffraction experiments at ISIS, UK which is mentioned in Chapter 7.

4.2.2 Other samples

Several small samples were cut from the tubes for metallographic observation, EBSD studies and bulk texture measurements with neutron diffraction experiments. Those samples will be explained in the related chapters.

4.3 References

[1] Hartnell P. Manufacture of Reproduction Superheater Bifurcations and Tube Butt welds for Creep-Fatigue Testing by British Energy (Report No: 29285-B-TR-00-001). Doosan Babcock Energy, 2008.

[2] ASTM E 8/ E 8M-08: Standard Test Methods for Tension Testing of Metallic Materials. 2008.

4.4 Tables & Figures

Pre-strained and welded tubes	Degree of plastic deformation	Label of tubes	Label of the remote-end tensile specimens	Label of the cross-weld tensile specimens
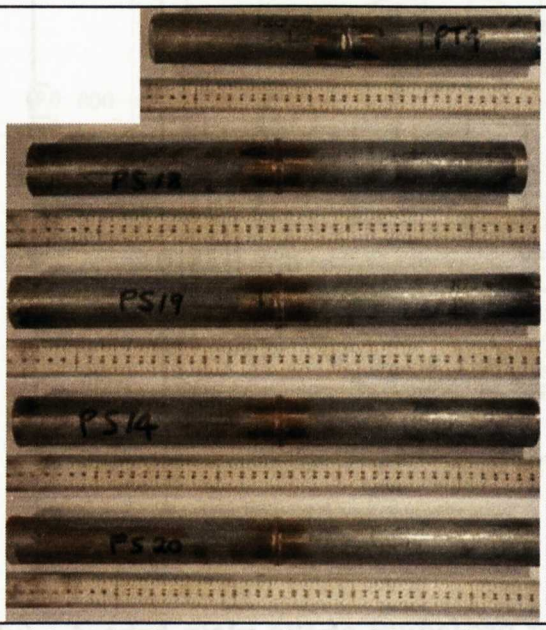	0%	A_0	B_0, $B_{0\text{-HT}}$	C_0, $C_{0\text{-HT}}$
	10%	A_{10}	B_{10}, $B_{10\text{-HT}}$	C_{10}, $C_{10\text{-HT}}$
	15%	A_{15}	B_{15}, $B_{15\text{-HT}}$	C_{15}, $C_{15\text{-HT}}$
	20%	A_{20}	B_{20}, $B_{20\text{-HT}}$	C_{20}, $C_{20\text{-HT}}$
	25%	A_{25}	B_{25}, $B_{25\text{-HT}}$	C_{25}, $C_{25\text{-HT}}$

Table 4.1 Photographs and labelling of test specimens

	Cr	Ni	Mo	Mn	Si	Co	C
316H	16.89	11.25	2.04	1.55	0.53	0.089	0.05
316L	18.38	12.07	2.53	1.61	0.37	-	0.01

Table 4.2 The composition of the stainless steel tubing material (Type 316H) and the weld material (Type 316L)

Welding Type	TIG
Polarity	DCEN (Direct current electrode negative)
Shield & Purge Gas	Argon 99.995%
Current	65-140 A
Flow Rate	5 to 8 litres/min
Electrode	2.4 mm 2% Th or Ce Tungsten
Purge Rate	2 to 8 litres/min

Table 4.3 Welding procedure specification

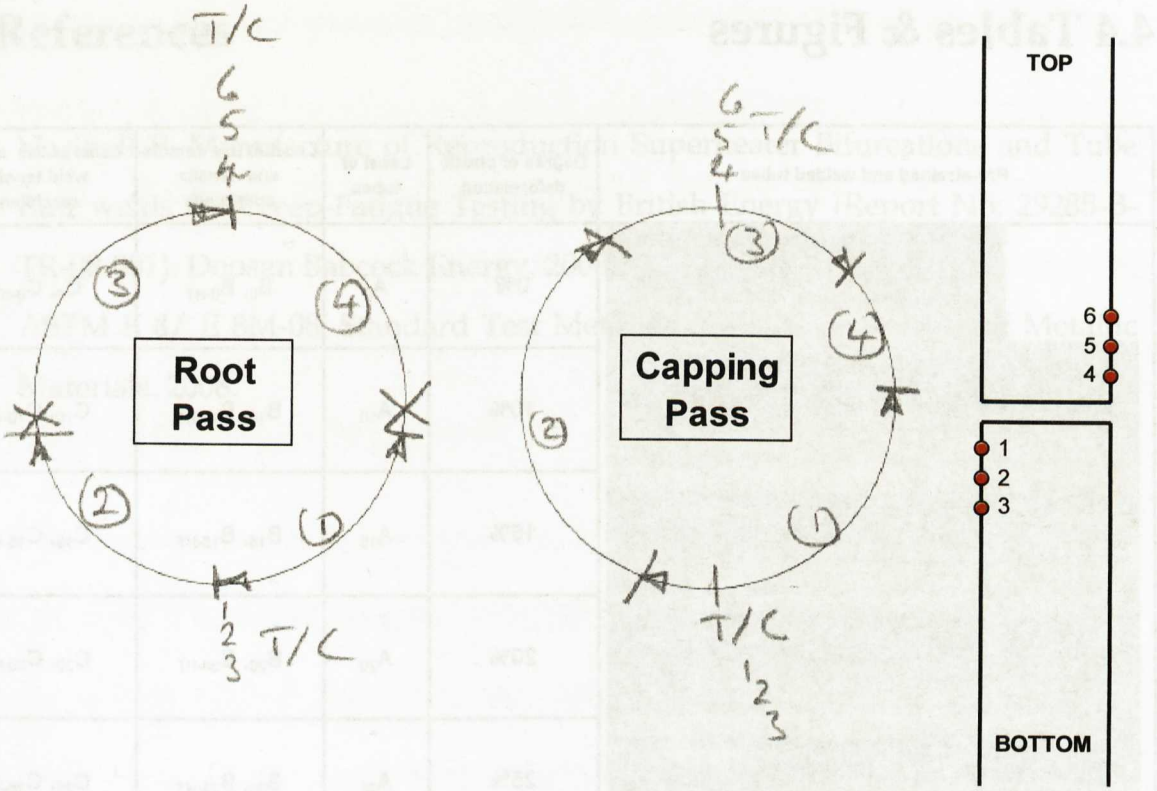

Figure 4.1 The schematic view of the welding procedure of the plain tube A_0. (×) shows the position of the root tacks and arrows are for the section of each pass. The positions of the thermocouples (1-6) are also shown on the vertical drawing of tube.

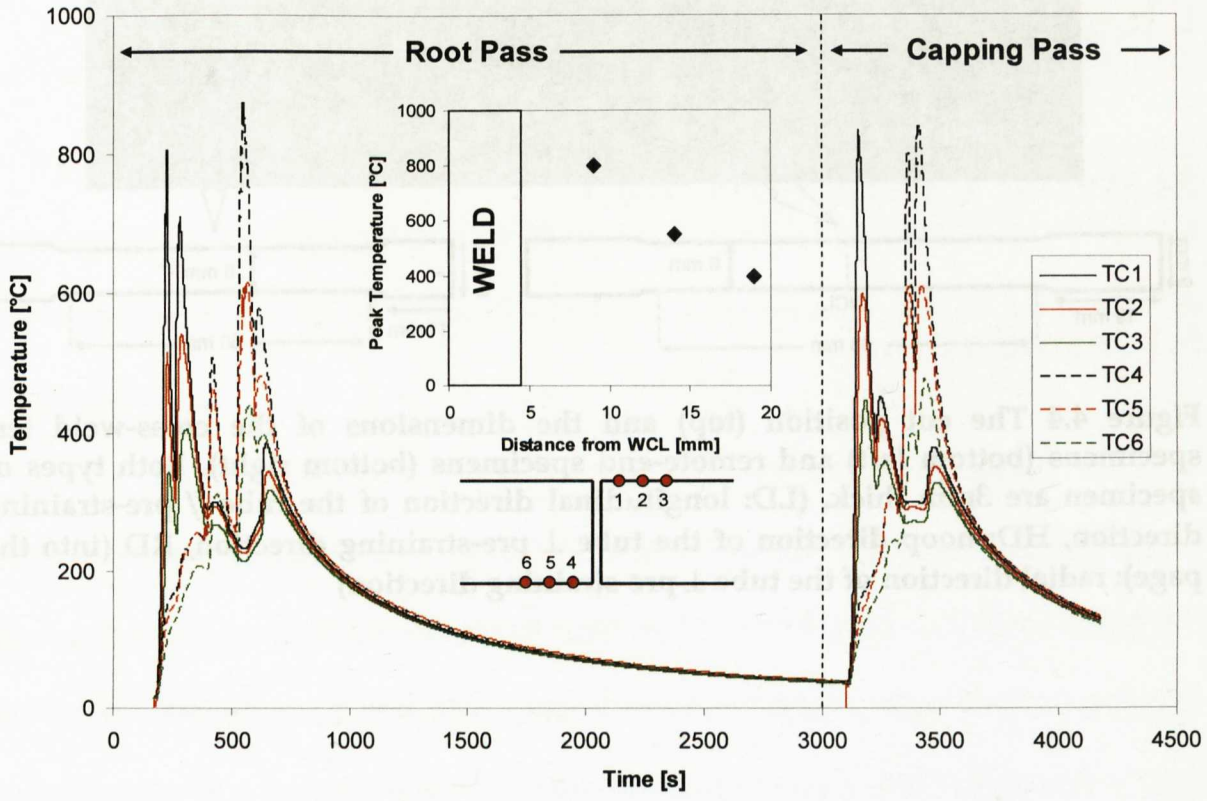

Figure 4.2 The temperature profile obtained during the welding of the plain tube

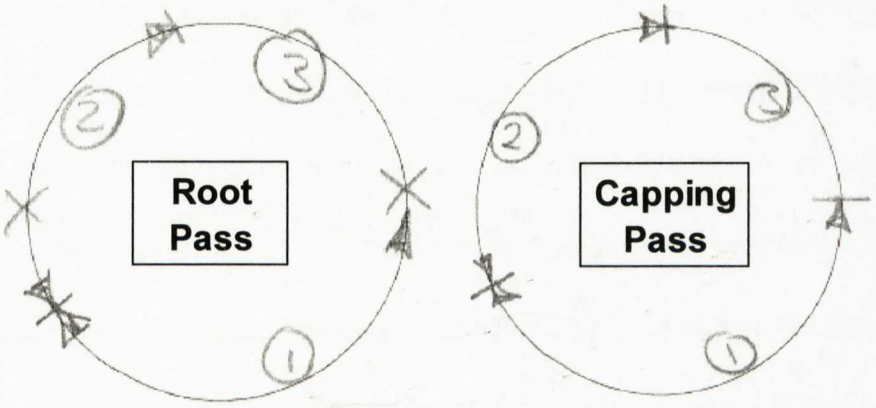

Figure 4.3 The schematic view of the welding procedure of pre-strained tubes (A_{10}, A_{15}, A_{20}, A_{25}). (×) shows the position of the root tacks and arrows are for the section of each pass.

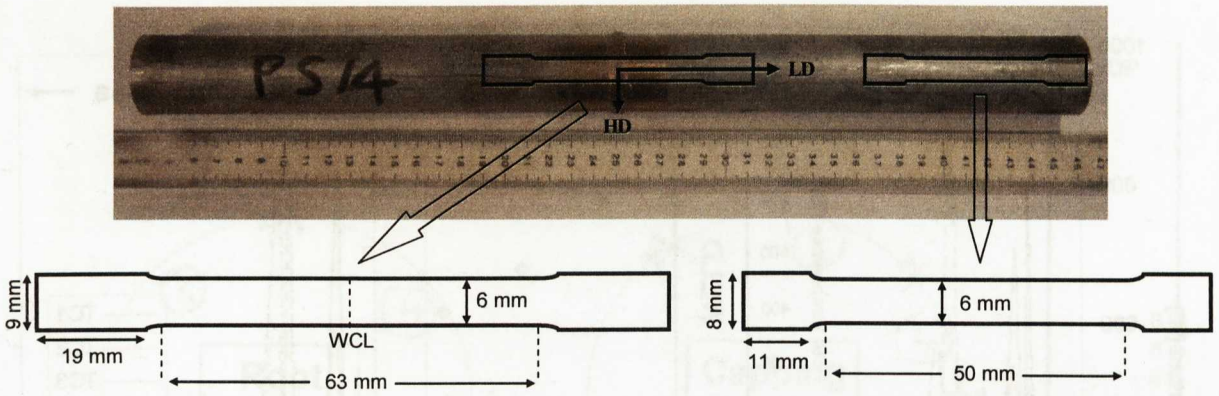

Figure 4.4 The cut position (top) and the dimensions of the cross-weld test specimens (bottom left) and remote-end specimens (bottom right). Both types of specimen are 3mm thick. (LD: longitudinal direction of the tube // pre-straining direction, HD: hoop direction of the tube ⊥ pre-straining direction, RD (into the page): radial direction of the tube ⊥ pre-straining direction)

Chapter 5

Material Characterisation

5.1 Introduction

The manufacture of the boiler units by bending or swaging introduces plastic strain in the tubes, which has effects on the evolution of microstructure during subsequent welding, heat treatment or high temperature service. One of the most significant effects is the potential change in grain size after these thermal treatments due to recrystallization. Plastic strain increases the driving force for recrystallization by lowering the onset temperature and the time required for recrystallization [1]. Grain growth can also occur after these thermal treatments. For example, Shibata et al [2] observed that grain growth occurs in the heat affected zone in austenitic stainless steel. Plastic strain also promotes the formation of precipitates by shifting the time-temperature-precipitation (TTP) diagram to shorter times [1].

In order to avoid solidification cracking of austenitic stainless steel, weld metals are often designed to contain a controlled amount of delta-ferrite. Delta-ferrite in weld metals forms as dendrites prior to solidification of austenite at the peritectic temperature ~1450°C and is retained during rapid cooling. However, since it is a meta-stable phase, depending on the temperature it dissolves into austenite, carbides and intermetallics at elevated temperatures. Delta-ferrite is known to have a deleterious effect on the creep rupture strength of type 316 steels [3].

In this project, the effect of tube shaping was simulated by axial prestraining of plain straight tubes in order to introduce different levels of plastic strain. As explained in Chapter 4, the plain and deformed tubes were cut and then welded. Half of the same set of samples extracted from the welded tubes were heat-treated at a soaking temperature of 1050°C for 15 min under vacuum and quenched to 50°C with nitrogen gas.

The aim of this chapter is to present the microstructural evolution in the tube material due to pre-straining, welding and heat treatment. The grain size before and after heat treatment of plain, 10%, 15%, 20% and 25% tube material was investigated. The effect of the plastic strain on grain size after welding was also investigated measuring the variation of grain size across the weld affected area in 20% prestrained and welded tube. The HAZ microstructure of the 20% prestrained and welded tube was examined using optical and electron microscopes for the existence of weld-induced precipitation. The microstructure of the weld metal before and after heat treatment was also studied. The ferrite-measurements were conducted using a ferrite meter to understand the transformation of delta-ferrite after heat treatment.

5.2 Microstructural Examination

Small coupons were machined out from the end of the tubes A_0, A_{10}, A_{15}, A_{20} and A_{25} where the parent material was not affected by welding but pre-strained at different levels. In addition, coupons which contain the weld metal, HAZ and base metal were also sectioned from tubes A_0 and A_{20}. A set of these coupons was heat

treated as mentioned above and all coupons metallographically prepared for the microstructural examination before and after heat treatment.

The sample preparation included sequential grinding with grades 220, 500, 800, 1200, 2500 and 4000 emery papers and polishing on soft cloths using suspensions containing 9, 6 and 1 μm diamond particles. To reveal the grain boundaries under the optical microscope, the samples were then electrolytically etched in 60% nitric acid solution for a maximum of 1 min with 1.2V as described in [4]. This etching process reveals grain boundaries, weld passes and slightly twin boundaries. In addition, oxalic acid and Murakami's reagent were used to reveal the carbide precipitations [4].

The linear intercept method [5] was used to measure the average grain size. This method relies on the number of the intersections of grains with linear lines which are uniformly drawn on the micrograph. The ratio between the length of the linear line and the number of intersections gives the average grain size.

5.2.1 Microstructure of the parent metal before and after prestraining

The effect of pre-straining on the microstructure was examined by comparing the micrographs of non-strained and pre-strained parent materials. The microstructures before and after 10, 15, 20 and 25% prestraining are given in Figure 5.1. The grain size measurements after deformation are tabulated in Table 5.1. It has been observed that pre-straining does not have a significant effect on the grain size.

5.2.2 Microstructure of the parent metal after heat treatment

The non-strained and deformed samples were heat treated at a soaking temperature of 1050°C for 15 min under vacuum and quenched to 50°C with nitrogen gas and their corresponding microstructures are given in Figure 5.2. The grain size measurements after heat treatment are tabulated in Table 5.1. It can be seen that the grain size of the deformed samples after heat treatment is approximately doubled, while there is no significant change in the grain size of the non-strained material. The increase in grain size is thought to be due to the excess soaking time. Heat treatment between 955°C to 1120°C for 3 to 5 min per 2.5 mm (0.10 in.) of thickness and followed by rapid air cooling is known to fully soften the steel [6]. Furthermore, the decrease in recrystallization temperature due to the presence of plastic strain (Figure 5.3) may have resulted in recrystallization and grain growth.

5.2.3 Microstructure of the weld metal before and after heat treatment

The microstructure of the weld metal before and after heat treatment is given in Figure 5.4. It can be seen that both microstructures consist of mainly austenite and some delta ferrite. The solidification behaviour of the weld metal can be described by using the diagram in Figure 5.5(a). On the left side of 18Cr-12Ni composition, the primary solidification phase is austenite whereas on the right side it is delta-ferrite. The microstructure before the heat treatment suggests that the primary solidification phase is austenite although the composition of the weld metal in Table 4.2 is almost on the composition of 18Cr-12Ni. Note that this diagram is for 70% iron and in the

composition of the weld metal there are additional elements such as molybdenum. EBSD results also confirmed that the primary solidification phase is austenite. Austenite and delta-ferrite coexist in the liquid as indicated in the small triangular area in Figure 5.5(a). It is also seen that austenite is stable below 1200°C. This type of solidification mode in which secondary ferrite coexists with primary austenite phase is called AF solidification. Dendrites of austenite grow into the liquid as shown in Figure 5.5(b). Delta-ferrite which is formed via a eutectic reaction is entrapped between the austenite dendrites and resists transformation to austenite during weld cooling since it is enriched in ferrite promoting elements. The ferrite content was measured in the weld metal using a Ferrite Meter which magnetically detects the ferrite and ~5±0.5% ferrite was found in the weld metal. Heating up to 1050°C during heat treatment will accelerate the transformation of delta-ferrite to austenite and during soaking at that temperature delta-ferrite dissolves partially into austenite [7]. Note that ferrite does not transform into carbides because at 1050°C the carbides are dissolved in the austenite matrix. The ferrite measurements in the weld metal by ferrite meter showed that there is still ~1±0.5% ferrite after heat treatment. The network of the ferrite breaks down after heat treatment as it was observed in Figure 5.4(b).

5.2.4 Microstructure of the heat-affected-zone (HAZ) before and after heat treatment

The microstructures of the HAZ generated after welding in the non-strained and 20% pre-strained material are given in Figure 5.6. It can be seen that there is a

non-uniform grain size distribution in both microstructures. There does not seem any significant effect of welding on grain size in the HAZ of the non-strained material (Figure 5.6(a)). However, in the 20% pre-strained material the grains near the fusion boundary are considerably larger (Figure 5.6(b)). The effect of welding on the grain size in the 20% prestrained material can be seen better in (Figure 5.7 (a)). The effect of welding is significant in 1-1.5mm wide region in front of the fusion boundary (i.e. the region between the fusion boundary and the red dashed line on Figure 5.7(a)). The grains are coarser (~45μm) near the fusion boundary. In the far end of that region the grains are relatively smaller (~25μm). The microstructure of 20% pre-strained material along the tube length after heat treatment is presented in Figure 5.7(b). It can be seen that grains are reasonably larger after heat treatment. The grain size measurements across the weld in the non-strained and 20% prestrained tubes before and after heat treatment is given in Figure 5.8.

EBSD was used to measure the low angle boundaries (LABs) in the HAZ region of the 20% prestrained and welded tube (Figure 5.9). Briefly, LABs which will be discussed in detail in Chapter 7, form due to dislocation structures such as dislocation pile-ups near grains or dislocation arrays inside the grain depending on the level of plastic deformation. Figure 5.9 shows that the dislocation structures due to plastic deformation disappeared in a 1.5 mm wide region as a result of welding. The grain size measurement and the LAB distribution across the weld suggest that the welding annealed this region and caused grain growth.

The interfacial microstructure of the non-strained and 20% strained tube material before and after heat treatment is given in Figure 5.10. For as welded

condition of non-strained and 20% pre-strained base metal, it can be seen that some grains adjacent to the fusion boundary are partially melted and surrounded with some flake-like structures on the grain boundaries (Figure 5.10 (a & c)). The residual elements S, P and Si in the composition of the austenitic stainless steel are considered as detrimental because they promote liquation cracking in the weld metal and HAZ by forming a liquid film at the grain boundaries as a result of segregation of low-melting constituents at the grain boundaries [8]. The liquid film creates a potential risk of a crack initiation if there is enough straining in the surrounding [9]. Sulphur is strongly rejected into the liquid during solidification of austenite, rapidly lowering the melting point of the interdendritic liquid. Thus the potential for forming low melting eutectics remains strong even with very low sulphur contents in austenite (>0.005%) [10]. It was also reported that austenitic stainless steel weld metals are susceptible to liquation cracking if the amount of Si is greater than 0.3% [11]. Kou [9] suggests that liquation results in the formation of a 'ghost boundary' network, which represents the position of the original grain boundaries broadened by liquation. Therefore, these flakes are likely to be liquid films formed after the partial melting of the grains adjacent to the fusion boundary. These flakes still exist after heat treatment at 1050°C (Figure 5.10 (b & d)). Although the levels of residual elements and the observation of ghost grain boundary network suggest that these structures resemble liquid films remaining after the welding, this phenomenon needs further understanding and requires detailed characterization with SEM/EDX.

Thick sections of austenitic stainless steels are also susceptible to sensitization after welding depending on the cooling rate. The plastic strain promotes the

sensitization of the welds. Sensitization occurs as a result of the precipitation of carbides such as $M_{23}C_6$ preferentially along the grain boundaries. The carbides are visible after the austenitic stainless steel is etched electrolytically with 10% oxalic acid solution or with Murakami's reagent [4]. However, no carbides were observed in the HAZ after welding even when the base metal had been cold-worked. SEM images which were taken very close to the fusion boundary show that the grain boundaries are carbide free (Figure 5.11). The reason why there is no precipitation is due to the fact that the rapid cooling does not allow Cr atoms to diffuse into the grain boundaries and form carbides. Based on the Weiss and Stickler's TTP diagram (see Figure 2.26) the carbide formation is favoured in the range of temperature between 500 and 900°C [12]. Davis [13] suggests that the minimum sensitization time for a 300-series stainless steel alloy with 0.05% C is about 30 minutes. In addition, Weiss and Stickler [12] observed that $M_{23}C_6$ carbide which is the fastest carbide precipitation in austenitic stainless steels begins to form after 6 minutes for AISI 316 steel which was aged at 810°C subsequent to 20% cold-work. Temperature profiles recorded at 5mm away from the fusion boundary during welding show that the temperature reaches its peak (~850°C) and drops down to 300°C in less than 2 minutes (see Figure 4.2). The total time which the material at 5mm away from fusion boundary is subjected to the root and cap passes is about 4 minutes and is not enough for the precipitation.

5.3 Hardness Test

Hardness profiles across the weld have been obtained for the as-welded and heat-treated cross-weld specimens. For this purpose, one side of each specimen was

polished as described in section 5.2. Vickers hardness tests were performed using an automated hardness test machine with a load of 5kgf. The load was optimized on a similar stainless steel dummy sample so that the indent penetrates enough to obtain relevant data under the surface (Figure 5.12).

Figure 5.13 gives the variation of hardness values across the welded region for specimens C_0, C_{10}, C_{20}, $C_{0\text{-HT}}$, $C_{10\text{-HT}}$ and $C_{20\text{-HT}}$. Prior to heat treatment (see specimens C_0, C_{10} and C_{20} in Figure 5.13), there is a large increase in hardness values with plastic strain in the base metal away from the weld. However, the hardness values of the weld are similar since the welding conditions were kept the same for all the welds. The transition region from the weld metal to the unaffected base metal occurs within about 12 mm from the fusion boundary. Note that in that region there is a slight variation in hardness for non-strained specimen C_0. After heat treatment at a soaking temperature of 1050°C for 15 min, the hardness drops below 140 H_V and is almost homogenized through the specimen except weld (see specimens $C_{0\text{-HT}}$, $C_{10\text{-HT}}$ and $C_{20\text{-HT}}$). The weld is slightly harder than the heat treated base metal and has almost similar hardness for specimens $C_{0\text{-HT}}$, $C_{10\text{-HT}}$ and $C_{20\text{-HT}}$. Interestingly; the hardness of the base metal in specimens $C_{10\text{-HT}}$ and $C_{20\text{-HT}}$ is lower than in specimen $C_{0\text{-HT}}$. This can be attributed to the fact that after the heat treatment the grain size of the prestrained material is larger than that of the plain material.

5.4 References

[1] Marshall P. Austenitic Stainless Steels: Microstructure and Mechanical Properties: Elsevier Applied Science Publishers, 1984.

[2] Shibata S, Mekaru S, Fukumoto I, Watanabe T. Effects of plastic strain on grain growth in the heat affected zone in austenitic stainless steel. Welding International 1997;11:23.

[3] Thomas RG, Yapp D. Effect of heat treatment on type 316 stainless steel weld metal. Welding Research Supplement 1978:316.

[4] Voort GFV. Metallography: Principles and Practice: ASM International, 1999.

[5] ASTM E112-96(2004)e2: Standard Test Methods for Determining Average Grain Size. 2004.

[6] ASM Handbook, Vol. 4: Heat Treating: American Society for Metals, 1990.

[7] Lippold JC, Kotecki DJ. Welding Metallurgy and Weldability of Stainless Steel: John Wiley & Sons, 2005.

[8] Messler RW. Principles of Welding: Processes, Physics, Chemistry, and Metallurgy: Wiley-VCH, 1999.

[9] Kou S. Welding Metallurgy: Wiley-Blackwell, 2003.

[10] Matsuda F, Katayama S, Arata Y. Solidification crack susceptibility in weld metals of fully austenitic stainless steels - Solidification crack susceptibility and amount of phosphide and sulphide in 310 weld metal. Transactions of JWRI 1981;10:201.

[11] Robinson JL, Scott MH. Liquation cracking during the welding of austenitic stainless steels and nickel alloys. Phil. Trans. R. Soc. Lond. 1980;A295:105.

[12] Weiss B, Stickler R. Phase instabilities during high temperature exposure of 316 austenitic stainless steel. Metallurgical and Materials Transactions B 1972;3:851.

[13] Davis JR. Corrosion of Weldments. ASM International, 2006.

[14] Katayama S, Fujimoto T, Matsunawa A. Correlation among Solidification Process, Microstructure, Microsegregation and Solidification Cracking

Susceptibility in Stainless Steel Weld Metals(Materials, Metallurgy & Weldability). Transactions of JWRI 1985;14:123.

5.4 Tables & Figures

Plastic Deformation	Grain size (μm) before HT	Grain size (μm) after HT
0%	33.3 ± 0.5	27.8 ± 2.3
10%	27.2 ± 2.7	60.4 ± 4.3
15%	28.7 ± 0.9	57.5 ± 6.9
20%	28.9 ± 4.1	53.5 ± 8.5
25%	32.3 ± 6.9	62.1 ± 6.3

Table 5.1 Grain size measurements before and after heat treatment of non-strained and deformed samples.

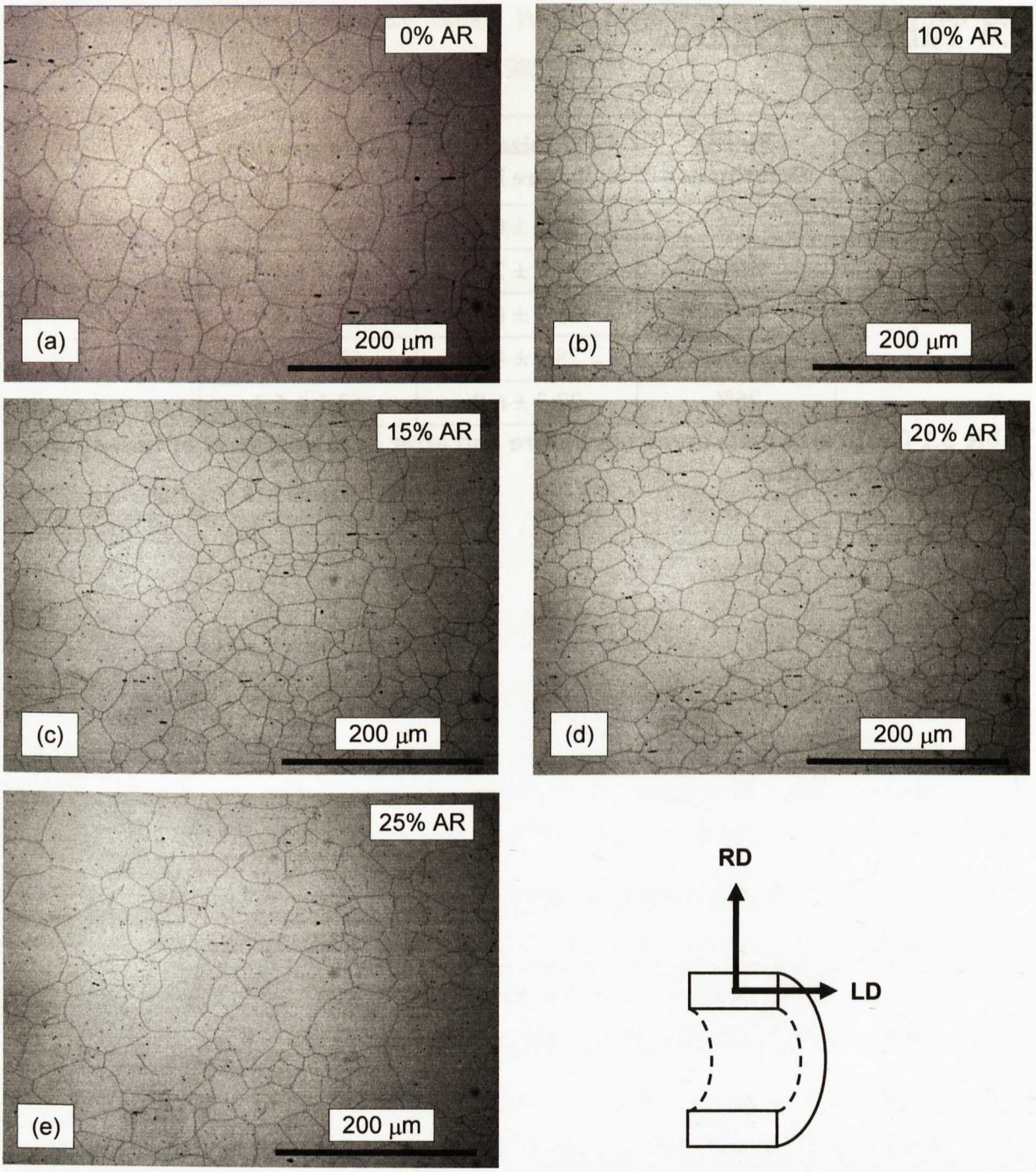

Figure 5.1 The microstructures (250×) of the parent metal before prestraining (a) and after 10% (b), 15% (c), 20% (d) and 25% (e) prestraining. (LD: longitudinal direction, RD: radial direction)

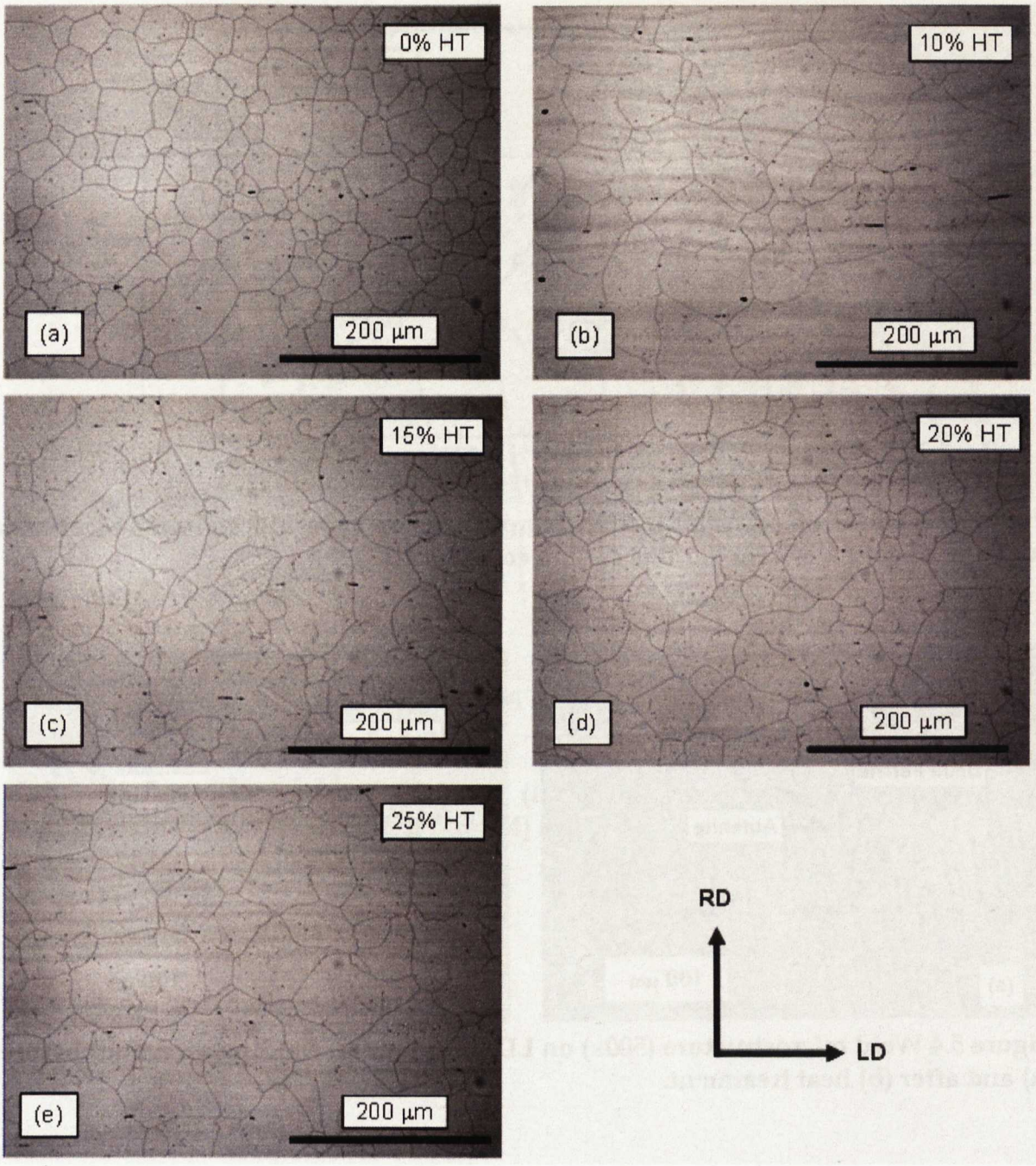

Figure 5.2 The microstructures (250×) of the non strained (a), 10% (b), 15% (c), 20% (d) and 25% (e) prestrained parent metal after heat treatment

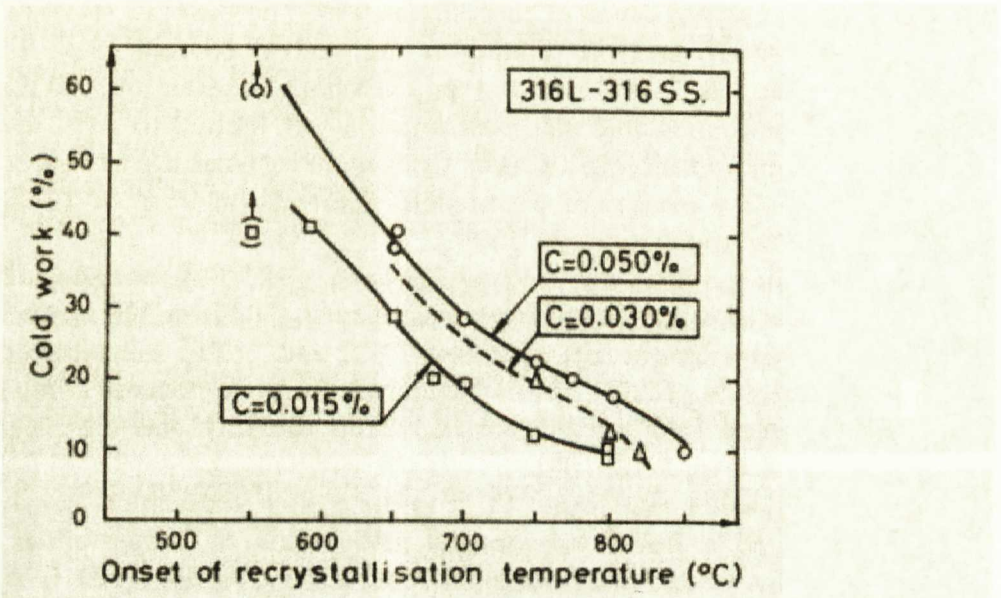

Figure 5.3 Onset of recrystallization temperature in type 316 stainless steel as a function of cold work for various carbon contents [1]

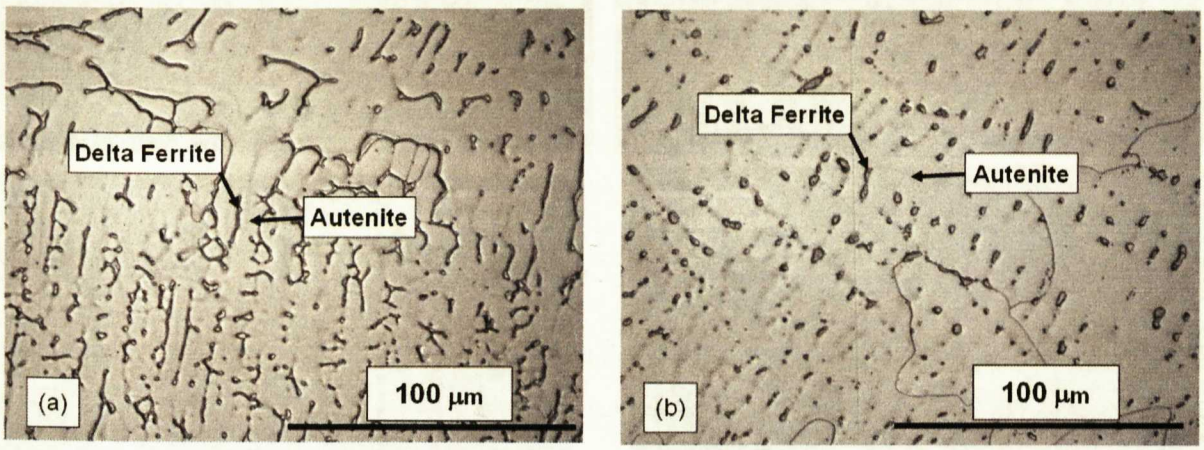

Figure 5.4 Weld microstructure (500×) on LD-RD plane (⊥ welding direction) before (a) and after (b) heat treatment.

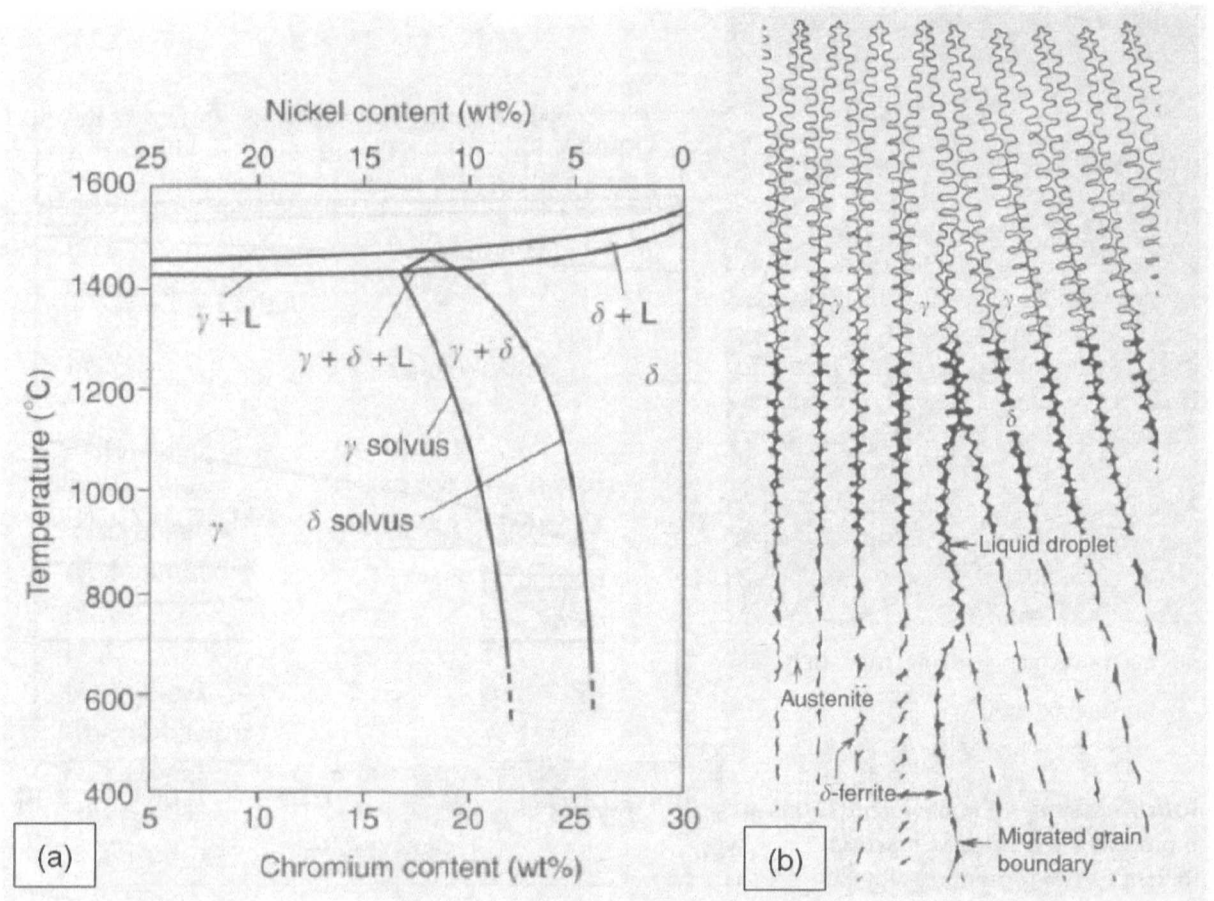

Figure 5.5 Fe-Cr-Ni system at 70% iron (L :liquid, γ :austenite, δ :delta-ferrite) (a) Microstructure after AF solidification [14] (b)

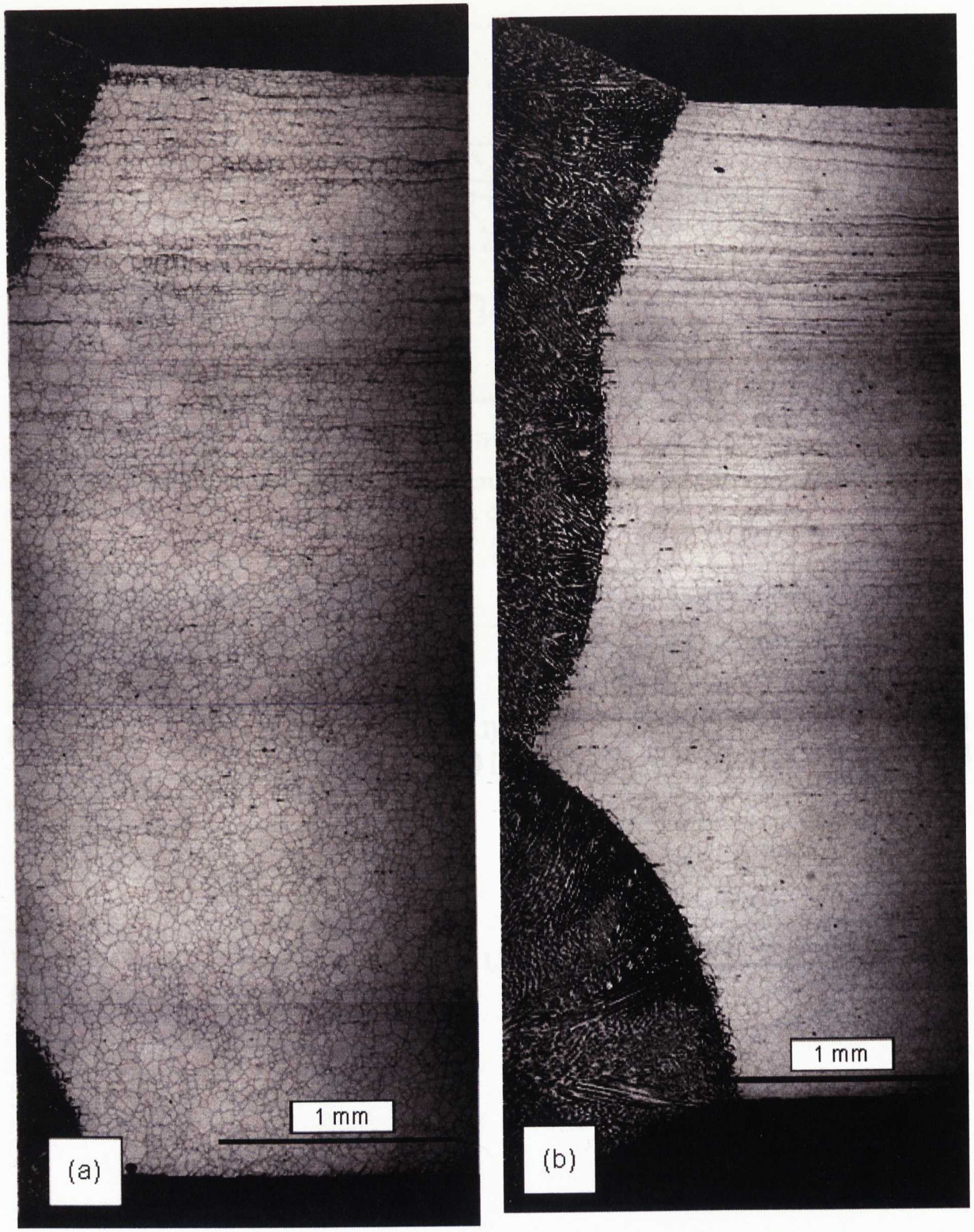

Figure 5.6 The microstructure (50×) of the HAZ through wall thickness after welding onto non-strained (a) and 20% strained (b) tube material.

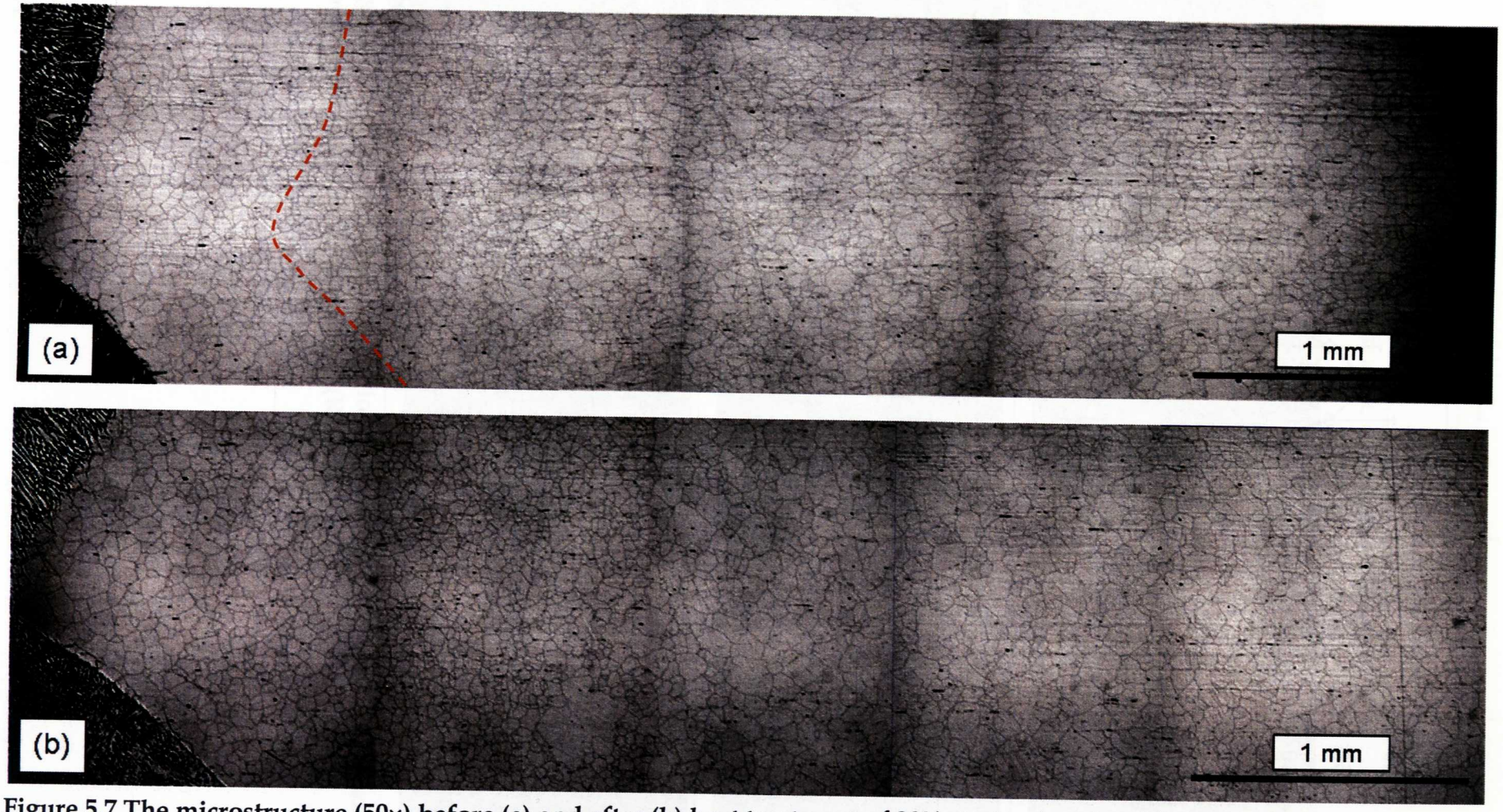

Figure 5.7 The microstructure (50×) before (a) and after (b) heat treatment of 20% strained and welded tube material

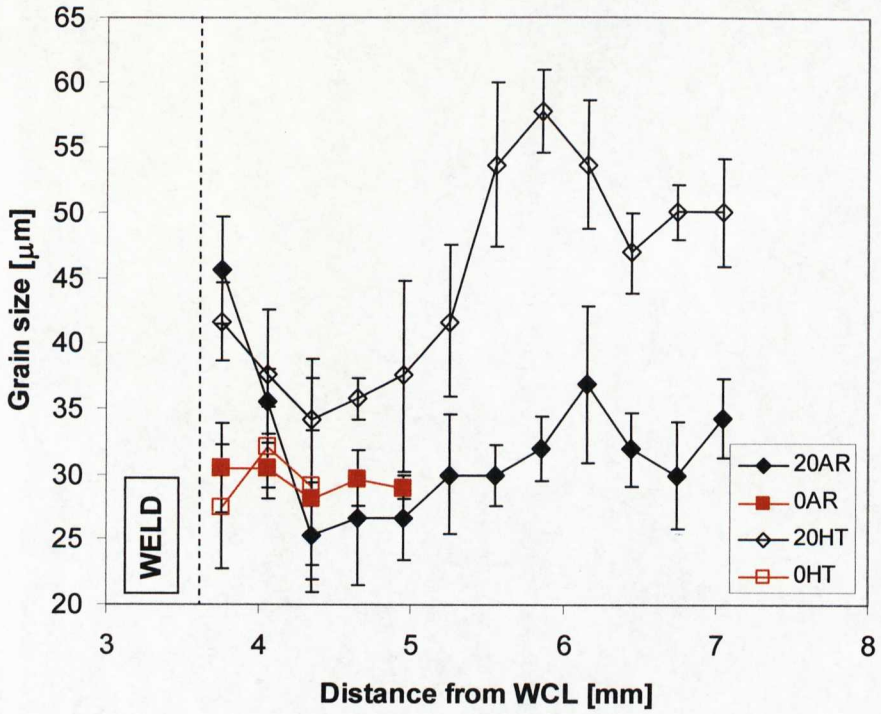

Figure 5.8 The grain size measurements across the weld in non-strained and 20% strained and welded tubes before and after heat treatment

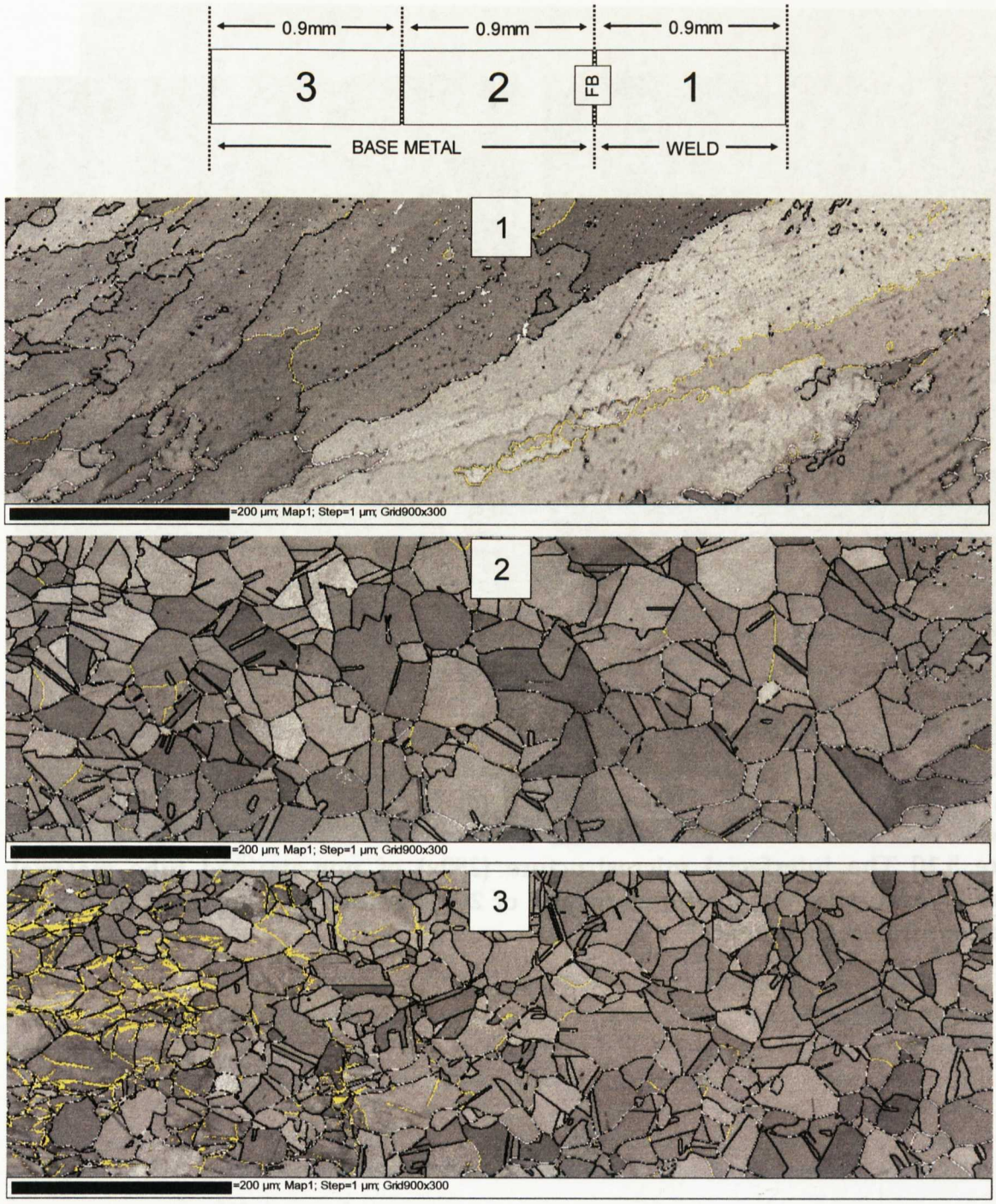

Figure 5.9 The distribution of low angle (yellow) and high angle (black) boundaries in the HAZ of tube A_{20} (RD-LD plane)

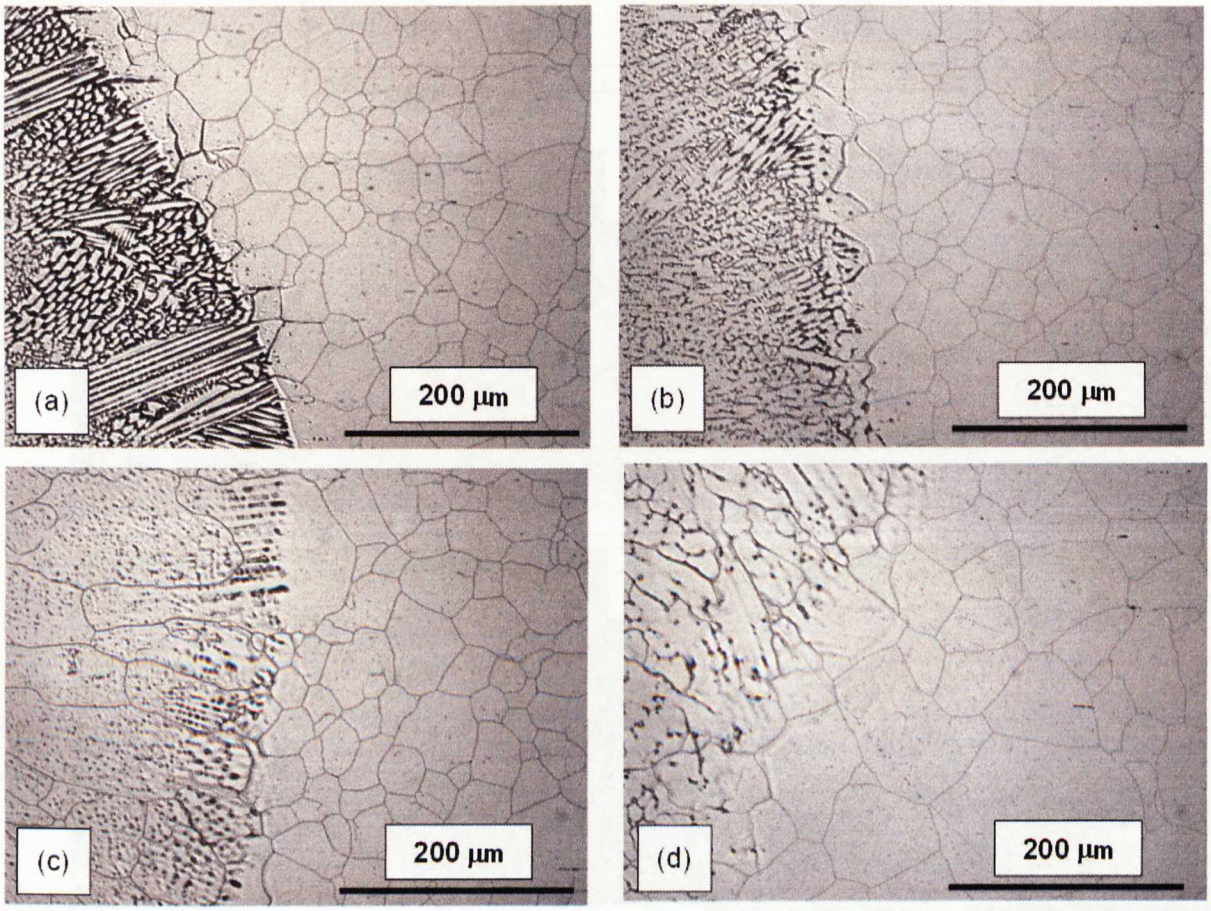

Figure 5.10 The interfacial microstructure (250×) of non-strained tube material before (a) and after heat treatment (c) and of 20% strained tube material before (b) and after (d) heat treatment.

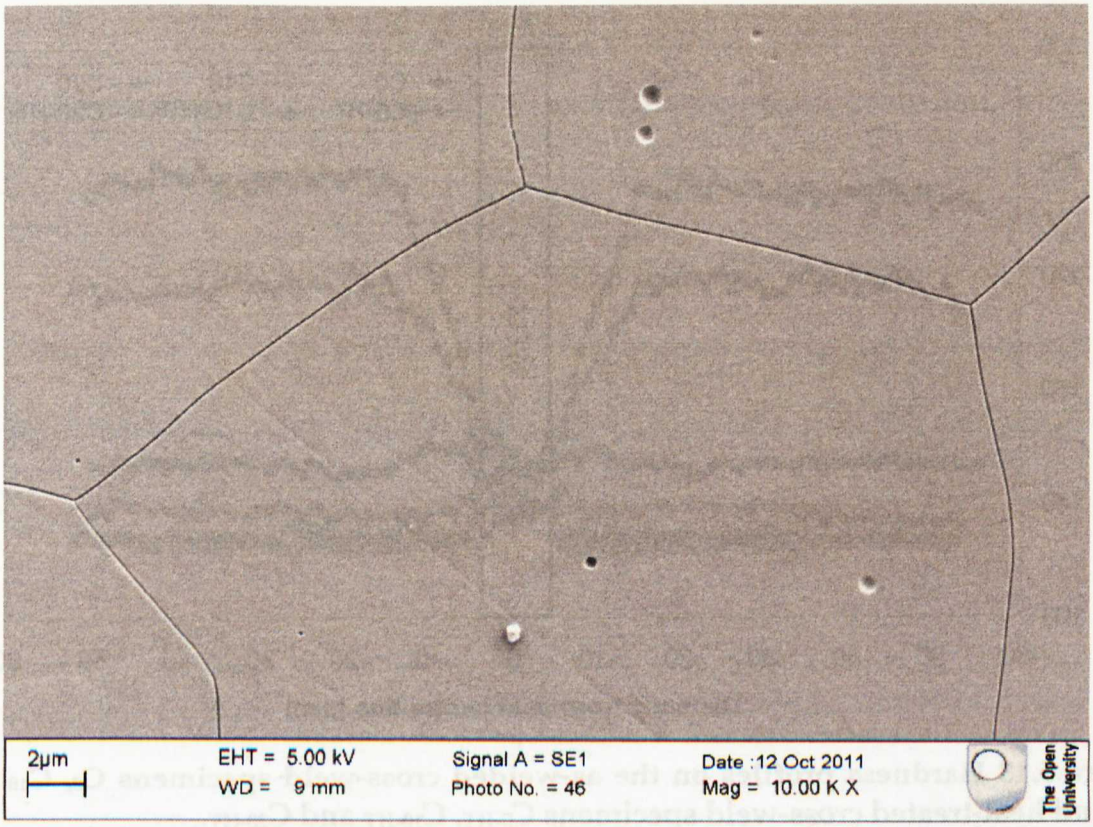

Figure 5.11 SEM image of HAZ near the fusion boundary in 20% prestrained and welded tube

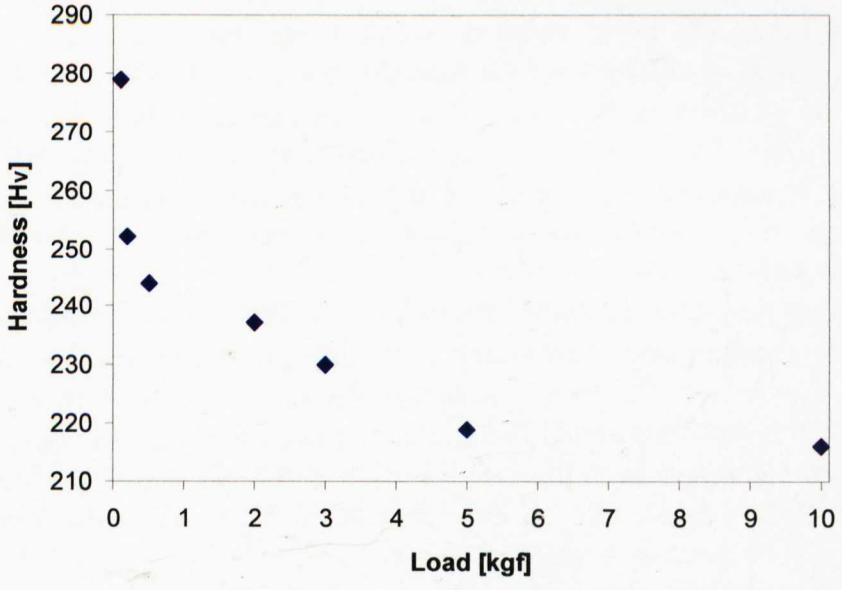

Figure 5.12 The load optimization for hardness measurements

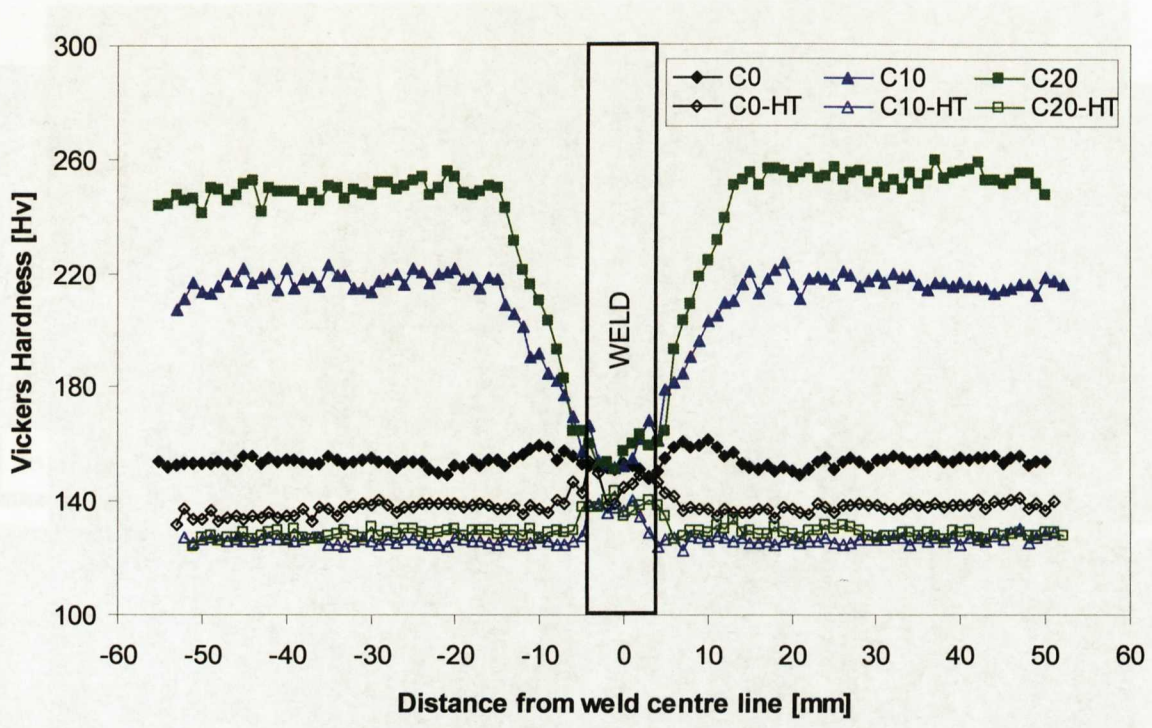

Figure 5.13 Hardness profiles on the as-welded cross-weld specimens C_0, C_{10} and C_{20} and heat-treated cross-weld specimens $C_{0\text{-HT}}$, $C_{10\text{-HT}}$ and $C_{20\text{-HT}}$.

Chapter 6

Digital Image Correlation (DIC) Integrated Tension Tests

6.1 Introduction

The structural integrity, performance and life of austenitic stainless steel weldments in power generation plants is determined by the mechanical properties of the weld metal, heat affected zone (HAZ) and base metal. These properties depend on the full fabrication history including cold bending and swaging, welding, heat treatment and the effects of service ageing. For example, many metres of austenitic stainless steel tubes are bent, swaged, welded and heat treated to produce heat exchanger units in order to be installed in steam raising power plants. Prior to the instalment the mechanical properties of the virgin tube have been greatly altered during manufacturing steps.

The tube-shaping operations such as bending and swaging accumulate plastic deformation in the stainless steel. The plastic deformation can improve the strength of austenitic stainless steels but on the other hand it increases the susceptibility to stress corrosion and creep damage [1, 2]. ASME Boiler and Pressure Vessel Design code [3] suggests that the limit of forming strain for 316H material which is going to operate between 580°C and 675°C is 20% and if it exceeds that threshold, the material

should be annealed above 1040°C to restore its mechanical properties, tensile strength, creep strength and creep ductility to the start of life values. In addition to the tube shaping, welding is required to produce tube junctions where the main tube with a larger diameter is connected to a U-bent tube. However, very little is known about the effects of welding onto plastically deformed tubes. The effect of heat during welding influences the material near the weld in two ways: softening and hardening. In the case of welding onto bent or swaged tube, if the temperature is high enough, annealing occurs and this softens the previously work-hardened material. Current construction practices for 316H tubes forbid welding onto material that has experienced more than 15% plastic strain, without first resolution heat treating the material [4]. If the base metal near the weld is a soft material, the thermal cycles during welding cause strain hardening or plastic strain near the weld fusion zone [5]. As a result of hardening or softening the material properties change in near-weld regions and this causes a strength variation in the heat affected region. In addition to the tube-shaping and welding, post weld heat treatment (PWHT) is applied to the welded components to relieve the weld residual stresses which can cause premature failures during operation [6]. PWHT significantly alters the material properties across the weld pool as well as the weld residual stresses.

The local strength variation in the weld-affected regions is important in fracture assessments [7] and elevated temperature life assessments [8]. For example, the propagation of cracks in the weld-affected regions is governed by the strength variation at the tip of the crack [9]. The numerical models which are developed to understand the structural integrity of the welds are usually based on bi-material

(weld and base) assumptions ignoring the heat affected zone (HAZ) [7, 10], but the spatial variation of material properties needs to be captured in the analysis if the engineering assessments are to be improved.

Several techniques such as testing of micro-specimens [11], instrumented ball indentation [12] and digital image correlation (DIC) integrated tensile testing [13] have been employed for measuring the variation of local material properties. Many of these techniques require specialized equipment and a great deal of time to characterize various weld regions. In addition, the spatial resolution and accuracy that can be achieved using micro-specimens are limited by the ability to isolate the individual weld regions. Although the resolution obtainable by ball indentation is much better, the technique requires several assumptions and semi-empirical formulas. On the other hand, DIC overcomes many of the limitations and disadvantages of the testing of micro-specimens and instrumented ball indentation.

Digital image correlation (DIC) is an optical full-field displacement/strain measurement technique which is simply based on computational tracking of the patterns on digital images taken before and after the deformation (or on a sequence of successive digital images during deformation). The light intensity on the recorded image is in grey level. As a result of the illumination of the artefact (paint spots) or natural surface features (roughness) on the surface the grey level intensity varies throughout the image. The DIC algorithm divides the reference image into sub-regions provided that each sub-region or "subset" has a unique traceable intensity pattern. By cross-correlating the subset pattern in successive images, the relative displacement vector of each subset is calculated in pixels with sub-pixel accuracy [14].

This spatially resolved displacement/strain measurement with DIC enables the investigation of the local material properties of heterogeneous materials such as functionally graded materials, welded components and composite materials.

DIC has been used by many researchers to determine the local material properties of friction stir weldments [13, 15-23], arc weldments [24-30] and laser beam weldments [31, 32] during tensile testing. The earliest implementation of this was reported by Reynolds and Duval in 1999 [13]. A cross-weld tensile specimen (welding direction $\perp$ loading direction) was machined from the welded component and the specimen surface where the images will be taken was either cleaned to reveal the natural surface features or sprayed with white and black paint to create artificial surface features. The specimen was put into the grips and the patterned surface is illuminated with a white light source. A reference image was taken from the illuminated patterned surface prior to loading. Thereafter, the test was started under displacement control and successive images are captured at specified time intervals. With the help of a DIC algorithm these images are correlated with the reference image by using a correlation function and the in-plane displacement distribution is computed. In order to construct the stress-strain curves for each subset the strain is derived from the smoothed in-plane displacement map and stress is obtained from the global load which is recorded from the load cell at specified time intervals corresponding to the image acquisition rate. The use of global stress means that the stress is assumed to be uniform through the specimen until the start of necking in the soft region. This assumption is called the "iso-stress assumption" [13]. The material

properties such as offset proof stress, a vital design parameter for structural integrity, are then obtained from these local stress-strain curves.

The advantage of this method over other techniques (e. g. micro-sample testing and ball indentation) measuring local material properties is the ability to obtain local material properties from the tension test of a single cross-weld tensile specimen. However, there are some limitations related to the method of strain calculation, the use of global stress, the constraints due to specimen geometry (especially the weld geometry) and the strength mismatch level, which may result in anomalous stress-strain curves as reported in references [24] and [29]. These will be discussed in detail in section 6.5.2.

In the present chapter, as a part of an EDF sponsored project investigating the effect of fabrication history on 316H tube weldments, the local and global tensile properties of the weldments after different manufacturing steps (prestraining, welding and heat treatment) has been studied by performing DIC integrated tension tests. The offset proof strength variation across the weldment was obtained on different cross-weld tensile specimens from the local stress-strain curves which were constructed using the local displacement measurements by DIC and the global load measured by the load cell unit of the tensile test machine. However, anomalies were observed on the local stress-strain curves obtained in the cross-welds tensile specimens whose base metal was pre-strained before welding. Those experimental local stress-strain curves were validated using finite element modelling by investigating (1) strength mismatch effect, (2) the influence of strain calculation method and (3) the use of global load. The prediction of offset proof strength

variation across the weld from the local stress-strain curves with some anomalies was also tested using finite element simulation.

6.2 Experimental Procedure

6.2.1 Materials

A set of plastically-strained and butt-welded tubes were supplied for the experimental programme by EDF (Table 4.1). The untreated tubes (referred to the tubes before plastic straining and welding) were manufactured by extrusion and then solution annealed at 1100°C for 3 minutes followed by water quenching. The tubing material is AISI Type 316H austenitic stainless steel with the composition given in Table 4.2. The initial tubing geometry was 38 mm in outer diameter and 4 mm in wall thickness. The test specimens were fabricated as follows; (1) four tubes were pulled uniaxially in tension up to 10, 15, 20 and 25% plastic strain. The pre-straining process was done using a strain rate of ~0.15%/s with a large servo-hydraulic rig. Adaptors were welded to the ends of the pipes so that they could be easily fitted to the universal joints for gripping. Adapters were chopped after this step. The strain was monitored by a side-mounted extensometer, 4 strain gauges fitted at 90° intervals around the circumference of the centre of the pipe and with some markings on the pipe length and the test stopped at the appropriate total strain. (2) These strained tubes plus a non-strained tube were cut into two halves. (3) Matching half-tubes were then welded together (after root tack welding) using a tungsten inert gas (TIG) welding process with Type 316L filler metal (Table 4.2 and Table 4.3). The weld

contains two passes: root pass and cap pass. During the root pass the tacks were incorporated into the weld.

Flat cross-weld and remote-end tensile test specimens were machined out around the circumference of the tubes by electro-discharge machining (EDM). The cut position and the dimensions of the tensile specimens are given in Figure 4.4. The tubes, cross-weld and remote-end tensile specimens are labelled as shown in Table 4.1. Some of the specimens were labelled as "HT" to show that they were heat treated at a soaking temperature of 1050°C for 15 min under vacuum and quenched to 50°C with nitrogen gas.

6.2.2 Tensile testing

Tension tests on remote and cross-weld specimens (B_0, B_{10}, B_{20}, $B_{0\text{-HT}}$, $B_{10\text{-HT}}$, $B_{20\text{-HT}}$ and C_0, C_{10}, C_{20}, $C_{0\text{-HT}}$, $C_{10\text{-HT}}$, $C_{20\text{-HT}}$) were carried out using a screw-driven tensile testing machine with a 30kN load cell. Mechanical wedge action grips were used to fix the specimens into the machine. Before each test commenced, the loading and specimen alignment was checked in order to avoid subjecting the specimen to any bending or torsion, i.e. to ensure the loading was pure uniaxial tension [33, 34] . Two universal joints were used to improve axial alignment. Additionally, grooved thin plates which fit to the shoulder of the specimens were employed in the wedge grips to obtain a perfect axial positioning in the wedge grips. A calibration tensile specimen was prepared by gluing four strain gauges to each surface at same height. After the specimen is attached to the wedge grips (connected to the universal joints) by using grooved thin plates a load was applied and the alignment was checked from the readings on each strain gauge.

In addition, the specimens were preloaded up to 100MPa for the settlement in the grips and then the load was released. Once a reasonable alignment was obtained, the real tests were commenced.

6.2.3 Digital image correlation (DIC)

The full field distribution of strain was obtained throughout the DIC integrated tensile tests of the remote-end and cross-weld specimens. The speckle pattern required for the DIC measurements was achieved by white light illumination of the rough surface produced by EDM [27]. A DC fibre optic light source was used to illuminate the surface. After correcting the alignment of the specimen and grips, the tensile tests were performed with a constant extension rate of 0.1mm/min. During the tests, images of the front surface of the specimens were captured by a digital SLR camera (Nikon D300), with a sensor size of 4,288 x 2,848 pixels (12.3 Mega Pixels), and a 200 mm macro lens. The images were taken every 10 seconds. The load and extension were recorded every second. Analysis of the images was performed using commercial DIC software [35].

To analyse the images captured during the tension tests the DIC parameters were optimized as described in section 3.5. The pixel size of images for each test was about 11 μm. As a first step of analysis, all images were shift-corrected with respect to a reference image, which is usually the first image captured. A rectangular area was defined in the middle of the specimen as a working space, where the displacement vectors were to be calculated. This rectangular area does not include whole of the specimen width because, for practical reasons, the working space selected is based on the last image where the specimen has narrowed considerably due to the Poisson

effect. The effect of defining the working space on a partial width on the local stress-strain curves will be discussed in section 6.4.2.2 and 6.5.2. In-plane displacement vectors in the loading direction were calculated within the user-defined working space by multi-scanning the images using a '256x256 subset size with 50% overlap and 2 passes' and a '128x128 subset size with 50% overlap and 6 passes' respectively (Figure 6.1).

The flow chart for the determination of the proof stress distribution from the DIC displacement measurements is given in Figure 6.2. The details of this procedure will be explained in the following sections.

6.2.3.1 Strain computation

Reynolds *et al* demonstrated the calculation of strain in the loading direction by taking the first derivative of the polynomial function which was fitted to the displacement in the loading direction [13]. This technique enabled the local stress-strain curve at any point on the sample surface to be obtained and it has been used by his colleagues in further studies of a friction stir weld [15, 16]. Another strain calculation method is to compute strain on a user-defined gauge length including a set of adjacent subsets and averaging the strain for each row along the width [5, 26-28]. In this study, the latter was used to compute the strain from local DIC displacement measurements. However, the strain averaging was not done on the full-width of the specimen but on the partial width which was included in the user-defined working space.

After the displacement map in the loading direction was obtained using the DIC software, the strain was calculated by differentiating the displacement in a user-defined gauge length using a Matlab script (see section 3.5). This provided smoothed strain data. However, as explained in section 3.5, the use of a large gauge length may result in loss of the actual strain variation. The error in the calculated strain is estimated to be around 50-100 microstrain; this is based on the precision of the DIC method which is given as 0.02 pixel displacement [35]. It is assumed that the strain across the width is constant. So, in order to smooth the data and improve the computational efficiency, the axial strain on each row of the subsets was averaged across the width of the specimen (Figure 6.2). The validity of this assumption was checked with finite element analysis and will be discussed later in section 6.5.2.

6.2.3.2 Prediction of offset proof stress

Stress-strain curves were constructed with the averaged strain data for each row and the global stress (iso-stress assumption) as shown in Figure 6.2. Lockwood and Reynolds have experimentally and numerically studied the validity of the iso-stress assumption and the level of constraint due to the specimen geometry [16]. They reported that the iso-stress assumption is convenient to extract the local material properties and that the constraint due to the thickness of the specimen has an influence on the deformation behaviour.

A linear line is fitted to the data points in a user-defined range within the elastic regime. This linear line is offset to an input value (0.2%, 1.0%, 2.0% etc) and the

proof stress at the input value is taken as the stress component of the point where the offset line and the stress-strain curve intersect.

6.3 Finite Element Modelling

Numerical models were developed to validate the experimental local stress-strain curves which have shown some anomalies by investigating (1) the constraint effects in under-matched strength condition ($\sigma_{y\text{-base}} > \sigma_{y\text{-weld}}$), (2) the effect of strain computation technique and (3) the iso-stress assumption. The reliability of the prediction of offset proof strength variation across the weld from the local stress-strain curves showing some anomalies (e.g. the change in slope of elastic line with increasing stress, which will referred as "reduced-strain" trend hereafter) was also investigated using finite element simulation.

During the tensile testing of a cross-weld specimen with a significant strength mismatch level, the stronger metal can constrain the deformation of the weaker metal and bi-axial stresses can develop at the interface where they join. The constraint of transverse strain at the interface and the development of bi-axial stresses may alter the local stress-strain curves if it is considered that the stress and strain to construct the local curves are measured as axial stress and strain in the loading direction. This effect can be observed clearly in an extreme condition where the strength abruptly changes at the weld/base metal interface. In order to observe the constraint effect of strength variation and the development of bi-axial stress at the interface on local stress-strain curves in such an extreme case, a bi-material model was developed for the simulation of the tensile testing of an under-matched cross-weld tensile specimen

($\sigma_{y\text{-base}} > \sigma_{y\text{-weld}}$) without a HAZ. Secondly, a multi-material model was developed, which is a more realistic approach to simulate the cross-weld specimens used in the DIC integrated tension tests. Unlike the bi-material model, rather than a sudden change, this model has a HAZ region where there is a smooth transition of strength between the weld metal and the base metal. This model was used to investigate the effect of the strain computation technique and the use of global stress on local stress-strain curves in the HAZ region where the anomalies were experimentally detected.

Numerical models were analyzed using ABAQUS Version 6.7 [36]. The 2D plane stress assumption was used since Lockwood and Reynolds have found that plane stress model gives very comparable results with DIC measurements in thin (2.7mm) tensile specimens [16]. Quadrilateral CPS8R (reduced integration, eight-node element) type plane stress elements were used. The boundary conditions are as in the actual tension tests of cross-weld specimens; i.e. the bottom end of the specimen was fixed and the top end was pulled with a constant displacement rate of 0.1mm/min. In this study, all FE analyses were non-linear (NLGEOM=ON) and based on isotropic elastic–plastic materials with isotropic work-hardening.

6.3.1 Bi-material model

A 2D bi-material model was developed in order to understand the constraint effect of strength mismatch on local stress-strain behaviour around the base/weld interface. The material inputs for the weld and base metal are given in Figure 6.3. In this model, the yield strength of the weld metal was taken to be lower than the base metal, as in the case of the material studied in this study. There is a physical interface

between weld and base metal, where the material properties abruptly change. Therefore, it is expected that there will be some constraint effect near the interface due to the large strength mismatch [10].

6.3.2 Multi-material model

The 2D bi-material model represents the extreme constraint effect due to the large strength mismatch at the weld/base interface. However, in real specimens for both C_{10} and C_{20} there is not an abrupt change in material properties at the weld/base interface. In these specimens there is a gradually softened zone (referred to as the HAZ hereafter) where the local yield strength increases continuously from the weld to unaffected base metal. For this reason, a 2D multi-material model was developed, where the yield strength was assumed to increase linearly from weld material to the unaffected base metal as shown in Figure 6.4. The size of each zone was estimated by using the hardness map of specimen C_{10}. Note that there is no interface between the unaffected base metal and HAZ. Many researchers studying numerical simulations of the tension tests of cross-weld specimens have commonly used a partitioned HAZ material in their FE model [16, 19, 37]. However, in this type of model the material properties vary in a stepwise manner between the weld and the unaffected base metal; and the artificial interface between each HAZ partition creates discontinuities in the stress profile across the interface. In the multi-material model used in this study, instead of using a partitioned HAZ material, a continuous HAZ material in which the properties are functionally graded was inserted to the model by running ABAQUS user-subroutines USDFLD and SDVINI [36].

The results obtained from this numerical simulation were used to understand the effect of strain computation technique and the use of global stress on local stress-strain curves in the HAZ region where the anomalies were experimentally detected.

6.4 Results

The results obtained from the DIC integrated tension tests of (1) the flat remote-end specimens (B_0, B_{10}, B_{20}, $B_{0\text{-HT}}$, $B_{10\text{-HT}}$, $B_{20\text{-HT}}$) which only contain the parent tube material and (2) the cross-weld tests specimens (C_0, C_{10}, C_{20}, $C_{0\text{-HT}}$, $C_{10\text{-HT}}$, $C_{20\text{-HT}}$) are reported in this section. The numerical results obtained from the bi-material and multi-material model approaches are also presented here.

6.4.1 DIC integrated tension tests

6.4.1.1 Remote-end specimens

Remote-end tensile test specimens (B_0, B_{10}, B_{20}, $B_{0\text{-HT}}$, $B_{10\text{-HT}}$, $B_{20\text{-HT}}$) were extracted from positions remote from the influence of the welds; therefore, they have homogenous material properties in the gauge length. The tests were performed with an extension rate of 0.1mm/min. A side extensometer (Instron, 25mm gauge length) was attached to the specimens as shown in Figure 6.5. For the DIC measurement, images were taken every 10 seconds and the dashed area which fits within the gauge length of the extensometer (Figure 6.5) was analysed as mentioned above. DIC strain measurement in the dashed region was averaged to compare the strain from the extensometer. The load was recorded from the load cell attached to the crosshead of the Instron testing machine.

The engineering stress-strain curves for the remote-end specimens (B_0, B_{10}, B_{20}, $B_{0\text{-HT}}$, $B_{10\text{-HT}}$, $B_{20\text{-HT}}$) and a tabulation of 0.2% and 1% proof stresses derived from these curves are given in Figure 6.6. Results from the extensometer and DIC show a good correlation for all specimens.

Prior to the heat treatment it is clearly seen that the proof stress was increased with the plastic deformation. The 0.2% proof stress was more than doubled after 20% plastic deformation. The slope of hardening for B_{10}, B_{20} decreases compared to B_0.

After the heat treatment the effect of plastic deformation on stress-strain curve disappeared and the tensile strength of $B_{0\text{-HT}}$, $B_{10\text{-HT}}$, and $B_{20\text{-HT}}$ dropped below that of B_0. Interestingly, stress-strain curves for $B_{10\text{-HT}}$, $B_{20\text{-HT}}$ are below the curve for $B_{0\text{-HT}}$. This can be attributed to the fact that the plastic strain energy locked in the material triggers the recrystallization and grain growth mechanisms and the strength decreases with coarser grain size according to the Hall-Petch relation.

6.4.1.2 Cross-weld specimens

Cross-weld tensile test specimens (C_0, C_{10}, C_{20}, $C_{0\text{-HT}}$, $C_{10\text{-HT}}$, $C_{20\text{-HT}}$) were extracted across the weld pool; therefore, the material properties vary along the gauge length which includes the weld pool, the HAZ and the unaffected base metal. It is likely to have constant material properties in the unaffected base metal, however, in the weld pool and the HAZ the properties might be graded. The tests were performed with an extension rate of 0.1mm/min. Four strain gauges (SGs) were glued on the specimen as shown in Figure 6.7. The alignment was double-checked with a pair of SGs attached on opposite faces of the specimen 20 mm away from the

weld centre line (WCL). Two more SGs are on the back surface at the middle of the weld and in the HAZ (6.5 mm away from WCL). The local stress-strain curves constructed with the strain data obtained from these SGs were compared to the stress-strain curves constructed with DIC strain. Note that the iso-stress, which was calculated from the load recorded from the load cell attached to the crosshead of the Instron testing machine, was employed to construct both types of stress-strain curve. Images were taken in every 10 seconds from the half-length of the specimens as indicated in Figure 6.7 and analysed as described in Figure 6.2.

Local stress-strain curves obtained at the weld centre

Stress-strain curves, which were constructed with the strain data from SGs and DIC at the weld centre, are given in Figure 6.8. Results from the two measurement techniques show a good correlation overall, although there are some small differences between two different stress-strain curves which can be attributed to the fact that these measurements were made on opposite sides of the test specimen. Stress-strain curves obtained from specimens C_0, C_{10}, C_{20} at the weld centre represent the weld metal tensile behaviour prior to heat treatment and it is obviously seen that they are very similar. The tensile behaviour of the weld metal after heat treatment is demonstrated with the stress-strain curves obtained from specimens $C_{0\text{-}HT}$, $C_{10\text{-}HT}$, $C_{20\text{-}HT}$ at the weld centre. The effect of heat treatment on the stress-strain behaviour of the weld is clearly seen: 0.2% proof stress of the weld metal prior to heat treatment is between 265-275 MPa, however, it decreases to 200-220 MPa after the heat treatment.

Local stress-strain curves obtained at a distance of 6.5mm from the WCL

Stress-strain curves, which were constructed with the strain data from SGs and DIC at the position of 6.5mm from the WCL, are given in Figure 6.9. Results from the two measurement techniques show a good correlation for specimens C_0, C_{10} and $C_{0\text{-HT}}$, $C_{10\text{-HT}}$, $C_{20\text{-HT}}$. However, DIC and SG stress-strain curves for specimen C_{20} deviate from each other just after first yield point (~340MPa), where the weld metal is strain-hardening after yielding at ~210MPa. The anomaly on this curve will be discussed in section 6.5.2. The gap in C_{20} DIC data at 0.7% strain was due to a connection problem between the camera and PC that occurred during the experiment. The stress-strain curve obtained from the SG on specimen C_{10} ends at 0.8% strain because the SG detached during testing. It can be seen from Figure 6.9 that the proof stress decreases after heat treatment. Interestingly, stress-strain curves of specimens $C_{10\text{-HT}}$ and $C_{20\text{-HT}}$ are below $C_{0\text{-HT}}$.

Local stress-strain curves obtained at a distance of 10mm from the WCL

At 10mm from the WCL, strain data was only obtained from DIC. Stress-strain curves which were constructed with DIC strain data at 10mm from the WCL are given in Figure 6.10. There is a sudden change in the shape of the curves for specimens C_{10} and C_{20} at around 340 MPa where the weld metal is strain-hardening after yielding at ~210MPa. There is an anomaly (i.e. the change in slope of elastic line with increasing stress) on the curves obtained from specimens C_{10} and C_{20} and this will be discussed in section 6.5.2. For specimens $C_{0\text{-HT}}$, $C_{10\text{-HT}}$ and $C_{20\text{-HT}}$, the stress-strain properties at 10mm are very similar to the stress-strain properties at 6.5mm.

Local stress-strain curves obtained at a distance of 20mm from the WCL

The stress-strain curves obtained from SG and DIC measurements at 20mm from the WCL are given in Figure 6.11. Similar to the position of 10mm, there is again a sudden change in the shape of the curves for specimens C_{10} and C_{20} at around 340 MPa. At 20mm from the WCL the stress-strain curve of C_{10} has both elastic and plastic region, however, C_{20} is still in the elastic region and does not deform plastically. The stress-strain curve of C_{10} is very similar to B_{10} (Figure 6.6), therefore, beyond that point there is no effect of welding for specimens C_{10} and C_{20}. Heat-treated specimens $C_{0\text{-HT}}$, $C_{10\text{-HT}}$ and $C_{20\text{-HT}}$ have again demonstrated similar stress-strain behaviour as in Figure 6.9 and Figure 6.10.

The stress-strain curves obtained from the base metal (HAZ + unaffected base metal) at different positions suggest that the welding and heat treatment has a considerable influence on the material properties of the non-strained and pre-strained base metal. It was observed that the pre-strained base metal becomes softer closer to the fusion boundary after welding. Note that some of the stress-strain curves obtained from this weld-affected zone in the pre-strained base metal show some anomalies. The non-strained base metal was also observed to be affected by the welding process. The material properties of the weld and base metal were lowered after the heat treatment. Stress-strain curves obtained from the heat-treated specimens ($C_{0\text{-HT}}$, $C_{10\text{-HT}}$ and $C_{20\text{-HT}}$) at different positions in the base metal suggest that the material properties are very similar at these positions.

For better understanding of the variation in material properties, the proof stress distribution is given in Figure 6.12 which plots the variation of 0.2% proof

stress along the half-length of cross-weld specimens based on analysis of the DIC stress-strain curves and strain gauge data. In specimen C_0, the proof stress increases from a minimum of 268 MPa in the weld region to a maximum of 319 MPa at about 10mm from the WCL and then drops gradually to a steady value of 285 MPa at about 25mm from the WCL. In specimen C_{10}, the proof stress increases steadily from a minimum of 260 MPa in the weld region to a maximum of about 565 MPa at 16mm from the WCL, where it levels off. The trend in proof stress for specimen C_{20} is similar to C_{10} but in this case the material beyond 8mm did not show any yielding (since fracture already took place in the softer weld metal before the yield stress level of the material beyond 8mm was reached) and hence the proof stress could not be derived. In specimen $C_{0\text{-HT}}$, the proof stress increases from a minimum of 200 MPa in the weld region to a maximum of about 250 MPa at 7mm from the WCL and it remains almost constant beyond that point. In specimens $C_{10\text{-HT}}$ and $C_{20\text{-HT}}$, the trend in proof stress distribution is quite similar. Apart from a small increase just after the weld interface, the proof stress in the weld region and base metal is very comparable, i.e., specimens $C_{0\text{-HT}}$, $C_{10\text{-HT}}$ and $C_{20\text{-HT}}$ show almost identical yielding behaviour. The proof stresses obtained from SGs are tabulated in Figure 6.12. Results from the DIC and the SGs show a good correlation in general. However, the proof stress obtained from the SG on specimen C_0 at WCL is 290 MPa whereas the DIC gives 275 MPa. Similarly, the proof stress obtained from the SG on specimen C_{20} at 6.5mm is 70 MPa higher than DIC. Note that the SGs are on the opposite half and at the back surface of the specimen. Proof stresses obtained from the back and front SGs at 20mm away

from WCL for specimens C_0 and C_{10} are very similar, which confirms the alignment of the loading fixture and the specimen was correct.

6.4.2 Finite element modelling

6.4.2.1 Bi-material model

The local stress-strain behaviour of the middle domains (red domains) around the interface, obtained from the simulation of the tension test of a bi-material cross-weld specimen is presented in Figure 6.13. Note that stress and strain were obtained in the loading direction.

It can be clearly seen that the stress-strain behaviour of the weld material in the centre of the weld pool (domain 1) and near the interface (domain 2) is different. The weld material in weld pool, in both domains, yields at 300 MPa. After yielding, however, higher tensile stress is required closer to the weld/base metal interface to introduce the same level of strain both in the centre of the weld pool and near the interface. Similar to the weld, the stress-strain behaviour of the base metal near and away from the interface is also different. The stress-strain curves obtained from the domains between the interface and 7.625mm away from the WCL suggest that the base metal in the region of the interface (domain 3) to 5.875mm from the WCL (domain 4) undergoes plastic deformation whereas the domains beyond 5.875mm (domain 4) show only elastic behaviour. Compared to the input stress-strain curve lower axial stress is required to deform the base metal in the region where plastic deformation takes place. It is also seen that in the region between the interface and 7.625mm from the WCL the stress-strain curves have a deviation at ~300 MPa. This

deviation disappears at 7.625mm and the base metal follows the input stress-strain curve beyond that point.

For a better understanding of the stress-strain behaviour in the weld and base metal around the interface, the true stress variation across the width of the specimen, for both in the loading (σ_{yy}) and transverse (σ_{xx}) directions are mapped in Figure 6.14(a) and Figure 6.14(b), respectively. According to Figure 6.14(a), σ_{yy} is tensile through the width of the specimen. In the weld pool it is concentrated at the corners and in the mid-width slightly away from the interface. In the base metal σ_{yy} is concentrated at the edges of the specimen closer to the interface and reaches 550MPa in that region while it is approximately 330MPa in the mid-width. Figure 6.14(b) presents the distribution of stress (σ_{xx}) in the transverse direction. The weld metal near the interface is in tension whereas the base metal near the interface is in compression. The stress field disappears at the edges and increases in the mid-width. The stress adjacent to the interface approaches 195MPa in the weld side, whereas it reaches -265MPa in the base metal side. It is clearly seen from Figure 6.14(a) and Figure 6.14(b) that bi-axial stresses develop around the interface when the weld undergoes plastic deformation. The stress and total strain distribution along line AA in the base metal are plotted in Figure 6.14(c). σ_{yy}, stress in the loading direction, approaches 550 MPa near the edges of the specimen whereas in the mid-width it is about 345MPa. σ_{xx}, the stress in the transverse direction, is almost zero near the edges; however it gradually decreases to -185MPa as getting closer to mid-width. ε_{yy},

the strain in the loading direction, is 0.002 in the middle of the specimen, however, it increases abruptly towards the edges and reaches 0.0035. The average ε_{yy} is slightly higher than 0.002. ε_{xx}, strain in the transverse direction, is -0.0015 at the mid-width and increases gradually towards the edges but suddenly drops to -0.0013 from -0.0008 near the edges.

6.4.2.2 Multi-material model

It was shown that there are some anomalies on the experimental stress-strain curves which were reported in section 6.4.1.2. In order to investigate whether these anomalies are caused by a real material behaviour or are a result of experimental inadequacies, such as the use of the iso-stress assumption, true-stress versus true-strain curves in the HAZ region were examined. The effect of strain averaging along the width and the use of iso-stress on the shape of a local stress strain curve in HAZ are demonstrated in Figure 6.15 by plotting four different stress-strain curves to present the local deformation behaviour at 12.75mm away from the WCL. These curves are compared with the input stress-strain curve (see dotted black line on Figure 6.15) in the same figure. Note that the stress and the strain used to construct these curves are in the loading direction as this was the direction measured during DIC integrated tension tests. These four stress-strain curves are;

(1) "stress @ mid-width" vs. "strain @ mid-width" curve (see dashed blue line on Figure 6.15) which was constructed by the axial stress and axial strain calculated for the middle domain (black domain) at 12.75mm from the WCL. This curve

represents the original local deformation behaviour in this domain when the whole specimen is under tension.

(2) "averaged-width stress" vs. "averaged-width strain" curve (see dashed red line on Figure 6.15) which was constructed by the axial stress and strain, both averaged along the width (all black domains + the red domain in the middle) at 12.75mm from the WCL. This curve represents the original local deformation behaviour averaged over the domains lying along the width at a distance of 12.75mm from the WCL.

(3) "iso-stress" vs. "strain @ mid-width" curve (see solid blue line on Figure 6.15) ⇒ curve (1) was modified by using "iso-stress" instead of "stress @ mid-width" because experimental local-stress-strain curves can only be constructed using the "iso-stress" since the local stress can not be measured. Therefore, this curve represents one of the extremes for the experimental way of constructing the local stress-strain curve which employs local strain at a point and "iso-stress". This enables the spatially-resolved local deformation behaviour on the sample surface to be obtained, as it was used by Reynolds and Duvall [13].

(4) "iso-stress" vs. "averaged-width strain" curve (see solid red line on Figure 6.15) ⇒ curve (2) was modified by using "iso-stress" instead of "averaged-width stress" due to not being able to measure local stress. This curve represents another extreme for the experimental way of constructing the local stress-strain curve which employs averaged-strain along the width at a specific distance from WCL and "iso-stress".

The iso-stress assumption in DIC analyses means that the stress, which is used to construct the local stress-strain curves, is uniform through the specimen and is calculated by dividing the global load to the original cross-section of the specimen. Similar to that assumption, the stress averaged across the width at 24.5mm away from the WCL was considered as the "iso-stress" in the FE analyses. At 24.5mm away from the WCL and further away towards the end of the specimen the axial stress is uniform across the width and there is very small deformation in the transverse direction during the simulation.

From Figure 6.15, it can be seen that at a distance of 12.75mm from the WCL the middle of the specimen starts to yield at lower stress (see curve (1) and curve (2)). However, soon after yielding, for the same strain levels, stress at the mid-width is always higher than the stress averaged across the width. Note that both of these curves are below the input stress-strain curve (dotted black line).

The use of iso-stress instead of "averaged-width stress" does not influence the stress-strain behaviour until 0.004 true strain (see curve (2) and curve (4)). On the other hand, the use of iso-stress instead of "stress @ mid-width" considerably modifies the stress-strain behaviour (see curve (1) and curve (3)). On curve (3), the most significant modification is the "reduced-strain" trend, i.e., the change in the slope of elastic region after 350MPa. This "reduced-strain" trend on curve (3) was observed in the experimental local stress-strain curves at 10mm (in the HAZ) from the WCL for specimens C_{10} and C_{20} (Figure 6.10). Note that curve (3) employs "strain @ mid-width" whereas the experimental local stress-strain curves employ averaged-width strain. This will be discussed in detail in section 6.5.2, but it is worth

mentioning here that this conflict briefly happens because of the definition of the working space which was selected as described in section 6.2.3.

For a better understanding of the stress-strain behaviour in the unaffected base metal, the HAZ and the weld pool, true stresses in the loading and transverse directions are mapped in Figure 6.16(a) and Figure 6.16(b) respectively. Before the plastic deformation starts in the softest region, i.e. in the weld pool, the σ_{yy} distribution is almost uniform through the specimen. Once the weld yields and the size of the deformation zone starts growing progressively in the HAZ, stress is redistributed between the deformed zone and non-deformed zone. On the interface between the deformed and non-deformed zone, σ_{yy} gets larger near the edges of the specimen. The stress (σ_{yy}) concentration near the edges at different global stress levels is clearly seen in Figure 6.16(a). The onset of yielding in the weld disturbs the stress state in the transverse direction as well as the stress state in the loading direction. Just after the weld yields, the σ_{xx} distribution near the weld/HAZ interface for the multi-material model is very similar to the σ_{xx} distribution near the weld/unaffected base metal interface for the bi-material model (see Figure 6.14(b)). However, these stresses are lower in the multi-material model compared to those in the bi-material model since the strength gradient on weld/HAZ interface is less. It can be seen in Figure 6.16(b) that as the deformation zone proceeds in the HAZ, the non-deformed zone is in compression whereas the adjacent deformed zone is in tension. The compression-tension zone in Figure 6.16(b) disappears after the strongest

section of the HAZ deforms and compressive stresses remain around the HAZ/unaffected base metal interface.

The total predicted strain (ε_{yy}) distribution is also given in Figure 6.16(c). It is seen that in the sections where there is small deformation (<0.022), ε_{yy} is not uniform across the width and is concentrated near the edges of the specimen. For the regions where larger deformation (>0.022) takes place, ε_{yy} is almost uniform across the width.

In brief, Figure 6.16 clearly shows that the distribution of local stress and local strain is not uniform in the HAZ and near the interfaces (weld/HAZ and HAZ/ unaffected base metal) during the deformation. It also shows that bi-axial stresses develop especially in the HAZ as a result of the strength gradient.

It was shown in Figure 6.15 that "iso-stress assumption" and "strain-averaging across the width" of the specimen influence the local stress-strain curves. Experimentally, local stress-strain curves which were constructed with the iso-stress assumption and strain averaging across the width were used to predict the 0.2% offset proof stress along the half length of the cross-weld specimens (see Figure 6.12). In order to check the reliability of the experimental prediction of 0.2% offset proof stress distribution, numerical local stress-strain curves which are constructed with FE results by using the same experimental assumptions were employed to predict 0.2% proof stress. In Figure 6.17, 0.2% proof stress determined from the input stress-strain curves is compared with the 0.2% proof stress distributions predicted from two types of local stress-strain curves; curve (3) which is "iso-stress" vs. "strain @ mid-width" and curve (4) which is "iso-stress" vs. "averaged-width strain". It can be seen that

although the DIC experimental procedure modifies the local stress-strain curves, the effect of the use of these local stress-strain curves on 0.2% proof stress distribution is almost negligible. Particularly in the HAZ, compared to the input proof stress, curve (3) gives slightly higher proof stress (~10MPa more), whereas curve (4) gives lower proof stress (~4MPa less).

6.5 Discussion

6.5.1 Strain measurement

Three different strain measurement techniques were used in the tension tests and it was observed that DIC is in good agreement with extensometer and strain gauges (SGs). The stress-strain curves of remote-end specimens (Figure 6.6), which were constructed with the strain data measured by DIC and extensometer, are very similar even though the extensometer measures strain on one edge of the specimen whereas the DIC measures averaged surface strain on the front surface. The local stress-strain curves which were constructed with the local strain measurements by DIC and SGs at symmetrically same position (Figure 6.7) on the cross-weld specimens are also in reasonable agreement (Figure 6.8, Figure 6.9 and Figure 6.11). Some discrepancies between the stress-strain curves constructed with SG and DIC strain data can be attributed to (1) gluing and alignment of the strain gauges (2) the strain measurement positions for DIC and SG (3) DIC data sampling corresponding to the gauge length of SGs. Bonding SG to the specimen is very critical. If the bonding is not strong enough, the SG will peel off during the test (see C_{10} SG curves in Figure 6.9 and Figure 6.11). Misalignment of the strain gauge can also cause improper strain

measurements. The SGs were glued to the bottom half of the back surface whereas DIC was performed on the top half of the front surface (Figure 6.7), i.e., SG and DIC measurement positions are symmetrical with respect to the centre of the specimen. It is likely that the material properties through the thickness of the specimen may vary slightly. For example the material properties of the weld centre on the front and back surfaces are possibly different since the back surface represents the root pass whereas the front surface represents the cap pass (Figure 6.8).

6.5.2 Local stress-strain curves

Local strains were measured with DIC and SGs during the tension tests of cross-weld specimens. However, it is not possible to measure local stresses in a composite specimen during the tension test. Therefore, for the construction of local stress-strain curves, the global stress (i.e. the applied load divided by the initial cross-sectional area of the gauge section) was used instead of local stress (iso-stress assumption). Additionally, strain was smoothed by (1) using a user-defined gauge length and (2) taking the average across the width (Figure 6.2). Subsequently, local stress-strain curves were constructed with smoothed strain under iso-stress assumption. In general, these curves are very similar to ordinary stress-strain curves obtained from a homogenous tensile specimen. However, it was observed that there are some anomalies at around 340 MPa on some of the experimental curves obtained from C_{10} and C_{20} specimens (Figure 6.9, Figure 6.10 and Figure 6.11). FE analyses of bi-material and multi-material models were useful to understand why these anomalies exist on some curves, which are discussed below.

6.5.2.1 Constraint effect due to strength mismatch

The 2D bi-material model is an extreme case of strength mismatch on the weld/unaffected base metal interface. According to the input stress-strain curves the weld starts to deform at 300 MPa and base metal starts to deform at 500 MPa (Figure 6.3). In a tension test of a homogenous specimen the stress is purely axial and no stress develops in the transverse or through thickness direction in the gauge length until necking. Similarly, in the tension test of a bi-material cross-weld specimen it is expected that the soft region, i.e. the weld, yields at 300MPa and the base metal is elastically loaded until the stress reaches 500MPa. However, the local stress-strain curves in the deformed base metal in Figure 6.13 indicate that the base metal near the interface yields below 500MPa whereas the base metal far away from the interface is still elastically loaded. Unlike a typical trend in a stress-strain curve of a homogenous tensile specimen, these curves near the interface seem to follow an unusual path.

On the other hand, the local stress-strain curves near the interface in the weld material suggest that after the weld material yields at 300MPa, a higher stress is required compared to the input curve to maintain plastic deformation in the weld material near the interface (Figure 6.13). The reason for weaker base metal and stronger weld metal near the interface is the development of stresses in the transverse direction near the interface due to strength mismatch. Unlike the pure axial stress developing in a homogenous specimen during plastic deformation under tension, the stress near the interface in a cross-weld specimen is not pure axial, but it is bi-axial. It was observed in the model that in the transverse direction near the interface compressive and tensile stresses developed in the base metal and weld metal,

respectively (Figure 6.14(b)). Kim *et al* [10] explain that for under-matched strength mismatch conditions the strong base metal constrains the Poisson strains in the weld metal near the interface and this constraint creates tri-axial stresses around the interface. Rodrigues *et al* [37] suggest that these tri-axial stresses increase the material's axial strength in the soft metal and decrease the axial strength of the strong metal. This phenomenon can be explained with the equivalent stress concept. Equivalent stress is a scalar stress value that can be computed from the stress tensor and when it reaches a critical value known as the yield strength, the material starts to yield. The equivalent (von Mises, σ_v) stress for a 3D stress tensor is given by the equations:

$$\sigma_v = \frac{1}{\sqrt{2}}\sqrt{(\sigma_{xx}-\sigma_{yy})^2+(\sigma_{yy}-\sigma_{zz})^2+(\sigma_{xx}-\sigma_{zz})^2+6(\sigma_{xy}^2+\sigma_{yz}^2+\sigma_{zx}^2)} \quad (6.1)$$

$$\sigma_v = \frac{1}{\sqrt{2}}\sqrt{(\sigma_1-\sigma_2)^2+(\sigma_2-\sigma_3)^2+(\sigma_1-\sigma_3)^2} \quad (6.2)$$

where $\sigma_{xx}, \sigma_{yy}, \sigma_{zz}$ are normal stresses in the x, y and z-directions, respectively. $\sigma_{xy}, \sigma_{yz}, \sigma_{zx}$ are shear stresses and $\sigma_1, \sigma_2, \sigma_3$ are principal stresses [38]. Note that the y-direction corresponds to the loading direction. In the case of a homogenous specimen under tension, the equivalent stress is equal to σ_1. Therefore, once σ_1 reaches the level of σ_{yield}, the material starts to yield. For a 2D stress tensor, Eq. (6.1) and (6.2) become:

$$\sigma_v = \frac{1}{\sqrt{2}}\sqrt{(\sigma_{xx}-\sigma_{yy})^2+\sigma_{yy}^2+\sigma_{xx}^2+\sigma_{xy}^2} \quad (6.3)$$

$$\sigma_v = \frac{1}{\sqrt{2}}\sqrt{(\sigma_1-\sigma_2)^2+\sigma_1^2+\sigma_2^2} \quad (6.4)$$

The 2D bi-material simulation in this study showed that shear stress develops near the interface at the edges, but there is no shear stress in the middle. Therefore, normal stresses are equal to the principal stresses in the middle of the specimen. Principal stresses will be used instead of normal stresses in the further explanation of the constraint effect of strength mismatch in the middle of the specimen.

Due to the constraint effect by strength mismatch, σ_2 starts to develop around the interface after the yielding in the weld. Using Eq. (6.4) it can be estimated that compressive σ_2 stress $(-\sigma_1 < \sigma_2 < 0)$ near the interface in the base metal increases the equivalent stress and the base metal starts to deform at lower σ_2. Conversely, tensile σ_2 stress $(0 < \sigma_2 < \sigma_1)$ near the interface in the weld delays the deformation of the weld material. Note that this estimation is valid in the middle of the specimen. One should use Eq. (6.3) to estimate the equivalent stress in other regions where shear stress exists.

In the multi-material model, it was seen that bi-axial stresses also develop in the HAZ between the deformed soft region and the adjacent strong region in addition to the bi-axial stresses near the weld/HAZ interface (Figure 6.16(b)). In the HAZ the middle of the specimen yields at lower stress compared to the averaged-width; however, the stress required to continue the plastic deformation in the middle of the specimen is higher than the average-width (see curve (1) and curve (2) in Figure 6.15). This happens due to the continuous redistribution of the stresses between the deformed and non-deformed region (Figure 6.16(a & b)). The compressive stresses in the transverse direction decrease the strength in the middle of the specimen and it yields at a lower stress compared to the averaged-width. However, once the middle

of the specimen has already deformed, the adjacent deforming region in the middle of the specimen will introduce tensile stresses in the transverse direction in the deformed region and higher stress is required to continue plastic deformation compared to the averaged-width.

6.5.2.2 The effect of DIC experimental procedure

The experimental local stress-strain curves obtained from specimens C10 and C20 with DIC at 10mm and 20mm away from the WCL show some anomalies (Figure 6.9, Figure 6.10 and Figure 6.11). It was observed that these anomalies occur when the weld metal is strain-hardening after it yielded. Two of these anomalies will be discussed in this section;

Anomaly (1): The DIC derived local stress-strain curve obtained at 6.5mm away from WCL for specimen C_{20} (Figure 6.9)

Anomaly (2): The DIC derived local stress-strain curve obtained at 10mm away from the WCL for specimens C_{10} and C_{20} (Figure 6.10)

Anomaly (1)

In Figure 6.9, as mentioned in section 6.4.1.2, it was observed that the DIC derived local stress-strain curve for specimen C_{20} at 6.5mm away from the WCL follows an unusual path whereas SG derived local stress-strain curve is normal.

It was found that this anomaly arises due to the difference between these two strain measurement techniques. The DIC experimental procedure to obtain the local strains is given in Figure 6.2. It uses a user-defined parameter "k" (1,2,3,4) which determines the gauge length to calculate the local strain for each subset from the local

displacement data. In this study, "k" was selected as 3, so the strain was calculated for each subset in a 7-subset-long gauge length and the calculated strain is assigned to the middle subset in the gauge length. Moreover, the local strains are averaged along the width. On the other hand, SG, whose gauge length is less than 3-subset-long, was attached in the middle of the specimen. The working principle of SG was explained in Chapter 3. Simply, it measures the average strain in the area where it is attached by calibrating the resistance change of the wires in the gauge length as the deformation proceeds. Clearly when the data extracted from differing gauge lengths, the strain values obtained by SG and DIC do not completely agree. Therefore, DIC analysis for specimen C_{20} was repeated to obtain the strain from the similar area where SG was attached, therefore, the strain was calculated using k=1,2 and 3 (which means the gauge length is 3-,5-,7-subset-long) and was not averaged along the width. After this re-analysis, it was observed that higher k produces the anomaly on the DIC derived local stress-strain curve. The stress-strain curves constructed using SG and DIC strain data reanalysed with k=1 are in good agreement (Figure 6.18). However, it is seen that "reduced-strain" trend which was seen on numerically produced curve (3) in Figure 6.15 appears on the DIC derived local stress-strain curve even after re-analysis with k=1. The reason why SG did not show "reduced-strain" trend could not be explained. It may be possible that the transverse sensitivity of SGs, when the underlying deformation is not purely uniaxial, as explained in section 3.4.2, could lead to measurement errors.

Anomaly (2)

The experimental local stress-strain curves, which were obtained at 10mm (in the HAZ) from the WCL for specimens C_{10} and C_{20} (Figure 6.10), have shown some anomalies (i.e. "reduced-strain" trend when yielding). These experimental curves employ the "average-width strain" which means that the strain at 10mm from the WCL was averaged across the width. Note that the strain was averaged along a partial width which was included in the working space. Although these experimental curves employ "average-width strain", they resemble the numerically obtained curve (3) (in Figure 6.15) which employs "strain @ mid-width". This conflict arises due to the selection of the working space before starting the computation of the displacement vectors. The working space where the displacement vectors were calculated was defined as a rectangle which does not include the full width of the specimen but some part of the width as explained in section 6.2.3. Therefore, the axial strain distribution along the width becomes important. The axial strain (ε_{yy}) distribution along the width at a distance of 12.75mm from WCL was obtained from the multi-material model and presented in Figure 6.19. It is seen that at the global stress at which the "reduced-strain" trend was observed the strain significantly varies along the width. Therefore, it is likely to see this trend on the local stress-strain curve unless the working space includes the full width. To summarize, this "reduced-strain" trend occurred primarily because of (1) the use of global stress and (2) averaging of the strain along a partial width which was included in the working space.

The sharpness of the "reduced-strain" trend on curve (3) presented in Figure 6.15, is less pronounced compared with the experimental curves (see local stress-strain curves for specimens C_{10} and C_{20} presented in Figure 6.10)). The strength mismatch level between the weld metal and the unaffected base metal may have an influence on the sharpness of the "reduced-strain" trend. The strength mismatch level (M) can be described as the ratio of the yield strength of the weld to that of the base metal ($M = \frac{\sigma_y^{weld}}{\sigma_y^{base}}$). The strength mismatch level of the multi-material FE model, specimen C_{10} and specimen C_{20} are 0.6, 0.47 and 0.38, respectively.

6.5.2.3 Reliability of proof stress distribution

As discussed above, the experimental procedures in DIC and the constraint due to the strength mismatch significantly modifies the local stress-strain curves which are used to predict the proof stress for example at 0.2% offset (see the stress-strain curves of specimens C_{10} and C_{20} in Figure 6.10 and Figure 6.11, note that DIC averaged-strain and iso-stress were used). The numerical results showed that although the local stress-strain curves are altered by some means, the distribution of proof stress predicted from these curves is very similar to the distribution of input proof stress along the half length of the specimen (Figure 6.17). For the cross-weld specimens in which the material properties are similar to the properties in multi-material model, i.e. material properties do not change abruptly between the weld, the HAZ and the unaffected base metal, it is likely to have a reliable proof stress distribution. However, in a case similar to the bi-material model in which the material

properties abruptly change on the weld/base metal interface, the proof stress may not be very reliable near the interface since the tri-axial stresses may significantly decrease or increase the strength of the material in the loading direction. As a result, in order to check the reliability of the proof stress distribution it is better to understand the tri-axial stresses developing due to the constraint of strength mismatch.

The multi-material model can represent the specimen C_{10} because for both the unaffected base metal undergoes plastic deformation under tension. However, it can not represent specimen C_{20} very well because the base metal beyond ~10mm from the WCL in specimen C_{20} did not deform when the specimen was ruptured from the weld as was mentioned in section 6.4.1.2. For that reason, the local stress-strain curves beyond 6.5mm from WCL were not included for the prediction of the 0.2% proof stress in specimen C_{20}.

6.5.3 Effects of manufacturing steps on tensile properties

The global and local tensile properties of the remote-end specimens and cross-weld specimens were obtained through tension tests using three strain measurement techniques (DIC, SG and extensometer). The local stress-strain curves at different positions from the WCL (at the weld centre, 6.5mm, 10mm and 20mm away from the WCL) are presented in Figures 6.9-6.12 for all cross-weld specimens. The 0.2% proof strength distribution on the cross-weld specimens are also presented in Figure 6.12. In addition, the global tensile properties of the remote-end and cross-weld specimens are given in Table 6.1. The variation of the tensile properties after each manufacturing

step (pre-straining, welding and heat treatment) will be discussed in this section using relevant microstructures and hardness measurements from Chapter 5.

6.5.3.1 Pre-straining

Pre-straining has a remarkable effect on the strength and ductility of the parent material and cross-weld specimens. The 0.2% proof strength of the parent specimens B_0, B_{10} and B_{20} are 295MPa, 557MPa and 689MPa, respectively (Table 6.1). The increase in the strength is due to the accumulation of plastic strain in the material after pre-straining [39]. The accumulated plastic strain after prestraining can be qualitatively determined by a hardness measurement. The hardness values of the non-strained, 10% pre-strained and 20% prestrained parent material are 154, 218 and 251 H_V, respectively (Figure 5.13). On the other hand, the ductility of the parent specimen decreases with pre-straining. The engineering strain at failure of specimens B_0, B_{10} and B_{20} is 62%, 39% and 25%, respectively (Table 6.1). The corresponding true strain values at failure, calculated using the relation $\varepsilon = \ln(1+e)$, are 48%, 32% and 22%, respectively. It can be seen that the true strain at failure drops proportionally to the increase in pre-straining. Note that 316H austenitic stainless steel still has some ductility after 20% prestraining.

Pre-straining has an influence on the fracture behaviour of the cross-weld specimens. The failure behavior of specimens C_0, C_{10} and C_{20} will be explained using the overall extension recorded from the cross-head displacement, since an extensometer was not used in the tests of these specimens. The tensile test limits for specimens C_0, C_{10} and C_{20} were set to 15mm overall extension. C_0 did not fail,

whereas C_{10} and C_{20} ruptured in the weld metal correspondingly at 9.2mm and 7.3mm extension (Table 6.1). From the tension tests, the global ultimate tensile stress (UTS) for specimens C_{10} and C_{20} was found to be 598MPa and 580MPa, respectively (Table 6.1). In both specimens, yielding started in the weaker weld metal. When specimen C_{10} reached its global UTS (598MPa), the base material of specimen C_{10} had already yielded at ~560MPa. However, when specimen C_{20} reached its global UTS (580MPa), the base material of specimen C_{20} had not yielded because the 0.2% offset proof stress of B_{20} suggests that it yields at ~589MPa. Therefore, as expected, the ductility of the cross-weld specimen was found to decrease as the strength of the parent material (i.e. the amount of pre-straining) increases.

6.5.3.2 Welding

As mentioned in Chapter 4, the tubes A_0, A_{10} and A_{20} were produced by welding two corresponding halves of the plain tube, 10% pre-strained tube and 20% pre-strained tube, respectively. As-welded hardness profiles across the weld are shown in Figure 5.13. The effect of welding on 0.2% proof stress variation along the half length of the cross-weld specimens C_0, C_{10} and C_{20} which were extracted from the tubes A_0, A_{10} and A_{20}, is also shown in Figure 6.12.

AISI 316L was used as a weld filler material and the welding parameters were kept the same when the tubes A_0, A_{10} and A_{20} were welded. It was found that the 0.2% proof stress in the weld is between 260-280MPa and is similar for specimens C_0, C_{10} and C_{20}. It was also observed that the hardness of the weld in all three tubes is the same (150 H_V).

The slight increase in proof stress (Figure 6.12) and hardness (Figure 5.13) of specimen C_0, in the base metal between 5 and 25mm from the WCL is associated with hardening during the welding process. The hardening in the base metal near the fusion boundary was reported in the thermo-mechanical welding simulations of the stainless steels [40, 41]. The hardening response of this stainless steel tube during a welding thermo-mechanical cycle is very complicated because of the wide range of imposed temperature, strain rate and strain range and because of the potential recovery, recrystallization, creep and visco-plastic effects at high temperatures [40]. Smith *et al* [40] have developed a numerical model for the accurate prediction of the weld residual stresses in 3-pass groove welds of a 316L stainless steel plate. In their simulation, the material model was based on a thermo-mechanical hardening behaviour which considers the cyclic strain hardening and annealing phenomena. They observed that plastic strain accumulation occurs in the base metal adjacent to the weld bead after each weld thermo-mechanical cycle. Their observation was confirmed by spatially resolved proof stress data on cross-weld samples cut from each weld pass using ESPI (electron speckle pattern interferometry) integrated tension tests [5]. They measured 4-6.5% plastic strain in the heat-affected zones of different cross-weld samples. Similarly, Shan *et al* [41] has developed a 3D thermo-mechanical model of a single-bead-on-plate weld (316L stainless steel) and reported accumulation of 4-8% plastic strain near the weld bead in the base metal due to welding.

The effect of welding onto plastically strained materials in terms of hardness and 0.2% proof stress can be seen in Figure 5.13 and Figure 6.12 in this chapter,

respectively. There is a marked drop in hardness and proof stress for the pre-strained and welded samples approaching the weld from about 16mm away from the WCL. This is caused by the welding process. Base metal near the weld was heated to temperatures where dislocation annealing mechanisms are known to take place. The temperature profiles recorded during the welding of plain tube is given in Figure 4.2. The peak temperatures reached 800°C, 550°C and 400°C at 9, 14 and 19mm away from the WCL, respectively. It is known that the annealing temperature of a metal can be lowered by increasing the amount of cold work [42]. It was observed that the grain size increases from 25μm to 45μm in a 1mm long zone near the fusion boundary (Figure 5.8). The LAB boundaries which were presented in Figure 5.9 also show that the dislocation structures disappear in a region ~1.5mm from the WCL. These findings suggest that the pre-strained base metal adjacent to weld (1-1.5mm from the fusion boundary) was annealed due to the heat produced by welding. The gradual decrease in proof stress towards the fusion boundary may be explained with partial softening (recovery) i.e. the gradual decrease in the existing dislocation density with the effect of the heat during welding. Figure 7.11(d) and Figure 7.18 confirm that dislocation density gradually decreases from 16mm towards the fusion boundary.

6.5.3.3 Heat treatment

Heat treatment at 1050°C with a soaking time of 15mins has a significant influence on the mechanical properties of the parent and cross-weld specimens. The 0.2% proof strength of the remote-end specimens dramatically decreases after heat treatment. The 0.2% proof stress of specimens $B_{0\text{-}HT}$, $B_{10\text{-}HT}$ and $B_{20\text{-}HT}$ are 249, 218 and

225MPa, respectively (Table 6.1). The ultimate tensile strength (UTS) of specimen $B_{0\text{-}HT}$ slightly increases whereas the UTS of the pre-strained and heat treated specimens ($B_{10\text{-}HT}$ and $B_{20\text{-}HT}$) decrease as the amount of pre-straining increases (Table 6.1). Surprisingly, the stress-strain curves of the specimens $B_{10\text{-}HT}$ and $B_{20\text{-}HT}$ are below the stress-strain curve of specimen $B_{0\text{-}HT}$. This is due to the Hall-Petch grain size effect [43, 44]. Prior to the heat treatment, the grain size of both non-strained and pre-strained material is ~30μm in the straining direction. However, after the heat treatment the grain size of the plain material is 27.8μm, whereas the grain size of the pre-strained materials was almost doubled (>50 microns) (Table 5.1). Therefore, a coarser grain size resulted in a lower strength. Mahalingam *et al* [45] have observed a similar effect of heat treatment on grain size. They studied the effect of heat treatment at 1150°C for 0.5 hour on the grain size of plain and prestrained 316H material with 112 microns initial grain size and observed that the grain size of 316H plain material is smaller than the grain sizes of heat treated 10-20% prestrained material after the heat treatment. On the other hand, ductility is not affected after the heat treatment if the material is not pre-strained. However, the pre-strained material recovers its loss in ductility due to pre-straining (Table 6.1).

Heat treatment also alters the mechanical properties of cross-weld specimens. The proof stress of the weld metal drops by 60MPa after heat treatment. Austenitic stainless steel welds contain unstable delta ferrite which prevents hot-cracking during solidification. Similarly, AISI 316L contains a small amount of delta-ferrite (~5%) (Figure 5.4 and Figure 5.5). However, since delta-ferrite is an unstable phase, it partially transforms to austenite at 1050°C as explained in Chapter 5. Decreasing

ferrite content is generally known to result in a decrease in room-temperature strength [31].

The decrease in 0.2% proof stress of the base metal in specimens $C_{0\text{-}HT}$, $C_{10\text{-}HT}$ and $C_{20\text{-}HT}$ is similar to the decrease in the proof stress of parent specimens $B_{0\text{-}HT}$, $B_{10\text{-}HT}$ and $B_{20\text{-}HT}$. The hardness profiles on heat-treated cross-weld samples confirm the proof stress distribution on cross-welds $C_{0\text{-}HT}$, $C_{10\text{-}HT}$ and $C_{20\text{-}HT}$. The global ultimate tensile strength of the cross-weld specimens is also lowered after the heat treatment (Table 6.1). Additionally, the tensile extension of the specimens $C_{0\text{-}HT}$, $C_{10\text{-}HT}$ and $C_{20\text{-}HT}$ is given in Table 6.1. It was observed that heat-treated cross-weld specimens are more ductile than the cross-weld specimens without heat treatment.

It can be concluded that the effect of pre-straining on the mechanical properties has been eradicated by the heat treatment process.

6.6 Conclusion

- Tension tests of remote-end specimens and cross-weld specimens were successfully performed with a proper alignment of the test specimen in the grips.

- The strain measurement during the tension tests of the non-heat treated and heat treated remote-end specimens was done with extensometer and DIC. Although these two techniques measure the strain at different places, a good agreement was found between them.

- The tension tests of the remote-end specimens (B_n) showed that prior to the heat treatment 0.2% proof strength and the UTS of the plain tube material increases with the prestraining, but the ductility decreases. After the heat treatment the loss in

ductility is recovered and the proof strength and UTS decrease. It was found that after the heat treatment the proof strength and UTS of tube material which had been prestrained dropped below that of the plain material, and this was related to the Hall-Petch relation.

- The strain measurement during the tension tests of the non-heat treated and heat treated cross-weld specimens was done with SG and DIC. Overall a good agreement was found between these two techniques although the position of the measurements is different.

- The local and global mechanical properties of the non-heat treated and heat treated cross-weld specimens were obtained through the DIC integrated tension tests.

- The local stress-strain curves were constructed using the DIC local strain data and the global stress. Anomalies were observed at around 340MPa on the local stress-strain curves of cross-weld specimens (C_{10} and C_{20}) with prestrained base metal whereas the local stress-strain curves obtained from remaining cross-weld specimens (C_0, $C_{0\text{-HT}}$, $C_{10\text{-HT}}$, $C_{20\text{-HT}}$) are normal. To understand whether these anomalies are a real material effect or produced due to the DIC experimental procedure, the tension test of a cross-weld specimen was simulated using a bi-material and a multi-material model.

- The bi-material model showed that bi-axial stresses develop around the interface between the soft weld metal and strong base metal. It was observed that the base metal near the interface yields at an axial stress lower than the yield stress although the base metal away from the interface does not yield at the same stress level. The distribution of stress in the transverse direction showed that compressive

and tensile stresses develop in the base and weld metal near the interface, respectively.

- A multi-material model with continuous material properties in the HAZ was a more realistic approach compared with the bi-material model. The local yield strength along the HAZ linearly decreases from 500MPa (the yield strength of the base metal) to 300MPa (the yield strength of the weld metal). It was observed that bi-axial stresses also develop progressively in the HAZ between the already deformed and adjacent deforming region. The bi-axial stresses in the multi-material model are less than those in the bi-material model, but they influence the local stress-strain curves, which were constructed using the local axial strain and global axial stress, in the HAZ. It was found that the use of global axial stress to construct the local stress-strain curve in the HAZ where the bi-axial stresses progressively develop produces a "reduced-strain" anomaly.

- Another anomaly can arise due to the selection of the user defined gauge length (k=1, 2, 3, 4) for the computation of local strain from the DIC calculated local displacement. The user defined gauge length was initially selected as "k=3" for the strain computation. However, it was seen that this selection influenced the local stress-strain curve at 6.5mm from the WCL on the cross-weld specimen C_{20}. For this specimen the strain was recomputed using "k=1". It was found that the anomaly disappears and the DIC and SG derived stress-strain curves are in good agreement.

- It can be concluded that the anomalies on the local stress-strain curves are combination of real material effect and the experimental procedure. The strength variation along the specimen causes localization of stress and strain during

deformation, and the DIC derived local stress-strain curves are highly sensitive to localized deformation. The selection of the user-defined gauge length and the strain averaging can severely affect the local stress-strain curves depending on the axial strain distribution in the material. The use of global stress is another experimental factor contributing to the anomalies in the case of using it with strain in the middle or strain averaged in partial width.

- The 0.2% proof strength variation across the weld was determined on non-heat treated and heat treated cross-weld specimens using the DIC derived local stress-strain curves. For the non-heat treated specimens, it was found that welding had a marked effect on the 0.2% proof strength of the base metal within the 25mm of the WCL. Evidence of strain hardening due to the constraint and weld thermomechanical cycles was observed in the plain tube, and evidence of softening was seen in the 10% and 20% pre-strained tubes. On the other hand, it was observed that the effect of prestraining was removed and the proof strength along the specimen was almost homogenized after the heat treatment at 1050°C for 15min.

- The determination of the 0.2% proof strength on the cross-welds with a prestrained base metal was verified using the multi-material FE model. Numerical results showed that the anomalies appearing due to the strength mismatch level of 0.6 and the experimental procedure produce 4-10MPa difference between the input proof strength and predicted proof strength.

6.7 References

[1] Kamaya M, Wilkinson AJ, Titchmarsh JM. Quantification of plastic strain of stainless steel and nickel alloy by electron backscatter diffraction. Acta Materialia 2006;54:539.

[2] Willis M, McDonaugh-Smith A, Hales R. Prestrain effects on creep ductility of a 316 stainless steel light forging. International Journal of Pressure Vessels and Piping 1999;76:355.

[3] ASME Section I, ASME Boiler and Pressure Vessel Code, Section I: Rules for Construction of Power Boilers. New York, USA: ASME, 2010.

[4] Spindler M. Effects of plastic strain and heat treatment on microstructure and properties of 316 stainless steel tubing (Personal communication). 2008.

[5] Turski M, Smith MC, Bouchard PJ, Edwards L, Withers PJ. Spatially Resolved Materials Property Data From a Uniaxial Cross-Weld Tensile Test. Journal of Pressure Vessel Technology 2009;131:061406.

[6] Lampman S. Weld integrity and performance: ASM International, 1997.

[7] R6 Revision 4 Assessment of the Integrity of Structures containing Defects. Gloucester, UK: British Energy Generation Limited, 2009.

[8] R5 Issue 3 Assessment Procedure for High Temperature Response of Structures. Gloucester, UK: British Energy Generation Limited, 2003.

[9] Kocak M. Structural integrity of welded structures: Process - Property - Performance (3P) relationship. 63rd Annual Assembly & International Conference of the International Institute of Welding 11-17 July 2010. Istanbul, Turkey, 2010.

[10] Kim Y-J, Oh C-S. Finite element limit analyses of under-matched tensile specimens. Engineering Fracture Mechanics 2006;73:1362.

[11] Çam G, Erim S, Yeni Ç, Kocak M. Determination of mechanical and fracture properties of laser beam welded steel joint. Welding Journal 1999;78 (6):193.

[12] Malow TR, Koch CC, Miraglia PQ, Murty KL. Compressive mechanical behavior of nanocrystalline Fe investigated with an automated ball indentation technique. Materials Science and Engineering A 1998;252:36.

[13] Reynolds AP, Duvall F. Digital image correlation for determination of weld and base metal constitutive behavior. Welding Research Supplement 1999:355.

[14] Sutton MA, Orteu J-J, Schreier HW. Image Correlation for Shape, Motion and Deformation Measurements: Basic Concepts, Theory and Applications. New York, USA: Springer, 2009.

[15] Lockwood WD, Tomaz B, Reynolds AP. Mechanical response of friction stir welded AA2024: experiment and modeling. Materials Science and Engineering A 2002;323:348.

[16] Lockwood WD, Reynolds AP. Simulation of the global response of a friction stir weld using local constitutive behavior. Materials Science and Engineering A 2003;339:35.

[17] Sutton MA, Yang B, Reynolds AP, Yan J. Banded microstructure in 2024-T351 and 2524-T351 aluminum friction stir welds: Part II. Mechanical characterization. Materials Science and Engineering A 2004;364:66.

[18] Liu S, Chao YJ. Determination of global mechanical response of friction stir welded plates using local constitutive properties. Modelling and Simulation in Materials Science and Engineering 2005;13:1.

[19] Genevois C, Deschamps A, Vacher P. Comparative study on local and global mechanical properties of 2024 T351, 2024 T6 and 5251 O friction stir welds. Materials Science and Engineering: A 2006;415:162.

[20] Hatamleh O. Effects of peening on mechanical properties in friction stir welded 2195 aluminum alloy joints. Materials Science and Engineering: A 2008;492:168.

[21] Zadpoor A, Sinke J, Benedictus R. The effects of friction stir welding on the mechanical properties and microstructure of 7000 series aluminium tailor-welded blanks. International Journal of Material Forming 2008;1:1311.

[22] Brown R, Tang W, Reynolds AP. Multi-pass friction stir welding in alloy 7050-T7451: Effects on weld response variables and on weld properties. Materials Science and Engineering: A 2009;513-514:115.

[23] Hatamleh O, Mishra RS, Oliveras O. Peening effects on mechanical properties in friction stir welded AA 2195 at elevated and cryogenic temperatures. Materials & Design 2009;30:3165.

[24] Sutton M, Yan J, Avril S, Pierron F, Adeeb S. Identification of heterogeneous constitutive parameters in a welded specimen: Uniform Stress and Virtual Fields Methods for material property estimation. Experimental Mechanics 2008;48:451.

[25] Sierra G, Wattrisse B, Bordreuil C. Structural analysis of steel to aluminum welded overlap joint by digital image correlation. Experimental Mechanics 2008;48:213.

[26] Kartal M, Molak RM, Turski M, Gungor S, Fitzpatrick ME, Edwards L. Determination of weld metal mechanical properties utilising novel tensile testing methods. Applied Mechanics and Materials 2007;7-8:127.

[27] Acar MO, Gungor S, Ganguly S, Bouchard PJ, Fitzpatrick ME. Variation of mechanical properties in a multi-pass weld measured using digital image correlation. Society of Experimental Mechanics (SEM) Annual Conference Proceeding 2009:288.

[28] Acar MO, Gungor S, Bouchard PJ, Fitzpatrick ME. Effect of prior cold-work on the mechanical properties of weldments. Society of Experimental Mechanics (SEM) Annual Conference Proceeding 2010:283.

[29] Adeeb S, Horsley D, Yan J, Sutton MA, Reynolds AP. Local stress-strain response of an axial X100 girth weld under tensile loading using digital image correlation. ASME Conference Proceedings 2006;2006:339.

[30] Molak RM, Paradowski K, Brynk T, Ciupinski L, Pakiela Z, Kurzydlowski KJ. Measurement of mechanical properties in a 316L stainless steel welded joint. International Journal of Pressure Vessels and Piping 2009;86:43.

[31] Boyce B, Reu P, Robino C. The constitutive behavior of laser welds in 304L stainless steel determined by digital image correlation. Metallurgical and Materials Transactions A 2006;37:2481.

[32] Robino CV, Boyce BL. Constitutive properties of dissimilar metal laser welds. Trends in Welding Research 2008 (ASM International) 2009:610.

[33] Christ BW, Swanson SR. Alignment problems in the tensile test. Journal of Testing and Evaluation (JTE) 1976;4:405.

[34] Gray TGF, McCombe A. Influence of specimen dimension and grip in tensile testing steel to EN 10 002. Ironmaking and Steelmaking 1992;19:402.

[35] LaVision. DaVis 7.2 Data Acquisition and Visualization Software.

[36] ABAQUS Standard/User's Manual, Version 6.7.: Dassault Systemes 2007.

[37] Rodrigues DM, Menezes LF, Loureiro A, Fernandes JV. Numerical study of the plastic behaviour in tension of welds in high strength steels. International Journal of Plasticity 2004;20:1.

[38] Dieter GE, Bacon D. Mechanical Metallurgy: McGraw Hill Book Co., 1988.

[39] Smith DJ. The influence of prior loading on structural integrity. Comprehensive structural integrity London: Elsevier, 2003.

[40] Smith MC, Bouchard PJ, Turski M, Edwards L, Dennis RJ. Accurate prediction of residual stress in stainless steel welds. 2011 (accepted by Computational Material Science but not published yet).

[41] Shan X, Davies CM, Wangsdan T, O'Dowd NP, Nikbin KM. Thermo-mechanical modelling of a single-bead-on-plate weld using the finite element method. International Journal of Pressure Vessels and Piping 2009;86:110.

[42] Marshall P. Austenitic Stainless Steels: Microstructure and Mechanical Properties: Elsevier Applied Science Publishers, 1984.

[43] Hall EO, Sylwestrowicz W. The deformation and ageing of mild steel. Proceedings of the Physical Society. Section B 1951;64:747.

[44] Petch NJ. The cleavage strength of polycrystals. J. Iron Steel Inst 1953;25:174.

[45] Mahalingam S, Flewitt P, Knott J. Effect of pre-strain on grain size distributions in 316H austenitic stainless steel. Journal of Materials Science 2011:1.

6.8 Tables & Figures

Specimen	0.2% Proof Stress (MPa)	UTS(MPa)	Failure strain (%)	Extension (mm)
B_0	295	635	62	33.2
B_{10}	557	681	39	20.7
B_{20}	689	738	25	14
$B_{0\text{-HT}}$	249	655	63	37
$B_{10\text{-HT}}$	218	615	65	38.9
$B_{20\text{-HT}}$	225	565	61	36.7
C_0	265	> 598	-	> 15
C_{10}	265	598	-	9.2
C_{20}	265	580	-	7.3
$C_{0\text{-HT}}$	240	550	36	22.3
$C_{10\text{-HT}}$	211	525	40	25.5
$C_{20\text{-HT}}$	215	521	38	23.2

Table 6.1 0.2% offset proof stress, ultimate tensile stress (UTS), failure strain and extension for parent and cross-weld specimens. Note that failure strain which was obtained from extensometer is the strain when the specimen ruptured and extension is the cross-head displacement. For cross-weld specimens, proof stress and UTS are the global values. (All values of stress and strain are engineering stress and strain)

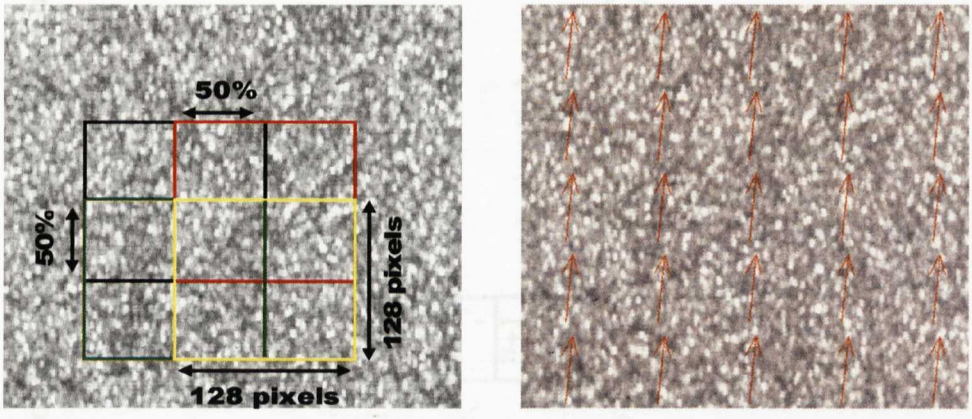

Figure 6.1 Reference image and the subsets used for the calculations (left) and the displacement vectors on the image of the deformed surface (right).

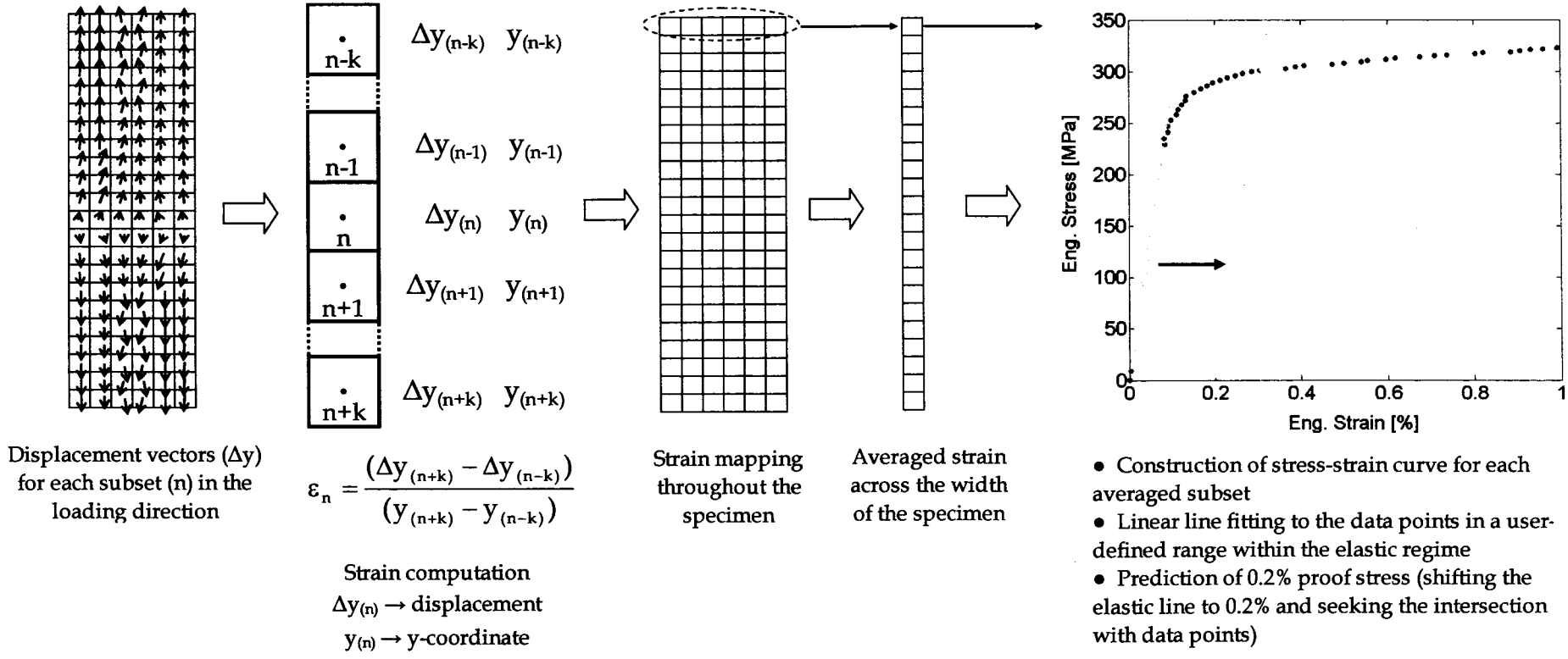

Displacement vectors (Δy) for each subset (n) in the loading direction

$$\varepsilon_n = \frac{(\Delta y_{(n+k)} - \Delta y_{(n-k)})}{(y_{(n+k)} - y_{(n-k)})}$$

Strain computation
$\Delta y_{(n)} \rightarrow$ displacement
$y_{(n)} \rightarrow$ y-coordinate

Strain mapping throughout the specimen

Averaged strain across the width of the specimen

- Construction of stress-strain curve for each averaged subset
- Linear line fitting to the data points in a user-defined range within the elastic regime
- Prediction of 0.2% proof stress (shifting the elastic line to 0.2% and seeking the intersection with data points)

Figure 6.2 Flow chart for the determination of the proof stress distribution from DIC displacement measurements with Matlab scripts.

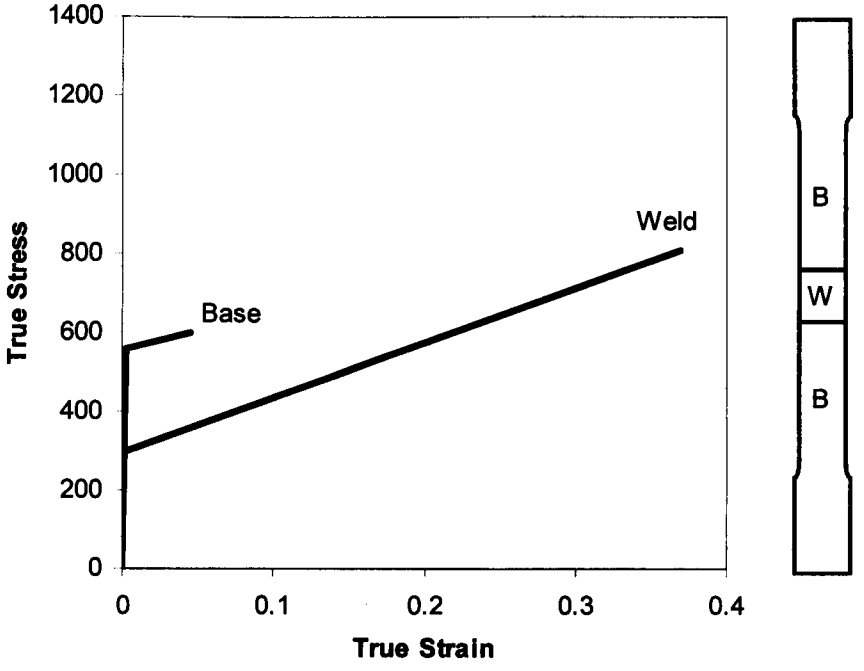

Figure 6.3 Material properties input for bi-material model.

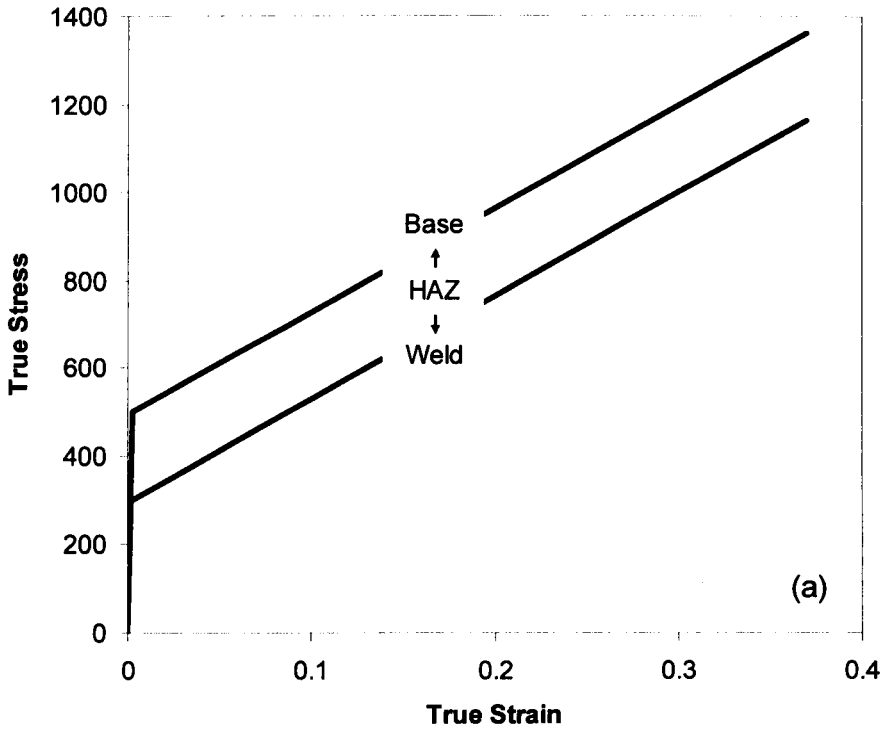

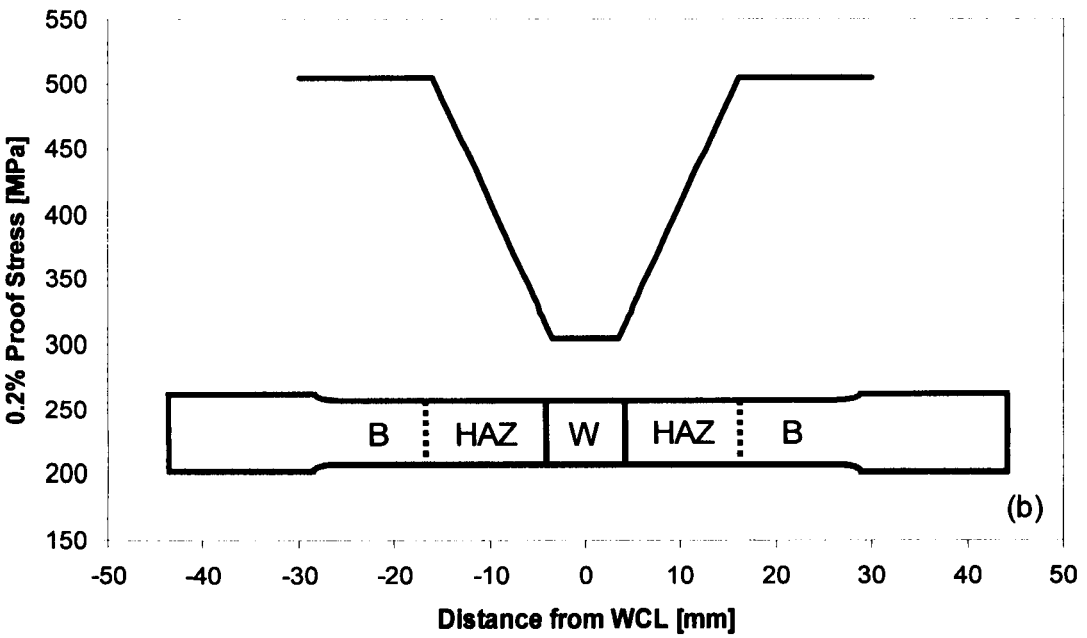

Figure 6.4 Material properties input for multi-material model. (a) Input stress-strain curves (b) Input 0.2% proof stress distribution along the specimen. Note that material properties in HAZ change continuously and there is no interface between unaffected base metal and HAZ.

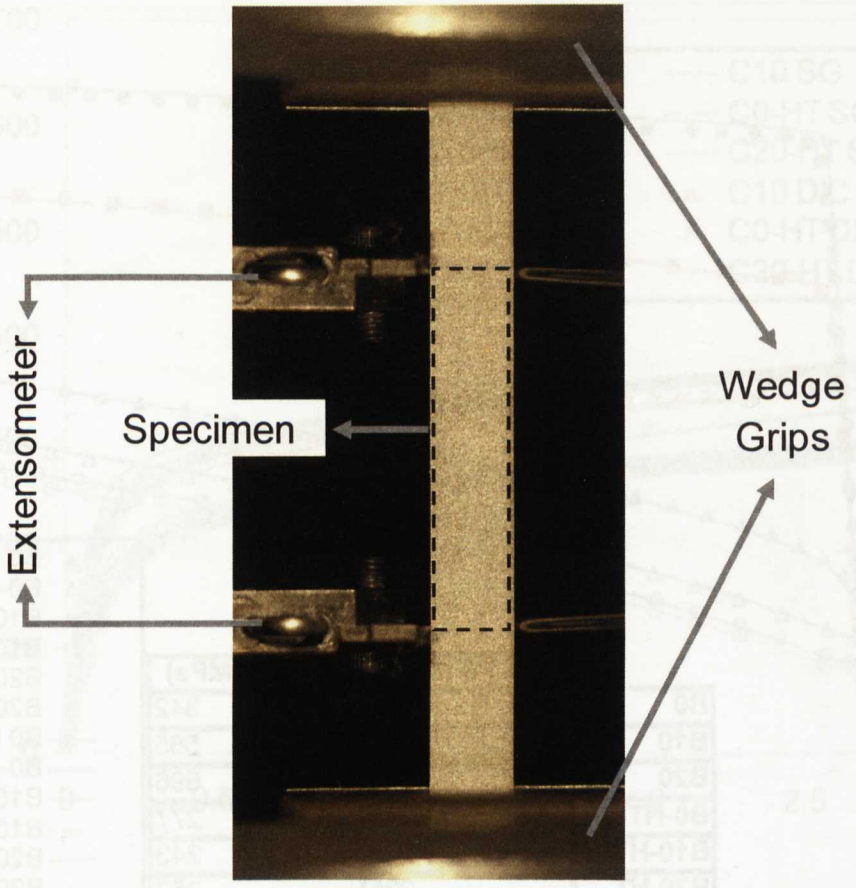

Figure 6.5 Remote-end specimen is positioned in wedge grips. A side extensometer is attached to the specimen and DIC analysis is performed in the dashed area.

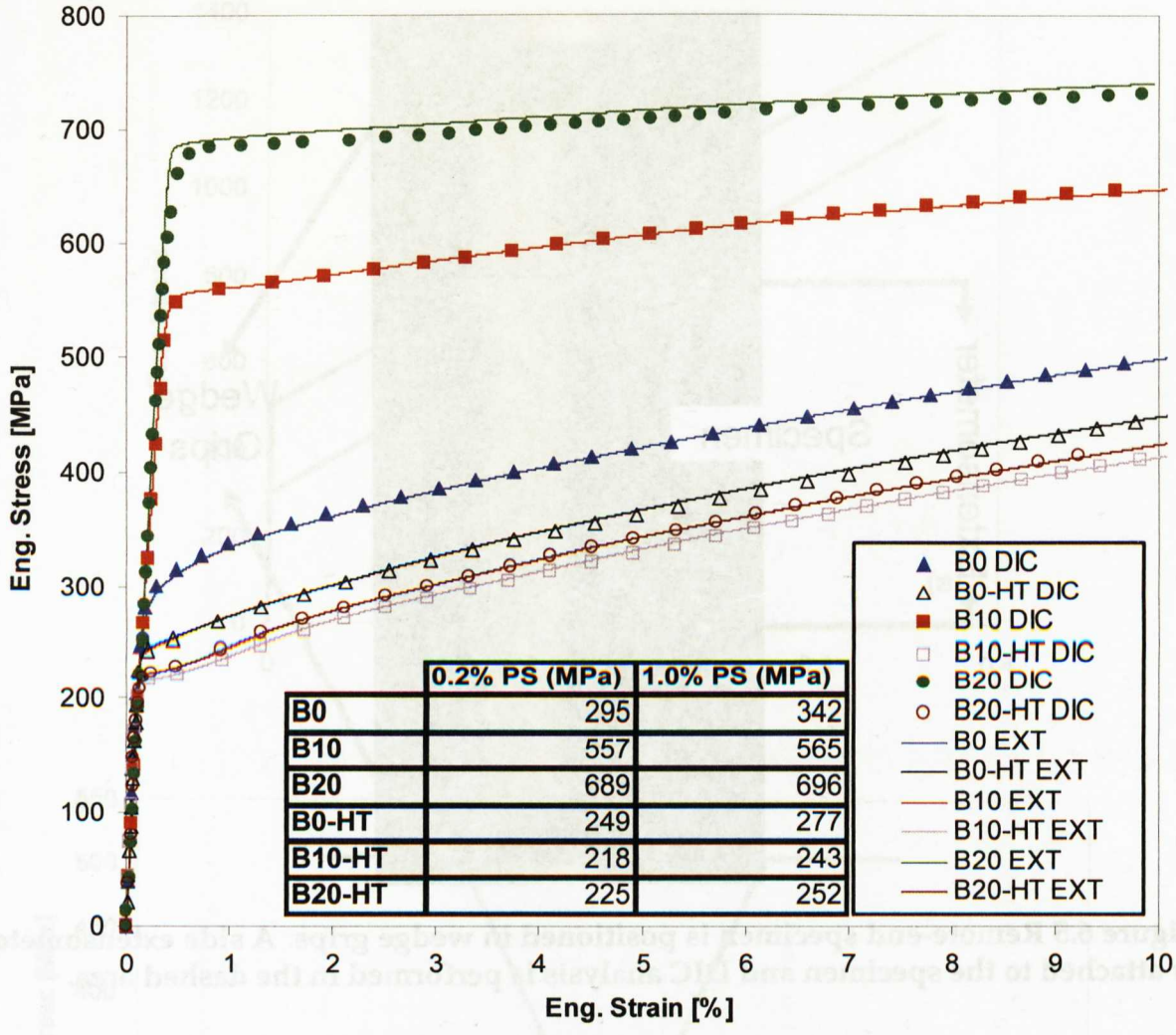

	0.2% PS (MPa)	1.0% PS (MPa)
B0	295	342
B10	557	565
B20	689	696
B0-HT	249	277
B10-HT	218	243
B20-HT	225	252

Figure 6.6 Engineering stress-strain curves obtained from the tension tests of as-received and heat treated remote-end specimens. DIC and extensometer (EXT) results are compared. 0.2% and 1% proof stress were also tabulated.

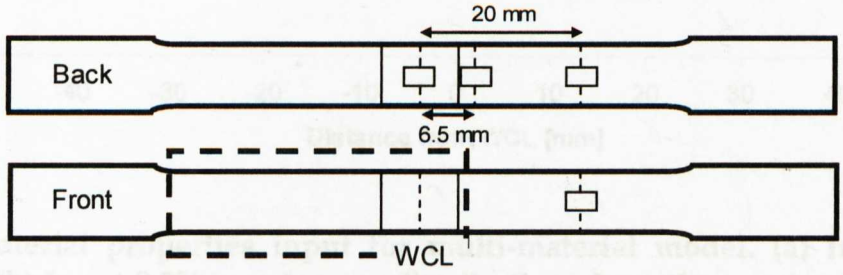

Figure 6.7 Positions of SGs on the back and front surfaces of cross-weld specimens.

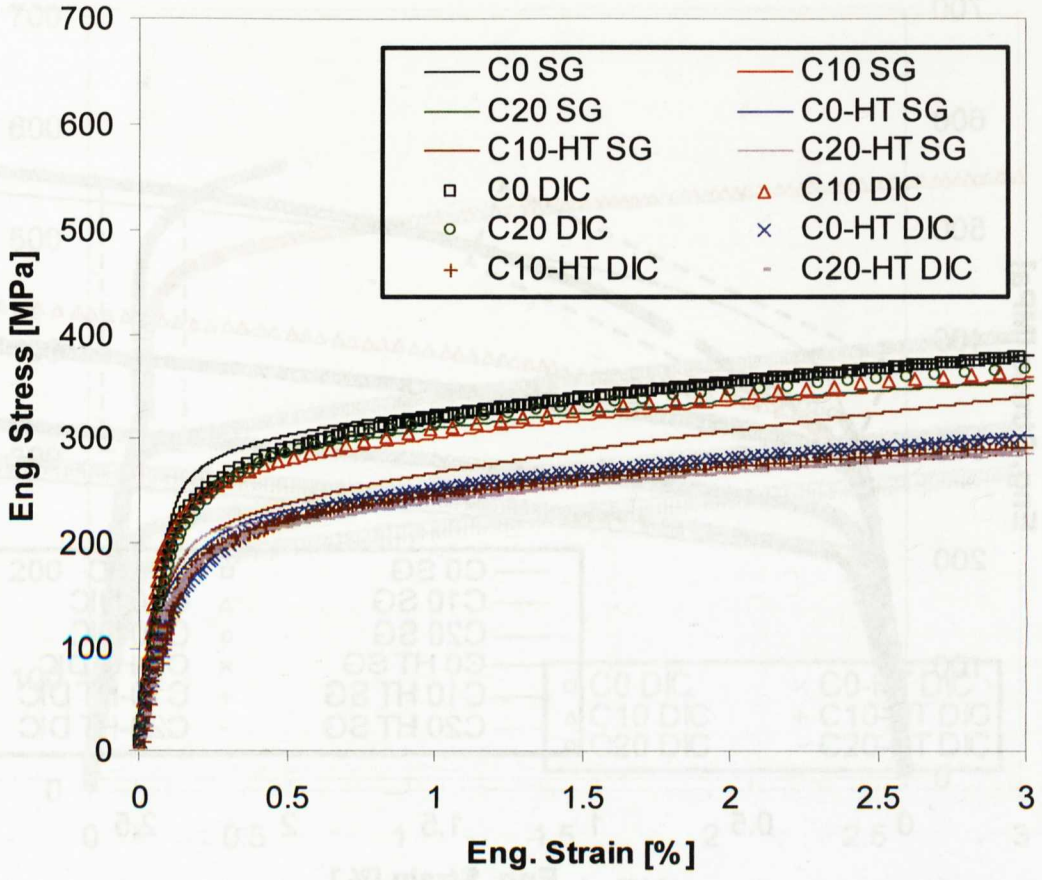

Figure 6.8 Stress-strain data measured using strain gauges (SG) and DIC at the weld centre of cross-weld specimens.

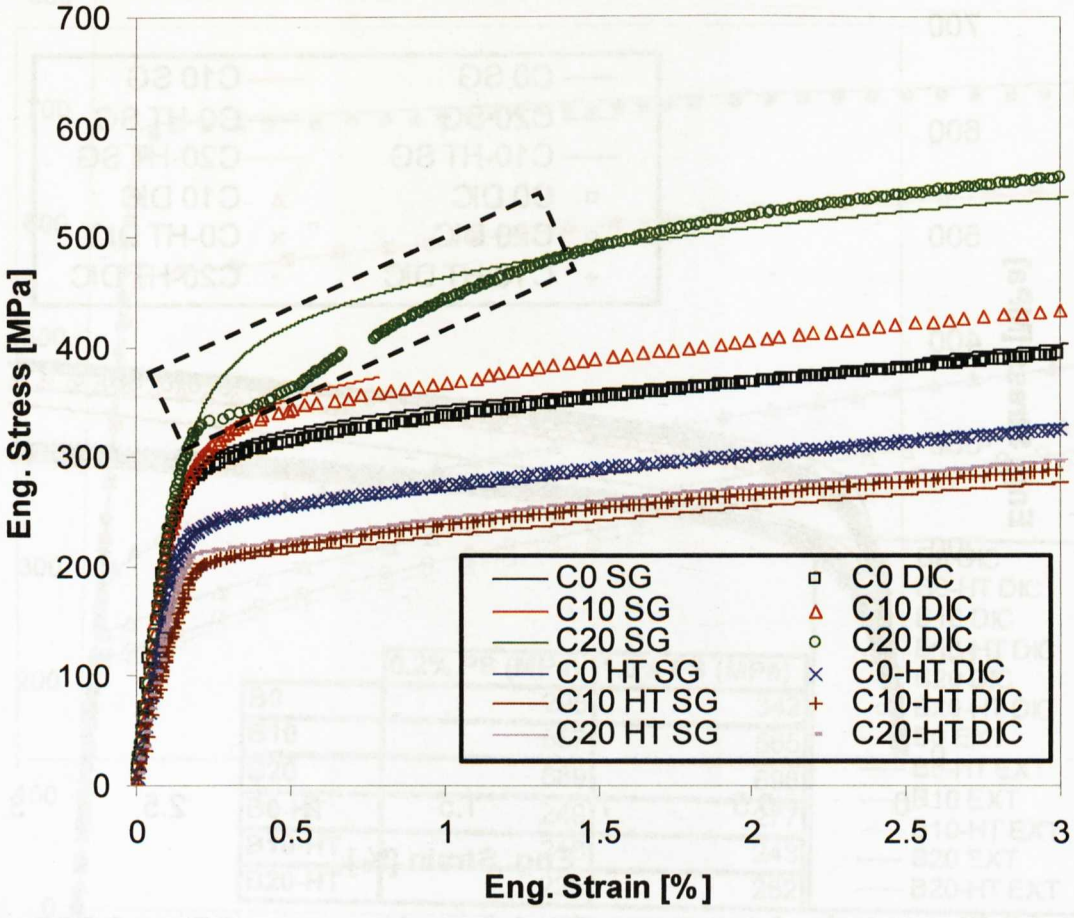

Figure 6.9 Stress-strain data measured using SG and DIC at 6.5mm from the WCL of cross-weld specimens.

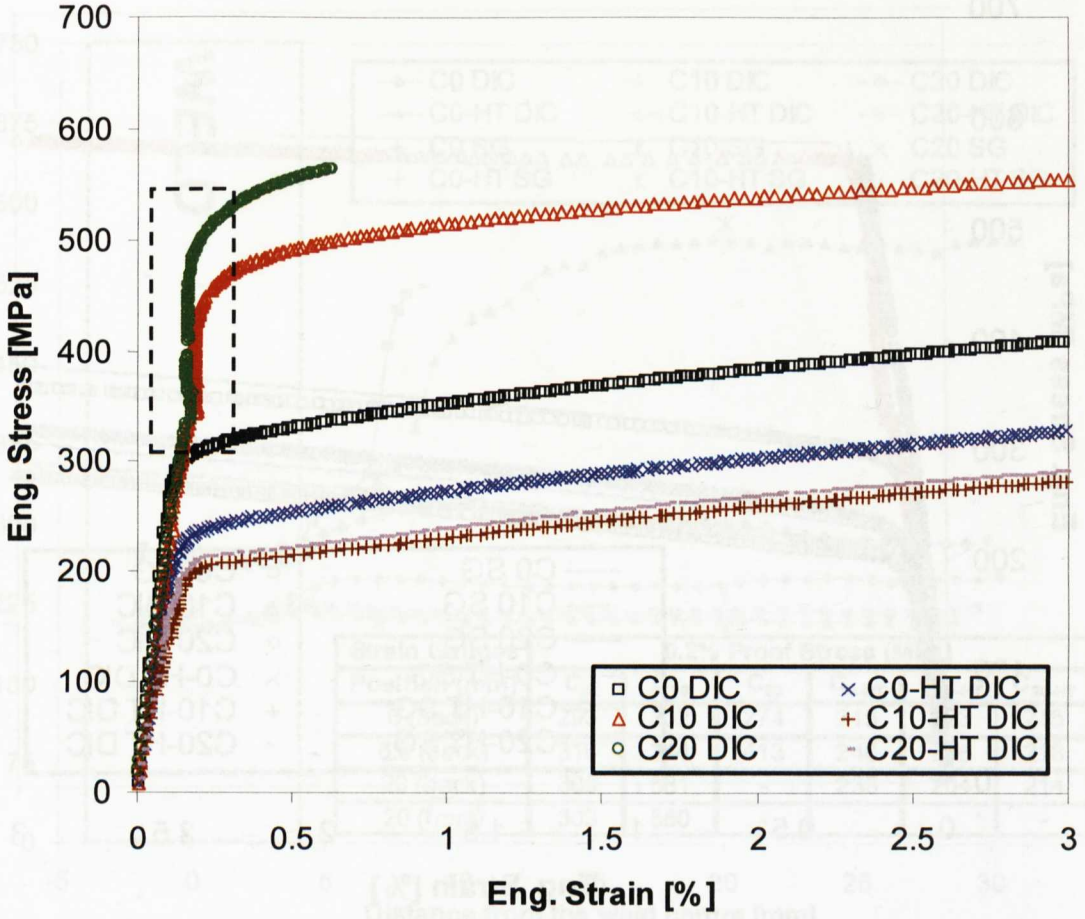

Figure 6.10 Stress-strain data measured using DIC at 10mm from the WCL of cross-weld specimens.

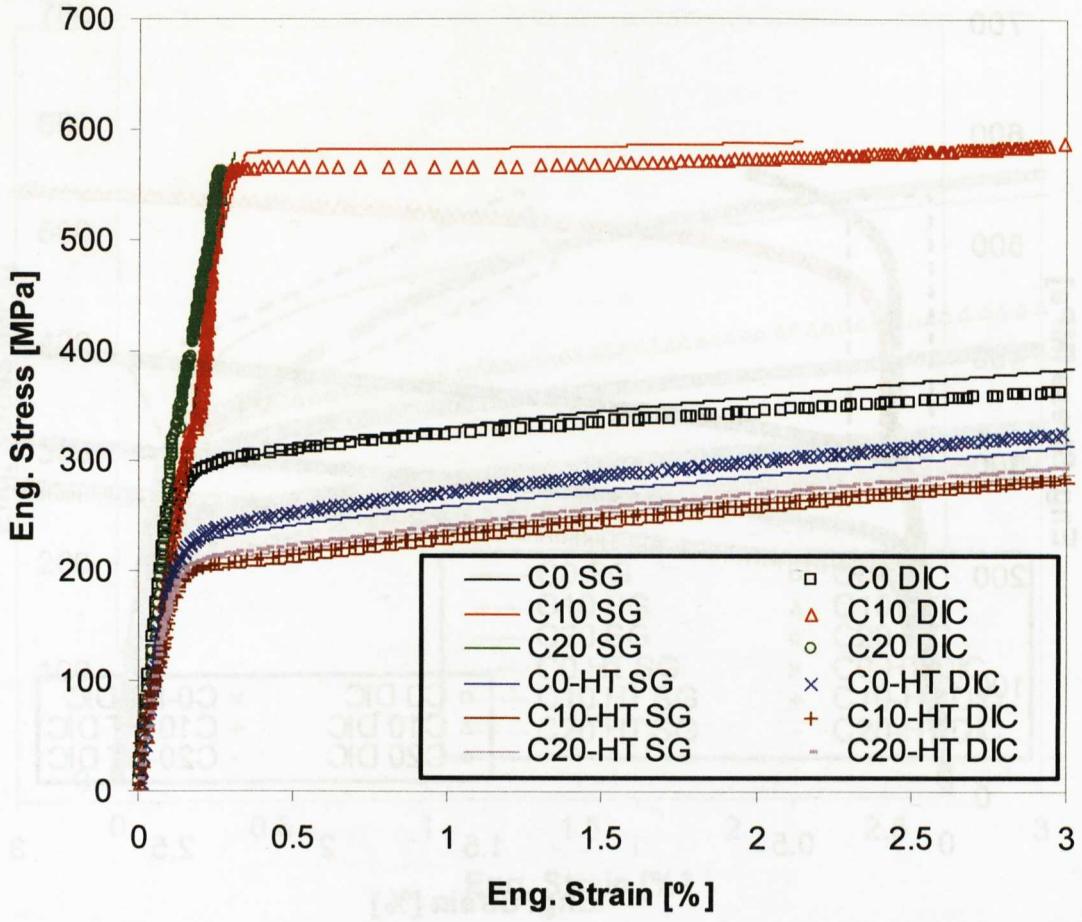

Figure 6.11 Stress-strain data measured using SGs and DIC at 20mm from the WCL of cross-weld specimens.

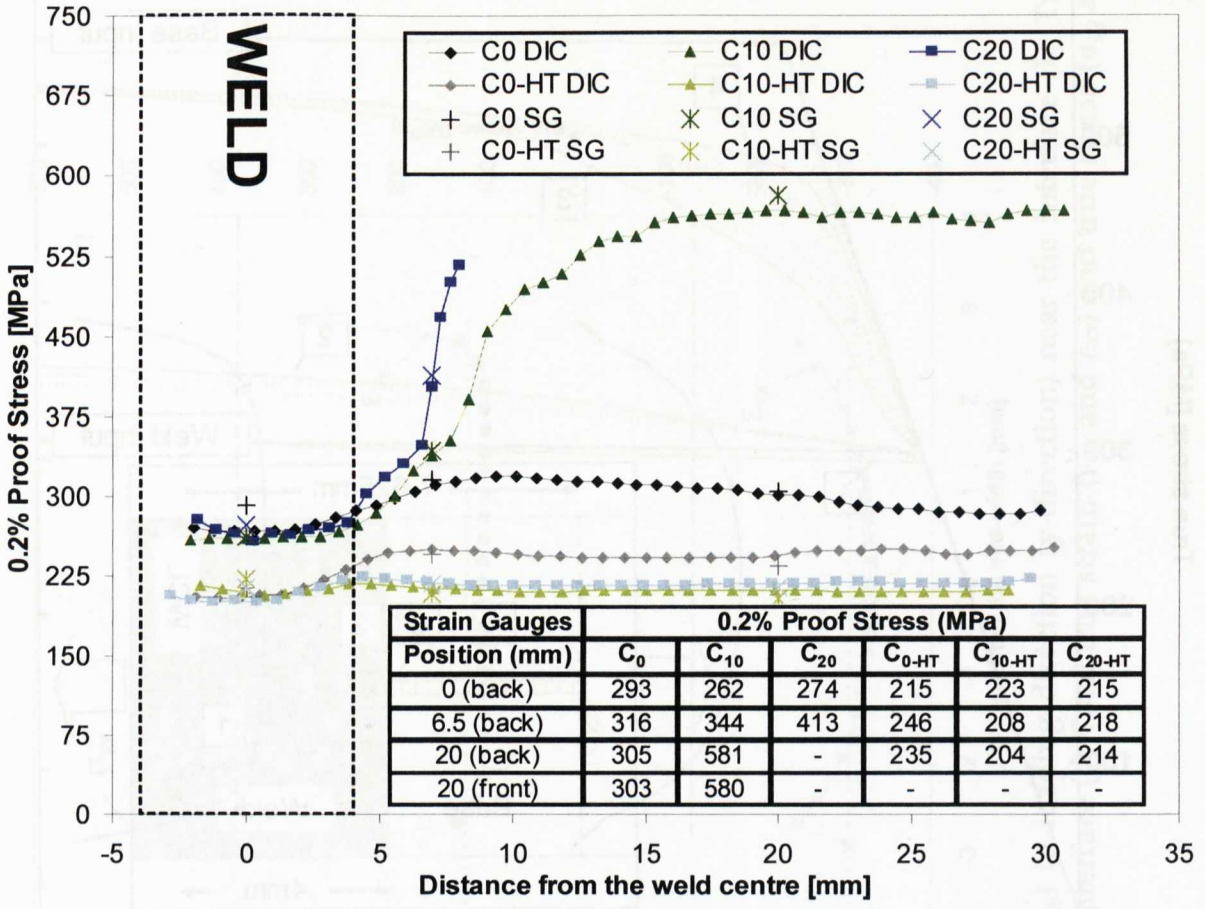

Strain Gauges	0.2% Proof Stress (MPa)					
Position (mm)	C_0	C_{10}	C_{20}	$C_{0\text{-HT}}$	$C_{10\text{-HT}}$	$C_{20\text{-HT}}$
0 (back)	293	262	274	215	223	215
6.5 (back)	316	344	413	246	208	218
20 (back)	305	581	-	235	204	214
20 (front)	303	580	-	-	-	-

Figure 6.12 Variation in 0.2% proof stress moving away from the WCL for cross-weld specimens (derived from SG and DIC data). Solid symbols represent the DIC data. Other symbols at WCL, 6.5mm and 20mm represent SG data. Light colours are for the heat treated samples labelled with HT. 0.2% proof stress obtained from SG is also tabulated for different positions.

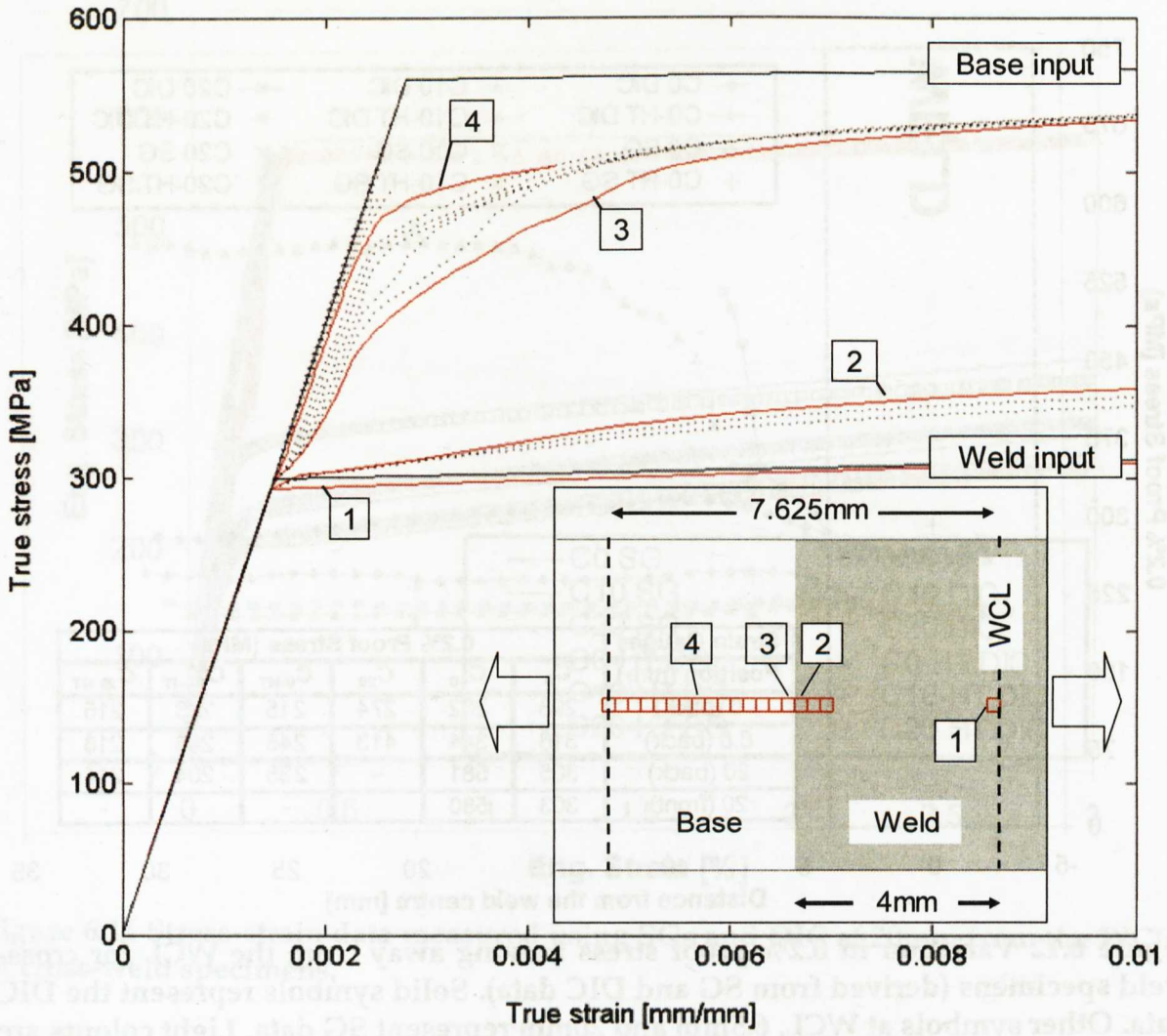

Figure 6.13 Local stress-strain curves (dotted lines, ····) obtained from red domains as shown in the schematic view of the bi-material model. Note that stress and strain are in the loading direction. Solid red lines correspond to the local stress-strain curves of domain 1, 2, 3 and 4. Solid black lines (—) correspond to the input stress-strain curves.

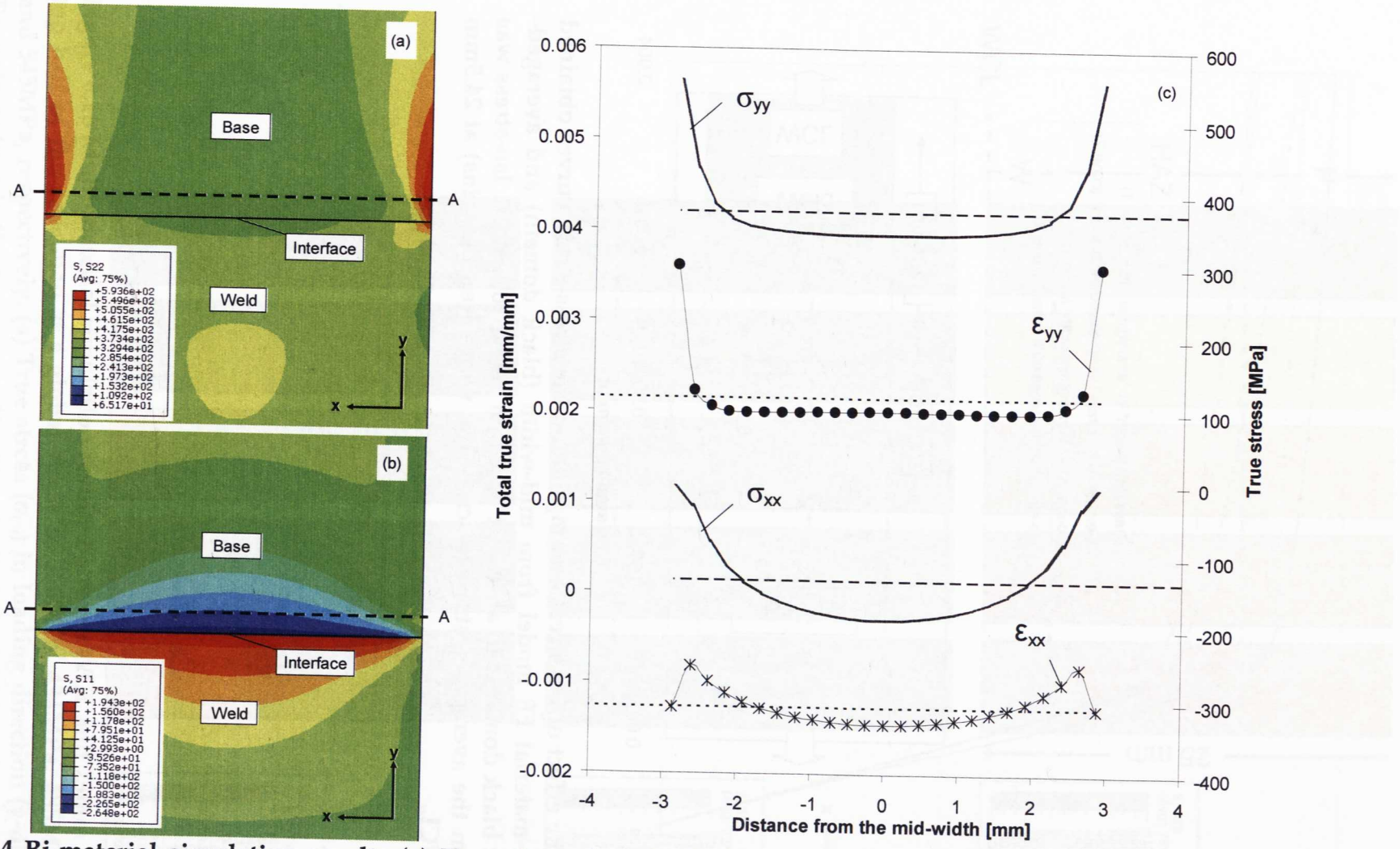

Figure 6.14 Bi-material simulation results (a) True stress (σ_{yy}) in loading direction (y-direction) near the interface (b) True stress (σ_{xx}) in the transverse direction (x-direction) near the interface (c) Total true strain (ε_{yy} and ε_{xx}) and true stress (σ_{yy} and σ_{xx}) distributions on line AA (at 375.8MPa global stress)

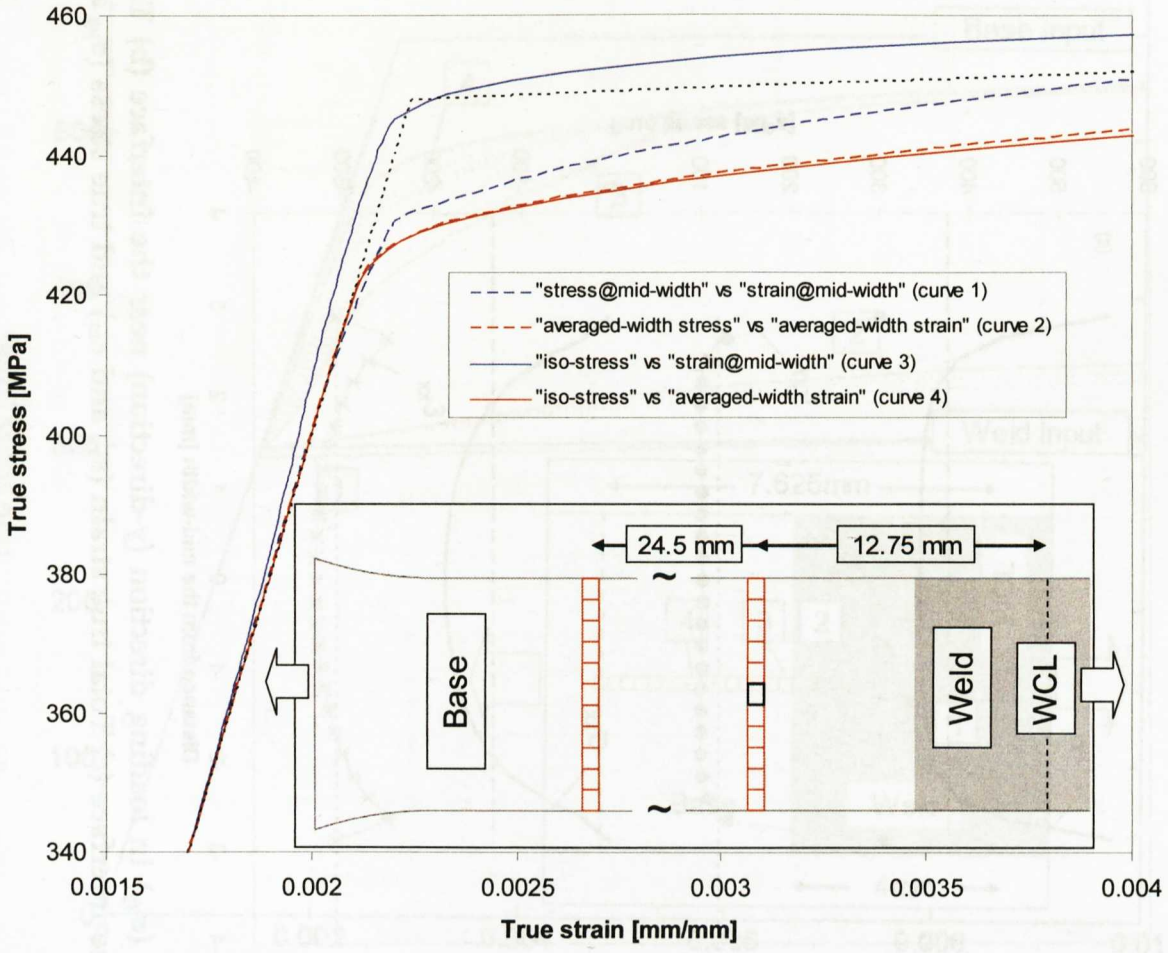

Figure 6.15 The effect of iso-stress assumption on the stress-strain curves obtained by the multi-material FE model from mid-width (black domain) and averaged-width (red & black domains in a row) at 12.75mm away from WCL. Iso-stress was obtained from the average of stresses across the width (red domains) at 24.5mm away from WCL.

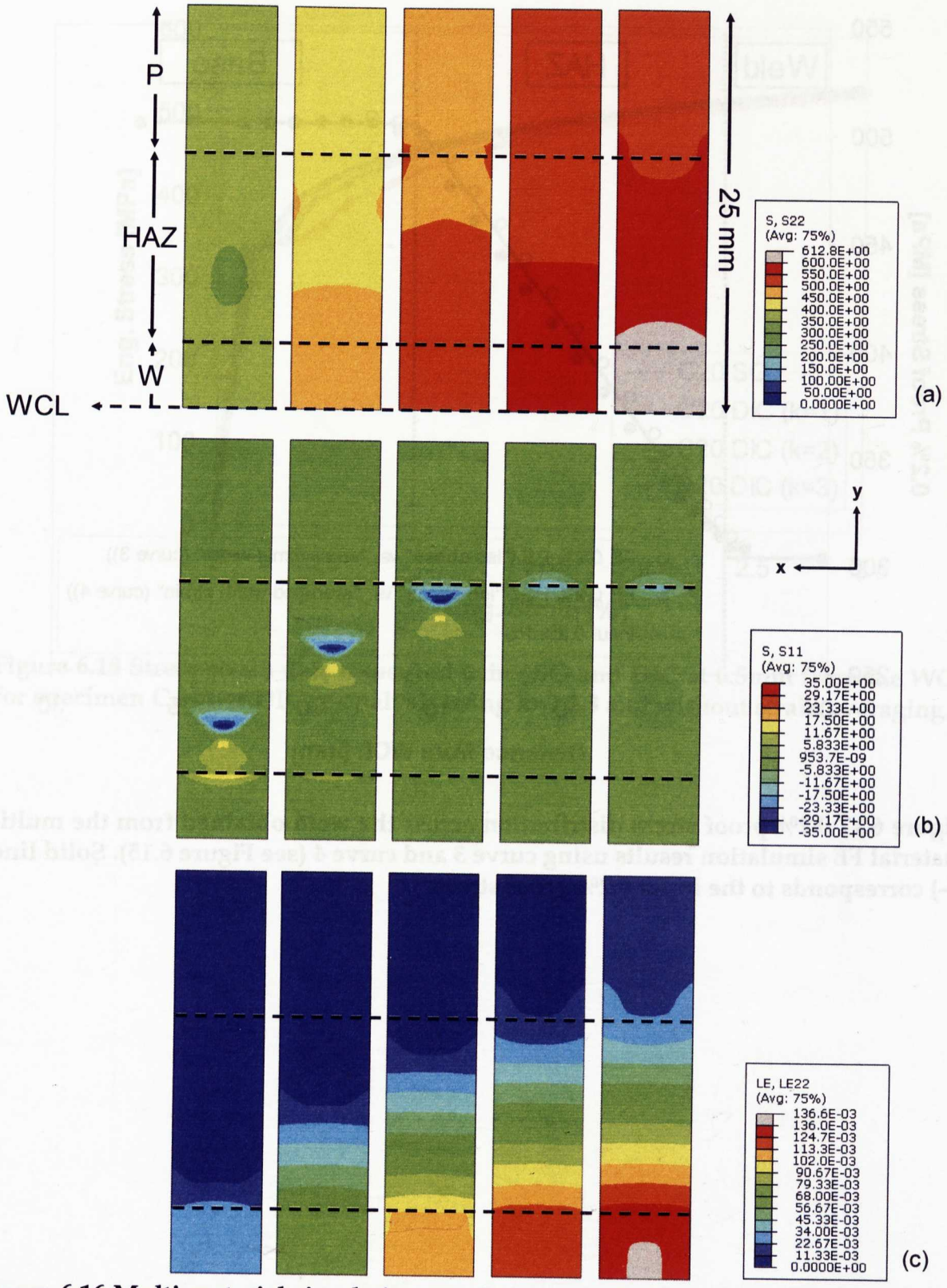

Figure 6.16 Multi-material simulation results between WCL and 25mm away in the top half of the specimen at a global stress of 356MPa, 434MPa, 485MPa, 518MPa and 545MPa, respectively. (a) True stress (σ_{yy}) in loading direction (y-direction) (b) True stress (σ_{xx}) in the transverse direction (x-direction) (c) Total true strain (ε_{yy}) in the loading direction (y-direction)

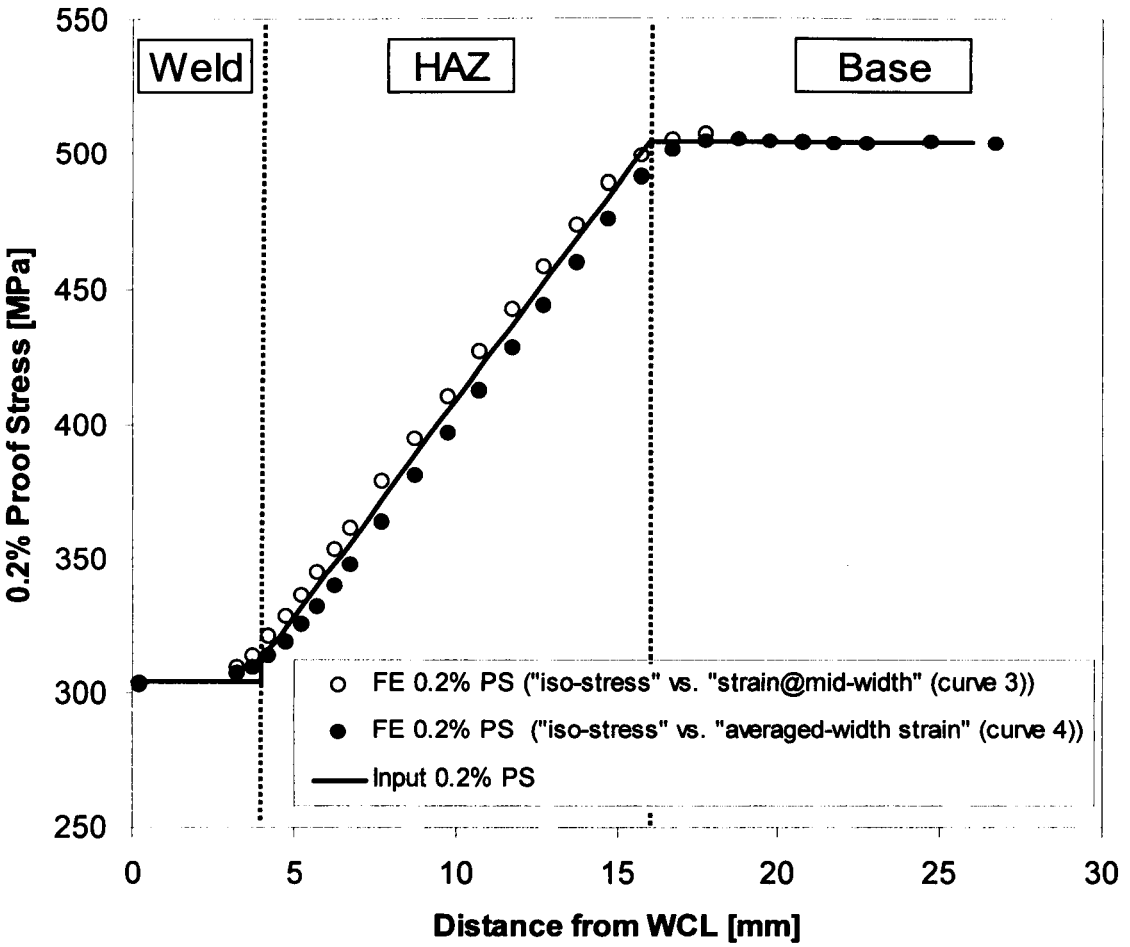

Figure 6.17 0.2% proof stress distribution across the weld obtained from the multi-material FE simulation results using curve 3 and curve 4 (see Figure 6.15). Solid line (—) corresponds to the input 0.2% proof stress.

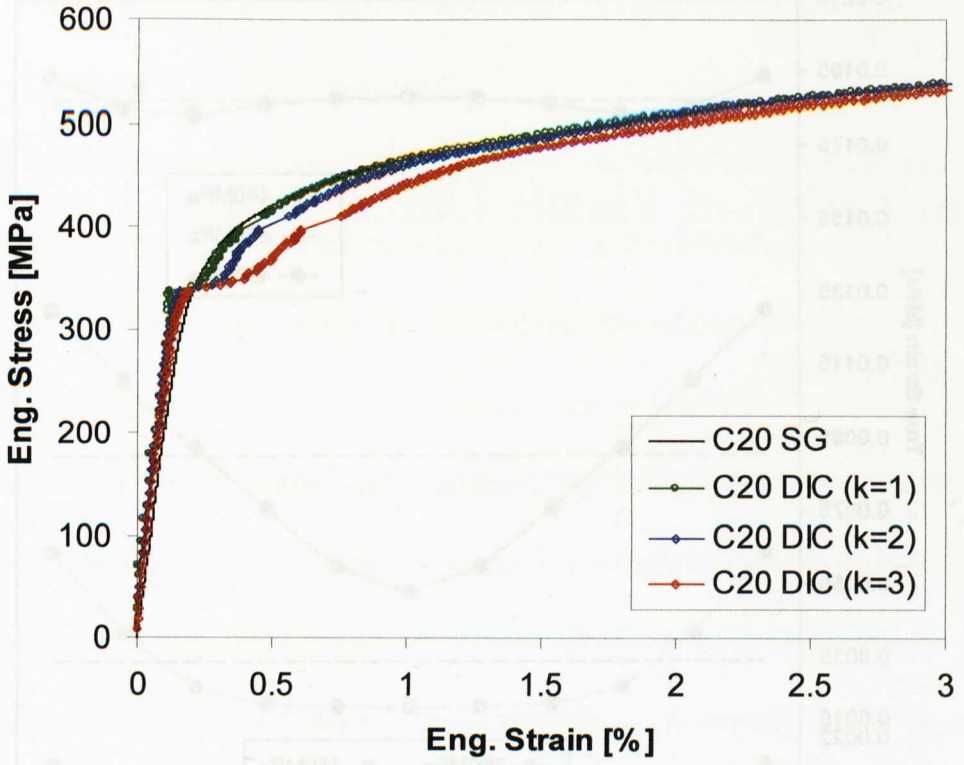

Figure 6.18 Stress-strain data measured using SG and DIC at 6.5mm from the WCL for specimen C_{20} after DIC re-analysis using k=1,2,3 and without strain averaging.

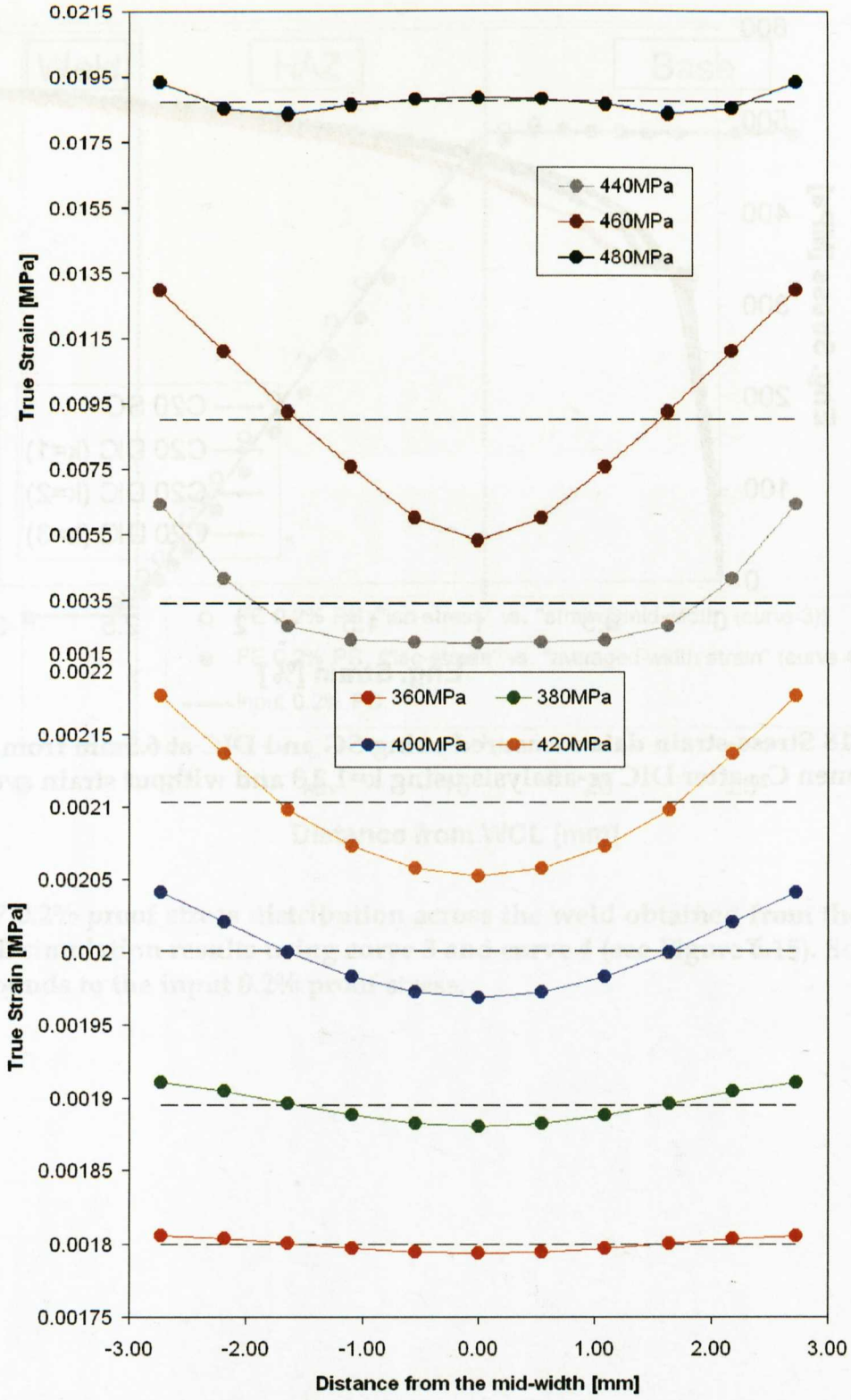

Figure 6.19 The strain (ε_{yy}) distribution along the width at a distance of 12.75mm from WCL at different stresses. The dashed lines show the average strain along the width. Note that this distribution was obtained from multi-material model and the selected stresses are global stresses.

Chapter 7

Determination of Plastic Deformation

7.1 Introduction

In power generation plants, energy is transferred to the power generator turbines *via* heat exchanger units which are exposed to high temperatures and pressures. Many metres of austenitic stainless steel tubes are bent, swaged and welded to produce these heat exchanger units. During tube-shaping and welding operations plastic deformation takes place when the critical load is exceeded. This influences in-service performance of the material unless the effect of plastic deformation is fully annealed out. The ASME Boiler and Pressure Vessel Design code [1] specifies that the limit of forming strain for 316H material which is going to operate between 580°C and 675°C is 20% and if it exceeds that threshold, the material should be annealed at min. 1040°C to restore its mechanical properties, tensile strength, creep strength and creep ductility to the start of life values. Furthermore, current construction practices in the UK for 316H tubes forbid welding onto material that has experienced more than 15% plastic strain, without first resolution heat treating the material [2]. Although the standard codes and construction practices put some limitations, it is sometimes not possible to follow these rules strictly especially when the whole boiler was constructed as a single unit which was then too large and too complex and contained different tubing materials [3]. Therefore, the tubing

material in-service is likely to have some degree of prior plastic deformation arising after tube-shaping and welding operations.

Plastic deformation is considered as one of the major factors in stress corrosion cracking [4-9] of austenitic stainless steels. Prior plastic deformation or pre-strain has also a significant impact on creep failure of AISI 316 stainless steel [10-14]. Creep resistance increases with plastic strain, whereas creep ductility drastically decreases [10]. In both cases prior plastic deformation plays an important role in the failure mechanisms. Therefore, prior to the installation of the unit the degree of plastic deformation should be determined.

Various techniques have been used for qualitative and quantitative determination of the plastic deformation in metals. Hardness measurement and x-ray diffraction peak broadening are used for the qualitative determination of the plastic strain. However, there is no direct method to measure the degree of plastic deformation accurately. Recently, there have been promising attempts at the development of experimental methods to measure plastic deformation, based on the observation of crystallographic changes in materials after plastic deformation using neutron diffraction [15, 16] and electron back-scattered diffraction (EBSD) [17].

When an elastically and plastically anisotropic polycrystal (e.g. austenitic stainless steel) is loaded, certain crystallographic changes occur in the material (see section 2.2.4 Anisotropy in Stainless Steel in Chapter 2 Literature Review for detailed explanation). Elastic anisotropy means that the elastic stiffness of a crystal is dependent on its orientation relative to the applied load. The yield stress may also depend on the orientation of the crystal, which makes the material plastically

anisotropic. Because of elastic and plastic anisotropy, the austenitic stainless steel has a highly complex stress-strain response [18].

As the material elongates under uniaxial load, the slip direction will tend to rotate towards the loading direction [19], which means that the grains are reoriented with increasing plastic deformation. When the load is released, residual strains develop over a length scale of the grain size. Here, residual strain is the combination of residual intergranular strains (Type II) and residual intragranular strains (Type III) [20]. Intergranular strains self-equilibrate over a length scale of the grain size after reorientation of grains. These elastic strains develop due to elastic anisotropy of the grain and the constraint of neighbouring grains. Intragranular strains are generated over a scale smaller than the grain size. Their origin is generally crystal defects such as dislocations, solute atoms and vacancies. Hereafter, we assume that the residual strains are mostly composed of intergranular strains and will use the term "residual intergranular strains" as previously used in the literature by other researchers [18, 21-26] .

Another crystallographic change with plastic deformation is the increase in dislocation density and the formation of dislocation bands and arrays. Severe cold working of an annealed metal will increase the dislocation density from around 10^7 to 10^{11} dislocations/cm^2 [27]. In a grain, as the deformation proceeds, dislocations intersect each other and start to lose their mobility, i.e. dislocations pile-up, which explains the strain hardening process. With further plastic deformation they begin to condense into bands and arrays. These structures can be considered as low angle

boundaries (LAB) where the separation between two crystallographic orientations is only a few degrees, not as big as in a high angle grain boundary (>15°) [27].

Diffraction techniques enable the tracking of the changes in residual intergranular strains and the dislocation density with increasing plastic deformation. Among these techniques neutron diffraction is more attractive as it has a good penetration in many metallic alloys (e.g. 50mm in steel) and is able to measure a gauge volume in the bulk. In a time-of-flight instrument as the incident beam is composed of different wavelengths, it is possible to obtain diffraction peaks for a series of crystallographic *hkl* planes. The peak position obtained for a *hkl* plane is shifted depending on the accumulated strain on this plane. The accumulated strain on each plane is different due to the differences in elastic stiffness. Therefore, the peak shift changes for individual planes. The calculation of strain from a TOF diffractogram is explained in Chapter 3. By using the peak shifts in a TOF diffractogram, Pang *et al* have measured the residual intergranular strains developed after unloading from 8% uniaxial straining of a rolled 309H stainless steel in the rolling direction [21]. They constructed residual strain pole figures for 111, 200, 331 and 224 planes and found that high tensile residual strains exist on 200 planes in the direction of straining (// to rolling direction). Peng *et al* also measured residual intergranular strains at different specimen orientations in AISI 304 stainless steel with 3 μm grain size after they were unloaded from 7.5, 29.8 and 44.7% uniaxial straining [22]. They observed almost a linear relationship between residual intergranular strains on individual planes in the loading direction and the macroscopic plastic deformation. The intergranular strain results obtained from the unloaded condition

[21, 22, 24] and in-situ tensile testing [25, 26] showed that intergranular strains which arise due to plasticity can be used to provide a semi-quantitative trace of the macroscopic plastic deformation. Daymond *et al* [15] have proposed an approach to fit the differences in strains observed for the various diffraction peaks to a single parameter called "anisotropy strain" (see section 2.2.4). By comparing with calibration data, obtained for example from a uniaxial loading test, a correlation can be drawn between the "anisotropy strain" and the macroscopic plastic strain. This approach was used for fcc [15, 28] and bcc [29] materials with some success. In this study, the measurements of residual intergranular strain at different specimen directions have provided useful information on the history of the plastic deformation in the material after pre-straining and welding. Moreover, the anisotropy strain has been used to quantify the plastic deformation in pre-strained and welded AISI 316H austenitic stainless.

Peak width or broadening of individual diffraction peaks also contains important information about the plastic deformation history of the material. There are two origins of peak broadening: instrumental and intrinsic changes (grain size, dislocation density and level of micro-strain in the grain). As long as the diffraction experiment is done on the same instrument, i.e. the instrumental broadening is kept the same, it is possible to observe the effect of plastic deformation on peak broadening. Wang *et al* [30] and Huang *et al* [31] suggest that the main factor on peak broadening is the intragranular strains resulting from the increased dislocation density. Peak broadening was successfully used to determine the plastic deformation in tension/compression of aluminium and steel specimens [16, 32], in a MIG (metal

inert gas) welded aluminium alloy [16, 32], around the crack tip of preloaded cracked steel beams [32], near a fatigue crack in AISI 316LN steel [33], in ferritic steel compact tension test specimens [29], during a tension test of IF (interstitial free) steels [26], in an ex-service pearlitic steel railway rail [34], in a friction stir welded aluminium alloy [35] and in nickel based alloy under monotonic-tension and low-cycle-fatigue loading [31]. In the present work, the peak broadening has been used to quantify the plastic deformation in pre-strained and welded AISI 316H austenitic stainless in different specimen directions.

Electron back scattered diffraction (EBSD) enables the measurement of crystal orientation on the specimen surface. Elastic scattering in accordance with Bragg's law as the incident electron beam is focussed on the specimen surface produces unique diffraction bands on the EBSD detector. The whole diffraction pattern which includes the diffraction bands is called "the Kikuchi diffraction pattern". Each band in the Kikuchi pattern represents a specific *hkl* plane in the crystal. The band width corresponds to the d-spacing of the plane and the angle between two bands is related to the angle between corresponding *hkl* planes. The experimental diffraction patterns are indexed by comparing them with known diffraction patterns stored in the software database and then the orientation of the crystal at that indexed measurement point is found. Many researchers have used the misorientation angle (the orientation change between adjacent measurement points) distribution in the sampling area to determine the degree of deformation; e.g. in cold worked AISI 304 stainless steel and nickel alloy (Alloy 600) [36], AISI 316 stainless steel subjected to creep deformation [37], in HAZs from 304L, 304 and 316L welds using GTAW (gas

tungsten arc welding) [9] and in inertia welded nickel based superalloy [38]. Brewer *et al* has used the distribution of low angle boundaries (LABs) to visualize the influence of plastic strain near the crack tip [39]. In this chapter, the fraction of the LABs was related to plastic deformation by using plain, 10%, 15%, 20% and 25% deformed AISI 316H stainless steel samples. A prestrained and welded specimen was also investigated in the same manner.

In this study, the plastic strain in prestrained and welded tubes was also predicted using the hardness measurements presented in Chapter 5 and local stress-strain curves presented in Chapter 6 in addition to the neutron diffraction and EBSD.

The effect of heat treatment will not be discussed in this chapter as the heat treatment at a soaking temperature of 1050°C for 15 min. annealed out all the effects of plastic deformation.

7.2 Experimental Procedure

7.2.1 Test specimens

A set of five plastically pre-strained and welded tubes were supplied by British Energy, UK. The base metal was AISI Type 316H austenitic stainless steel with composition 16.89 wt% Cr, 11.25 wt% Ni, 2.04 wt% Mo, 1.55 wt% Mn, 0.53 wt% Si, 0.089 wt% Co, 0.05 wt% C, less than 0.05% of other elements and the balance being Fe. The grain size of the plain material was about 30 μm. The 1% proof strength of the non-strained material was 367 MPa and Young's modulus for this type of material is about 195 GPa. The tubing (prior to plastic straining) was approximately 38 mm in (outer) diameter and 4 mm in thickness.

The test specimens were fabricated as follows; (1) four tubes were pulled uniaxially in tension up to 10, 15, 20 and 25% total strain in order to simulate plastic deformation associated with fabrication processes in a controlled way. (2) These four strained tubes plus a non-strained tube were cut into two halves. (3) Matching half-tubes were then welded together using a tungsten inert gas (TIG) welding process with Type 316L filler metal. The tubes from which the samples were cut are listed in Table 4.1.

The remote-end tensile test specimens B_0, B_{10}, B_{15}, B_{20}, B_{25} and cross-weld tensile test specimens C_0 and C_{20}, which were listed in Table 4.1, were used to investigate the residual intergranular strains and peak width at Engin-X before used for tensile tests. The cut position and the dimensions of the specimens are given in Figure 4.4. Note that cutting the cross-weld strips will relax the type-I residual stresses developed after welding.

For the crystallographic texture measurements at FRMII, 3x3x3 mm^3 cubes were cut from the remote-end of A_0, A_{10}, A_{15}, A_{20} and A_{25} tubes and labelled as shown in Table 7.1.

Some metallography samples were also sectioned from the tubes to be used for EBSD experiments. These samples are listed in Table 7.2.

7.2.2 Neutron diffraction experiments

7.2.2.1 Residual intergranular strain and peak width measurements at Engin-X

The lattice strain was measured parallel and perpendicular to the pre-straining direction and at some angles between those directions as shown in Figure 7.1. The data was collected from the two collimator banks at ENGIN-X which is able to provide data for two orthogonal scattering vectors at the same time. ISIS provides a white beam of neutrons to create time-of-flight diffraction patterns. At Engin-X the range of the wavelengths in the beam is 0.5-6Å, which means that the data is available from a range of *d*-spacings. The first four peaks in the diffraction pattern were selected for the analysis (Figure 7.2). To obtain the *d*-spacing and the peak widths of individual peaks a single peak fitting routine implemented in OpenGenie [40] was used. This routine uses a pseudo-Voigt function which fit very well the observed peak profiles in neutron diffraction [41]. The measurements were performed in the mid-length of the remote-end specimens (B_0, B_{10}, B_{15}, B_{20}, B_{25}) to determine intergranular strains and peak width for 0, 10, 15, 20 and 25% pre-straining conditions (Figure 7.3(a)). The cross-weld specimens C_0 and C_{20} were used to determine the change in intergranular strains and peak width due to welding by measuring at the weld centre, and 7, 9, 12, 16 and 29 mm away from weld centre line (Figure 7.3(b)). Since the thickness of the strips is small, two adjacent strips were glued together at the outer surfaces with respect to the pipe geometry in order to average as many grains as possible by using a 3 × 3 × 5 mm^3 gauge volume. 10

minutes of counting time were used per measurement to ensure good peak width signal. The measurements at specimen directions from 45°(LD) to 90° were obtained at the north bank and the ones from 90° and 135°(HD) were obtained at the south bank. Measurements of d-spacing at different specimen directions at the mid-length of specimen B_0 were averaged and used as reference (d_0) for each specific *hkl* plane to calculate the residual intergranular strains at the other measurement points on cross-weld and remote-end specimens. The strain is calculated by using Eq. (7.1);

$$\varepsilon_{lat}^{hkl} = \frac{d^{hkl} - d_0^{hkl}}{d_0^{hkl}} \tag{7.1}$$

The peak widths were obtained as full-width at half maximum for each individual peak.

7.2.2.2 Crystallographic texture measurement at Stress-Spec

Crystallographic texture of the deformed parent material was determined by experiments at Stress-Spec, FRMII. A neutron wavelength of $\lambda = 1.5480$ Å was obtained from the (511) planes of a Ge monochromator. The cubic samples listed in Table 7.1 were centred on an Eulerian cradle which has phi (φ) and chi (χ) rotations (Figure 7.4). The spherical coordinate system used to describe the angular orientation of the sample is demonstrated in Figure 7.5. The detector was positioned at specific (2θ) angles to obtain diffraction from the 111 and 200 planes. Pole figures for 111 and 200 were obtained by measuring the Bragg peak intensity on a 5°×5° grid. Each pole figure was produced with step mode (discontinuously) by rotating chi (χ) from 0° to 90° in 19 steps and phi (φ) from 0° to 360° in 72 steps. MTEX software [42] was used

for the recalculation of 111, 100, 110 and 311 pole figures from experimental 111 and 200 pole figures.

7.2.3 Electron back-scattered diffraction (EBSD)

EBSD measurements were performed by using a field-emission gun scanning electron microscope (Zeiss Supra 55VP FEG SEM) fitted with a Nordlys EBSD detector. EBSD data was obtained by automatically scanning the electron beam with 20kV accelerating voltage over the polished surface of the specimen which was tilted at 70° from the horizontal. The working distance between the sample and phosphorus screen in front of the EBSD detector was set to 15±0.1mm. The acquisition and post-processing of EBSD data was done with HKL Channel 5 software. For EBSD analysis the austenite (fcc) phase was selected from the HKL database for all samples because no ferrite (bcc) phase was expected to exist in the base 316H material. The experimental details for the samples which were labelled as in Table 7.2 are given below.

Parent samples (P_0, P_{10}, P_{15}, P_{20} and P_{25}) were machined out using EDM from the remote-end of the tubes A_0, A_{10}, A_{15}, A_{20} and A_{25}, where the material is not affected by the welding process. Samples were mounted in a thermosetting resin. The sample preparation included sequential grinding with grades 220, 500, 800, 1200, 2500 and 4000 emery papers and polishing on soft cloths using suspensions containing 9, 6 and 1 μm diamond particles. A final polishing was done with OP-S colloidal silica suspension for 2 min to remove the mechanically deformed surface layer on specimens. An area of 300×300μm in the middle of the polished surface was scanned by an electron beam with a step size of 1 μm in order to investigate any change in the

fraction of low angle boundaries (LAB) with increasing plastic deformation. Note that observations were made on the longitudinal-radial direction (LD-RD) plane. In addition, the hoop-radial direction (HD-RD) plane was also studied for sample P_{25} in order to make a comparison with the LD-RD plane.

A cross-weld sample (W_{20}) was cut from tube A_{20} and its surface was prepared as explained for the parent samples. Initial measurements were made on the LD-RD plane with a step size of 3μm in an area of 1.8mm×9.6mm. Because this area is large for single scanning, it was divided into four adjacent areas and the measurements were stitched afterwards. This sample was used to look into the change in the fraction of low angle boundaries away from the WCL as well as the local variation of pre-existing texture after welding. For that purpose, the specimen surface was scanned again with 1μm step size in a similar region.

7.3 Results

7.3.1 Residual intergranular strains

Residual strains were measured by using neutron diffraction on 111, 200, 220 and 311 planes for both remote (B_0, B_{10}, B_{15}, B_{20} and B_{25}) and cross-weld specimens (C_0 and C_{20}) at LD, HD directions and at several angles in between. Each measurement on different *hkl* planes represents an average interplanar strain in the gauge volume which contains over a million grains.

Parent specimen

The variation of residual strains as a function of sample direction from LD (45°) to HD (135°) is plotted in Figure 7.6(a), (b), (c), (d) and (e). In the undeformed

state of the material, there does not seem any significant residual strain in any orientation. However, as can be seen in Figure 7.6(b) to (e), considerable residual strains developed in the material in all orientations as a consequence of the plastic deformation. Tensile strains accumulate on 200 and 311 planes from 45° (LD) to 100°; tensile strains on (200) are somewhat higher than those in 311 plane. On the other hand, 111 and 220 planes sustain compressive strains. Residual strains on 111 planevary significantly from 45° (LD) to 100° whereas those on 220 vary slightly. With increasing plastic deformation residual strains on all planes between 45° (LD) and 100° become greater. From 100° to 135° (HD) residual strains almost level off. Note that at any level of plastic deformation the largest residual strains concentrated on LD, i.e., in the pre-straining direction. Therefore, we can conclude that residual intergranular strains are sensitive to the loading direction, i.e. they are direction-dependent. Since the strongest residual strains build up in the direction of pre-straining, it is better to look at the variation of strains in that direction with increasing plastic deformation (Figure 7.7 (a)). A similar relationship between residual intergranular strains and plastic deformation was observed by Peng *et al* [22] who measured the residual intergranular strains in the loading direction after unloading from 7.5%, 29.8% and 44.7% plastic.

The anisotropy strain ε_A was calculated from the averaged residual strains on 200 and 111 planes over 45°(LD) - 135°(HD) according to the equation 2.15 in Chapter 2 Literature Review. 111 and 200 planes were selected because these planes represent the extremes of elastic stiffness in stainless steel. The variation of anisotropy strain

with plastic deformation is given in Figure 7.8. A linear fit was made for use in predicting the plastic deformation in cross-weld specimens.

Cross-weld specimen

The variation of residual strains as a function of sample direction from LD (45°) to HD (135°) is plotted for specimen C_0 at 7, 9, 12, 16 and 29mm away from the weld centre in Figure 7.9(a), (b), (c), (d) and (e). It can be seen that residual strains develop on all four planes after welding. The effect of welding on the residual strains on *hkl* planes appears to be random. However, similar trends are observed for the (220) plane from 45° (LD) to 75° at 9, 12 and 16mm away from WCL. Interestingly, at these distances from the WCL the strain on (220) is tensile after welding although it is compressive after pre-straining. In addition, 200 plane is the one least affected by welding.

The variation of residual strains as a function of sample direction from LD (45°) to HD (135°) is also plotted for specimen C_{20} at 7, 9, 12, 16 and 29mm away from the weld centre in Figure 7.10(a), (b), (c), (d) and (e). Note that specimen C_{20} was cut from the tube A_{20} (20% pre-strained and welded tube). As expected, it can be seen that the residual strains in specimen B_{20} (Figure 7.6 (d)) are very similar to the strains at 29mm in specimen C_{20} (Figure 7.10(e)). The residual strains relax closer to the weld (Figure 7.10(a), (b), (c) and (d)). It is interesting that tensile strains accumulate on the (220) plane at 7mm between 45° (LD) and 60°, becoming compressive at further points in the same range of specimen directions.

The variation of the residual strains in the prestraining direction (LD) along specimens C_0 and C_{20} is given in Figure 7.11 (a)-(c), respectively. It can be seen that

residual strains in the 220 plane in the prestraining direction is affected more than those on the other planes.

The anisotropy strain ε_A at 7, 9, 12, 16 and 29mm away from the weld centre for specimens C_0 and C_{20} was calculated from the averaged residual strains on 200 and 111 planes over 45°(LD) - 135°(HD) according to the equation 2.15 in Chapter 2 Literature Review. The variation of anisotropy strain along specimens C_0 and C_{20} is given in Figure 7.12 and will be used to predict plastic deformation with the calibration of the data in Figure 7.8.

7.3.2 Peak widths

The peak width at half maximum data in diffraction patterns can provide a qualitative comparison of the dislocation densities i.e. plastic deformation [26]. The peak width is a convolution of the initial peak width with changes in width caused by microstructural effects that are introduced by deformation. The most reliable peak width in Figure 7.6, Figure 7.7, Figure 7.9 and Figure 7.10 belongs to the 111 plane, which is the strongest peak, with a scatter of 150-200x10^{-6}. Although the peak widths obtained from the other planes are noisier, they were analysed as well.

Parent specimen

The peak widths obtained from specimens B_0, B_{10}, B_{15}, B_{20} and B_{25} at sample directions from LD (45°) to HD (135°) are presented in Figure 7.6(f-j), respectively. It can be seen that the peak widths become larger for all *hkl* planes at all specimen directions as the plastic deformation increases. The 111 peak width is virtually constant from 45°(LD) to 135°(HD) whereas there is some variation for the other

planes. This may suggest that the dislocation density is uniform in the specimen and not direction-dependent. If we assume that the peak width is not direction-dependent for any planes and take an average over the range of specimen direction from 45°(LD) to 135°(HD) and then plot the averaged peak width for hkl planes vs. plastic strain, a linear trend was obtained as shown in Figure 7.7(b) for all *hkl* planes except the (220) plane.

Cross-weld specimen

The 111 peak width results for specimen C_0 at 7, 9, 12, 16 and 29mm away from the WCL is plotted in Figure 7.9(f-j). The peak widths are essentially unchanged by the welding process despite changes in peak profiles had been expected due to the plastic strain induced by thermal expansions and contractions during welding. The reason for this could be due to the fact that the resolution of the peak width analysis may not be sufficient to show changes for these small plastic strains. However, it is seen that the peak widths are more scattered after welding compared to the variation in peak widths with specimen direction for parent specimens.

The 111 peak width results obtained from specimen C_{20} are also presented in Figure 7.10(f), (g), (h), (i) and (j). It is clear that the welding reduces the peak width near the weld; at 7mm from WCL 111 peak widths at different specimen directions are similar in the specimens C_0 and C_{20} (Figure 7.9(f) and Figure 7.10(f)). At 9mm, there are jumps at 45°(LD), 60° and 75°, which suggest that the effect of welding on the peak width is multi-axial. At other measurement points the peak widths are increasing progressively with distance from the WCL and at 29mm peak widths at different specimen directions become similar to B_{20} (see Figure 7.6(d)).

The variation of the peak width averaged over the range of specimen direction along specimens C_0 and C_{20} is given in Figure 7.11 (b)-(d), respectively. This variation was used to determine the plastic deformation in these specimens with the calibration of the data in Figure 7.7 (b).

7.3.3 Crystallographic texture

Parent specimen

The 111, 100, 110 and 311 pole figures obtained by using neutron diffraction for the cubes T_0, T_{10}, T_{15}, T_{20} and T_{25} are given in Figure 7.13. There is a small 111 texture in LD and small 110 texture in RD before the deformation. This suggests that the material was not totally annealed. 111 texture in LD increases with increasing deformation and reaches 8 times random after 25% deformation but there is no change in HD and RD (Figure 7.13(a)). Therefore, diffraction from the 111 plane in LD is more intense compared to the other directions. There is also a texture development for 100 plane in LD direction with increasing plastic deformation although it is small (2x random), (Figure 7.13(b)). This type of texture is called duplex <111> and <100> fibre texture.

For the 110 plane a small texture develops in RD and HD, meanwhile it is not affected in LD where the reflection for this plane is poor compared to HD and RD (Figure 7.13(c)). This explains the high error bar in residual intergranular strains measured on the 220 plane near LD (see Figure 7.6(a-e) and Figure 7.7(a)). There is no significant texture evolution for the 311 plane with increasing deformation apart from a small change in LD after 10% deformation (Figure 7.13(d)).

Cross-weld specimen

The sample W_{20} shown in Figure 7.14(a) was used to observe the change in local texture after welding onto 20% plastically strained material. Measuring the texture in this sample will be helpful to understand the residual elastic strains and peak width for specimen C_{20} (see Figure 7.10). Texture was retrieved from EBSD data for three different zones (4.6, 6.7 and 11.4mm) away from the WCL (Figure 7.14). The pole figures in Figure 7.14(d) which were obtained from zone-3 (11.4mm from the WCL) are similar to the ones in Figure 7.13 for the parent sample deformed at 20%. This means that the pre-existing texture in zone-3 is not affected from the heat dissipation during welding although hardness and proof stress distributions across the weld suggest that the region between the fusion boundary and 16mm away from WCL has been affected from welding. In zone-2 (6.7mm from the WCL) which is closer to the weld, the texture intensity of 111 in LD slightly drops down (Figure 7.14(c)). However, the pre-existing texture disappeared entirely in zone-1 (4.6mm from the WCL)) which is just near the fusion boundary (Figure 7.14(a)). There is no concentration for any plane at any specific direction, in other words the grains are randomly oriented in that zone. Since the temperature of the molten weld metal is very high (~1400°C) the grains near the fusion boundary are likely to be subjected to recovery and/or recrystallization and hence have a random orientation.

7.3.4 Low angle boundaries

Parent specimen

The distribution of LAB for parent samples P_0, P_{10}, P_{15}, P_{20}, P_{25} on LD-RD plane is given in Figure 7.15. Boundaries are defined according to the misorientation angle

between two adjacent points. For fcc metallic alloys, any misorientation angle greater than 15° is considered as a high-angle grain boundary (HAGB) and a misorientation angle between 2°-15° is taken as a low angle boundary (LAB) [38, 43]. In Figure 7.15, it is clearly seen that the distribution of LABs increases as the plastic deformation increases. The LABs are mostly concentrated near grain boundaries at small deformation (Figure 7.15(a-d)); however, it is observed that at higher deformation LABs also appear inside the grains due to the dislocation bands and arrays (Figure 7.15(e)). In a grain, as the deformation proceeds, dislocations intersect each other and start to lose their mobility, i.e. strain hardening begins. With further plastic deformation they begin to pile-up near grain boundaries and form bands and arrays inside the grains [19]. The fraction of the frequency of LAB (2-15°) to the total of all misorientation angles in the sampling areas were calculated and are presented in Figure 7.16. It is seen that the fraction of LAB increases almost linearly with increasing plastic deformation.

The LAB distribution on HD-RD and LD-RD planes was also compared for the parent sample P_{25}, as shown in Figure 7.17. A similar misorientation distribution was found on both planes. The fraction of LAB on HD-RD and LD-RD are 0.226 and 0.221, respectively, which means that the distribution of LAB is not direction-dependent.

Cross-weld specimen

The variation of LAB fraction as a function of distance away from the WCL on the LD-RD surface of the specimen W_{20} is given in Figure 7.18. It is seen that the LAB fraction is decreasing approaching the weld fusion boundary. Each point represents LAB fraction which was determined in an area of 300×900 μm^2 (height × width) in the

mid-height of the surface. Figure 7.18 was used to predict the variation of plastic deformation in specimen W_{20} with the calibration of the data in Figure 7.16.

7.4 Discussion

The development of residual strains with plastic deformation

In this study, the measurements of intergranular residual strains developed in specimens B_0, B_{10}, B_{15}, B_{20} and B_{25} have shown that tensile strains were accumulated on the 200 and 311 planes and compressive strains exist on the 111 and 220 planes. Similar results were reported in [22] for AISI 304 austenitic stainless steel which was subjected to intermediate levels of plastic deformation up to 44.7% and in [25] for AISI 316H austenitic stainless steel which was subjected to 3% plastic deformation. Larsson *et al* [24] claimed that there are two origins of the residual intergranular strains, which are elastic anisotropy and strain redistribution due to slip along preferred systems. They also stated that it is difficult to distinguish their contributions from each of the aforementioned factors. The sign of the intergranular strains can be explained with different elastic stiffness of the planes, i.e. elastic anisotropy. Daymond *et al* [25] reported the elastic stiffness of 111, 220, 311 and 200 planes in the loading direction as 245, 210, 180 and 150 GPa, respectively. The 111 plane is the stiffest whereas 200 plane is the least stiff. This indicates that when the specimen is unloaded, due to the elastic equilibrium among the grains, the less stiff planes i.e. 200 and 311 planes carry the tensile strain whereas stiffer planes, i.e. 111 and 220 planes, sustain the compressive strains.

Deformation mechanisms have also an influence on the residual strains. Slip along preferred crystallographic directions and planes may cause strain redistribution among the grains. Feaugas *et al* [44] explains how the stress/strain is redistributed between the grains and inside the grain during the deformation of 316L stainless steel. For austenitic stainless steel, due to low stacking fault energy, planar slip is observed and cross-slip is prevented. The grain boundaries act as strong barriers to slip. At the beginning of plastic deformation (<1.5%) dislocations pile up near grain boundaries and that imposes a stress concentration near the boundary, i.e. intergranular stresses. Therefore, increasing plastic strain during the early stages of deformation results in a higher stress concentration near the grain boundaries because the number of dislocations in the pile-up increases. Intergranular stresses start to decrease with the activation of multiple slip and cross-slip. By doing so, the intergranular stresses are relaxed and the plastic strain compatibility is maintained between the grains. Slip transmission across grain boundaries and activation of dislocation sources in neighbouring grains also reduce the intergranular stresses. Further deformation after the activation of cross-slip and multiple slip produces heterogeneous dislocation structures like dislocation bands and arrays of dislocations inside the grains, therefore, intragranular stresses increase. It was reported that the difference between inter- and intra-granular stresses becomes zero at about 6% plastic deformation [44]. Note that, as discussed in the literature [18, 21-26], the term "residual intergranular strains" was preferred to be used to define the residual strains measured with neutron diffraction because the intragranular strains were thought to be negligible. However, Feaugas's explanation suggests that the intragranular strains

cannot be neglected because they are as significant as the intergranular strains after 6% deformation. It can be concluded that the residual strain measured with neutron diffraction after plastic deformation beyond 6% deformation is composed of (1) intergranular strains which arise due to the elastic anisotropy of *hkl* planes and (2) intragranular strains which arise due to the heterogeneous dislocation structures inside the grains.

Larsson *et al* [24] found that the initial texture has an influence on the residual strain distribution. He observed that the strain distribution becomes more complex after the deformation of an austenitic stainless steel with an initial texture of 1.6× random texture. In the present study, 3× random texture has been found in specimen T_0 for 111 plane in the loading direction (Figure 7.13). Therefore, this might have influenced the residual strain distribution. The texture in specimens B_0, B_{10}, B_{20} and B_{25} (Figure 7.13) suggests that duplex <111> and <100> fibre texture forms before 10% deformation and it becomes stronger as the deformation proceeds. Multiple slip is effective on the formation of fibre texture [45]. The intensity ratio of <111> to <100> is about 3.5 after 25% plastic deformation. Such a duplex texture is often observed in fcc materials subjected to axisymmetric flow and the ratio of the polar intensity varies with the stacking fault energy of the material [22]. A high volume fraction of grains oriented in <111> and <100> directions parallel to the loading direction would influence the generation of residual strains. The low strain level on the 111 plane can be explained by the fact that a high number of grains are oriented in <111> direction parallel to the pre-straining direction as well as the high stiffness of 111 plane. Similarly, high strains on the 200 plane can be attributed to the increasing number of

grains oriented in <100> direction parallel to the pre-straining direction and the low stiffness of 200 plane.

Prediction of plastic deformation in tube A_0 andA_{20} using anisotropy strain

As mentioned in section 7.1, Daymond *et al* [15] used residual strains to predict the plastic deformation via *anisotropy strain*. Their technique requires "residual strains vs. macroscopic plastic strain" calibration curve similar to the curve given in Figure 7.8. A linear line was fit to that curve and was used as a calibration to predict the plastic deformation in specimens C_0 and C_{20} across the weld from the distribution of anisotropy strains presented in Figure 7.11. The variation of the predicted plastic deformation on specimens C_0 and C_{20} across the weld using anisotropy strain is given in Figure 7.19. The ~2% increase of plastic deformation in the base metal of specimen C_0 can be attributed to the cyclic hardening due to double pass welding and the constraints such as root tack welds before the root pass. The base metal of specimen C_{20} was 20% pre-strained. It is seen that plastic deformation in this specimen is decreasing closer to the weld. This can be explained by partial recovery which means that dislocation annihilation occurs partially with the effect of heat as a function of distance from the WCL [27]. In addition, the prediction of plastic deformation across the weld using anisotropy strain is consistent with the hardness results obtained across the weld on the surface of specimens C_0 and C_{20} (see Figure 5.13).

Prediction of plastic deformation in tube A_0 and A_{20} using peak widths

According to Feaugas's explanation of inter- and intra-granular strains, it can be concluded that the plastic deformation can be tracked with the dislocation density and structures such as pile-ups near grain boundaries and heterogeneous dislocation

structures inside the grains. Peak width measurements by neutron diffraction on B_0, B_{10}, B_{15}, B_{20} and B_{25} suggests that dislocation density increases with increasing deformation for any *hkl* plane in any specimen direction (Figure 7.6(f-j)). Lewis and Truman [29] stated that the peak broadening is insensitive to the diffraction vector direction. Therefore, it is a measure of equivalent plastic strain. The peak widths averaged over the specimen directions from LD to HD for specimens B_0, B_{10}, B_{15}, B_{20} and B_{25} are given in Figure 7.7 (b). Linear lines were fit to the 111, 200 and 311 plane responses. The peak width on specimens C_0 and C_{20} at different positions away from the WCL were also averaged over LD-HD as shown in Figure 7.11 (b) and (d), respectively. The corresponding plastic deformation at different positions from the WCL for specimens C_0 and C_{20} was calculated from the linear fits obtained from specimens B_n. The prediction of plastic deformation on specimens C_0 and C_{20} by using the averaged peak widths is given in Figure 7.20. The plastic deformation in specimen C_0 is almost zero when data from 200 and 311 planes are used. However, the 111 plane gives ~1% deformation at 12 mm. Cyclic hardening due to double pass welding might have increased the dislocation density in that region. The reason why only the 111 plane shows such a trend can be that at small deformation, less than 1.5% before the multiple slip and cross-slip are activated, there is only planar slip on the 111 plane [44]. The variation of plastic deformation in specimen C_{20} across the weld is similar to that obtained from anisotropy strain. It is also interesting that similar trends were obtained from the 111, 200 and 311 planes and this is consistent with the hardness results obtained across the weld on the surface of specimen C_{20} (see Figure 5.13).

Prediction of plastic deformation in tube A_{20} using EBSD

The dislocation structures such as pile-ups near grain boundaries and heterogeneous dislocation structures inside grains can be detected by EBSD as the presence of these structures results in small misorientations, i.e. low angle boundaries (LAB) around them [46]. LAB fraction is useful to quantify the changes in misorientations with increasing plastic deformation. Figure 7.16 shows that the LAB fraction varies almost linearly with increasing plastic deformation. This linearity was used as a calibration to determine the variation of plastic deformation in specimen W_{20} which has a 20% prestrained base metal subjected to heat during welding. The prediction of plastic deformation on specimen W_{20} by using LAB fraction is given in Figure 7.21. Rearrangement of dislocations and partial annihilation occur as a result of heat dissipated during welding; therefore, the misorientations produced by the pile-ups near grain boundaries and heterogeneous dislocation structures inside grains are affected. The trend in Figure 7.21 is similar to the prediction obtained using the anisotropy strains in Figure 7.19 and using the peak widths in Figure 7.20.

Prediction of plastic deformation in tube A_0, A_{10} and A_{20} using hardness

The hardness profiles on the as-welded cross-weld specimens are given in Figure 5.13. The hardness of the plain, 10% pre-strained and 20% prestrained material which is not influenced by welding is 154, 218 and 251 H_V, respectively. The hardness measurements on cross-weld samples can be used to predict the plastic deformation in tubes A_0, A_{10} and A_{20} by calibrating these measurements with a linear fit to the hardness of the plain and pre-strained base metals as shown in Figure 7.22(a). The

prediction of plastic deformation on specimens C_0, C_{10} and C_{20} using hardness is presented in Figure 7.22(b).

Prediction of plastic deformation in tube A_0, A_{10} and A_{20} using DIC

The local stress-strain curves which were mentioned in Chapter 6 can also be used to predict the plastic deformation in tubes A_0, A_{10} and A_{20}. The local engineering stress-strain curves were obtained using the DIC integrated tension test of the specimen C_0, C_{10} and C_{20}. For the prediction of plastic deformation, true stress-strain curves were calculated from engineering stress-strain curves. The effective true plastic strain at local positions can be found by shifting the local true stress-strain curves with respect to a reference curve. The amount of the shift at which the hardening parts of local true stress-strain curve and the reference curve coincides gives the effective true plastic strain (Figure 7.23). The true stress-strain curve of plain material was used as a reference curve. This process was performed for every local stress-strain curves by using a MatLab script and the plastic strain was determined spatially on the sample surface. The plastic strain predicted using local stress-strain curves on specimens C_0, C_{10} and C_{20} is presented in Figure 7.24. Due to the fact that the base metal beyond 9mm in specimen C_{20} did not deform when the weld ruptured, predictions of plastic strain were done using the local curves in the region from 4mm to 9mm from the WCL.

Comparison of the plastic deformation in tube A_{20} predictions

A comparison of plastic deformation predictions using several techniques is given in Figure 7.25. It is seen that there is a good agreement in the trends of different predictions. EBSD, DIC and hardness predicts almost the same value at ~5mm from

WCL. Similarly, the predictions of DIC, ND-peak width and hardness at ~9mm from WCL are comparable. There is more deviation for neutron diffraction and EBSD predictions whereas DIC and hardness agree very well up to 9mm from the WCL. Note that EBSD, DIC and hardness are surface measurements and ND is a bulk measurement.

For hardness measurements, the surface of the sample was ground and polished as explained in Chapter 5 Material Characterization. The hardness measurement may be affected by surface preparation if the indent penetration is not deep enough (see Figure 5.13). In these hardness measurements 5kgf was used and it was observed that the indent penetrates enough to obtain relevant data under the surface (Figure 5.12). Although the hardness and DIC predictions are very similar, the calibration curve, which was a linear fit to the hardness values of plain, 10% and 20% prestrained material, should be improved by adding the hardness measurements at more prestraining levels between 0% and 20%.

In Chapter 6, it was discussed that the DIC experimental procedure may cause anomalies on the local stress-strain curves. Therefore, the prediction of plastic strain may also be affected due to the anomalies. In the same chapter, it had been observed that the anomalies appear below 1% deformation and the curves were normal at higher deformation (>1%). This observation suggests that the prediction of plastic strain using local stress-strain curves is reliable above 1% plastic strain. The predictions using DIC and hardness are in good agreement, which also confirms that the prediction using local stress-strain curves obtained by DIC is reliable.

It is seen that EBSD predicts about 1-4% more plastic strain relative to the prediction based on hardness measurements. For EBSD measurements a conventional surface preparation technique, which included grinding and polishing, was used. It is possible that the surface grinding might have altered the dislocation structure on the sample surface, which resulted in higher plastic deformation prediction.

In Figure 7.25 it can be seen that prediction of plastic strain using ND-anisotropy strain is in good agreement with other methods at 12 and 16mm whereas at 9mm where the other methods agree well, it predicts 6% less.

It was also observed that ND-peak width prediction, which was based on the full-width at half maximum (FWHM) of the peaks generated by the diffraction from 111 planes in the gauge volume, are 1-6% less than hardness. The peak width greatly depends on the dislocation intensity [30, 31]. The dislocation density may vary in the gauge volume because of double pass welding process. It is also difficult to differentiate the broadening effects of plastic deformation from those due to local material variations during welding process [29].

The difference in the degree of plastic deformation predicted by EBSD and ND techniques can probably be attributed to the fact that EBSD is a surface measurement, whilst, neutron diffraction is a bulk measurement. Note that the area where the LAB fraction was represented as a point on Figure 7.21 contains almost 300 grains whereas the volume where the neutron diffraction was applied contains over a million grains.

7.5 Conclusion

- Plastic deformation introduces many crystallographic changes such as the development of residual strains at the granular level, an increase in dislocation density and formation of dislocation pile-ups near grain boundaries, and dislocation bands and arrays inside the grains. These changes can be used to understand the deformation history of the material and quantify the degree of deformation.

- As the material is unloaded after 10, 15, 20 and 25% plastic deformation, significant residual strains develop in the loading direction due to the elastic anisotropy and strain redistribution due to slip along preferred systems. Texture results showed that the 111 and 200 planes are oriented perpendicular to the pre-straining direction with increasing plastic deformation. The strongest tensile strains develop on the 200 plane since it is more compliant compared to the 111 plane.

- Anisotropy strain was calculated using the averaged residual strains measured from 111 and 200 planes of the plain, 10%, 15%, 20% and 25% plastically deformed tube material. A linear line was fit to that data to be used for the prediction of the plastic strain in welded tubes. It was found that the prediction of plastic strain in specimen C_{20} using anisotropy strain was partially successful. The prediction of the plastic strain below 10% would be more accurate if the calibration curve was improved with more data points below 10% deformation and with a better curve fit.

- It was found that the increase in peak width linearly changes with increasing plastic deformation. Peak width is considered as a measure of dislocation density and is insensitive to the strain measurement direction. Therefore, variation of peak width

in welds can be calibrated with the linear relation between plastic deformation and peak width and can be used to quantify the plastic deformation in welds. The prediction of plastic deformation in specimen C_{20} which has a 20% prestrained base metal subjected to welding is promising.

- The low angle boundaries (LABs) due to the dislocation structures such as pile-ups near grain boundaries and dislocation bands and arrays inside the grains can be tracked by EBSD and can be used to quantify the plastic deformation. The fraction of LAB is a very simple and useful way of quantifying plastic deformation compared more complex methods, as long as the surface of the specimen is prepared very carefully and the optimum EBSD parameters (step size and magnification) are selected.

- It was observed that there is a good agreement in the predictions of the plastic strain in specimen C_{20} using DIC and hardness. These two techniques appear promising for the prediction of plastic strain.

7.6 References

[1] ASME Section I, ASME Boiler and Pressure Vessel Code, Section I: Rules for Construction of Power Boilers. New York, USA: ASME, 2010.

[2] Spindler M. Effects of plastic strain and heat treatment on microstructure and properties of 316 stainless steel tubing (Personal communication). 2008.

[3] Spindler M. Post-weld heat treatment of austenitic stainless steel welds in boiler units (Personal communication). 2011.

[4] Speidel MO, Magdowski RM. Stress corrosion cracking of nuclear reactor pressure vessel and piping steels. International Journal of Pressure Vessels and Piping 1988;34:119.

[5] García C, Martín F, Tiedra PD, Heredero JA, Aparicio ML. Effects of prior cold work and sensitization heat treatment on chloride stress corrosion cracking in type 304 stainless steels. Corrosion Science 2001;43:1519.

[6] Fournier L, Savoie M, Delafosse D. Influence of localized deformation on A-286 austenitic stainless steel stress corrosion cracking in PWR primary water. Journal of Nuclear Materials 2007;366:187.

[7] Yamazaki S, Lu Z, Ito Y, Takeda Y, Shoji T. The effect of prior deformation on stress corrosion cracking growth rates of Alloy 600 materials in a simulated pressurized water reactor primary water. Corrosion Science 2008;50:835.

[8] Ghosh S, Kain V. Effect of surface machining and cold working on the ambient temperature chloride stress corrosion cracking susceptibility of AISI 304L stainless steel. Materials Science and Engineering: A 2010;527:679.

[9] Angeliu TM, Andersen PL, Hall E, Sutliff JA, Sitzman S. Strain and microstructure characterization of austenitic stainless steel weld HAZs. National Association of Corrosion Engineers (NACE) Annual Conference, 2000.

[10] Marshall P. Austenitic Stainless Steels: Microstructure and Mechanical Properties: Elsevier Applied Science Publishers, 1984.

[11] Willis M, McDonaugh-Smith A, Hales R. Prestrain effects on creep ductility of a 316 stainless steel light forging. International Journal of Pressure Vessels and Piping 1999;76:355.

[12] Wilshire B, Willis M. Mechanisms of strain accumulation and damage development during creep of prestrained 316 stainless steels. Metallurgical and Materials Transactions A 2004;35:563.

[13] Auzoux Q, Allais L, Caës C, Monnet I, Gourgues AF, Pineau A. Effect of pre-strain on creep of three AISI 316 austenitic stainless steels in relation to reheat cracking of weld-affected zones. Journal of Nuclear Materials;400:127.

[14] Sherry AH. Advances and challenges in structural integrity. Applied Mechanics and Materials 2007;7-8:13.

[15] Daymond MR, Bourke MAM, Von Dreele RB, Clausen B, Lorentzen T. Use of Rietveld refinement for elastic macrostrain determination and for evaluation of plastic strain history from diffraction spectra. Journal of Applied Physics 1997;82:1554.

[16] Smith DJ, Leggatt RH, Webster GA, Macgillivray HJ, Webster PJ, Mills G. Neutron diffraction measurements of residual stress and plastic deformation in an aluminium alloy weld. The Journal of Strain Analysis for Engineering Design 1988;23:201.

[17] Kamaya M, Wilkinson AJ, Titchmarsh JM. Measurement of plastic strain of polycrystalline material by electron backscatter diffraction. Nuclear Engineering and Design 2005;235:713.

[18] Daymond MR. Internal Stresses in Deformed Crystalline Aggregates. Reviews in Mineralogy and Geochemistry 2006;63:427.

[19] Dieter GE, Bacon D. Mechanical Metallurgy: McGraw Hill Book Co., 1988.

[20] Hutchings MT, Withers PJ, Holden TM, Lorentzen T. Introduction to the characterization of residual stress by neutron diffraction: Taylor & Francis, 2005.

[21] Pang JWL, Holden TM, Wright JS, Mason TE. The generation of intergranular strains in 309H stainless steel under uniaxial loading. Acta Materialia 2000;48:1131.

[22] Peng RL, Oden M, Wang YD, Johansson S. Intergranular strains and plastic deformation of an austenitic stainless steel Materials Science and Engineering 2002;A334:215.

[23] Wang Y-D, Tian H, Stoica AD, Wang X-L, Liaw PK, Richardson JW. The development of grain-orientation-dependent residual stressess in a cyclically deformed alloy. Nat Mater 2003;2:101.

[24] Larsson C, Clausen B, Holden TM, Bourke MAM. Measurements and predictions of strain pole figures for uniaxially compressed stainless steel. Scripta Materialia 2004;51:571.

[25] Daymond MR, Bouchard PJ. Elastoplastic Deformation of 316 Stainless Steel Under Tensile Loading at Elevated Temperatures. Metallurgical and Materials Transactions A 2006;37A:1863.

[26] Quinta da Fonseca J, Oliver EC, Bate PS, Withers PJ. Evolution of intergranular stresses during in situ straining of IF steel with different grain sizes. Materials Science and Engineering: A 2006;437:26.

[27] Verhoeven JD. Fundamentals of Physical Metallurgy: Wiley, 1975.

[28] Korsunsky AM, Daymond MR, James KE. The correlation between plastic strain and anisotropy strain in aluminium alloy polycrystals. Materials Science and Engineering A 2002;334:41.

[29] Lewis SJ, Truman CE. Diffraction measurements for evaluating plastic strain in A533B ferritic steel - a feasibility study. Journal of Physics D: Applied Physics 2010;43:265501.

[30] Wang XL, Wang YD, Stoica AD, Horton DJ, Tian H, Liaw PK, Choo H, Richardson JW, Maxey E. Inter- and intragranular stresses in cyclically-deformed 316 stainless steel. Materials Science and Engineering: A 2005;399:114.

[31] Huang EW, Barabash RI, Wang Y, Clausen B, Li L, Liaw PK, Ice GE, Ren Y, Choo H, Pike LM, Klarstrom DL. Plastic behavior of a nickel-based alloy under monotonic-tension and low-cycle-fatigue loading. International Journal of Plasticity 2008;24:1440.

[32] Smith DJ, Webster GA. The measurement of prior plastic deformation in metallic alloys using the neutron diffraction technique. The Journal of Strain Analysis for Engineering Design 1997;32:37.

[33] Sun Y, Barabash R, Choo H, Liaw PK, Lu Y, Brown DW, Ice GE. Mutiscale plastic deformation near a fatigue crack from diffraction. Solid State Phenomena 2007;129:151.

[34] Jun TS, Hofmann F, Belnoue J, Song X, Hofmann M, Korsunsky AM. Triaxial residual strains in a railway rail measured by neutron diffraction. The Journal of Strain Analysis for Engineering Design 2009;44:563.

[35] Woo W, Ungár T, Feng Z, Kenik E, Clausen B. X-Ray and Neutron Diffraction Measurements of Dislocation Density and Subgrain Size in a Friction-Stir-Welded Aluminum Alloy. Metallurgical and Materials Transactions A 2009;41:1210.

[36] Kamaya M, Wilkinson AJ, Titchmarsh JM. Quantification of plastic strain of stainless steel and nickel alloy by electron backscatter diffraction. Acta Materialia 2006;54:539.

[37] Yoda R, Yokomaku T, Tsuji N. Plastic deformation and creep damage evaluations of type 316 austenitic stainless steels by EBSD. Materials Characterization;61:913.

[38] Preuss M, Withers P, Pang J, Baxter G. Inertia welding nickel-based superalloy: Part I. Metallurgical characterization. Metallurgical and Materials Transactions A 2002;33:3215.

[39] Brewer LN, Othon MA, Young LM, Angeliu TM. Misorientation mapping for visualization of plastic deformation via electron back-ccattered diffraction. Microscopy and Microanalysis 2006;12:85.

[40] Campbell SI, Akeroyd FA, Moreton-Smith CM. *Open GENIE - Analysis and Control,* Condensed Matter. 2002.

[41] Balzar D. Voigt-Function Model in Diffraction Line-Broadening Analysis Defect and Microstructure Analysis from Diffraction New York: Oxford University Press, 1999. p.94.

[42] Hielscher R, Bachmann F. MTEX Quantitative Texture Analysis Software. 2010.

[43] Dingley D. Progressive steps in the development of electron backscatter diffraction and orientation imaging microscopy. Journal of Microscopy 2004;213:214.

[44] Feaugas X. On the origin of the tensile flow stress in the stainless steel AISI 316L at 300 K: back stress and effective stress. Acta Materialia 1999;47:3617.

[45] Thurber WC. Deformation Textures in Uranium-Aluminium Alloy. Oak Ridge National Laboratory, 1958.

[46] Bate PS, Knutsen RD, Brough I, Humphreys FJ. The characterization of low-angle boundaries by EBSD. Journal of Microscopy 2005;220:36.

7.7 Tables & Figures

Plastic Deformation	Label
Plain	T_0
10%	T_{10}
15%	T_{15}
20%	T_{20}
25%	T_{25}

Table 7.1 The labelling of the samples which were used for texture measurements in Stress-Spec, FRMII

	Plastic Deformation	Label
Parent	Plain	P_0
	10%	P_{10}
	15%	P_{15}
	20%	P_{20}
	25%	P_{25}
Cross-Weld	20%	W_{20}

Table 7.2 The labelling of the samples which were used for EBSD

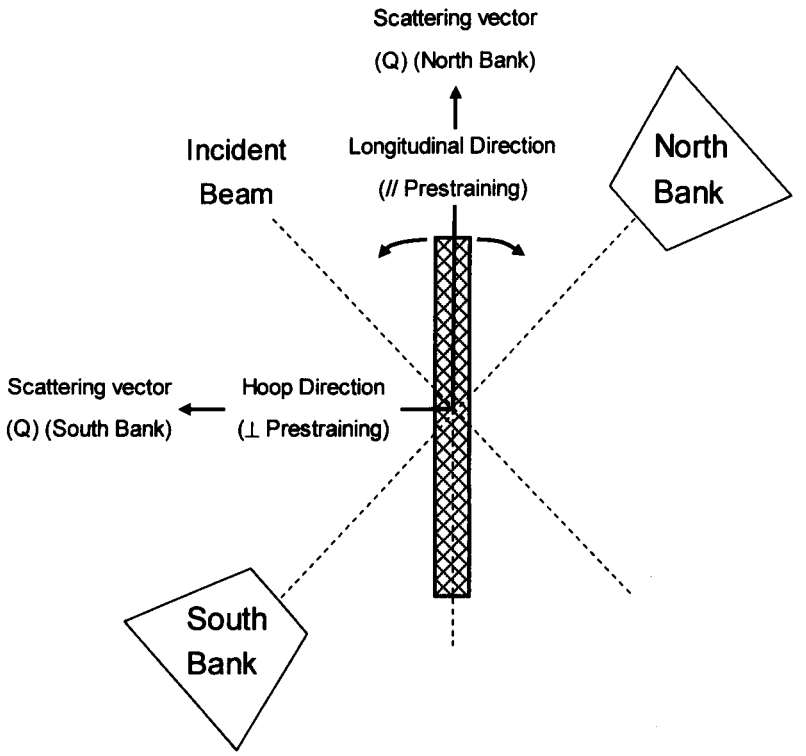

Figure 7.1 Orientation of the specimen with respect to the incident beam on Engin-X, ISIS. Longitudinal direction (LD) of the tube is parallel (//) to the pre-straining direction. Hoop direction (HD) was assumed to be perpendicular (⊥) to the pre-straining direction through the width of the specimen. Radial direction (RD) is the direction into the page and ⊥ to the pre-straining direction. To obtain measurements at different angles the specimen was rotated as indicated by the arrows while the centre of the specimen is fixed.

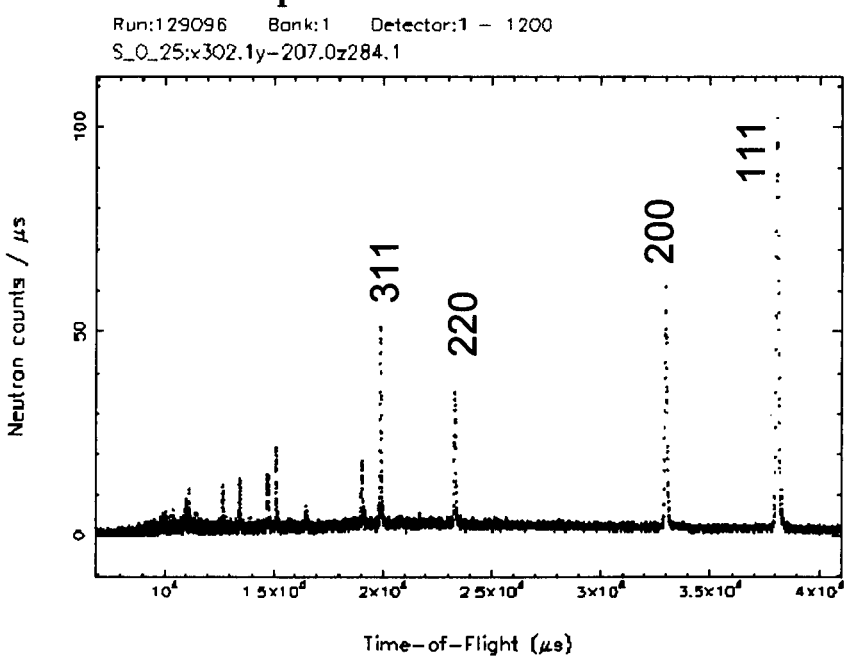

Figure 7.2 The diffraction pattern obtained at Engin-X, ISIS. The diffraction from 111, 200, 220 and 311 planes is also identified.

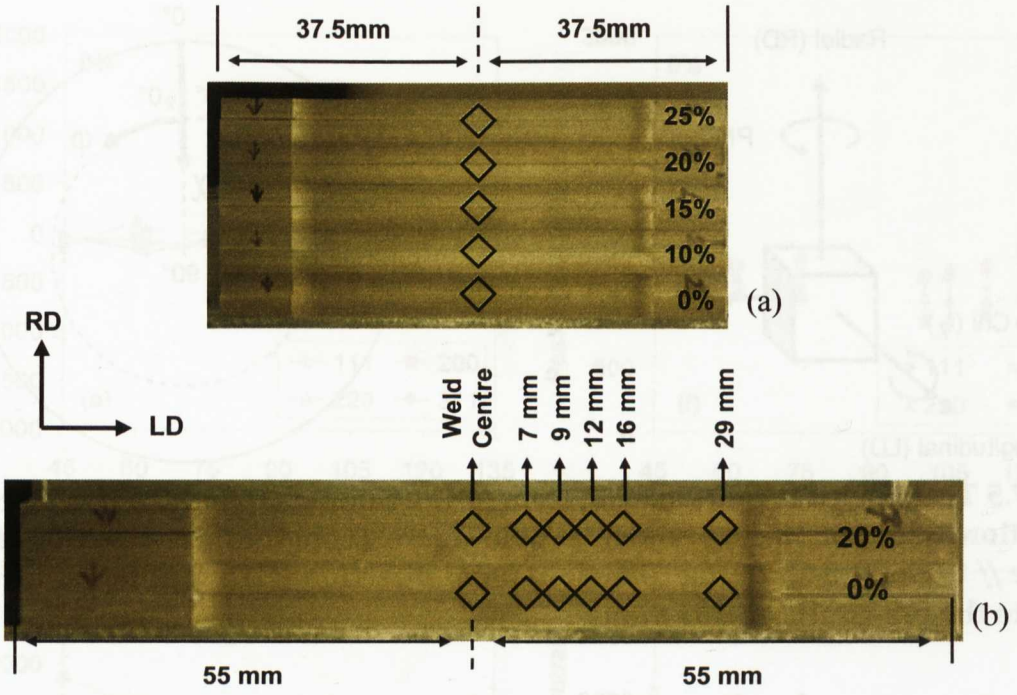

Figure 7.3 The measurement positions in the stacked: parent (remote-end) specimens (a) and cross-weld specimens (b)

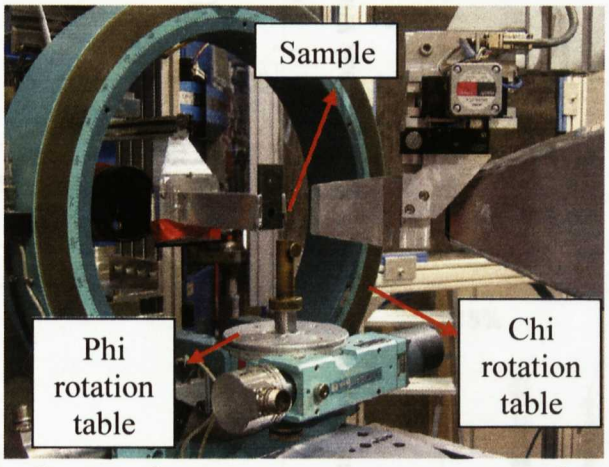

Figure 7.4 Experimental setup for texture measurement at Stress-Spec. The rotation angles on the Eulerian cradle are also shown.

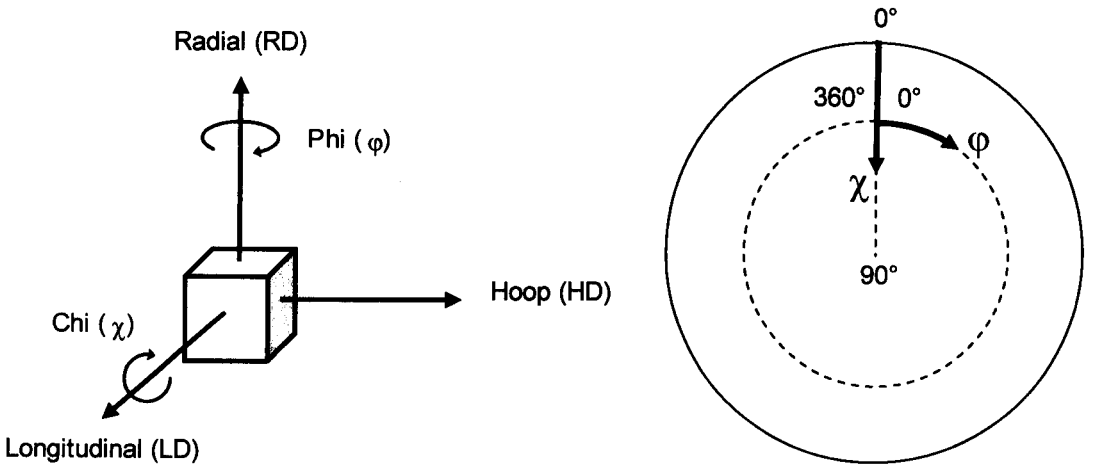

Figure 7.5 The spherical coordinate system of the sample (a) and the description of the rotation angles on the experimental pole figure. (Longitudinal direction (LD) of the tube // to the pre-straining direction, hoop direction (HD) and radial direction (RD) ⊥ to the pre-straining direction)

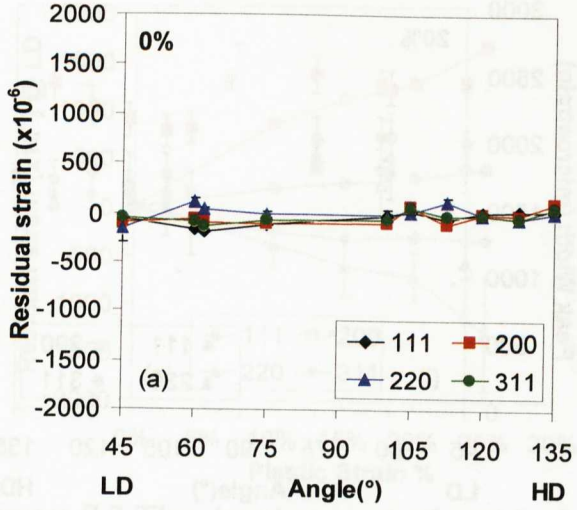
0%
Residual strain (x10⁻⁶)
2000
1500
1000
500
0
-500
-1000
-1500
-2000
111
200
220
311
(a)
45
60
75
90
105
120
135
LD
Angle(°)
HD

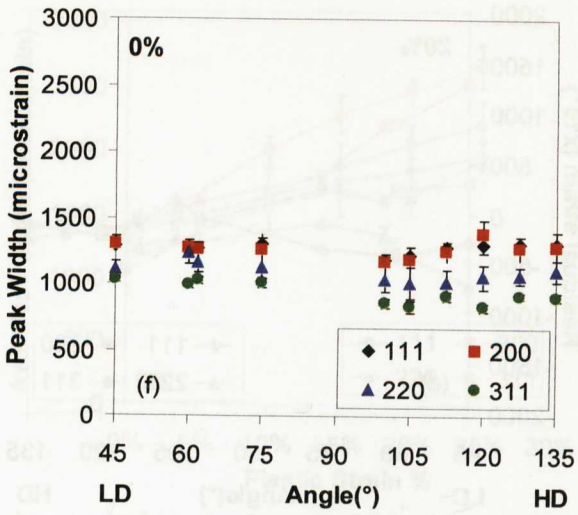
0%
Peak Width (microstrain)
3000
2500
2000
1500
1000
500
0
111
200
220
311
(f)
45
60
75
90
105
120
135
LD
Angle(°)
HD

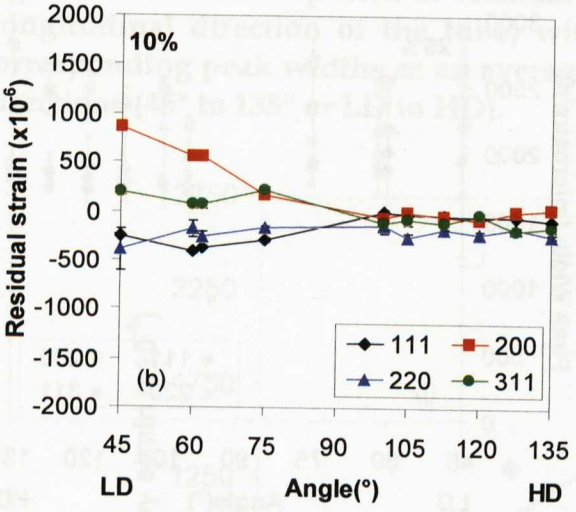
10%
Residual strain (x10⁻⁶)
2000
1500
1000
500
0
-500
-1000
-1500
-2000
111
200
220
311
(b)
45
60
75
90
105
120
135
LD
Angle(°)
HD

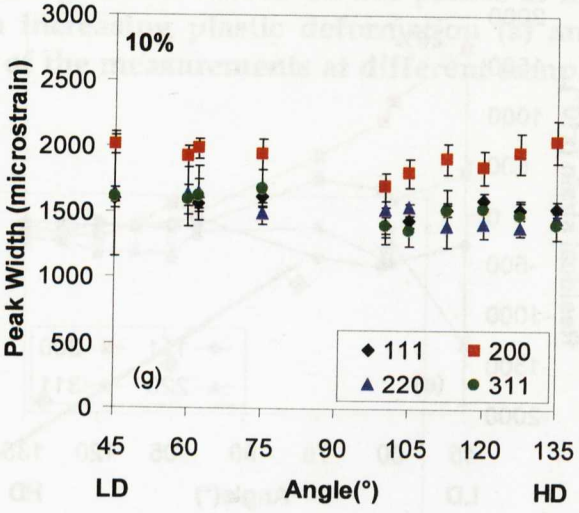
10%
Peak Width (microstrain)
3000
2500
2000
1500
1000
500
0
111
200
220
311
(g)
45
60
75
90
105
120
135
LD
Angle(°)
HD

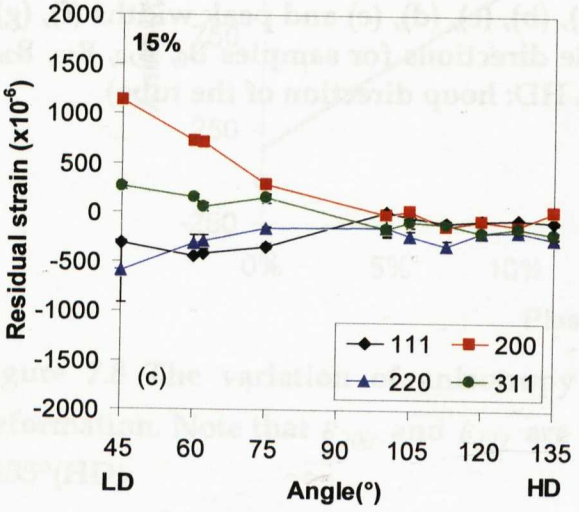
15%
Residual strain (x10⁻⁶)
2000
1500
1000
500
0
-500
-1000
-1500
-2000
111
200
220
311
(c)
45
60
75
90
105
120
135
LD
Angle(°)
HD

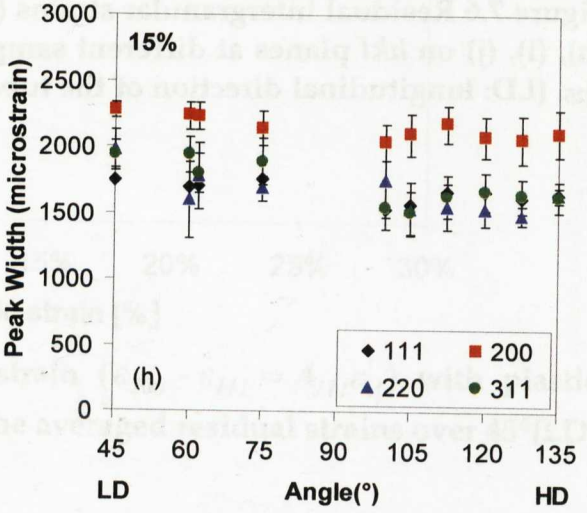
15%
Peak Width (microstrain)
3000
2500
2000
1500
1000
500
0
111
200
220
311
(h)
45
60
75
90
105
120
135
LD
Angle(°)
HD

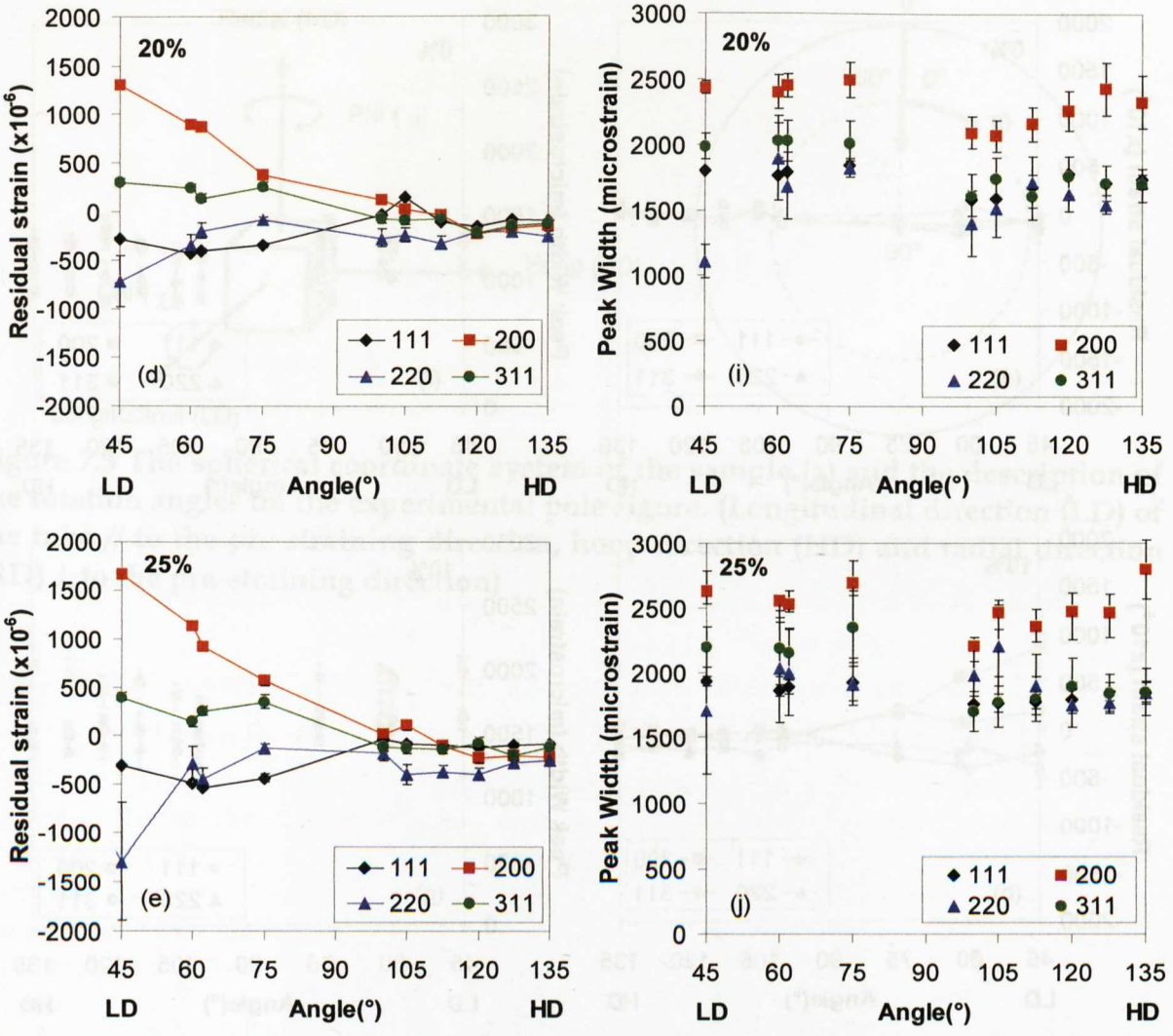

Figure 7.6 Residual intergranular strains (a), (b), (c), (d), (e) and peak widths (f), (g), (h), (i), (j) on *hkl* planes at different sample directions for samples B_0, B_{10}, B_{15}, B_{20}, B_{25}. (LD: longitudinal direction of the tube, HD: hoop direction of the tube)

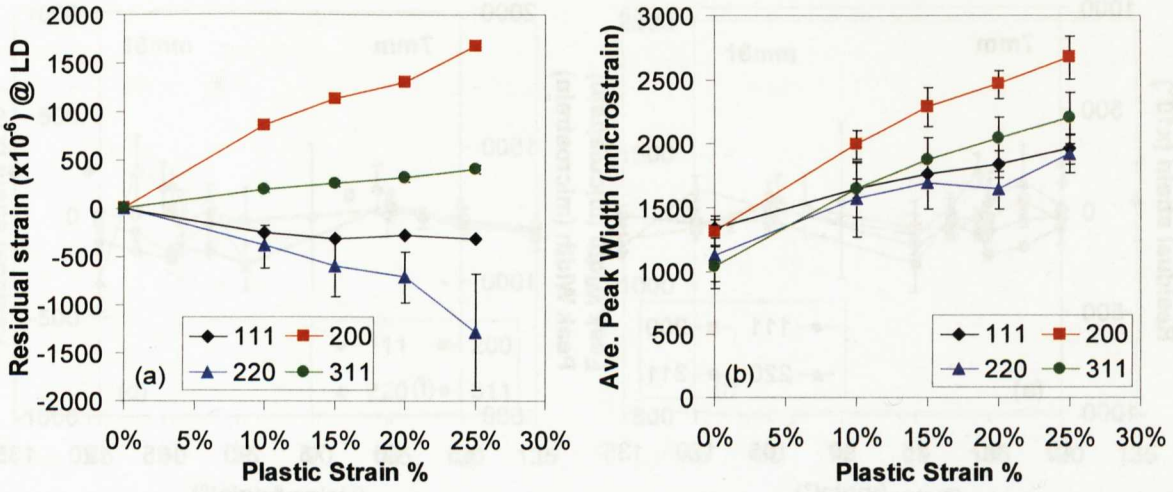

Figure 7.7 The development of residual intergranular strains on *hkl* planes at LD (longitudinal direction of the tube) with increasing plastic deformation (a) and corresponding peak widths as an average of the measurements at different sample directions (45° to 135° or LD to HD).

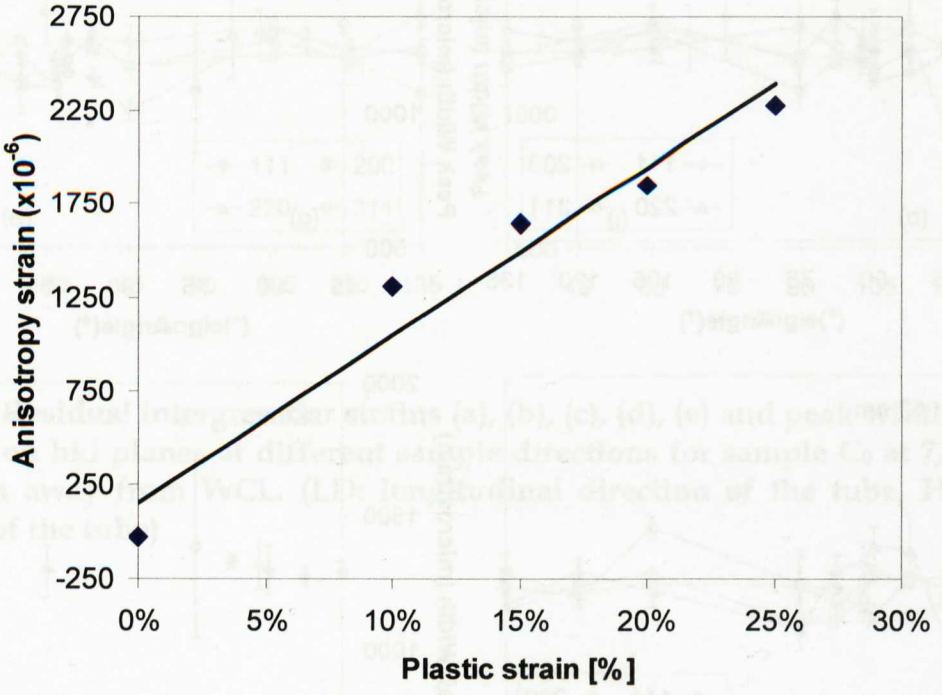

Figure 7.8 The variation of anisotropy strain ($\varepsilon_{200} - \varepsilon_{111} = A_{111}\varepsilon_A$) with plastic deformation. Note that ε_{200} and ε_{111} are the averaged residual strains over 45°(LD) - 135°(HD).

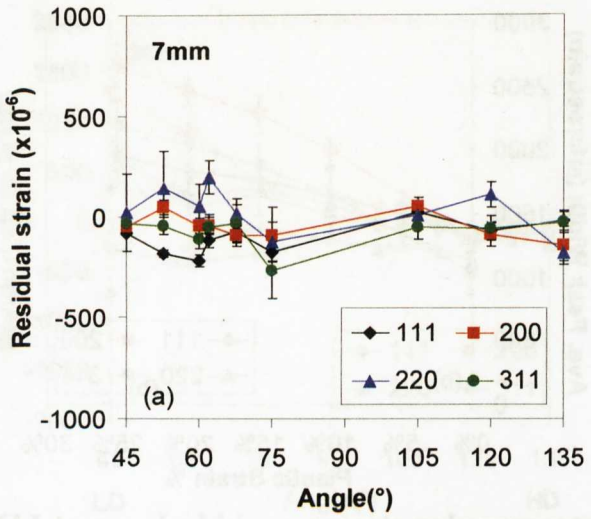
7mm
Residual strain (x10^{-6})
1000
500
0
-500
-1000
111
200
220
311
(a)
45
60
75
90
105
120
135
Angle(°)

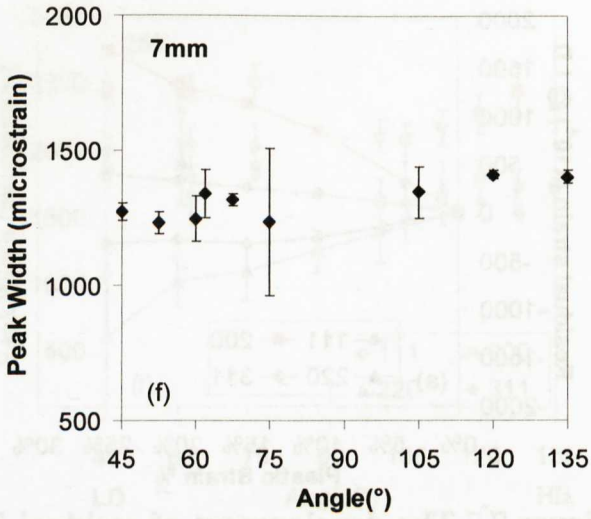
7mm
Peak Width (microstrain)
2000
1500
1000
500
(f)
45
60
75
90
105
120
135
Angle(°)

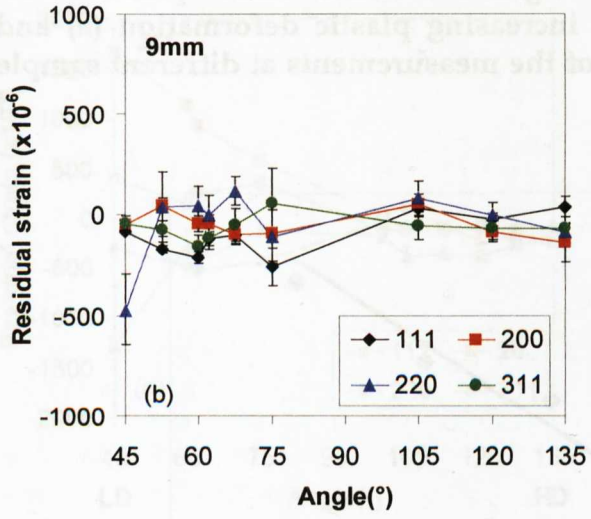
9mm
Residual strain (x10^{-6})
1000
500
0
-500
-1000
111
200
220
311
(b)
45
60
75
90
105
120
135
Angle(°)

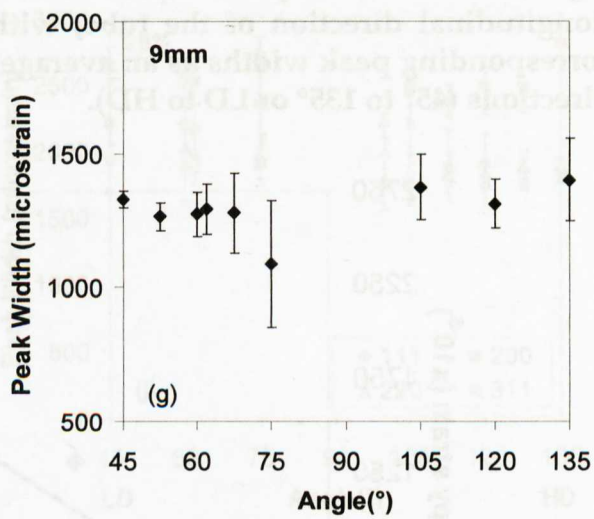
9mm
Peak Width (microstrain)
2000
1500
1000
500
(g)
45
60
75
90
105
120
135
Angle(°)

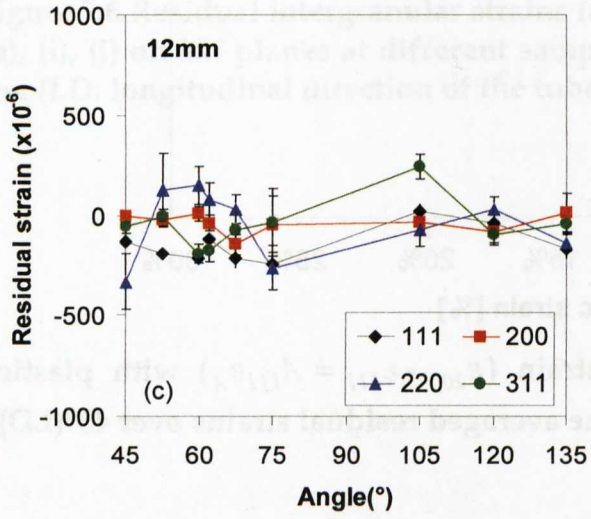
12mm
Residual strain (x10^{-6})
1000
500
0
-500
-1000
111
200
220
311
(c)
45
60
75
90
105
120
135
Angle(°)

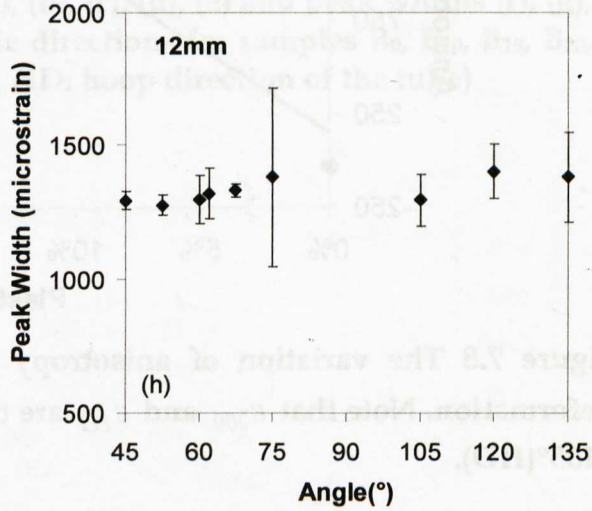
12mm
Peak Width (microstrain)
2000
1500
1000
500
(h)
45
60
75
90
105
120
135
Angle(°)

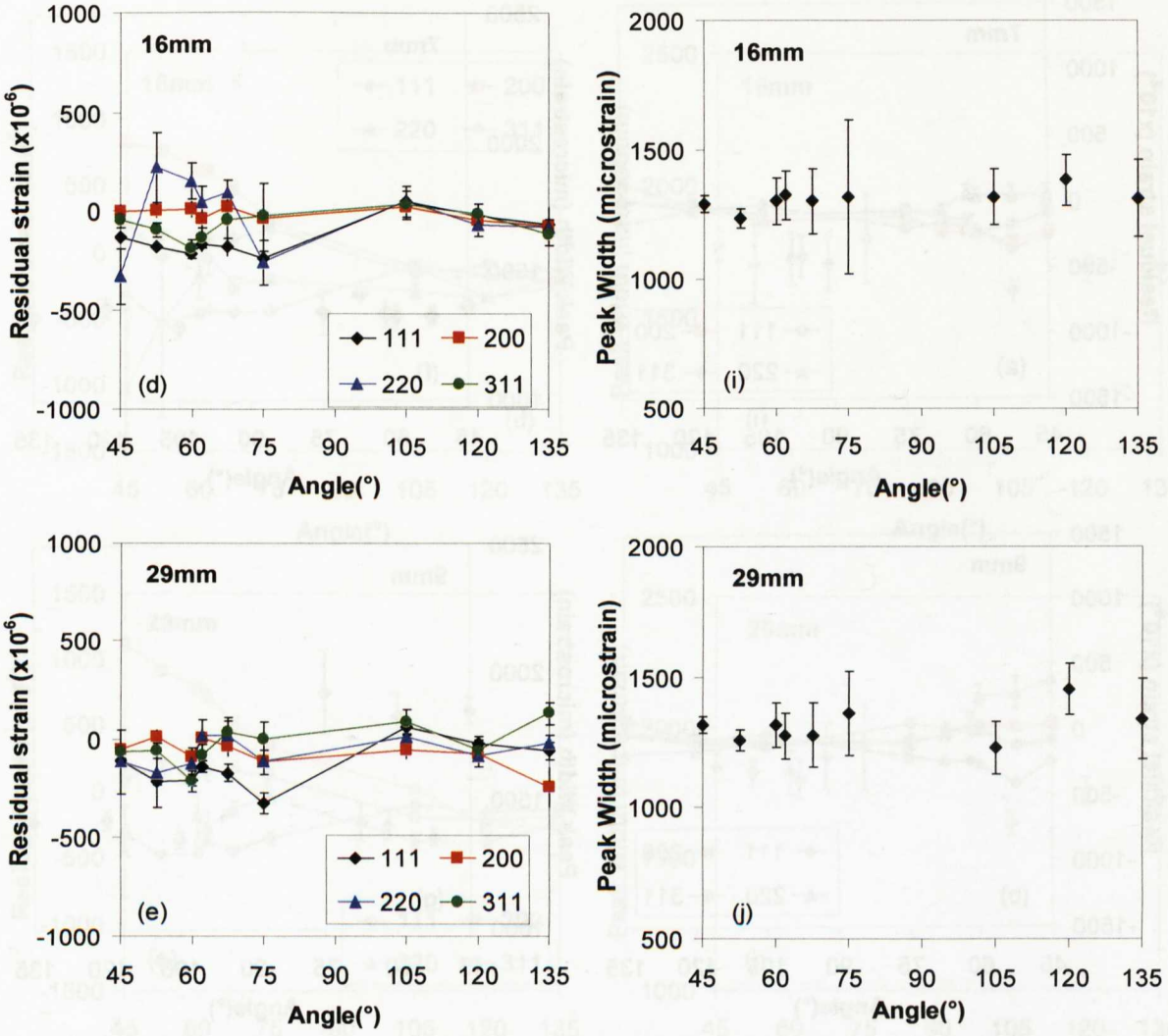

Figure 7.9 Residual intergranular strains (a), (b), (c), (d), (e) and peak widths (f), (g), (h), (i), (j) on hkl planes at different sample directions for sample C_0 at 7, 9, 12, 16 and 29mm away from WCL. (LD: longitudinal direction of the tube, HD: hoop direction of the tube)

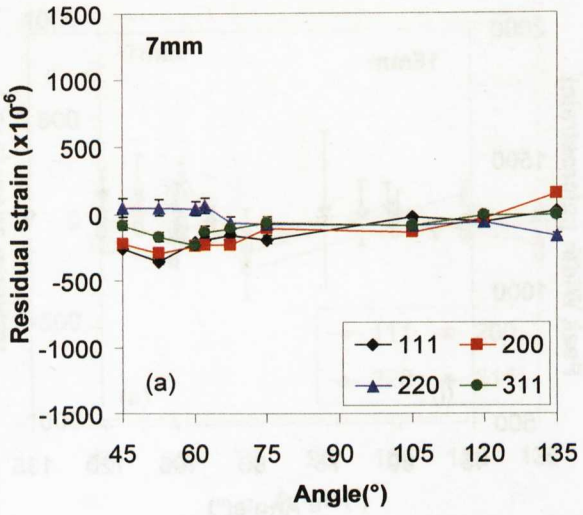
7mm
Residual strain (x10⁻⁶)
1500
1000
500
0
-500
-1000
-1500
45 60 75 90 105 120 135
Angle(°)
111 200
220 311
(a)

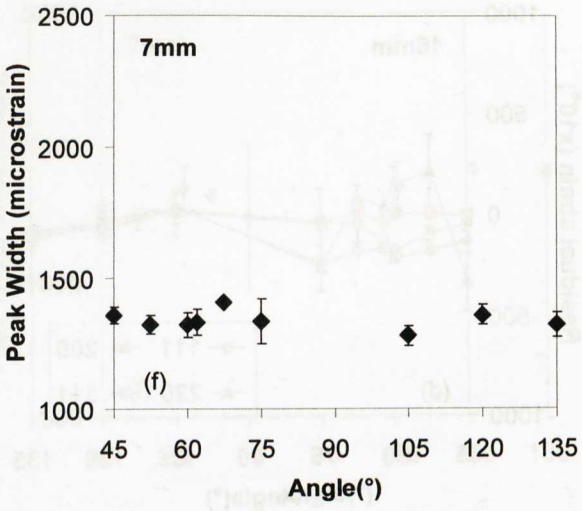
7mm
Peak Width (microstrain)
2500
2000
1500
1000
45 60 75 90 105 120 135
Angle(°)
(f)

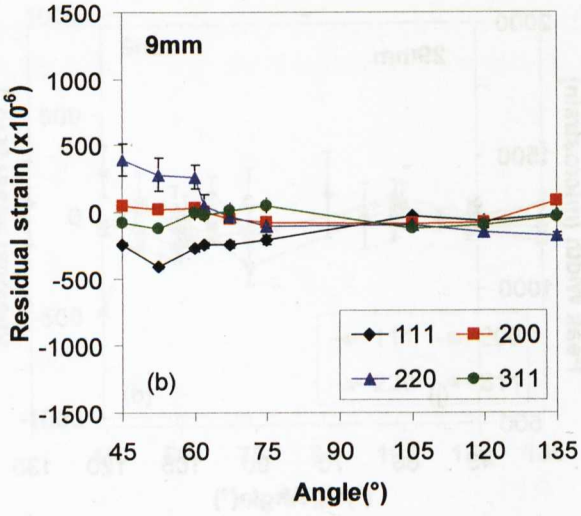
9mm
Residual strain (x10⁻⁶)
1500
1000
500
0
-500
-1000
-1500
45 60 75 90 105 120 135
Angle(°)
111 200
220 311
(b)

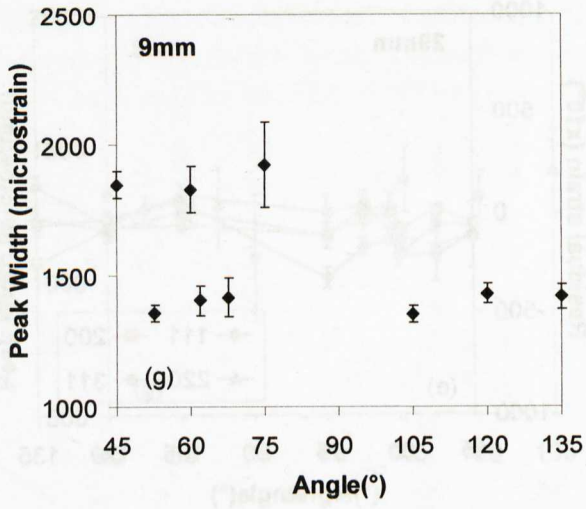
9mm
Peak Width (microstrain)
2500
2000
1500
1000
45 60 75 90 105 120 135
Angle(°)
(g)

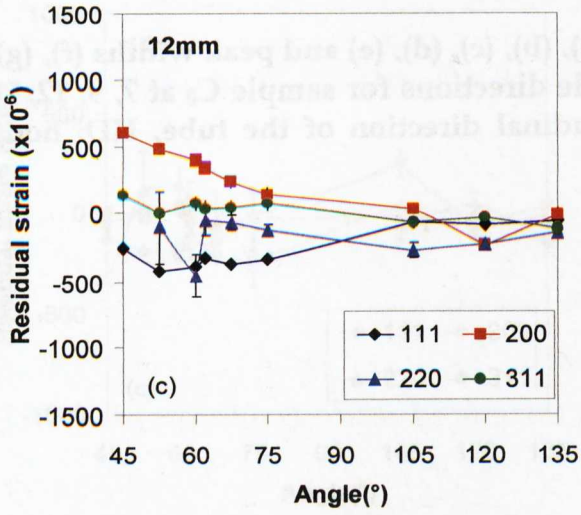
12mm
Residual strain (x10⁻⁶)
1500
1000
500
0
-500
-1000
-1500
45 60 75 90 105 120 135
Angle(°)
111 200
220 311
(c)

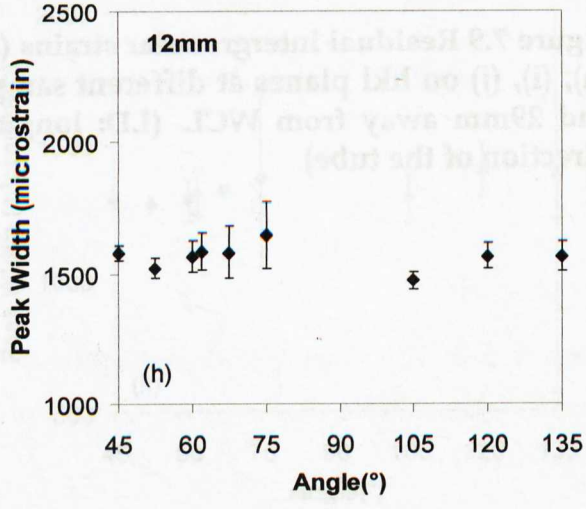
12mm
Peak Width (microstrain)
2500
2000
1500
1000
45 60 75 90 105 120 135
Angle(°)
(h)

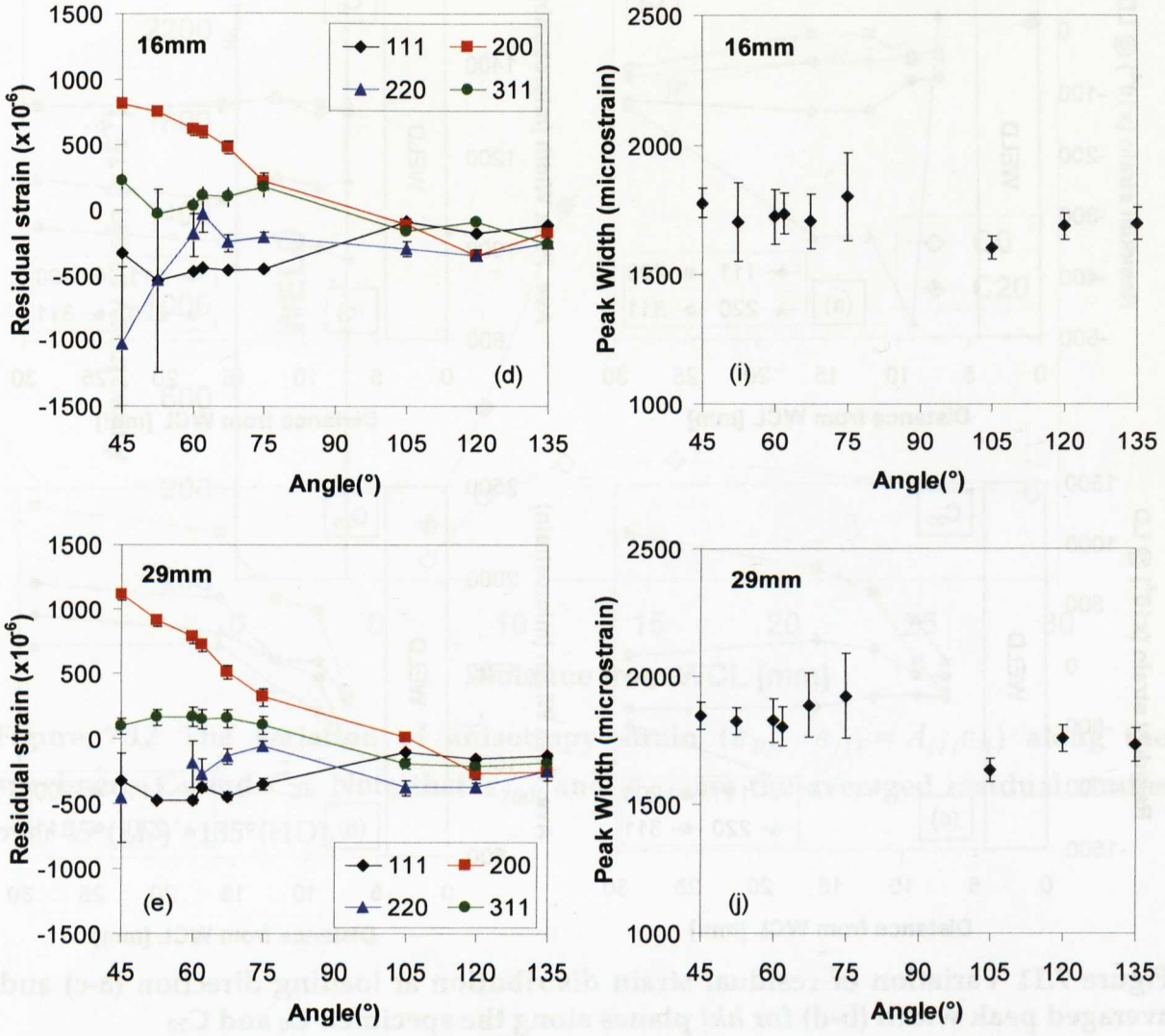

Figure 7.10 Residual intergranular strains (a), (b), (c), (d), (e) and peak widths (f), (g), (h), (i), (j) on hkl planes at different sample directions for sample C_{20} at 7, 9, 12, 16 and 29mm away from WCL. (LD: longitudinal direction of the tube, HD: hoop direction)

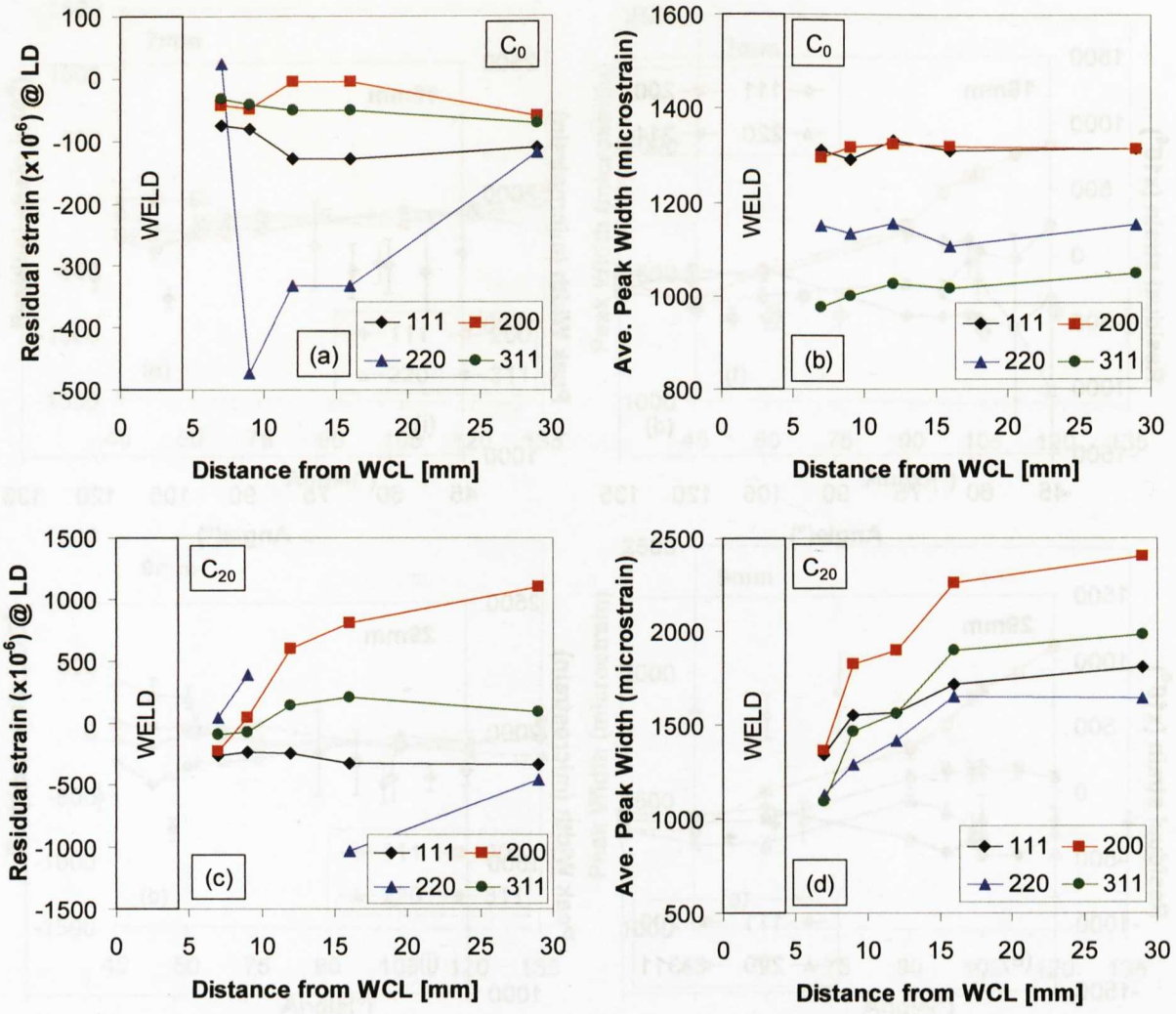

Figure 7.11 Variation of residual strain distribution at loading direction (a-c) and averaged peak width (b-d) for *hkl* planes along the specimen C_0 and C_{20}

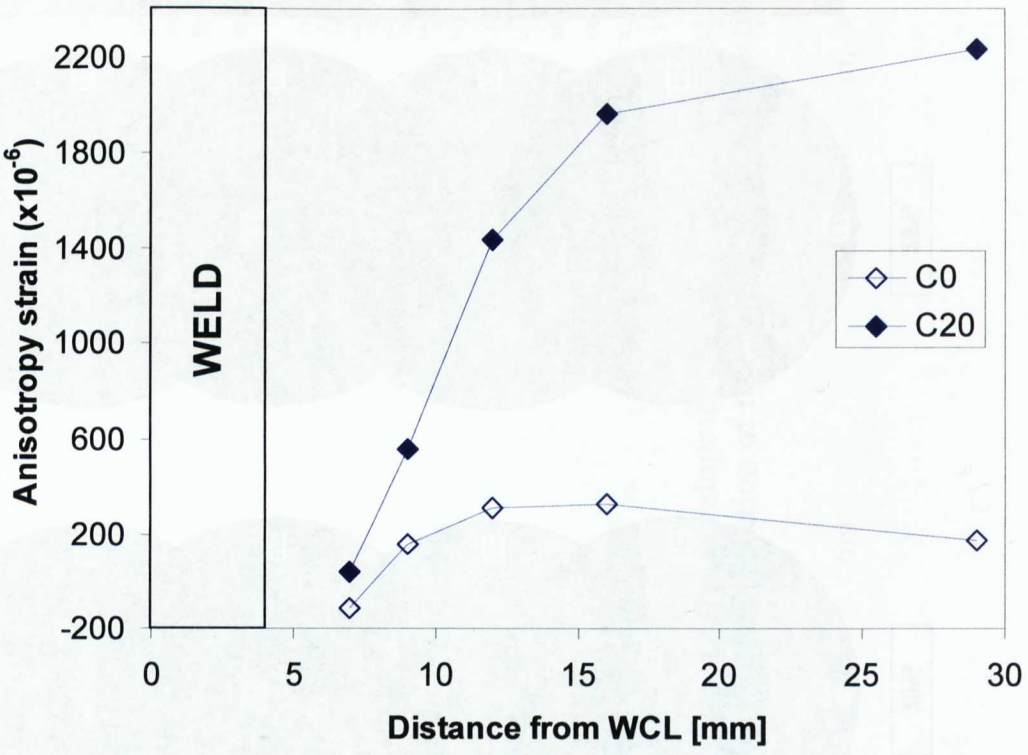

Figure 7.12 The variation of anisotropy strain ($\varepsilon_{200} - \varepsilon_{111} = A_{111}\varepsilon_A$) along the specimens C_0 and C_{20}. Note that ε_{200} and ε_{111} are the averaged residual strains over 45°(LD) - 135°(HD).

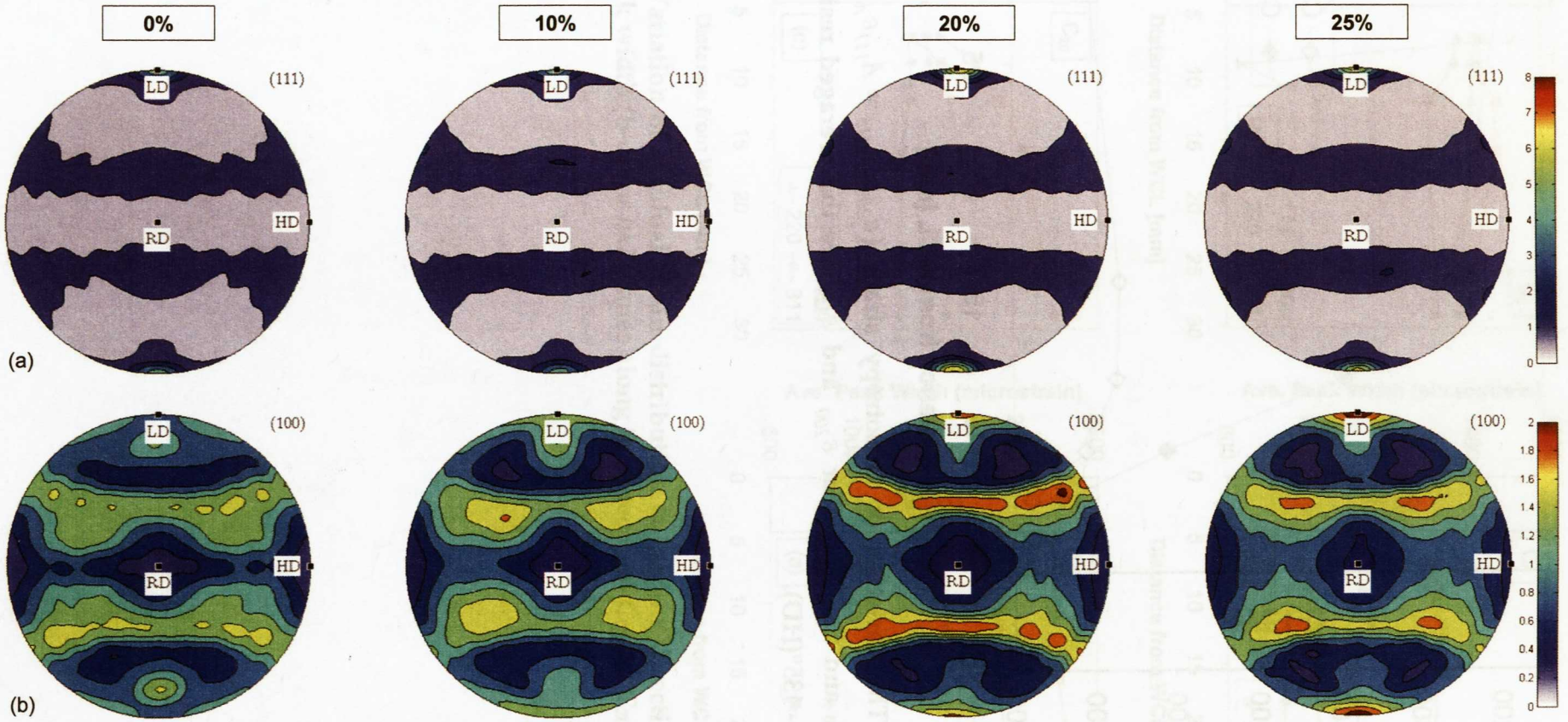
0%
10%
20%
25%
(a)
(b)
(111)
(100)
LD
RD
HD
8
7
6
5
4
3
2
1
0
2
1.8
1.6
1.4
1.2
1
0.8
0.6
0.4
0.2
0

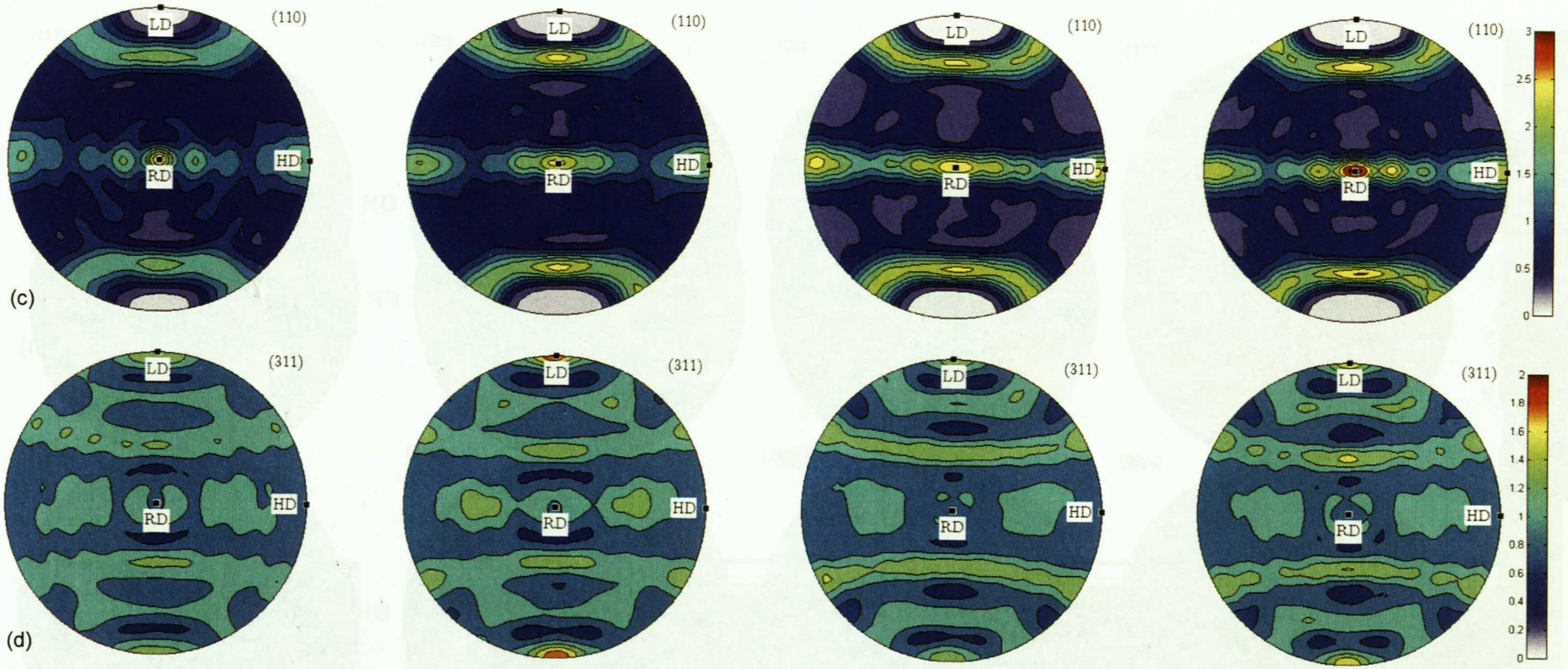

Figure 7.13 The pole figures of 111 (a), 100 (b), 110 (c) and 311 (d) planes showing the development of crystallographic texture in the parent material after 0, 10, 20 and 25% plastic deformation. (LD: longitudinal direction of the tube, HD: hoop direction, RD: radial direction)

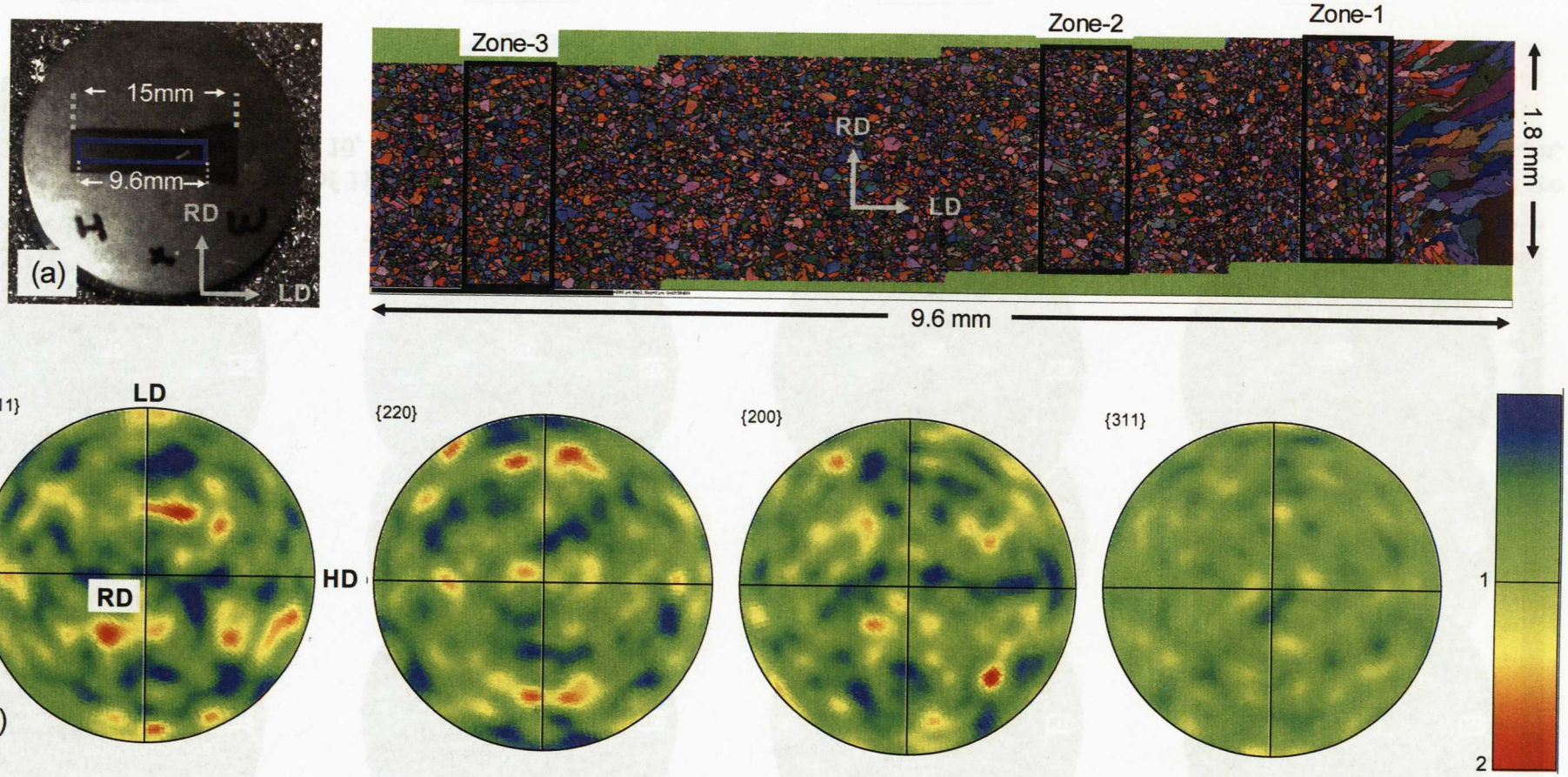
15mm
9.6mm
RD
LD
(a)
Zone-3
Zone-2
Zone-1
RD
LD
1.8 mm
9.6 mm
{111}
LD
RD
HD
{220}
{200}
{311}
1
2
(b)

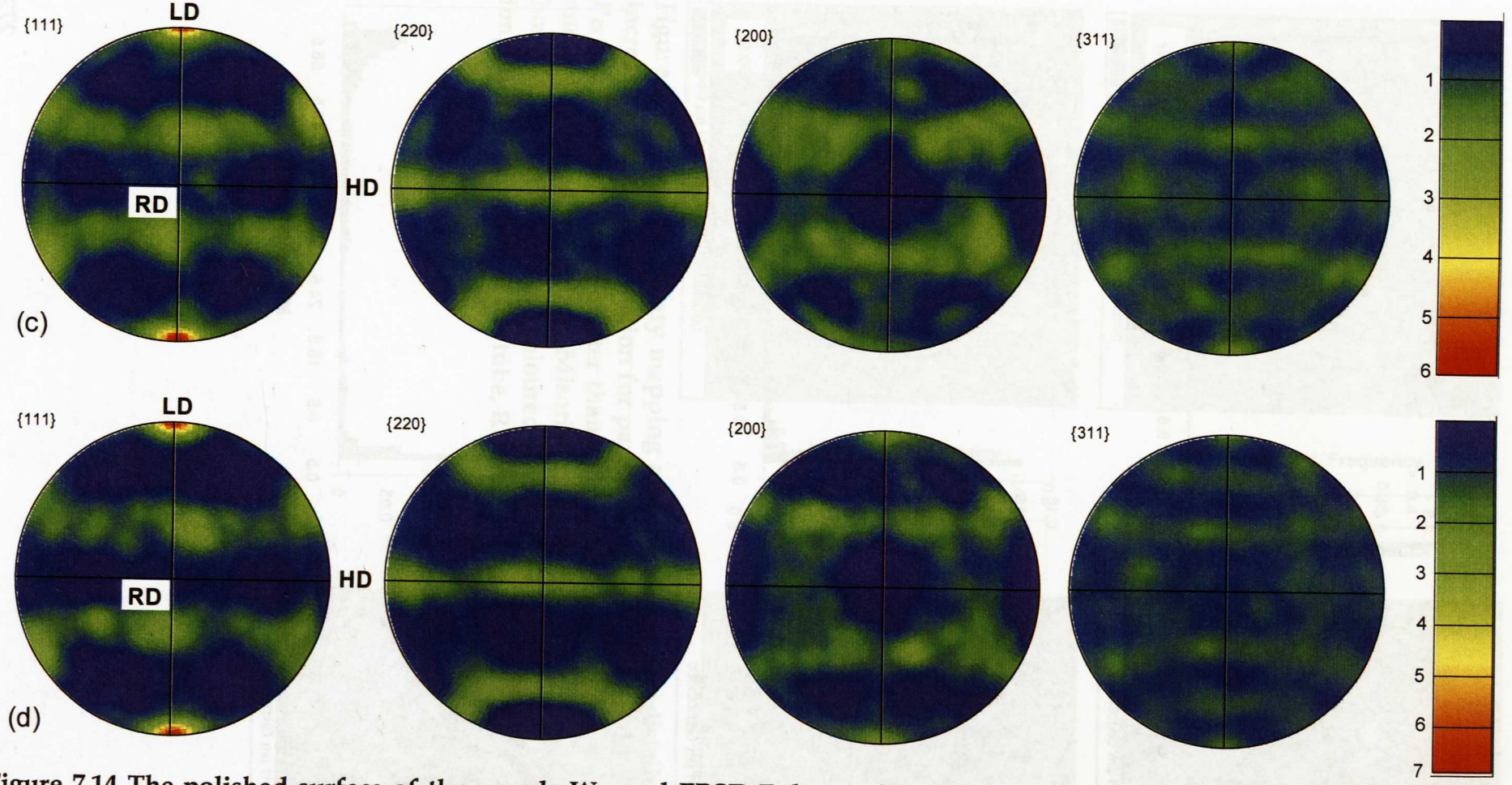

Figure 7.14 The polished surface of the sample W_{20} and EBSD Euler angles mapping obtained showing the different zones where the pole figures obtained (a) 111, 220, 200 and 311 pole figures are demonstrated in Zone-1(b), Zone-2 (c) and Zone-3 (d). (LD: longitudinal direction of the tube, HD: hoop direction, RD: radial direction)

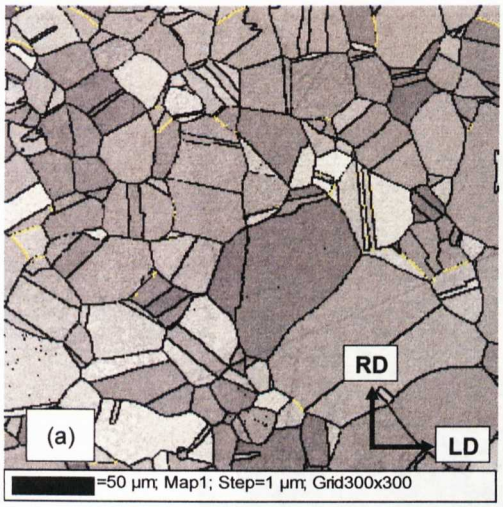
RD
LD
(a)
=50 µm; Map1; Step=1 µm; Grid300x300

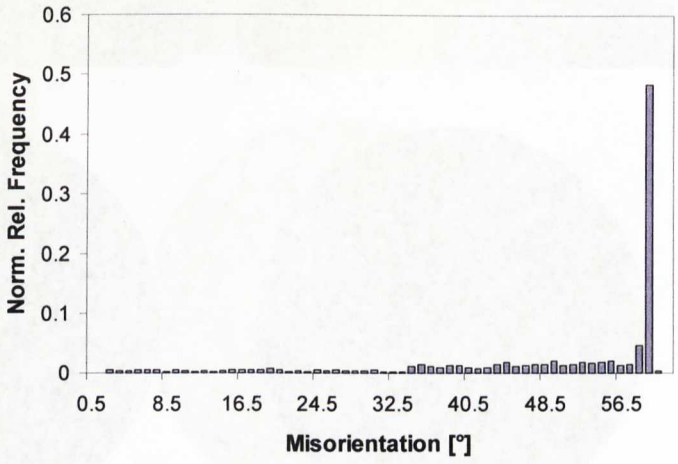
Norm. Rel. Frequency
0.6
0.5
0.4
0.3
0.2
0.1
0
0.5
8.5
16.5
24.5
32.5
40.5
48.5
56.5
Misorientation [°]

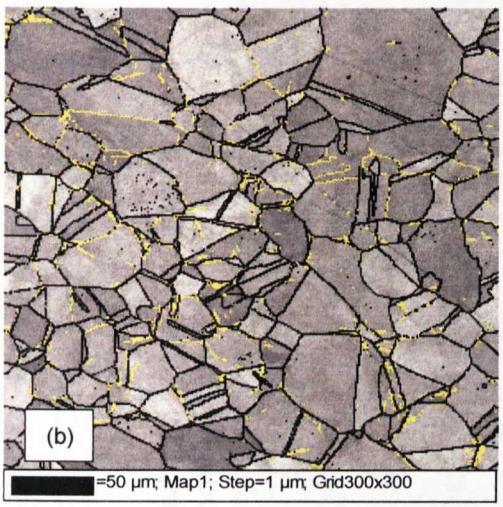
(b)
=50 µm; Map1; Step=1 µm; Grid300x300

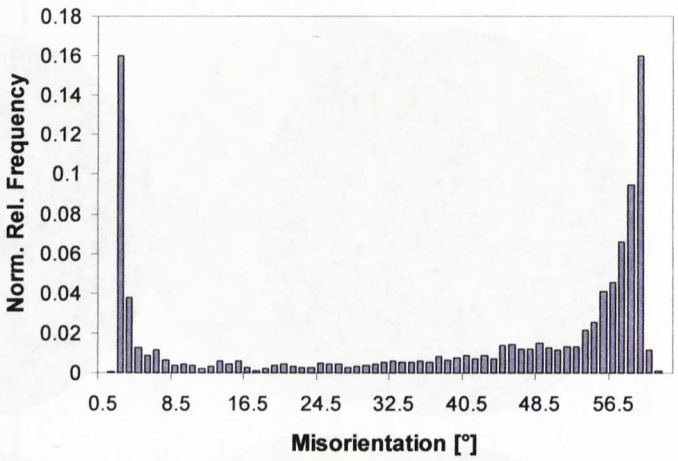
Norm. Rel. Frequency
0.18
0.16
0.14
0.12
0.1
0.08
0.06
0.04
0.02
0
0.5
8.5
16.5
24.5
32.5
40.5
48.5
56.5
Misorientation [°]

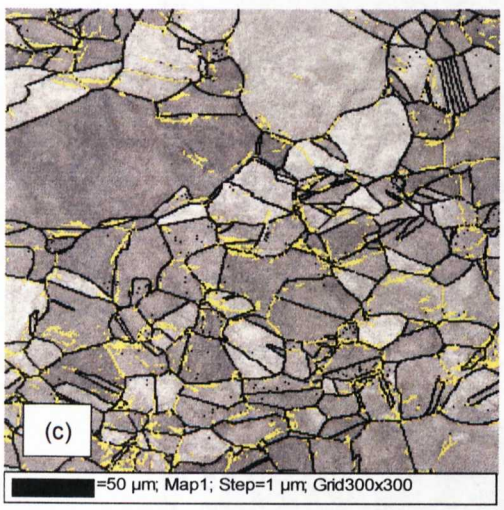
(c)
=50 µm; Map1; Step=1 µm; Grid300x300

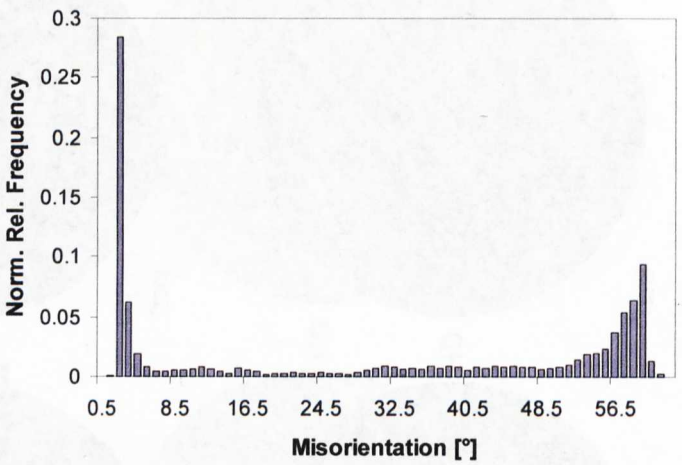
Norm. Rel. Frequency
0.3
0.25
0.2
0.15
0.1
0.05
0
0.5
8.5
16.5
24.5
32.5
40.5
48.5
56.5
Misorientation [°]

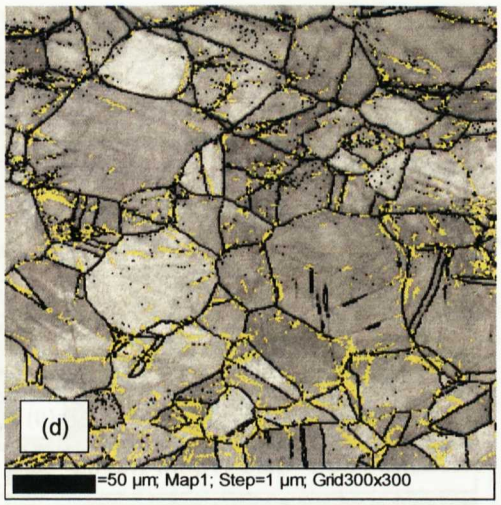

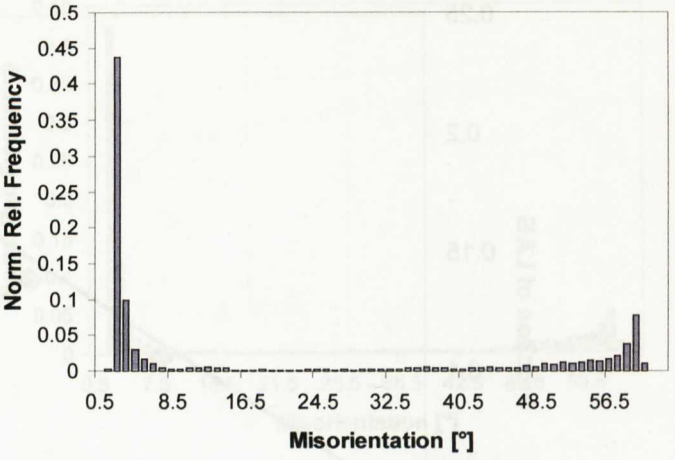

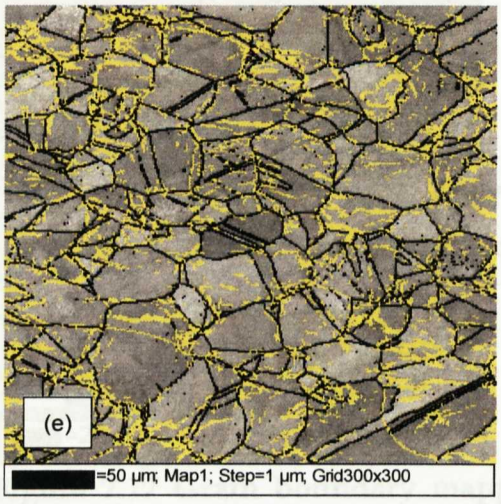

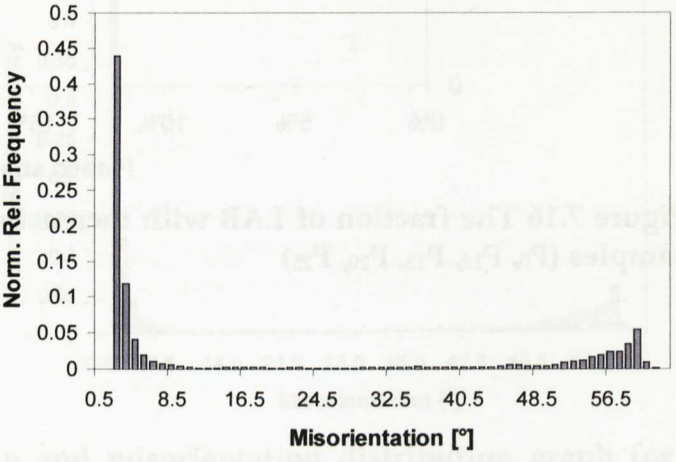

Figure 7.15 Grain boundary mapping and misorientation distribution graph with increasing plastic deformation for parent samples P_0 (a), P_{10} (b), P_{15} (c), P_{20} (d) and P_{25} (e). Misorientations greater than 15° are high angle grain boundaries (HAGB) and are coloured with black. Misorientation angle 2-15° represents low angle grain boundaries (LABs) and are coloured with yellow. The direction is given in (a). LD: longitudinal direction of the tube, RD: radial direction)

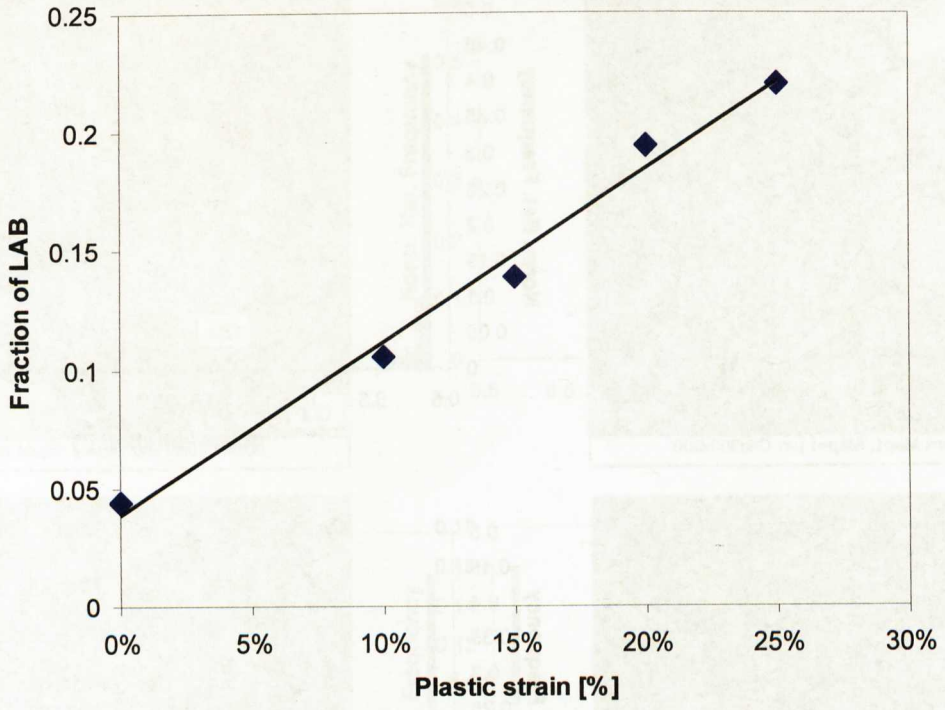

Figure 7.16 The fraction of LAB with increasing plastic deformation for the parent samples (P_0, P_{10}, P_{15}, P_{20}, P_{25})

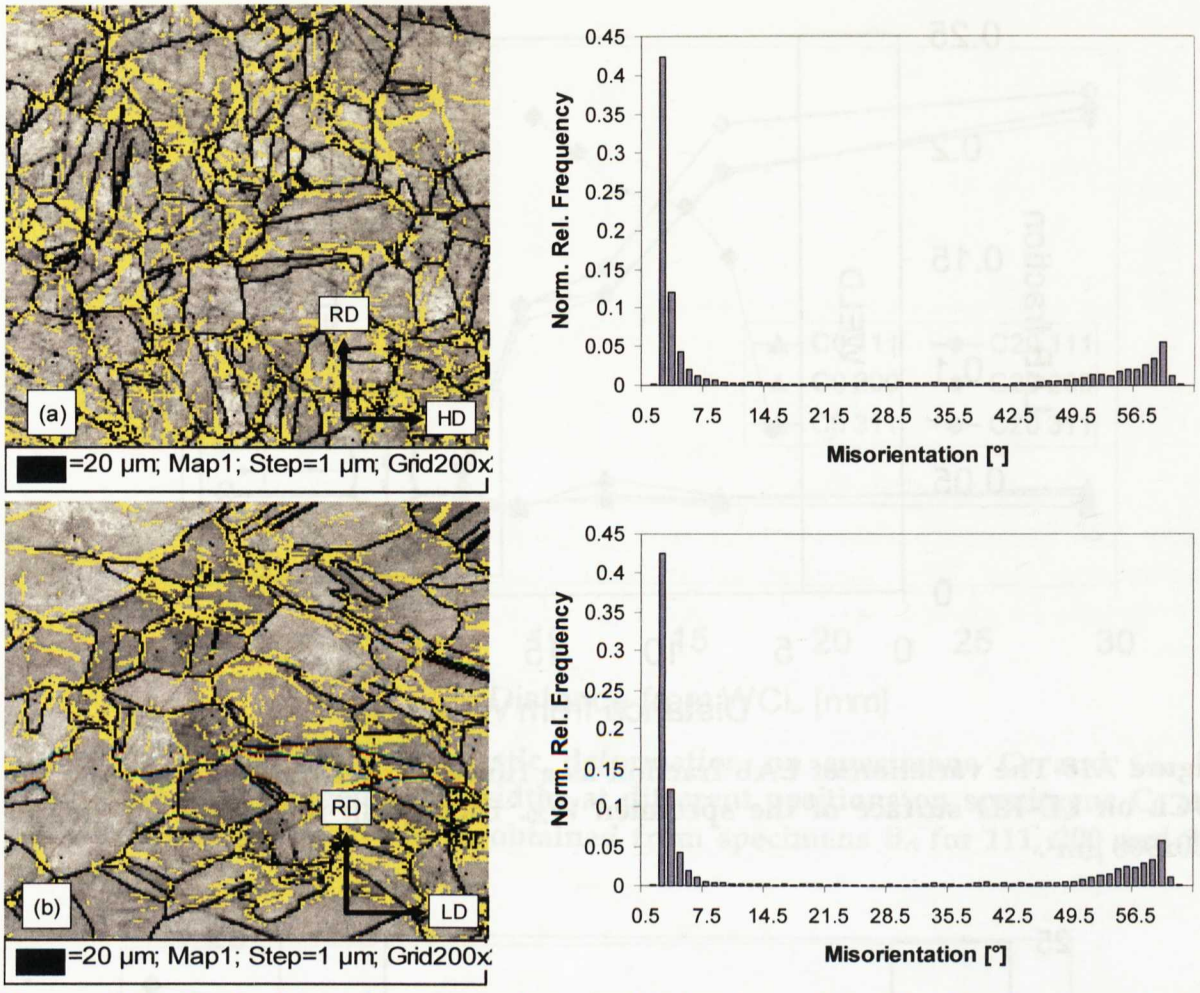

Figure 7.17 Grain boundary mapping and misorientation distribution graph for parent sample P_{25} on HD-RD (a) and LD-RD (b) planes. Misorientations greater than 15° are high angle grain boundaries (HAGB) and are coloured with black. Misorientation angle 2-15° represents low angle boundaries (LAB) and are coloured with yellow. (LD: longitudinal direction of the tube, HD: hoop direction, RD: radial direction)

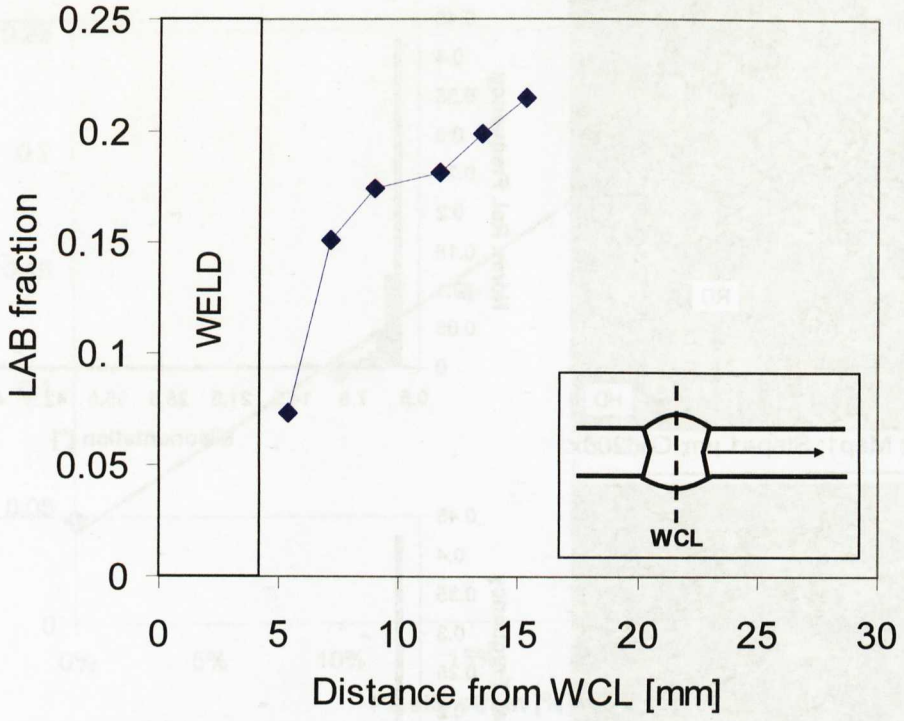

Figure 7.18 The variation of LAB fraction as a function of distance away from the WCL on LD-RD surface of the specimen W_{20}. Each point represents an area of 300x900 μm^2.

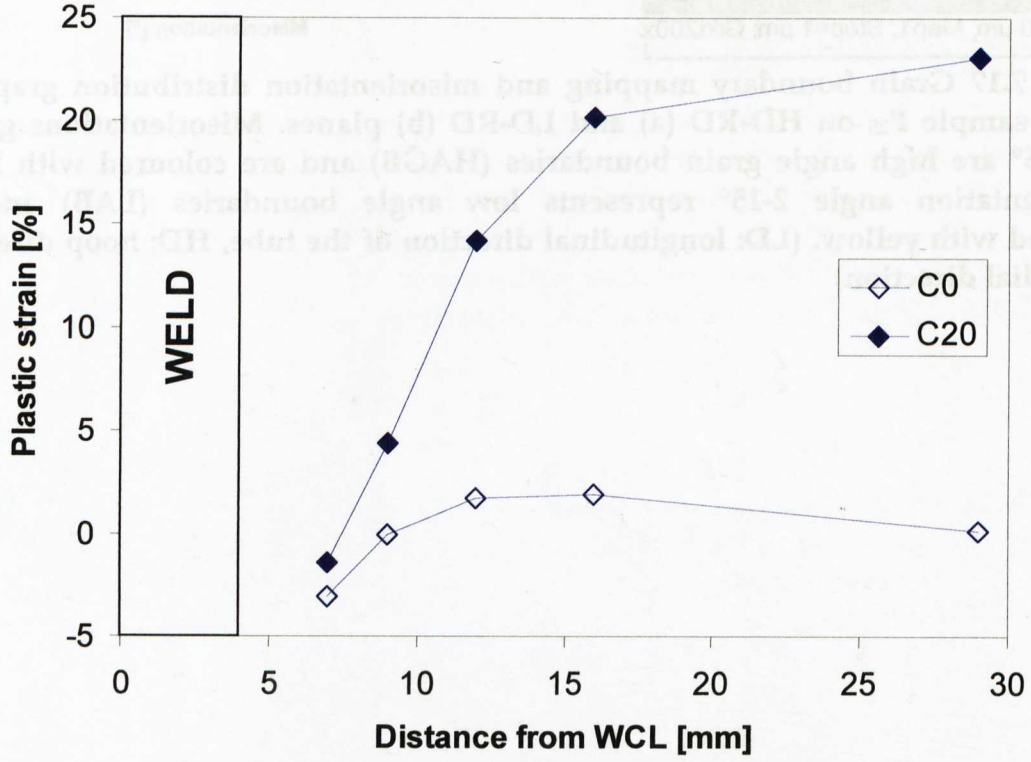

Figure 7.19 Prediction of plastic deformation on specimens C_0 and C_{20} by calibrating the anisotropy strains at different positions on specimens C_0 and C_{20} with the anisotropy strains obtained from specimens B_n.

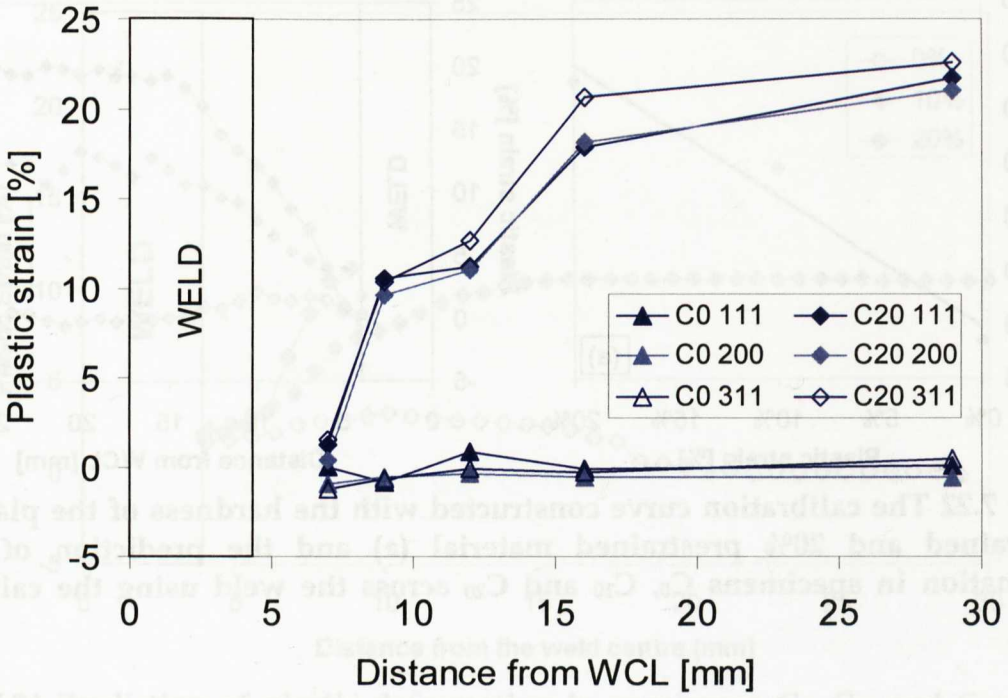

Figure 7.20 Prediction of plastic deformation on specimens C_0 and C_{20} by calibrating the averaged peak widths at different positions on specimens C_0 and C_{20} with averaged peak widths obtained from specimens B_n for 111, 200 and 311 planes.

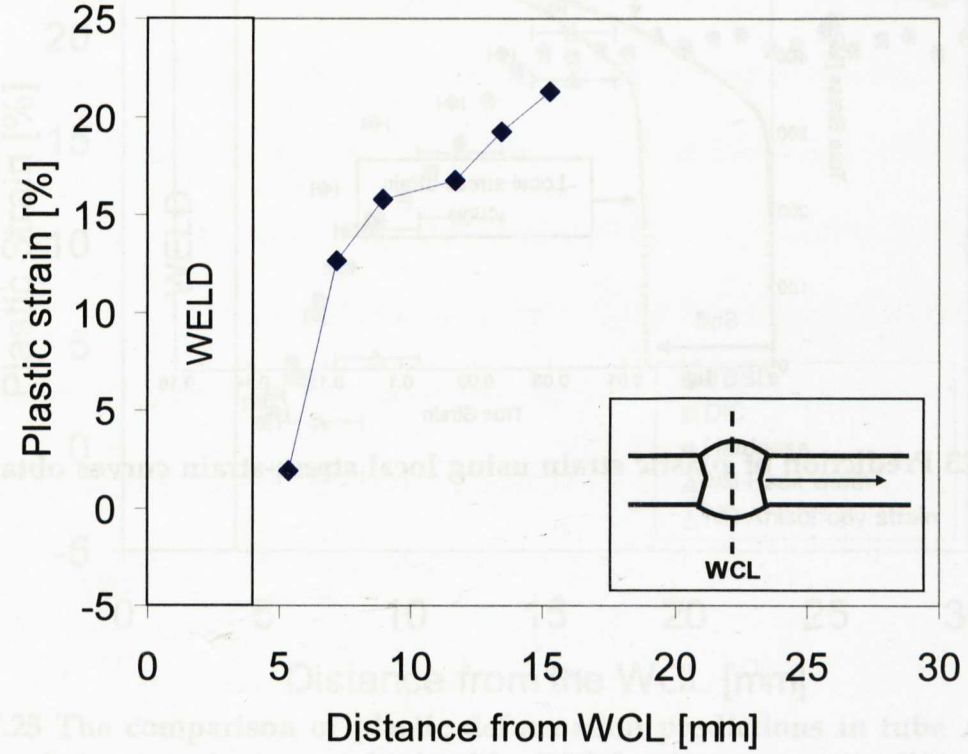

Figure 7.21 Prediction of plastic deformation on specimens W_{20} by calibrating the LAB fraction at different positions on specimen W_{20} with LAB fraction obtained from specimens P_n.

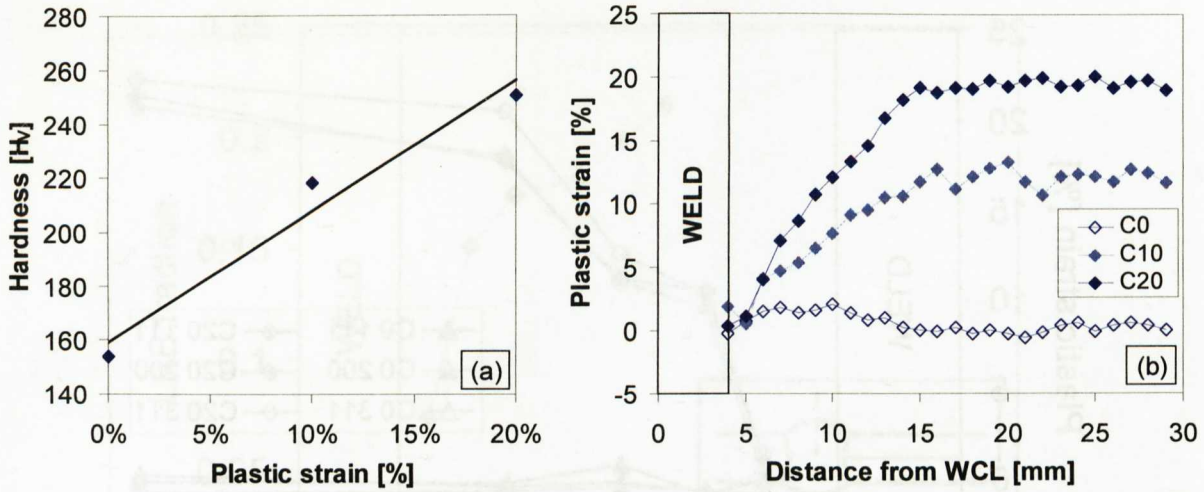

Figure 7.22 The calibration curve constructed with the hardness of the plain, 10% pre-strained and 20% prestrained material (a) and the prediction of plastic deformation in specimens C_0, C_{10} and C_{20} across the weld using the calibration curve

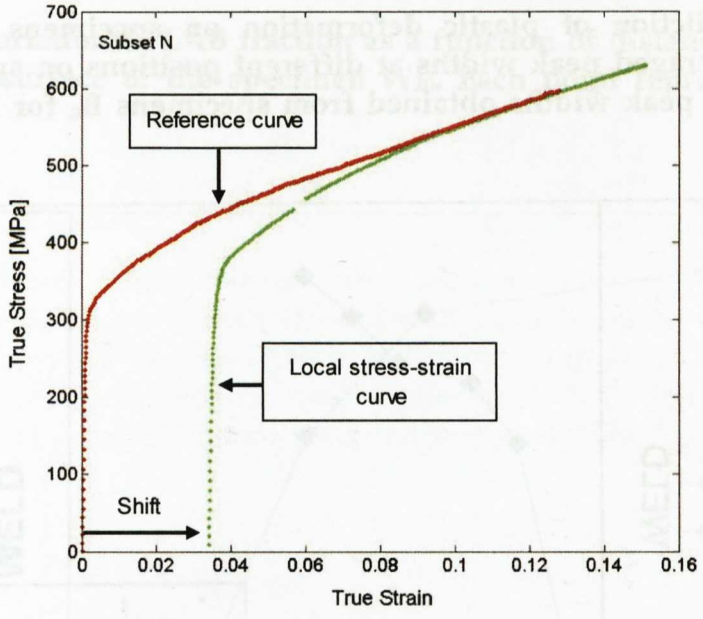

Figure 7.23 Prediction of plastic strain using local stress-strain curves obtained by DIC

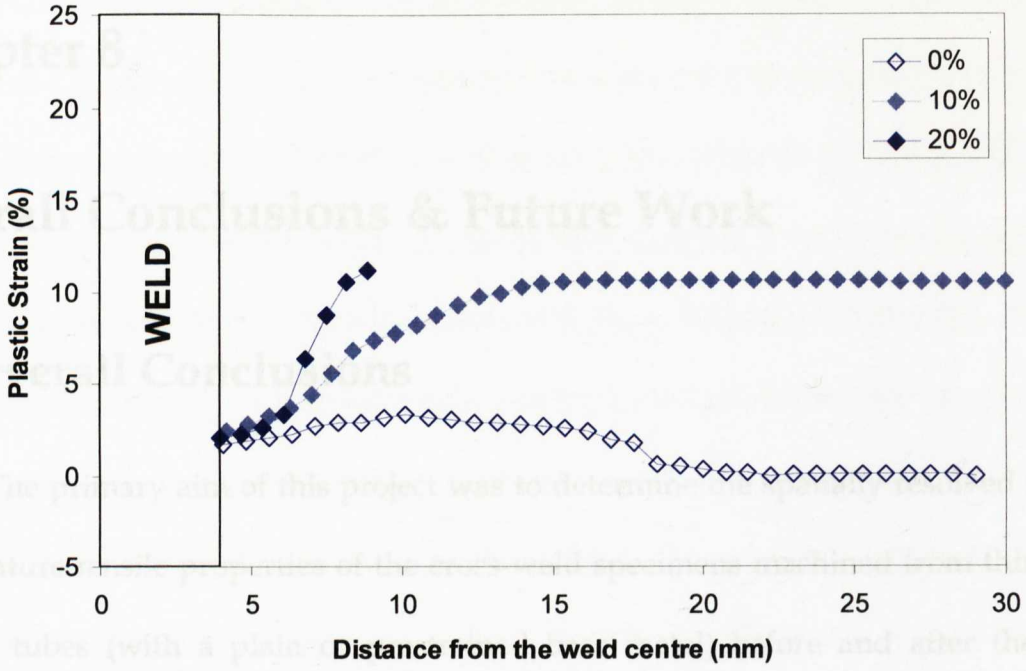

Figure 7.24 Prediction of plastic deformation in specimens C_0, C_{10} and C_{20} across the weld using the local stress-strain curves obtained by DIC

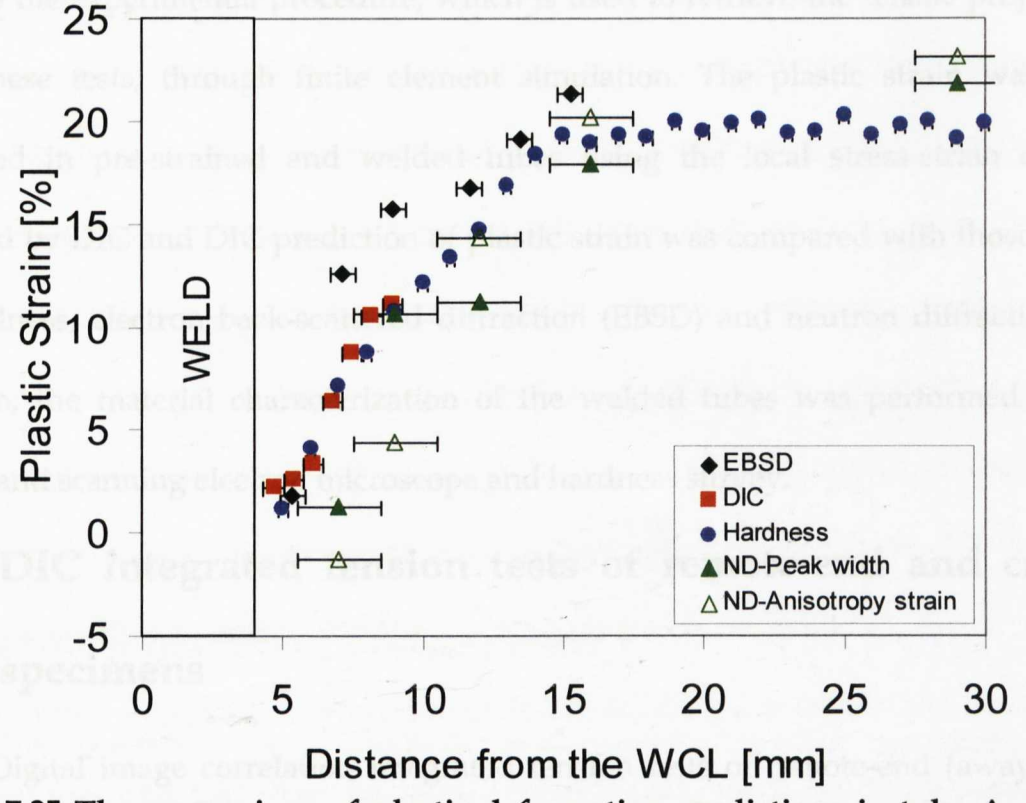

Figure 7.25 The comparison of plastic deformation predictions in tube A_{20} using EBSD, local stress-strain curves obtained by DIC, hardness, neutron diffraction 111 peak width measurements (ND-peak widths) and anisotropy strain (ND-anisotropy strain) and. Horizontal bars show the covered area where the measurement is done.

Chapter 8

Overall Conclusions & Future Work

8.1 Overall Conclusions

The primary aim of this project was to determine the spatially resolved room-temperature tensile properties of the cross-weld specimens machined from thin wall welded tubes (with a plain or prestrained base metal) before and after the heat treatment by using digital image correlation (DIC) integrated tension tests and to validate the experimental procedure, which is used to retrieve the tensile properties from these tests, through finite element simulation. The plastic strain was also predicted in pre-strained and welded tubes using the local stress-strain curves obtained by DIC and DIC prediction of plastic strain was compared with those done by hardness, electron back-scattered diffraction (EBSD) and neutron diffraction. In addition, the material characterization of the welded tubes was performed using optical and scanning electron microscope and hardness survey.

8.1.1 DIC integrated tension tests of remote-end and cross-weld specimens

Digital image correlation integrated tension tests of remote-end (away from the weld) and cross-weld specimens were successfully performed with a proper

alignment of the test specimen in the loading unit. DIC strain measurements were verified by using extensometer and strain gauges.

The effect of manufacturing steps (prestraining and heat treatment) on the mechanical properties of the plain tube material was determined by the tension tests of tube remote-end specimens. It was found that the strength increases with prestraining whereas the ductility decreases. After the heat treatment at 1050°C for 15 minutes the effect of prestraining disappeared; the strength of the heat treated specimens drops below that of the plain tube material and the loss in ductility after prestraining was observed to recover.

The effect of welding and heat treatment on the mechanical properties was investigated by the tension tests of the cross-weld specimens with plain and prestrained base metal. DIC is a powerful technique to determine the spatially resolved mechanical properties on cross-weld specimens. In order to extract spatially resolved mechanical properties on the cross-weld specimens, local stress-strain curves were constructed using DIC local strain measurement and global load data from the test frame. Anomalies were observed on some of the local stress-strain curves obtained from the weld-affected zones of the cross-weld specimens with prestrained base metals. To understand whether these anomalies are real or not, the tension test of a cross-weld specimen with a high strength mismatch between the weld metal and the base metal was simulated using bi-material and multi-material finite element models. Finite-element simulations showed that there are localized stress and strain regions, therefore, the distribution of the stress and the strain in the loading direction in a cross-weld specimen (with a high strength mismatch) under

tension is not similar to that in a homogeneous standard tensile test specimen. The numerical local stress-strain curves obtained from the multi-material model following the same experimental procedure to construct the local stress-strain curves confirmed that anomalies may appear as a result of the combination of the real material effect and the experimental procedure but they are not very detrimental to extract the local 0.2% offset proof strength. The variation of 0.2% offset proof strength on cross-weld specimens was determined using the local stress strain curves which were constructed with the DIC. The variation of the proof strength variation was in good agreement with the hardness survey on similar cross-weld specimens. Evidence of strain hardening due to constraint and weld thermomechanical cycles was found in the plain base metal near the weld pool and evidence of softening was seen in the prestrained base metal. On the other hand, after the heat treatment, the effect of prestraining and welding is cleaned out and the strength along the specimen was almost homogenized. The determination of the 0.2% offset proof strength on cross-weld specimens with prestrained base metal was also verified using the multi-material FE model. It was found that the experimental procedure to predict the variation of 0.2% proof strength along a cross-weld specimen with a strength mismatch between the weld metal and the base metal is reliable.

8.1.2 Determination of plastic strain

The local stress-strain curves were also used to predict the plastic strain remaining in the welded tubes by shifting the curves with respect to the reference stress-strain curve of the plain tube material. Plastic strain is known to be detrimental for high temperature performance of austenitic stainless steel tubes [1]. Therefore, it

needs a proper quantification. The plastic strain in the welded tubes was also predicted by using hardness, neutron diffraction (anisotropy strain and peak width) and EBSD.

For EBSD and ND predictions, the crystallographic changes such as formation of low angle boundaries, dislocation density and residual strains as a result of plastic deformation were used. The low angle boundaries, which originate from the dislocation structures near the grain boundaries and inside the grains, were used for the prediction of plastic strain by EBSD. The increase in dislocation density results in the broadening of a diffraction peak width. The dislocation density was measured using neutron diffraction and used for the prediction of plastic strain. Residual strains remain in the material after plastic deformation. The residual strains on each family of crystallographic planes are different as a result of FCC crystal elastic and plastic anisotropy. The residual strains were measured by neutron diffraction and anisotropy strain, which is the difference between the intergranular strains on the *hkl* planes having two extremes of elastic stiffness [2], was calculated for the prediction of plastic strain.

For hardness, neutron diffraction (anisotropy strain and peak width) and EBSD predictions, the measurements done in the welded tubes were calibrated with those in the plain, 10, 15, 20 and 25% prestrained tube material. DIC, hardness and ND-anisotropy strain was able to show the strain hardening in plain base metal due to constraint and thermomechanical weld cycles. An overall comparison of the predictions was done for the 20% prestrained and welded tube. The predictions of plastic strain are in a good agreement. Particularly, DIC and hardness were observed

to produce very similar values and are very promising for the prediction of plastic strain.

8.1.3 Material characterisation

There is almost no effect of prestraining (<25%) on the grain size of the plain tube material. After heat treatment, it was found that there is no grain growth for plain tube material whereas the grain size of the prestrained material was doubled. It was also found that the heat treatment cleans out the dislocation structures.

There is very little effect of welding on the microstructure of the plain and prestrained base metal. No carbides and intermetallics were observed through the SEM examination, except a small amount (%50) enlargement in grain size very near the weld region. The microstructure of the weld metal includes ~5% delta-ferrite which is detrimental for high temperature performance since it promotes precipitation of carbides and intermetallics during aging at 500-900°C [3]. The effect of heat treatment on the microstructure of the welds is limited with the grain growth as discussed for the plain and prestrained tube material. It was also observed that after heat treatment the networks between the delta-ferrite are broken and its amount decreases to ~1%.

8.2 Suggestions for future work

The spatially resolved room-temperature tensile properties on the cross-weld specimens machined from the thin wall welded tubes (with a plain or prestrained base metal) before and after the heat treatment was successfully determined by using digital image correlation (DIC) integrated tension tests and the experimental

procedure was validated through finite element simulation. It would be better to produce more accurate simulations (may be a 3D simulation) of the test of the cross-weld specimens with prestrained base metal by improving the material input data and to compare the numerical results from improved simulation with DIC experimental results.

The spatially resolved room temperature tensile properties are intended to be used in the engineering assessment procedures for the structural integrity and the life time of the boiler welds [4]. The application of the DIC technique to measure local deformations of weld-affected zones under creep conditions at the operating temperatures of these boiler tubes would provide a better understanding of material behaviour at regions where failures in service initiate.

DIC technique is a very promising technique to monitor the local deformations and to determine the local mechanical properties in the vicinity of the weldments when it is applied to the tension test of cross-weld specimens including the unaffected base metal, heat-affected zone and the weld zone. In this project, it was found that stress/strain localization may occur due to the strength mismatch between different zones for a specific specimen design. It is also known that the size of the weld-affected regions may affect the stress/strain localization [5]. Therefore, in order to improve the determination of spatially resolved mechanical properties from DIC integrated tension test of cross-weld specimens by minimizing the stress/strain localization, it would be useful to develop a new procedure for cross-weld specimen design through FE simulations considering the size of the weld-affected regions and the strength mismatch between them.

Several techniques were used to determine the plastic strain remaining in the weld-affected region of the 20% prestrained and welded tube. The overall comparison of the predictions showed that all techniques have a similar trend. It was observed that DIC and hardness are in very good agreement. However, the calibration curves of the techniques apart from DIC still need more data points for an improved calibration curve.

8.3 References

[1] Wilshire B, Willis M. Mechanisms of strain accumulation and damage development during creep of prestrained 316 stainless steels. Metallurgical and Materials Transactions A 2004;35:563.

[2] Daymond MR, Bourke MAM, Von Dreele RB, Clausen B, Lorentzen T. Use of Rietveld refinement for elastic macrostrain determination and for evaluation of plastic strain history from diffraction spectra. Journal of Applied Physics 1997;82:1554.

[3] Marshall P. Austenitic Stainless Steels: Microstructure and Mechanical Properties: Elsevier Applied Science Publishers, 1984.

[4] Spindler M. Post-weld heat treatment of austenitic stainless steel welds in boiler units (Personal communication). 2011.

[5] Kim Y-J, Oh C-S. Finite element limit analyses of under-matched tensile specimens. Engineering Fracture Mechanics 2006;73:1362.